DEPARTMENT OF GEOGRAPHY, UNIVERSITY OF SHEFFIELD

BUBBLES IN BASALTS

MEASURING AND MODELLING BASALTIC DEGASSING

Tom D. Pering

October 2015

A thesis submitted in partial fulfilment of the requirements for the degree of Doctor of Philosophy

Abstract

Basaltic degassing is driven by the release of CO_2, H_2O, and SO_2. Hitherto, the measurement of SO_2 has been commonplace due to the lack of significant ambient atmospheric content. UV camera technology is currently among the best of techniques to measure this SO_2 release from volcanoes given its high spatial and temporal resolutions. Given that an elevated CO_2 flux can be an indication of magma movement at depth, a reliable method of measuring this species at similarly high temporal resolutions would be valuable. A technique making this possible is described here. This technique combines measurements of SO_2 flux at Mt. Etna, using a UV camera, with CO_2/SO_2 gas ratios, which when multiplied together allow the creation of a contemporaneous CO_2 flux datasets at a time resolution of ≈ 1 Hz. This also allowed the comparison of degassing with infrasonic and seismic datasets. This comparison was facilitated by the development of a new analysis technique to investigate correlative trends between noisy environmental datasets. The technique works by combining the continuous wavelet transform of two separate signals, with correlation of their respective coefficients at matching timescales using Spearman's rank to produce a visually intuitive graphical plot. This revealed intriguing links between CO_2 degassing and seismicity.

Stromboli is renowned for its regular explosive activity. Through a permanent network of UV cameras at the summit area, a large number of explosive (120) and puffing events (80) were characterised in terms of their explosive and coda masses, termed the total strombolian event mass. Through this analysis, it was discovered that a large proportion of gas for each strombolian event is contained within the coda, ≈ 53 to 75% and for hornito events ≈ 70 to 84 %. The events were also characterised into six separate groups according to gas release pattern following the main eruptive burst. Through computational fluid dynamical simulations, for a range of appropriate strombolian eruption gas masses, the results demonstrated that there is potential for the release of daughter bubbles from the base of rising slugs. These daughter bubbles act to reduce the mass of slugs and can make slug flow unsustainable. Models were initiated over a suitable range of event masses, which demonstrated that ≈ 43 to 69% of the initial slug masses was released into the daughter bubble train. By applying the average mass loss rate, of ≈ 13.2 kg s^{-1}, with total event masses, slugs are unlikely to be self-sustainable below depths of ≈ 740 m. A non-linear relationship between the dimensionless inverse viscosity term, N_f, and mass loss rate was also discovered.

Also noted for its explosive activity is Mt. Etna. This activity includes hard to measure strombolian activity. During a rare period of activity at the Bocca Nuova summit crater ≈ 27 minutes of frequent but mild strombolian behaviour was captured using a UV camera. Given the unorthodox use of a rock background for the reflectance of light, calibration was tested and performed successfully on a basaltic background at the summit. Results show an SO_2 mass range of ≈ 0.1 – 14 kg and a total gas mass range, on combination with measured Multi-GAS ratios, of ≈ 0.2 – 74 kg. Compared to events at Stromboli the activity was more frequent with an ≈ 4 s modal repose and with much lower overall masses. On investigating temporal trends between events it was observed that the largest mass events were followed by longer repose periods before another event occurred, smaller events occurring more frequently, a feature which is termed repose gap behaviour. Given the rapidity and mass of events it is reasonable that this activity was driven by gas slugs and that they were travelling in close proximity to each other. Using existing fluid dynamical models for the wake interaction length, an area behind a slug where a trailing slug can begin to interact with a leading one, it is possible that slugs are close enough to interact and coalesce. Indeed, this would provide a plausible mechanism for the repose gap.

Building on the observations in the field at Mt. Etna a series of analogue laboratory experiments and computational fluid dynamics models were devised to investigate rapid strombolian activity, that driven by slugs. Behaviour of slugs acting independently of one another in a single-slug volcanic regime have been investigated thoroughly, however, the behaviour of slugs in a multi-slug volcanic regime have been neglected, largely a result of its comparative complexity. Laboratory experiments allowed the investigation of a series of average gas flow rates and hence slug lengths (i.e. overall gas volume fractions). The rates of expansion were also varied to simulate slug flow at depth and nearer to the magma surface. In particular, the process of coalescence was investigated. By comparing slug length at burst with repose time the repose gap feature was also identified. Given that values for rise speed, liquid, and conduit dimensions are known, this enabled the definition of the minimum period of repose as the wake length plus the length of the slug all divided by the rise speed of the base of the slug. This relation is validated successfully on the laboratory data and also on the collected Etna data. Additionally the laboratory analysis identified a previously unidentified feature whereby coalescence can occur between rising slugs, even when the trailing slug base is rising at a slower speed than the leading. This is likely related to the expansions of gas slugs. Computational fluid dynamics identified similar processes whereby the gap between

identically massed slugs was maintained by slug expansion which acted to increase the speed of slugs above them. It is only when slugs are initiated within the wake length that coalescence occurs. Further relationships were discovered between slug rise speed and gas volume fraction, whereby the average rise speed of a slug increases with regime volume fraction, and burst slug length and volume fraction.

Finally, building on the repose gap observations and developed relation, the observed relationships between slug length and gas rise speed with gas volume fraction are used to develop two separate models categorising the styles of volcanic activity which will be prevalent. The first, slug length model, is based upon repose time and slug lengths, with the second based upon overall volume fraction and repose time. The slug length model splits activity into: passive, puffing, strombolian explosive and strombolian rapid. This model performs well when applied to strombolian events, successfully differentiating between explosive and passive events. The volume fraction model applies fluid dynamical relationships for transitions to churn and annular flow, in addition to the already defined strombolian relationships, assumed here to play some part in defining the transition to hawaiian lava fountaining activity. This allows the definition of critical volume fractions above which large gas slugs or pockets can burst with increasing frequency until full lava fountaining behaviour is realised. Both models allow eruption parameters to be estimated via the delay time between events or vice versa. On comparison of known correlative relationships between gas emissions and seismicity a log relationship is discovered when all events are normalised to comparable parameters, suggesting that seismicity could also be incorporated into such a model in the future. In particular, the latter volume fraction model is the first step in developing a unifying theory of basaltic degassing based on a varying delay between events and could be particularly useful when used in tandem with real time gas emission data for eruption forecasting and understanding the fluid dynamical flow processes occurring in the sub-surface.

Acknowledgements

The following is an allegory of my PhD journey.

This Hobbit lived in a quiet part of Middle Earth called Hobbitfield. Hobbitfield was a curious place, populated by all manner of folk, from dark wizards to tree people. The tree people were friendliest but unusual in their geographically stereotypical ways. Anyhow, this Hobbit met Gandalf, who was a friendly chap and famous for appearances in Hogue, this Hobbit discovered that Gandalf had flying fireworks, but that they no longer flew. This Hobbit was immediately sent on an adventure to the western shores to meet Gandalf's faithful companions.

The western shores were beautiful but not as western as expected. This is when this Hobbit met Radagast. Unexpectedly Radagast and his faithful ninja squirrel had vacated the forests and were also involved in the budding firework industry. Curiously the ninja squirrel wore glasses. Radagast's fireworks didn't fly. Balotelli, who also liked fireworks, lived on the western shores. The ninja squirrel enjoyed mysterious ticking noises. This Hobbit was employed by Sauron, Suaron had a companion, who had met Azog the Defiler, or so he said.

Back to Hobbitfield and this Hobbits first house. Back to the western shores, where nectars blood red and coal black were consumed in excess, somehow leading to the discovery of a tome. Sam-wise read the tome and found it wanting. Back to Hobbitfield. Then to the eastern shores, which could also be western, this Hobbit couldn't rightly say. The penguins were there, but these penguins were from Middle Earth and liked the warm. This Hobbit liked penguins.

Dragons are the true goal, this hobbit went searching for Smaug the dragon at the Misty Mountain, you see, dragons, collect fireworks, all Hobbits need fireworks. The Misty Mountain was beautiful. This Hobbit met the people of Gondor, there were penguins with them. The Misty Mountain was well supplied with taverns, but to get off the Misty Mountain required a magic egg. The king of Gondor had a magic egg. The magic egg, some people from Gondor, the penguins and the Lady Galadriel escaped Smaug.

This Hobbits house had moved. Strider liked playing chess with Hobbits. This Hobbit moved again. The Lady Galadriel discovered a way to collect fireworks without a dragon. This

Hobbit moved again. Fireworks now dangled from Gandalf's ears. Strider liked tomes, but preferred epics, which contained the same tomes. Sam-wise didn't like tomes or epics at all.

The serious bit.

Prior to 2010, a career in volcanology was a fledgling hope on my radar. Three things played a role in inspiring a further interest: Earth Sciences lectures at the University of Reading but in particular lecturer Dr Hubbard, a stand-in for making those lectures and one of the most enthusiastic lecturers about his topic that I experienced at Reading, the eruption of Chaitén in 2008 which produced spectacular images (see Fig. 1.1. in Chapter 1), and the seminal book written by Francis and Oppenheimer who's captivating writing and explanation of volcanic activity inspired and piqued my intrigue to delve deeper.

I also have to thank the people who inspired my study in Geography. Firstly, to Miss Robson at Robert Mays School who's enthusiasm for the subject, particularly the physical geography side, lead to further study at A Level. Giving a presentation wearing female wigs and explaining ox-bow lakes particularly stick in my head. I would also be remiss for not mentioning Mr Smith particularly and other colleagues (Anne-Marie, Matt Perris) from the Geography Department at Lord Wandsworth College. Attending Lord Wandsworth was a turning point for me, in what up to this point did not look like an academic future.

From my Masters degree I have to thank Hugh Tuffen, Steve Lane and Mike James. Particular mentions for making the MSc in Volcanology and Geological Hazards a thoroughly enjoyable time go to: Matt Green, Kelly Johns, Ben Leonard, and Verity Grimsey. I also have to particularly thank Steve Lane and Mike James for contributions during my PhD.

From my PhD, my obvious thanks go to supervisor Andrew McGonigle for showing faith in my ability, giving me the opportunity to go to interview at Sheffield, and continued guidance and assistance over the past three years. Others within the department: Edward Hanna, Rob Bryant, Alan Smalley, Rob Ashurst, Emma Shelton and Michael Boultby (the latter two for endless strange finance requests). I would also be remiss for not mentioning those who have made this part of my journey an enjoyable one: Amy Jowett, Kate Orgill, James Douglas, Phil Jones, and Hannah Barrett.

From the Sicilian contingent, my other supervisor Alessandro Aiuppa and Giancarlo Tamburello for their unwavering support, advice and collaboration. Also from Italy: Marcello Bitetto, Sergio Calabrese (for the enjoyable Pizzi Deneri campaigns) and Andrea Cannata.

To all the other people I have encountered at conferences or fieldwork, including: Hannah Reynolds, John Browning, Tehnuka Ilanko. My apologies for the numerous others that I have almost certainly forgotten to mention.

To my family and friends. And last but by no means least, the support and encouragement of my wife, throughout this journey and undoubtedly beyond.

Contents

List of Acronyms and Abbreviations

AGU = American Geophysical Union
BN = Bocca Nuova Crater
CCD = Charged-Coupled-Device
CFD = Computational Fluid Dynamics
CO = Carbon Monoxide
CO_2 = Carbon Dioxide
COSPEC = Correlation Spectrometer
CVF = Critical Volume Fraction
CWT = Continuous Wavelet Transform
DOAS = Differential Optical Absorption Spectroscopy
DSLR = Digital Single-Lens Reflex camera
EGU = European Geosciences Union
FLAME = FLux Automatic Measurement
FTIR = Fourier Transform Infrared Spectroscopy
GMT = Greenwich Mean Time
GPS = Global Positioning System
H_2 = Hydrogen
H_2O = Water
H_2S = Hydrogen Sulphide
ICA = Integrated Column Amount
INGV = Istituto Nazionale di Geofisica e Vulcanologia
IVA = Integrated Volume Amount
NEC = North-East Crater
NSEC = New South-East Crater
PSD = Power Spectral Density
RMS = Root-mean-square
RSAM = Real-time seismic amplitude
SEC = South-East Crater
SiO_2 = Silicon Dioxide
SO_2 = Sulphur Dioxide
UV = Ultra-violet
VLP = Very-Long-Period
VOR = Voragine Crater

Notation and Greek Letters

Listed in order of first use

Chapter 1

I = Light intensity
λ = Wavelength
σ = Absorption cross-section
N = Number of molecules in light path
L = Plume width
A = Absorption
IP = Plume image
IB = Background image
α = SO_2 absorption filter
β = Non-SO_2 absorption filter

Chapter 2

Ψ_0 = Morlet wavelet function with associated dimensionless time frequency
η = Dimensionless time frequency
ω_0 = Wavelet dimensionless frequency
t = Time-step
x_n = Target signal
N = Maximum Nyquist defined scale
n = Length of the target signal or length of the dataset
$*$ = The complex conjugate
W_n = Wavelet
S = Wavelet Scale
r_s = Spearman's rank correlation coefficient
d = Ranked Spearman's output
t_d = Turbulent diffusion
D = Atmospheric dispersion coefficient
u = Plume speed

Chapter 3

λ' = Falling film thickness
N_f = Dimensionless inverse viscosity
ρ_m = Magma density
μ = Magma viscosity
g = gravity
r_c = Conduit radius
Fr = Froude number
u_{sl} = Slug base rise speed
P = Pressure

V = Volume
n = Number of moles
R = Real gas constant
T = Temperature

Chapter 4

l_{wake} = Wake length
l_{min} = Wake interaction length
r = Radius
h = Height
A' = Ratio of slug radius to conduit radius
r_{sl} = Slug Radius
λ = Ratio of specific heats
L = Slug length
L_0 = Initial slug length
P_0 = Initial pressure over the slug
Re_b = Reynolds bubble number
u_{slsw} = Rise speed of a slug swarm
SF = Scaling correction factor
AF = Acceleration factor
Eo = Eotvos number

Chapter 5

Rep_{min} = Minimum repose period
$Rep_{transition}$ = Transition repose period

Chapter 6

P^*_{slim} = Dimensionless measure of burst vigour
P_{surf} = Atmospheric pressure
r_b = Bubble radius (i.e. not slug radius)
u_b = Rise speed of a bubble
ρ_g = Gas Density
a_{cr} = Maximum bubble radius
gvf = Gas volume fraction
u_{th} = Theoretical slug base speed
l_E = Entry length of the bubble or slug
u_m = Combined rise speed of the liquid and gas
D = Conduit diameter
ρ_l = Liquid density
U_{gs} = Gas rise speed
σ = Surface tension
d_{th} = Theoretical displacement
d_r = Real displacement

v = Seismic wave velocity
r_{source} = Source radius
a = Absorption coefficient of granite
k = Wave number
w = Angular frequency

Figure Summary

Fig. 5.21: Here, tracks for experiments C9 (left hand column) and C15 (right hand column) are presented. (c), (d), and (e) display the rise speeds of the leading, middle and lower slugs respectively for C9 and (h), (i), and (j) for C15. The closer the slugs are to one another, the greater the effect of slug expansion on rise speed. This is particular clear in (f), where slug expansion appears to push the slug above it at a faster pace. The gap plus trailing length in each instance is observed to increase, indicating that the leading slug is indeed rising at a faster pace than the trailing slug. The theoretical speed is shown in gray (c, d, e ,h, i, j) for reference. **p.116**

Fig. 5.22: Here, tracks for experiments C13 (left hand column) and C18 (right hand column) are presented. As per Fig. 5.21, (c), (d), and (e) refer to the leading, middle and trailing slug speeds, and speeds for the four slugs are depicted in (g), (h), (i), and (j). For experiment C13 one coalescence event occurs, the middle slug into the upper slug. Following on from this the gap plus trailing length is seen to increase again demonstrating that this can increase even when coalescence occurs. C18 again demonstrates this increase in slug rise speed, influenced by the slug below. The theoretical speed is shown in gray (c, d, e, g, h, i, j) for reference. **p.117**

Fig. 5.23: Here, burst data pertaining to data collected during Etnean activity at the Bocca Nuova crater (described in full in Chapter 4) are presented. All data have been converted to burst volumes. Above the data plotted on a normal plot, below the data plotted on a log-log plot. Also added to both plots is the repose gap line (equation 5.4) and the repose transition line (equation 5.5). For a magma density of 2600 kg m^3, viscosity of 2000 Pa s^{-1} and conduit radius 1.5 m these parameters seem to match well with the observed activity, with the exception of a number of bursts less than 1 m^3 in volume. **p.118**

Fig. 5.24: Over 34,000 strombolian events from activity on the NEC on the 17th July 2014, which generated an infrasonic pressure pulse, are plotted here. Two areas of interest are identified, the first red line indicates a repose gap type feature, while the blue circled area appears to indicate an area which may break this feature. It is possible that the red line is related to the repose gap behaviour, while smaller bursts, associated with lower acoustic pressures can disrupt this trend. Data courtesy of Andrea Cannata (INGV, Osservatoria Etneo). **p.119**

Fig. 5.25: Here, the repose gap and transition equations are applied to data from Kremers et al. (2013) relating to strombolian activity from Yasur volcano. Again the criteria seem to hold up well, given parameters for magma density of 2600 kg m^3, viscosity of 1000 Pa s^{-1} and conduit radius of 1.5 m (this is also the dimension used to convert length data to volume data). Only one burst may have been influenced by those preceding it, while all others can be considered to be "single" bursts. **p.120**

Fig. 6.1: Reproduced from Chapter 1 to illustrate the flow regimes which drive basaltic volcanic activity. The flow regimes highlighted with red text, particularly mist flow, indicate flow regimes with no direct field analogue evidence or quantification. **p.126**

Fig. 6.2: Idealised bubble length model indicating the areas which are defined by the equations 6.1 to 6.6 in the text. In (a) a passive or effusive area where bubbles are near to spherical. In (b) bubbles sized between spherical transition and before a bubble becomes a slug. In (c) an area defined using equation 6.4 which indicates the burst of slugs in a non-explosive manner – i.e. puffing. In (d) all slugs with lengths above the puffing area in (c) will be explosive, while in (e) slug bursts occur so rapidly that they can begin to interact, the rapid strombolian area. The repose gap, where no bursts can occur is shown in (f). In (g) and (h) it is assumed that as bubbles get smaller they can burst more rapidly. **p.131**

Fig. 6.3: Critical volume fractions (*CVF*), for a range of conduit radii, conduit lengths, and gas volume fractions. This demonstrates that by increasing the conduit length the *CVF* for transitioning towards lava fountaining decreases, while decreasing the conduit radius achieves the same result. **p.133**

Fig. 6.4: In (a) the gas transition speeds to churn flow are displayed for a range of slug lengths and conduit diameters (D). These are calculated using equation 6.12. In (b) the gas at which transition speed to annular flow occurs is displayed for a range of magma densities. These speeds were calculated with equation 6.13. **p.134**

Fig. 6.5: Demonstrating the idealised volume fraction model. Here the colours represent the different areas which the model defines, similar to the areas in Fig. 6.2. The blue passive and puffing area refers to all single bubbles and slugs which do not burst explosively. The yellow area represents all slugs which burst as though they are in a single slug regime, and the purple area those in a rapid environment. The orange and pink areas show the volume fractions and repose times where activity can be assumed to transition towards Hawaiian lava fountaining activity. At the same time the repose gap area reduces allowing individual bubbles or pulses to burst more rapidly. Also shown on this plot is a grey shaded area where only non-terrestrial activity could exist on the plot. **p.135**

Table Summary

Equation Summary

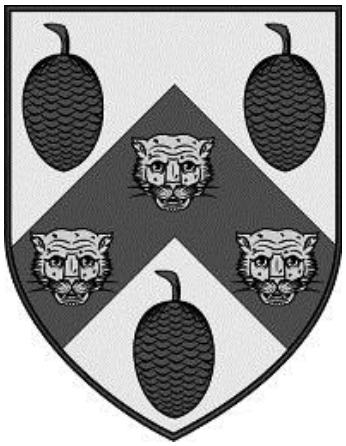

"*I fear I have tired you: but the subject of volcanos is so favourite a one with me, that it has led me on I know not how…*"

Sir William Hamilton
1769

1. Introduction

The aim of this chapter is to briefly introduce both the importance of monitoring volcanoes, in particular for basalts which are the focus of this thesis, and the types of degassing which are prevalent at such volcanoes. UV (Ultra-Violet) camera theory is introduced along with a number of previous studies demonstrating the utility of this technology. Finally the other theme of the thesis, volcanic conduit fluid dynamical modelling, is introduced, with particular reference to laboratory and computational studies.

1.1. The importance of volcanic monitoring

Volcanic eruptions are one of the most spectacular natural events to occur on this planet (Fig. 1.1.). With a large number of people living on or near to the flanks and at risk from these events (approximately 10% of Earth's population) predicting impending activity is a key focus for volcanologists (Peterson, 1986; Tilling & Lipman, 1993; Small and Naumann 2001). The major driver of this volcanic activity, ranging from basaltic to rhyolitic, and from strombolian to plinian, is gas (Mather, 2015). Monitoring and measuring gaseous emissions is therefore a vital part of eruption prediction. Volcanic monitoring of gas emissions can be performed in a variety of ways ranging from the use of satellites, which provide global but low temporal and spatial resolution of gas emissions from point sources (McCormick et al. 2014), to manual sampling (Giggenback, 1975; Symonds et al. 1994), and ground based remote sensing (Francis et al. 1998; Oppenheimer et al. 1998; Galle et al. 2003; Mori and

Fig. 1.1: The spectacular eruption of Chaitén, Chile with a lightning sheath surrounding the eruption column. (National Geographic, 2008).

Burton, 2006; Burton et al. 2007), see Fig. 1.2.

One of the major success stories with volcanic gas measurements was undoubtedly prior to the eruption of Pinatubo on the 15th June 1991, where the successful identification of a rapid increase in gas release in the weeks leading up to the eruption, in combination with seismic monitoring, led to the successful evacuation which saved thousands of lives (Harlow et al.

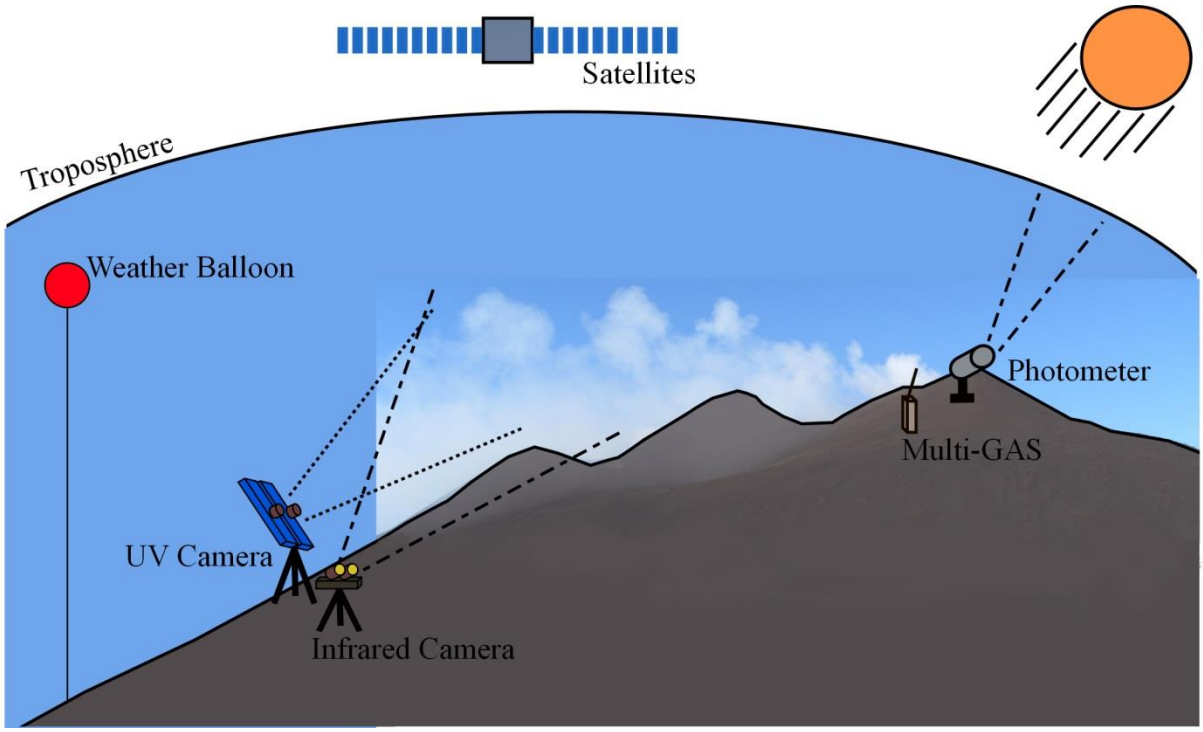

Fig. 1.2: Example methods for monitoring volcanic gas emissions. Drawings are overlain onto the view of the North-East Crater from the Pizzi Deneri volcano observatory .

1999). More recently, the recent volcanic activity in Iceland: Eyjafjallajökull, Grímsvötn, and Holuhraun (Bárðarbunga), has reiterated the importance of gas emissions to public health (Hansell and Oppenheimer, 2004) and aviation (Brooker, 2010; Gudmundsson et al. 2010). In particular the sustained basaltic fissure activity at Holuhraun contained echoes of the Laki fissure eruptions of 1783-1784, where the emission of large amounts of fluorine, in addition to other sulphurous gases (Stevenson et al. 2003; Self et al. 2005) caused widespread famine in Iceland (Vasey, 1991; Thordarson and Self, 2003), and potentially affected parts of Europe (Budd et al. 2011), including the United Kingdom. These events highlight the importance of monitoring volcanic gas emissions as both a forecaster of impending activity (Aiuppa et al. 2007) and monitoring emissions during events to predict dispersal of volcanic pollutants (Delmelle et al. 2002), and hence prevent avoidable deaths.

The obvious and devastating direct effects of volcanic eruptions include those involving pyroclastic density currents and lahars. Pyroclastic density currents are the hot clouds of ash, gas and rock which collapse from an eruption column and then rapidly move along the ground. Lahars occur when ashfall mixes with rainwater, or the rapid melting of snow, to create torrents which have the energy to carry large amounts of material and destroy homes. Here there are two infamous examples: firstly, the sudden flank collapse and pyroclastic density currents associated with the eruption of Mt. St Helens (USA) in 1980 which killed 57 people, (Bernstein et al. 1986). Secondly, in one of the most deadly recent volcanic episodes, when Nevado Del Ruiz (Colombia) erupted, causing pyroclastic density currents which mixed with snow and ice at the summit and generated lahars leading to the death of ≈ 23,000 people in Armero (Pierson et al. 1990; Voight, 1990).

The specific hazards of volcanic activity vary on a volcano-by-volcano basis. This thesis is particularly concerned with those caused as a result of basaltic degassing, which have been hitherto under-investigated at the high temporal resolutions necessary to delve into and understand the range of activities possible and their respective drivers. The next section outlines the most common types of basaltic degassing, and the specific drivers of each style, relevant to the content of this thesis.

1.2. Types of basaltic degassing

Basaltic volcanism is manifest in a variety of forms (Fig. 1.3), each driven by a different dominant flow regime (Fig. 1.4), with distinctive dominant bubble morphologies (Fig. 1.5). Basaltic volcanism can be split into three broad ranges of activity: effusive, passive and explosive. Effusive activity is specifically related to the production of lava flows from single or multiple vents. It can often be accompanied by minor explosive activity at the vent area. Passive activity encompasses the quiescent state of a volcano, involving the release of gas in a non-explosive manner from conduits, fumaroles, or lava lakes (Fig. 1.3). Passive degassing activity is dominated by the ascent and bursting of small spherical to deformed bubbles (see bubbles 1 and 2 in Fig. 1.5) at lower gas volume fractions in the flow (Fig. 1.4). This activity can be considered to be driven by a bubbly flow regime (Fig. 1.4), with bubbles that are both dependently and independently rising of the magma, which itself could be stagnant, downward or upward moving.

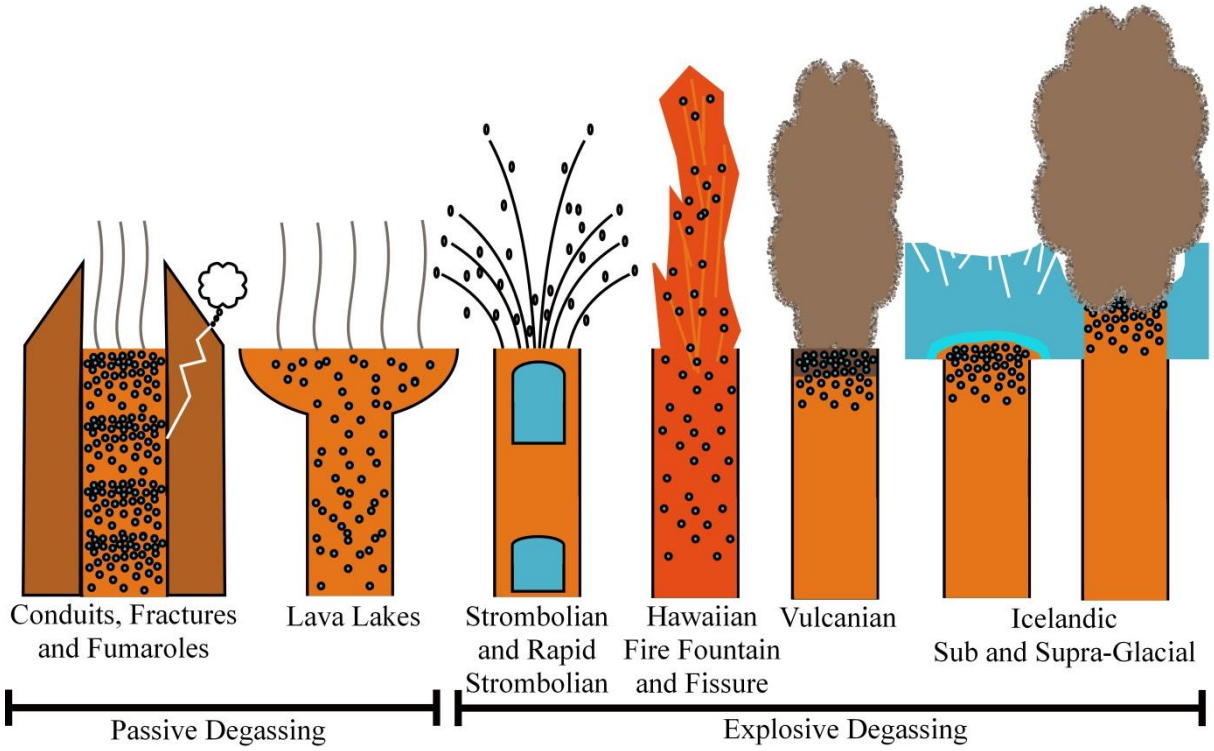

Fig. 1.3: The range of most common basaltic activities prevalent on the Earth, split into two main sections: Passive and Explosive Degassing.

The transition to explosive activity can be gradual or rapid (Parfitt and Wilson, 1995). As bubble size increases, the chances of producing explosive activity increase commensurately (James et al. 2009). The physics and fluid dynamics defining the rise speed and how these bubbles travel and interact also begin to change (Wallis, 1969). The major factors in defining eventual bubble sizes relate to their initial exsolution depth, and their ability to interact during ascent (Sparks, 1978). The overwhelming bulk of volcanic gases exsolve at depths of less than ≈4 km depth (Wilson, 1980; Gerlach, 1986; Giggenbach, 1996). As they ascend, each individual bubble experiences a reduction in pressure allowing the bubble to expand. It is this decompression which forces bubble forms and flow regimes to transition (Aloui et al. 1999).

Following on from a spherical or broadly spherical but deformed or elongated bubble, a bubble transitions to a "spherical cap" morphology (cap bubble for short, see bubble 3 in Fig. 5). A cap bubble rises at a speed which is limited by a falling film of liquid either side of the bubble, and hence the conduit width, with the rise speed also dependent on magmatic parameters (Viana et al. 2003; Llewellin et al. 2012). In cap form a bubble is unlikely to burst explosively (Wallis, 1969; James et al. 2009) but could be observed at the surface through the increased speed of gases at the surface, for example the puffing activity often referred to at Stromboli (Ripepe et al. 2002; Tamburello et al. 2012), and Mt. Etna (Tamburello et al.

2013). A cap bubble can be present in bubbly flow, through to cap and even in slug flow (Fig. 1.4). Cap bubbles could also be the drivers between the larger but passive bubble bursts at lava lakes (Bouche et al. 2010).

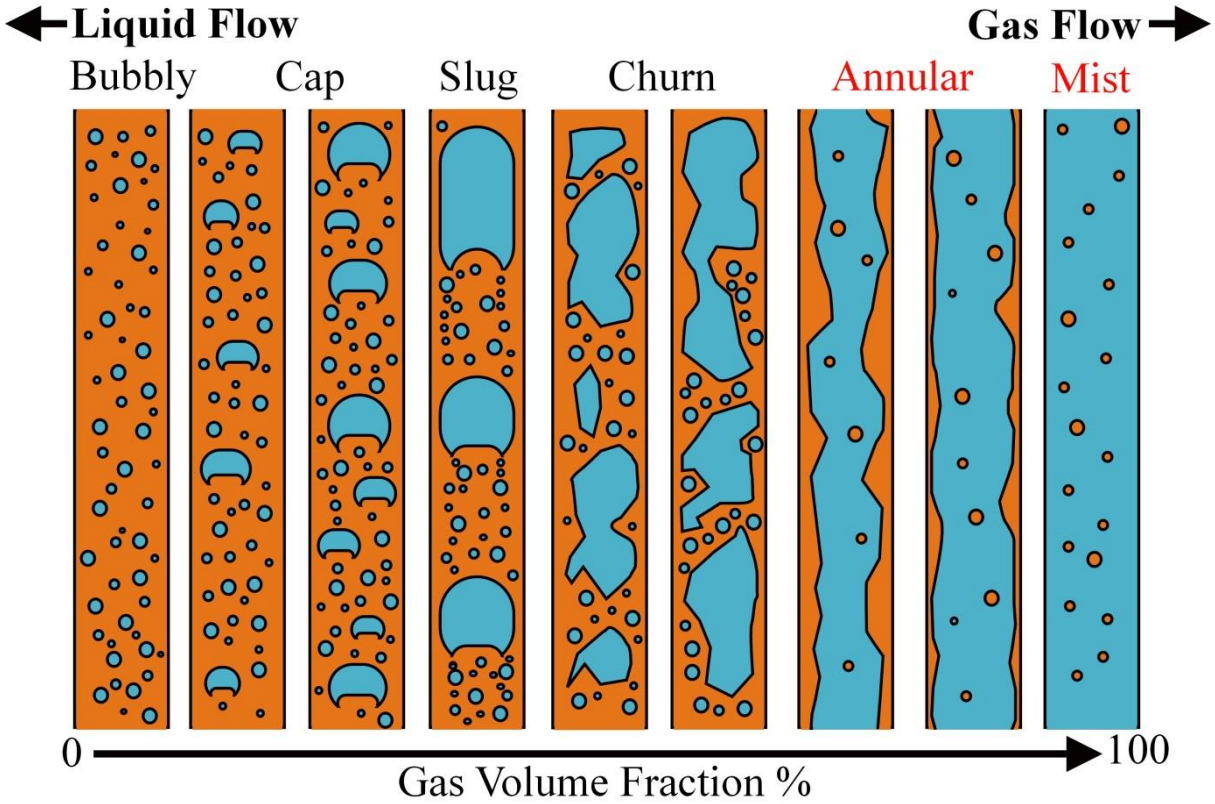

Fig. 1.4: Example flow regimes which can be present in liquids and magmas. Annular and Mist flow are highlighted red as there is no current direct proof that these are sustainable in terrestrial volcanism.

A cap bubble then graduates to a slug morphology, also termed a Taylor bubble. A bubble becomes a slug when the falling film around the sides reaches its minimum value and has a length equal to or above the diameter of the conduit (Davies and Taylor, 1950, Wallis, 1969). It is these slugs that expand rapidly and cause strombolian eruptions (Fig. 1.3) such as those at Stromboli. How such large slugs and rising gas masses are formed is still a matter of debate, although it seems that both potential formation mechanisms, be it the rise-speed dependent model (Wilson, 1980; Parfitt and Wilson, 1995) or foam collapse (Jaupart and Vergniolle, 1988; Jaupart and Vergniolle, 1989; Vergniolle and Brandeis, 1994) have merit at different volcanoes and for different activity conditions (Vergniolle and Jaupart 1990; Parfitt, 2004). Slugs are a major focus of this thesis. More in-depth detail on their behaviour is contained within chapters 4, 5, and 6. Similarly to a cap bubble, a slug, under certain conditions can still burst non-explosively at the surface (James et al. 2009).

If gas supply and gas volume fraction begin to increase, the flow regime will begin to transition towards churn flow. During churn flow, the normally axisymmetric shapes of gas slugs will begin to deform (bubble 5 in Fig. 1.5), breaking down the more predictable behaviour of gas slugs (Taitel et al. 1980). As volume fraction begins to increase again, a transition to annular flow will occur. It is during this transition that a change towards hawaiian lava fountaining will occur . Annular flow is characterised by a liquid film and core of gas which can also suspend liquid droplets within (Triplett et al. 1999; Seyfried and Freundt, 2000; Lane et al. 2001). Lava fountaining, which can occur from a single vent or fissure, involves the coupled ejection of large volumes of magma, which can then go on to feed lava flows, at speeds sufficient to push the fountain hundreds of metres above the vent. The final flow regime is mist or dispersed flow (Fig. 1.4). Here the gas phase completely disrupts the liquid film and is capable of entraining all of the liquid within the gas phase (Barnea, 1986; Triplett et al. 1999).

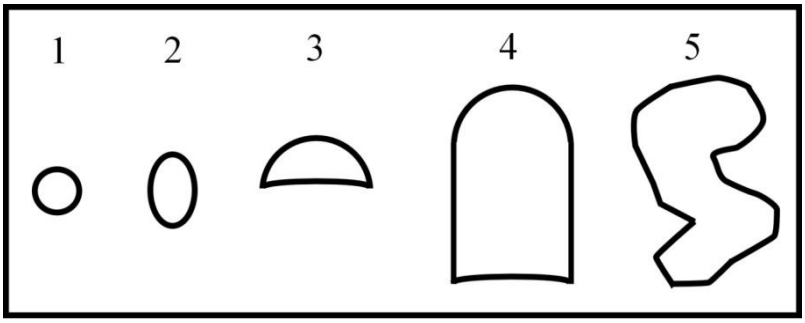

Fig. 1.5: Example bubble morphologies in a magma. 1, perfectly spherical, 2, deformed bubbles, 3, a spherical cap bubble, 4, a gas slug (sometimes referred to as a Taylor bubble), 5 – a deformed slug.

Other common forms of basaltic volcanism include vulcanian, typical of volcanoes such as Sakurajima (Fig. 1.6), typical Icelandic volcanism which can occur sub or supra-glacially (Fig. 1.3), and phreatic explosive volcanism which can occur on interaction with seawater. The current preferred method of measuring emissions from volcanoes in general, not only those which are basaltic, is the monitoring of SO_2, which, not only has a low background concentration, but absorbs strongly within the UV spectrum.

Of all the described degassing styles, passive degassing and strombolian activity have received the most focus. The overwhelming majority of such studies have only been quantitative in nature, with little consideration of the dynamics of the driving activity style, i.e. existing studies on gas emissions tend to list only released amounts of gas without considering how that gas reaches the surface. This thesis aims to address this research gap

through additional observations of basaltic activity and through comparison with mathematical and laboratory based models.

The next section provides an overview of SO_2 measurement techniques, including a more in-depth look at the method used within this thesis, the UV camera.

Fig. 1.6: Vulcanian eruption at Sakurajima, Japan.

1.3. A brief history of SO_2 measurement

Initially, the measurement of SO_2 was very limited and involved manual techniques such as direct sampling at fumaroles and vents (Symonds et al. 1994). Whilst these methods did allow a first determination of SO_2 flux (sometimes referred to as emission rate kg s^{-1}) there were a multitude of associated issues, including time resolution, the potential for contamination in transport of samples to the laboratory for analysis and the potential dangers or inaccessibility of the sampling area/summit of the volcano (Tamburello, 2011a).

In light of these difficulties, the benefits of using remote sensing techniques to measure gases became more apparent, including both airborne (i.e. satellites, not discussed here) and ground

based measurements. One of the earliest of these techniques was Correlation Spectrometry using Correlation Spectrometers (COSPECs; Newcomb and Millán, 1970; Moffat et al. 1971; Moffat and Millán 1971; Stoiber et al. 1983). This technique is based upon the solution to the Lambert-Beer Law:

$$I(\lambda) = I_0(\lambda) \cdot e^{-\sigma(\lambda) \cdot N \cdot L} \qquad \textbf{(Eq. 1.1)}$$

where *I(λ)* is the light intensity after passing through the plume (or target area), I_0 (λ) is the light intensity before passing through the plume, σ(λ) is the absorption cross-section for the particular gas of interested (e.g. SO_2), N is the number of molecules in the optical path and L is the plume width. SO_2 was quickly identified as an ideal target gas for these observations over the other common plume volatiles e.g., CO_2 and H_2O, due to its comparatively low background concentration and strong absorption features (Tamburello, 2011a).

COSPEC was then succeeded by Differential Optical Absorption Spectroscopy (DOAS) (Platt and Stutz, 2008). DOAS involved the use of smaller and less expensive USB spectrometers that were easier to use in a volcanic setting and involved analysis across the UV spectrum (McGonigle et al. 2002; Galle et al. 2003; Tamburello, 2011a). There are several differing DOAS techniques including: traversing DOAS, scanning DOAS and the cylindrical lens DOAS. Traversing DOAS, possibly the least useful of the three, involves travelling beneath a plume or area of interest (by car, boat or foot) with a vertically pointing USB spectrometer collecting down-welling skylight. An integrated column amount (ICA) can then be determined over the length of the traverse by integrating overhead concentrations over the plume width. This reading can then be used to determine SO_2 fluxes with knowledge of the plume transport speed (Tamburello et al. 2011a). Scanning DOAS involves an instrument which is in a fixed position; it can be particularly useful for permanent stations and offered a marked improvement in time resolution (a measurement every few minutes). An excellent example of such an application is the FLAME (FLux Automatic Measurement) network which allowed the real-time monitoring and transmission of SO_2 flux information at Stromboli to be measured by the observatory (Burton et al. 2009; Burton et al. 2015a). Finally, cylindrical lens DOAS achieved significant time resolution improvements with sampling periods reduced to 1 s (McGonigle et al. 2007). However, this technique was also not without its disadvantages, in particular in terms of a complex alignment procedure (Tamburello et al. 2011a). This eventually led to the development of the UV camera for the

remote sensing of SO_2 from volcanoes as a way of improving the time resolution of collected data and potentially reducing errors, in a straightforward measurement configuration.

Fig.1.7: The Apogee Alta U260 two camera , two filter, set-up. A cylindrical lens DOAS is also attached to aid with the calibration procedure.

1.3.1. The UV Camera

The UV camera technique was originally based on the use of the 'off-the-shelf' Apogee instruments. The two most commonly used models are the Apogee Alta U260 (shown in Fig. 1.7) and the Apogee Alta E6, although other cameras by different manufacturers are now in use. The technique was first employed by Mori and Burton (2006) and Bluth et al. (2007) and has since been frequently used by others in the study of SO_2 flux. There are two main techniques for determining flux based on these units. The first technique, which is recommended by Kantzas et al. (2010), uses two images from parallel mounted UV cameras (or by some authors, a single camera with rotating filters) and compares the images on a pixel by pixel basis. The cameras are fitted with bandpass filters, which permit transit of light at 310 nm and 330 nm, respectively, where SO_2 in the plume absorbs/does not absorb down-welling skylight. This technique allows a very high time resolution, potentially at ≈ 0.5 s (≈ 4 s when a single camera is used [Mori and Burton, 2006]) and uses the following equation to calculate SO_2 concentration:

$$A = -\log_{10}\left[\frac{\left(\frac{IP_\alpha}{IB_\alpha}\right)}{\left(\frac{IP_\beta}{IB_\beta}\right)}\right] \qquad \textbf{(Eq. 1.2)}$$

where IP is the image of the plume and IB is the background image, α refers to the filter which detects SO_2 absorption and β refers to the filter which does not. It is important to note here that SO_2 absorption occurs in a window between 260-320 nm (Vandaele et al. 1994). The filters are usually centred between 300-320 nm for the absorption of SO_2 and 320-340 nm if not. A final SO_2 concentration is achieved by calibrating the instruments prior to or during acquisition against cells of known SO_2 concentration (Kantzas et al. 2010; Tamburello, 2011a). Calibration using a co-aligned DOAS instrument is preferred by some researchers (Kern et al. 2010a; 2010b).

Alternatively, the second method is based upon the use of a single filter, solely in the SO_2 absorption band (Bluth et al. 2007). This does not allow for resolution between the attenuation of gas and the attenuation of aerosols, which also absorb in the ultraviolet (Kantzas 2010; Tamburello, 2011a). Therefore the equation for determining SO_2 concentration becomes:

$$A = -\log_{10}\left(\frac{IP_\alpha}{IB_\alpha}\right) \qquad \textbf{(Eq. 1.3)}$$

omitting a direct comparison to a background image. However, whilst this is an intrinsically simpler approach, ignoring the aerosol absorption could, in practice, create larger errors.

Despite the increasing popularity of this camera there are still several challenges faced when using this approach. For instance, achieving an ideal location for acquisition can be difficult due to the location of the sun and the vignetting issues that this results in: e.g., due to inhomogeneous solar illumination of the background sky (Kantzas et al. 2010). The light-dilution effect, with some recent attempts at quantification (Campion et al. 2015), where light intensity is effectively reduced by scattering amongst other light-paths can also induce large errors. In addition, climatic conditions can also play a part; if the plume is not visible due to fog or cloud cover then acquisition cannot occur. For a detailed discussion on the UV camera technique please see Kantzas et al. (2010). In addition, Tamburello et al. (2011b) have devised a user-friendly program, Vulcamera, which enables the use of the two-camera two-filter set-up in the field with relative ease and subsequent processing SO_2 flux data. As a result of these developments, the UV camera can now be used to investigate, for the first

time, the gas driven dynamics of rapidly occurring volcanic processes such as strombolian eruptions.

Fig.1. 8: The view of the North-East Crater plume of Mt. Etna form the Pizzi Deneri Volcano Observatory

1.3.2. Application of UV cameras to degassing

The main application of the UV camera to explosive basaltic eruptions, has been to strombolian activity due to issues with ash making gas remote sensing impossible in other classes of explosion, whose eruption plumes are rather more ash rich (Tamburello, 2011a). Dalton et al. (2010) used a ≈ 4 s resolution dataset to quantify the amount of gas released during a single strombolian eruption in combination with infrasonic data. This built on earlier work by Vergniolle and Brandeis (1996) and Vergniolle et al. (1996) who developed a method for assessing gas release using infrasonic measurements. Mori and Burton (2009) then used the UV camera to estimate gas mass from single strombolian eruptions at Stromboli and discovered that the acoustic method under-estimates the size of gas mass. Gas mass is an important feature in understanding degassing. It can unlock details about the exsolution source depth and potentially reveal information regarding the shallow plumbing system beneath volcanoes, particularly when using a multi-dataset approach.

In general, there has been a lot of investigation into the mechanisms and the processes affecting the explosive aspects of basaltic volcanism. However, a very recent discovery concerning passive degassing, which is discussed in Tamburello et al. (2013) and Chapter 2 highlights the great importance of this rather less spectacular degassing style. In this paper the authors propose that a periodic SO_2 degassing activity, which is observed on timescales of 40-250 s at the North-East crater of Mt. Etna, is caused by waves of bubbles which rise

within the conduit and burst at the surface producing the oscillating flux signal captured with the UV camera. This short-period degassing is referred to as "puffing" in the literature. Tamburello et al. (2013) also noted the presence of a longer period >2000 s flux modulation, however, they did not comment further due to the relatively short duration of the dataset. In addition a 2000 s variation is mentioned in Nadeau et al. (2011). These authors propose that the short-term variation is likely caused by waves in line with an earlier model detailed in Manga (1996) and further suggest that the cause may be related to time-dependent changes in bubble size and magmatic vesicularity. The process is likely limited to the upper 1 km of the conduit due to the lack of correlation with the seismic signal, which is generated at greater depth; however the authors do not pursue into this in detail. This work is important as it demonstrates that these characteristics may be present at other open-vent volcanoes. Indeed, Peters et al. (2014a), Girona et al. (2015), Ilanko et al. (2015a, 2015b), have all identified a periodic structure to degassing at Erebus over a ≈ 10 min window in SO_2, H_2O and gas ratios. This cyclic degassing process therefore warrants further research. Aiuppa et al. (2007) further signify the importance of studying passive degassing as it may prove useful in eruption forecasting.

Developments such as these have come about because of the high temporal resolution capabilities of the UV camera. SO_2 flux data can now therefore reveal aspects of basaltic degassing in much more detail than possible hitherto. Due to the low time resolution of collected SO_2 data in the past it was incomparable to seismic data. However, as sampling frequencies approached 1 Hz and faster it became possible to compare SO_2 flux data to similarly high resolution seismic and infrasonic data (McGonigle et al. 2009). There are several such examples of such work including Nadeau et al. (2011) at Fuego Volcano (Guatemala) who observed a correlation between SO_2 emission rates and volcanic tremor indicating that the generation of the seismic tremor and the rise and fall of SO_2 flux rates originate from the same source process. This work confirmed the long-held belief that there is a link between a rising gas slug and tremor as is discussed in Chouet et al. (2003). However, the mechanism is still highly unconstrained and Nadeau et al. (2011) conjecture that it could be caused by the oscillation of bubbles, a resonance in the conduit, the movement of the magma or the coalescence of bubbles. The high temporal resolution ability of the UV cameras allow the measurement of much more rapid strombolian, on the order of seconds, a goal which has yet to be achieved.

Due to its ease of access and frequent eruptions, Stromboli has been a strong target for study with the UV camera. A recent study by Tamburello et al. (2012) produced an in depth summary of both passive and active forms of degassing at Stromboli. The authors managed to extract the slug size and relate the size of the VLP (Very-Long Period) seismic signal to the amount of SO_2 released during an explosive eruption, similarly to McGonigle et al. (2009). This was key as it allowed the corroboration of the analysis by Chouet et al. (2003) which revealed that the source depth of tremor is at 300 m. However, the analysis by Tamburello et al. (2012) did more to highlight the small amount that explosive processes contribute to the daily SO_2 budget at Stromboli, a mere ≈ 7%. In total, active degassing (explosive events and puffing) was calculated to contribute ≈ 23% of SO_2 and passive ≈ 77%. This highlights the importance of further study into passive degassing and modelling of these processes. Indeed, because Stromboli possesses such reliable activity it is an ideal location to monitor and collect a large number of observations of strombolian activity. This will then enable this thesis to investigate variability and phenomena present within such a database.

Often the UV camera can be used in combination with other gas measurement or sampling equipment. One such instrument is the Multi-GAS analyser, which extra-actively samples gas at resolutions of temporal resolutions ≈ 0.5 Hz. These gases include CO_2, SO_2, and H_2O, the major constituents of gas within a magma (Shinohara 2005; Aiuppa et al. 2005). By combining measurements SO_2 flux with spot measurements of gas ratios using the Multi-GAS analyser, it is possible to estimate total fluxes from a source (e.g. Aiuppa et al. 2008). In particular, the UV camera is particularly useful when used in combination with a Multi-GAS analyser as the spatial capabilities of the camera can be used to co-locate the two instruments (Tamburello et al. 2011a).

The UV camera has also be used to investigate the degassing of more viscous magmas such as those at Santiaguito volcano (Guatemala), where a rheologically stiff lava dome is in place. Holland et al. (2011) used the camera to investigate degassing processes during the extrusion of the dome which has occurred since 1922. The high time resolution SO_2 flux data allowed a full assessment of the mode of degassing, which would have been difficult with previous methods. This work highlights the utility and adaptability of the camera to a variety of situations and further illustrates that volatiles are important in all varieties of volcanic settings.

1.4. A brief introduction to modelling basaltic degassing

Modelling of basaltic degassing is performed in two main ways: Firstly through analogue laboratory experiments, and secondly through computational fluid dynamics (CFD). The purpose of analogue experiments is to reduce the size of a volcanic system into a manageable and controllable environment. These then enable the investigation of scaled volcanic phenomena including, of particular importance for this thesis, slug flow (Del Bello et al. 2012, 2015; Jaupart and Vergniolle, 1988; James et al. 2004, 2006, 2008, 2009; Lane et al. 2013; Llewellin et al. 2012, 2013, 2014a). CFD provides an excellent way of modelling volcanic scale phenomena (Suckale et al. 2010a; 2010b), although, validation of observations using laboratory experiments (James et al. 2008), field-based observations, or existing mathematical relationships is still needed.

The majority of analogue experiments are directed at slug flow. Studies by James et al. (2008) and Del Bello et al. (2012) seek to provide a way to estimate final lengths of gas slugs at burst, along with values for overpressure which are a way of estimating explosivity of an event. James et al. (2009) followed on from this, devising a way to predict whether a gas slug will burst with or without overpressure. Previous experiments have also endeavoured to characterise geophysical signals associated with the ascent and burst of a gas slug (James et al. 2004; Lane et al. 2013). A series of more recent studies have focused on the burst mechanism of a slug, with a specific focus on Stromboli (Taddeucci et al. 2012; Del Bello et al. 2015). In particular, Del Bello et al. (2015) suggest that rheological heterogeneities nearer to the surface of the conduit at Stromboli (i.e. a more viscous cap) could act to disrupt and alter the way that slugs burst at the surface.

The studies cited in the last paragraph, to this point, have all concerned small scale laboratory experiments over conduits on the order of cms in diameter and several metres in length. Llewellin et al. (2012) used a larger scale tube on the order of a metre in diameter and tens of metres in length to improve previous estimates on liquid film thicknesses between the conduit wall and the gas phase of the bubble (Fulford, 1964; Karapantsios et al. 1989; Lel et al. 2005, Zhou et al. 2009). Llewellin et al. (2013; 2014a) are also among the first to begin to investigate the effects of multiple slugs in a conduit, as opposed to single slugs, beyond the postulations of Seyfried and Freundt (2000). Seyfried and Freundt (2000), in addition to James et al. (2004) began to consider the effects of an inclined conduit and heterogeneities in

the conduit on the stability and signals generated during slug flow. Witham et al. (2006) take this work further, but investigate oscillations in lava lakes.

Jaupart and Vergniolle (1988) have investigated the formation and collapse of foams, with a particular focus on Kilauea. Here, they used a tank (i.e. a magma chamber or storage zone) with a tube attached to the top to simulate a conduit. They then allowed the collection of bubbles at the top of the tank which led to the formation of a foam, which after a certain period collapsed in the conduit to produce a slug. Jaupart and Vergniolle (1989) then quantified this process.

Studies on slug flow using CFD are less commonplace within the volcanic literature. CFD operates by solving the Navier-Stokes equations for given liquids, predicting their motion. In particular CFD in a basaltic context solves the problem of how a gas would move within a magma. James et al. (2008) used 3D models to validate a mathematical relationship for predicting the length of volcanic slugs. Suckale et al. (2010b), using their own developed CFD model (Suckale et al. (2010a), and fluid dynamical consideration on the stability of bubbles (Clift et al. 1978; Grace et al. 1978), suggested minimum viscosity limits for stable slug flow (Suckale et al. 2010b; James et al. 2011). Capponi et al. (2014) have introduced CFD in an attempt to compare laboratory regime simulations of a rheologically thicker viscous cap to a full volcanic scale. The non-volcanic literature has used CFD to characterise the behaviour of coalescing slugs (Araujo et al. 2012, 2013), and characterise important features of a slug including its wake (Campos and Guedes de Carvalho, 1988; Nogueira et al. 2006).

The have been a large number of modelling studies conducted, particular of the single slugs which drive strombolian activity. However, these studies are self-contained and don't involve the use of empirical data for comparison. This thesis will therefore address this by combining, in unprecedented detail degassing measurements with modelling studies using CFD and existing mathematical models. In addition, work discussing the transitions between different styles of activity has been neglected for decades (e.g. Parfitt et al. 1995), this thesis will also look to build on this in a basaltic context but bringing in almost completely neglected drivers of more explosive styles of degassing such as hawaiian lava fountaining.

1.5. Objectives

The overall objective of this work is to combine measurements using UV cameras, with computational and analogue models of gas flow, to investigate the dynamics of basaltic degassing. The main objectives are described below.

1.5.1. Objective 1

Investigate trends in passive degassing using UV cameras. Here, the UV camera will be used to investigate recently observed trends in passive degassing and potential links to geophysical activity. Trends in passive degassing following on from explosive degassing are also important and will be investigated in combination with Objective 2.

1.5.2. Objective 2

Investigate explosive degassing using UV cameras. To address this objective, UV cameras will be used to measure strombolian activity at Mt. Etna and Stromboli. Here, I am particularly interested in activity generated by the rising and bursting of volcanic slugs.

1.5.3. Objective 3

Model explosive degassing. Here, models of slug driven activity will be developed and applied to understand the UV camera data collected for the purpose of addressing Objective 2. Two methods will be used, laboratory experiments and CFD. Little has been done to compare measurements of explosive degassing (as part of Objective 2) with models. This thesis will address this issue.

1.5.4. Objective 4

Investigate transitions between different styles of activity. There is a large gap in the volcanic literature addressing regime transitions between different styles of activity, particularly across the whole range of basaltic degassing from passive to hawaiian lava fountaining. This objective will draw on the results of investigations into Objective 2 and Objective 3, with the aim of developing a model to characterise and categorise basaltic degassing.

1.6. Thesis Structure

During the course of conducting the research for this thesis a number of the chapters and material contained therein have been prepared and submitted to international journals for publication. The following descriptions of each chapter outline where material has been published and the objectives which are thereby addressed.

Chapter 2 supports Objective 1. The work in this chapter has been included in three publications. The major portion of the work is contained in:

Pering, T. D. Tamburello, G., McGonigle, A.J.S., Aiuppa, A., Cannata, A., Giudice, G., Patanè, D., 2014a. High time resolution measurements of volcanic carbon dioxide degassing on Mt. Etna. Journal of Volcanology and Geothermal Research 270, 115-121, doi:10.1016/j.jvolgeores.2013.11.014.

This publication addressed the measurement of CO_2 fluxes during passive degassing by combining UV camera measurements of SO_2 and a Multi-GAS analyser, this then enabled the comparison of these datasets with geophysical data. However, a new technique, based on the continuous wavelet transform, was needed to undertake this:

Pering T.D., Tamburello, G., McGonigle, A.J.S., Hanna, E., Aiuppa, A., 2014b. Correlation of oscillatory behaviour in Matlab using wavelets, Computers and Geosciences 70, 206-212, doi:10.1016/j.cageo.2014.06.006

The final portion of this chapter with a contribution from a publication is from the following:

Tamburello, G., Aiuppa, A., McGonigle, A.J.S., Allard, P., Cannata, A., Giudice, G., Kantzas, E.P., Pering, T.D.,2013, Periodic volcanic degassing: The Mount Etna Example, Geophysical Research Letters 40 (1-5), doi:10.1002/grl.50924

This paper described the periodic nature of degassing at Mount Etna, with my work specifically on investigating the volcanogenic nature of these links included here.

Chapter 3 supports Objectives 1, 2 and 3. Both the explosive portion of a strombolian explosion from Stromboli and that released passively following an event are investigated and then compared to computational models. This work was presented at EGU in 2015:

Pering, T.D., McGonigle, A.J.S., James, M.R., Tamburello, G., Aiuppa, A., 2015a. Comparing computational models of slug rise at Stromboli with UV camera measurements of SO2 flux. In: EGU General Assembly 2015, Vienna.

Chapter 4 supports Objectives 2 and 3. This chapter describes measurements of rapid strombolian activity from the Bocca Nuova crater of Mt. Etna. Basic models are applied to aid the understanding and dynamics of the activity. This work is contained in the following publication:

Pering, T.D. Tamburello, G., McGonigle, A.J.S., Aiuppa, A., James, M.R., Lane, S.J., Sciotto, M., Cannata, A., Patanè, D., 2015b. Dynamics of mild strombolian activity on Mt. Etna. Journal of Volcanology and Geothermal Research 300, 103-111, doi:10.1016/j.volgeores.2014.12.013

Chapter 5 supports Objectives 3 and 4. By using laboratory experiments and computational fluid dynamics rapid strombolian activity, driven by multiple rising slugs, is investigated. This builds on observations made in Chapter 4 and is based on work presented at AGU in 2014:

Pering, T. D. McGonigle, A. J. S., James, M.R., Lane, S.J., Capponi, A., Tamburello, G., Aiuppa, A., 2014c. Observations on Multi-Slug Activity – Implications for Volcanic Processes. In: AGU Fall Meeting 2014 San Francisco.

Chapter 6 supports Objective 4. This final results chapter brings together the discoveries and observations in Chapters 4 and 5, with particular reference to unifying the study of the differing forms of basaltic degassing based on the rapidity of degassing. This work was introduced at AGU in 2014:

Pering, T. D. McGonigle, A. J. S., James, M.R., Lane, S.J., Capponi, A., Tamburello, G., Aiuppa, A., 2014c. Observations on Multi-Slug Activity – Implications for Volcanic Processes. In: AGU Fall Meeting 2014 San Francisco

Chapter 7 concludes the thesis with a discussion on the themes presented in Chapters 2 through 6 and the important take home messages for future studies advancing the combination of measurements of degassing with models. The conclusions of each chapter are also reiterated here.

2. High temporal resolution measurements of CO_2 and SO_2 using ultra-violet cameras

In Chapter 2 the UV camera, in combination with a Multi-GAS analyser, was used at Mt. Etna for the measurement of SO_2 and CO_2. This enables, for the first time, comparisons at high temporal resolutions of 1 Hz, between SO_2, CO_2 degassing and geophysical datasets. Within these datasets several periodic degassing and geophysical features are identified and discussed. This chapter and outlined techniques are based on work already published in three journals, including: *Pering, T. D. Tamburello, G., McGonigle, A.J.S., Aiuppa, A., Cannata, A., Giudice, G., Patanè, D., 2014a, High time resolution measurements of volcanic carbon dioxide degassing on Mt. Etna, Journal of Volcanology and Geothermal Research 270, 115-121, doi:10.1016/j.jvolgeores.2013.11.014*; *Pering T.D., Tamburello, G., McGonigle, A.J.S., Hanna, E., Aiuppa, A., 2014b, Correlation of oscillatory behaviour in Matlab using wavelets, Computers and Geosciences 70, 206-212, doi:10.1016/j.cageo.2014.06.006*; and on analysis contributed to *Tamburello, G., Aiuppa, A., McGonigle, A.J.S., Allard, P., Cannata, A., Giudice, G., Kantzas, E.P., Pering, T.D.,2013, Periodic volcanic degassing: The Mount Etna Example, Geophysical Research Letters 40 (1-5), doi:10.1002/grl.50924*

2.1. An introduction to gas measurement at Mt. Etna

Mt. Etna (37.734°N, 15.004°E) is a strato-volcano located in Sicily, Italy (see Fig. 2.1) and is the largest time-averaged contributor to volcanogenic emissions of both SO_2 and CO_2 in Europe (Allard et al. 1991; Gerlach, 1991). The latter results from magmas which are already CO_2 rich (Spilliaert, et al. 2006), increasing the importance of its detection and measurement. Mt. Etna fluctuates between periods of quiescence, where passive degassing dominates, and active periods dominated by "paroxysms" associated with lava fountaining and strombolian activity (GVP, 2013). There are currently five summit craters which demonstrate open vent persistent degassing behaviour: Bocca Nuova (BN), Voragine (VOR), North East Crater (NEC), South East Crater (SEC) and the recently formed New South East Crater (NSEC). Each of these craters, which have varying rates of emission, exhibit dominant forms of activity (e.g. Caltabiano et al. 2004; Aiuppa et al. 2008).

CO_2 is a vitally important volcanogenic species to measure as it exsolves at much greater depths than other most common species (Giggenbach, 1996). It therefore acts as a better measure of magma movement at depth, compared to the more commonly measured SO_2, and has greater potential for early warning of eruptive activity (Aiuppa et al. 2010). To date, CO_2 flux determinations at volcanic targets globally have been limited and are generally restricted to lower time resolutions on the order of minutes to hours, and associated with estimates based on ratios only, although contributions have been made by: Wardell et al. (2004) for Mount Erebus, Antarctica; Koepenick et al. (1996) for Ol Doinyo Lengai, Tanzania; Werner et al. (2006) for White Island, New Zealand; Werner et al. (2012a; 2012b) for Redoubt, Alaska and Poland et al. (2012) for Kilauea, Hawaii. A relatively recent development is the use of portable gas analysers, called Multi-GAS analysers (see Aiuppa et al. 2005; Shinohara, 2005). These allow the measurement of a number of gas species at high resolutions of ≈ 0.5 Hz, and have been used successfully on Mt. Etna, particularly for the measurement of rapidly altering gas ratios prior to eruptions (Aiuppa et al. 2008; 2010). Advancement in capabilities of measuring CO_2 fluxes, particularly at high temporal resolution on the order of seconds, would represent a significant advancement in volcanic remote sensing, allowing, for the first time comparison with contemporaneously acquired geophysical data.

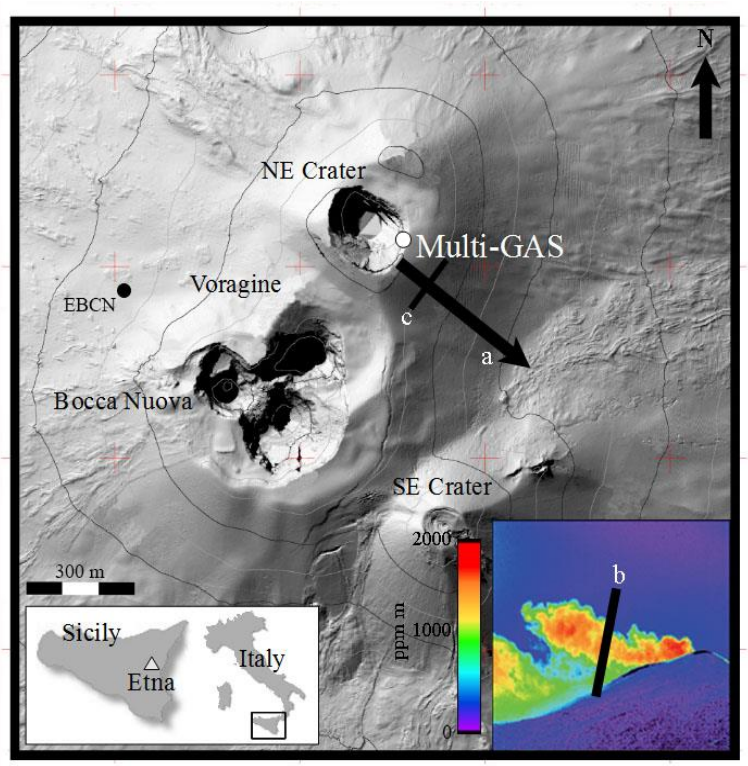

Fig. 2.1: Digital Elevation Model (DEM) of the summit area of Mt. Etna courtesy of Alessandro Aiuppa (Palermo University) and its location within Sicily and Italy. The black arrow at (a) illustrates the plume direction; inset (lower right) shows an example SO_2 absorption image during acquisition, where (b) shows the point of integration for determining the Integrated Column Amount (ICA) of SO_2, also shown at (c). Reprinted with permission from Elsevier.

By combining measurements of SO_2, using UV cameras, with a Multi-GAS analyser (Aiuppa et al., 2005; Shinohara, 2005) it is possible to create a contemporaneous CO_2 flux dataset at

equivalent temporal resolutions to that of the UV camera. The following sections describe the application of this technique to the North-East Crater of Mt. Etna and subsequent analysis.

2.2. Measurements of SO_2 flux and CO_2/SO_2 ratios at Mt. Etna

UV cameras were located at the Pizzi Deneri volcanic observatory (37.765763°N, 15.016640°E), ≈ 2 km from the NEC plume, for the purposes of measuring SO_2 emission rates from the NEC, which is typically the largest SO_2 contributor of all the summit craters (Aiuppa et al. 2008). For this campaign we used Apogee Alta U260 cameras. These cameras operate with 16 bit, 512 × 512 pixel Kodak-KAF-0261E cooled CCD array detector, UV lenses (Pentax B2528) of focal length = 25 mm and a field of view ≈ 24° are placed in front of each camera. Following this, 10 nm filters, centred at 310 nm for the absorption of SO_2 and 330 nm for where SO_2 doesn't absorb incident UV radiation, respectively, are placed in front of the lenses. Absorption images were captured at a temporal resolution of ≈ 0.5 – 1 Hz, using the Vulcamera software developed by Tamburello et al. (2011b). Vulcamera allows the user to fully control the UV cameras, including: dark current image acquisition (for correction of the natural noise of the CCD array), altering exposure settings (to ensure that the CCD array does not become saturated with light), vignetting image capture (to correct for the non-uniform distribution of light, as a result of inhomogeneous solar illumination and lens shape), and for calibration. Calibration was performed with four quartz cells which contained known concentrations of SO_2 (100, 200 1000, and 2000 ppm), resulting in a calibration line with an R^2 of > 0.99. When placed in front of each lens this allows the conversion of collected absorption images to calibrated values. For full details of the methodology see Kantzas et al. (2010).

Conditions on the measurement day (12th September 2012, between 08:45 and 09:45 GMT) were suitable, with a clear and uniformly lit background sky behind the non-grounded plume. Work by Lübcke et al. (2013) suggests that the cell calibration technique during measurement conditions such as those observed, including a near-transparent plume (i.e. not completely condensed) is suitable, without the need for additional DOAS assisted calibration, and is subject to low-levels of error (see also Kern et al. 2010a). Recent attempts by Campion et al. (2015) to provide estimates of potential error due to radiative transfer (i.e. via the light dilution effect), provide a step in the right direction for UV camera measurements. This work suggests that at a distance of < 4 km, error related to radiative transfer, during clear

conditions, could result in a ≈ 20 % underestimation in SO_2 flux calculated. As the camera was situated only ≈ 2 km from the source, one can speculate that error could be even lower.

Following the successful calibration of absorption images (example in Fig. 3), SO_2 flux was calculated using the Vulcamera code (Tamburello et al. 2011b). This involves integration of column amount values along the plume cross-section, in a perpendicular orientation to plume travel direction, to determine the integrated column amount (ICA) of SO_2 (see Fig. 2.1, line [b] in inset calibrated absorption image, also shown is this line with respect to the NEC crater at [c]). SO_2 flux can then be calculated by multiplying by the plume speed. Plume speed can be calculated in a number of ways, including the use of optical flow algorithms (e.g. Peters et al. 2015). However, here we use the frequently used cross-correlation technique (McGonigle et al. 2005; Williams-Jones et al. 2006), which works by taking two points along the plume and calculating two separate ICA time series. By combining knowledge of the distance between these two lines, cross-correlation can then produce a plume speed. During the hour of acquisition, this rate was relatively constant at 13.4 m s^{-1}. The final step in the production of an SO_2 flux dataset, given the instability of acquisition rate, which varied between ≈ 0.5 – 1 Hz, required linear interpolation to a uniform 1 Hz dataset.

Simultaneously, a Multi-GAS analyser was placed in the plume of the NEC crater, ≈ 100 m away from the vent, to measure CO_2/SO_2 ratios (see Fig. 2.1 for location). A Multi-GAS analyser is a self-contained unit used to measure a range of volcanogenic gases at high resolution, including: H_2O, CO_2, SO_2, H_2, CO, and H_2S. Here one was specifically interested in the measurement of CO_2 and SO_2 concentration, and their associated ratio. For the measurement of CO_2 the Muli-GAS uses an infrared sensor (Edinburgh Instruments, Gascard II). This sensor has a sensing range of 0 – 3000 ppm, suitable for use in a volcanic environment, and an error of ± 2%. The SO_2 sensor is an electrochemical sensor (City Technology 3ST/F0), with a range of 0 – 200 ppm, similar accuracy of ± 2%. Prior to use in the field, the Multi-GAS analyser was calibrated in the lab both over the sensor ranges as well as using a mix of CO_2 and SO_2 to simulate a volcanic plume. During all tests pure nitrogen was used as a zero baseline. Given the difference in response times of the two sensors (the t_{90} figure – i.e. the time taken to reach 90 % of actual value), measured error is higher at ≈ 15 %. Given the ability of the Multi-GAS analyser to sample at 0.5 Hz, the rapid response and ability of the sensors to react to changes in gas concentration is essential (i.e. one needs to be sure that observed oscillations in ratios are not a result of differences in sensor response time). Fig. 2.2 shows the results of a test using a known concentration of CO_2

and SO_2 pumped into the Multi-GAS inlet at a constant rate. During the first ≈ 70 s of the test, constant concentrations of CO_2 and SO_2 were used, demonstrating an error of ≈ 2 %. Gas concentrations of SO_2 and CO_2 were increased simultaneously to ≈ 30 ppm and ≈ 880 ppm respectively (again see Fig. 2.2) and then subsequently decreased. This test demonstrates that on periods of ≈ 10 s there is a small amount of error (≈ 15 %) associated with the differences in sensor response time. This gives confidence in the ability of the Multi-GAS to measure rapid changes in CO_2/SO_2 ratio.

Readings of SO_2 from the Multi-GAS analyser need no correction due to low atmospheric background levels; however, CO_2 does need to be corrected. By plotting raw CO_2 values against SO_2,the background level of CO_2 is taken as the intercept of the regression line with the y axis; a level of ≈ 200 ppm. The GPS time-stamped Multi-GAS readings were then interpolated to 1 Hz to allow direct comparison and combination with UV SO_2 fluxes.

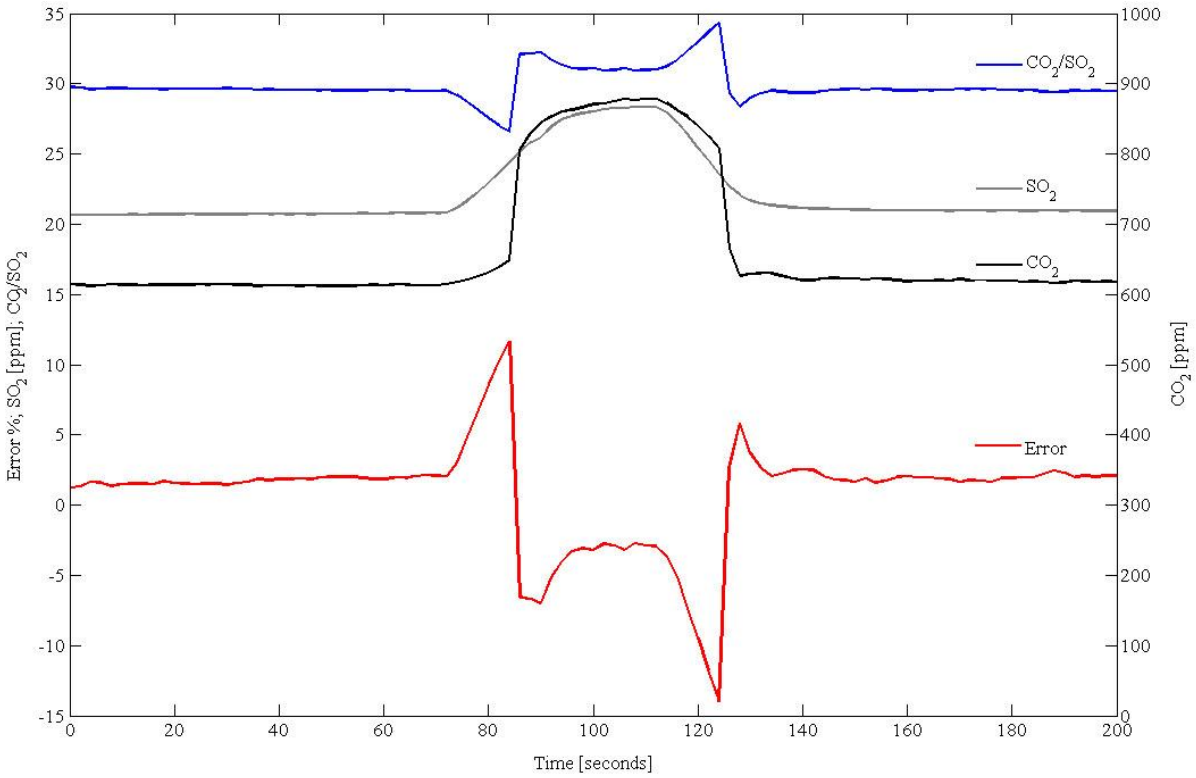

Fig. 2.2: The results of a laboratory controlled test of the Multi-GAS analyser (data courtesy of Giancarlo Tamburello and Alessandro Aiuppa, Palermo University). Reprinted with permission from Elsevier.

SO_2 flux estimation (i.e. the location of ICA determination) was performed ≈ 180 m downwind of Multi-GAS. To temporally synchronise the UV dataset with the Mulit-GAS the lag between the two was calculated at ≈ 13 s using the determined plume speed (e.g. the different view configuration between the UV camera and Multi-GAS unit needed to be

corrected for). Indeed, this value is corroborated as a lag of ≈ 13 s is also determined by cross-correlating UV SO_2 flux with Multi-GAS SO_2 readings.

2.2.1. Existing techniques for analysing and comparing trends in volcanic data

A number of techniques are used to probe periodic behaviours which are particularly prevalent in environmental signals. Amongst the most popular are the Fourier transform (e.g. Welch, 1967; Harris, 1978; Oppenheim et al. 1999), and the wavelet transform (e.g. Morlet et al. 1982; Daubechies, 1990; Colestock, 1993; Huang et al. 1998; Torrence and Compo, 1998; Grinstead et al. 2004). Fourier transforms (also known as power spectral densities [PSDs]) probe the frequency characteristics of a signal with no regard to stability of an oscillation with time, solely the power (Welch, 1967). Hence, Fourier analysis is valuable for long-lived but stable periods. However, a spectrogram (Short Fourier Transform) does show frequency change with time. There is a varying array of wavelet analysis techniques, including a discrete version. However, of these the continuous wavelet transform (CWT) is the one which can potentially provide more detailed information about the frequency characteristics (i.e. periodicities) and power of each frequency within a signal as a function of time. The wavelet technique works by conjugating a mother wavelet with the target signal. During this process the mother wavelet is scaled, according to a set of scales defined by the sampling rate of the signal. For example, for a signal 1000 s long, at a sampling rate of 1 s, 500 different scales of wavelet are created, equal to the theoretical lengths of a periodic oscillation at a scale of 1s, 2s, 3s, etc.. The range of scales is set at half the signal length according to the Nyquist criterion (Nyquist, 2002), which states that no oscillation longer than half the signal can be reliably detected, purely because only one full oscillation could be observed within the signal length. The resultant wavelet spectrum produced by the CWT then provides a normalised scale of match between the

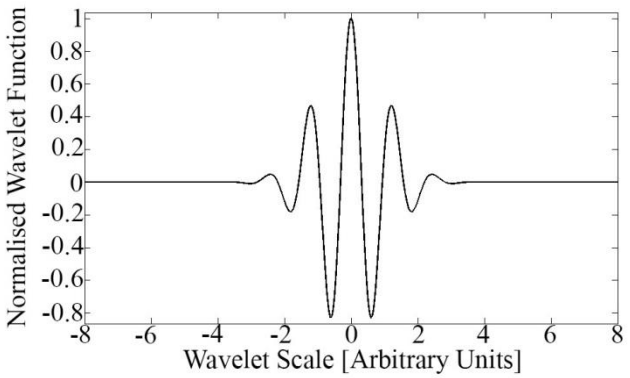

Fig. 2.3: An example mother wavelet, the Morlet wavelet (Morlet et al. 1982), generated using the Matlab® wavelet toolbox. Reprinted with permission from Elsevier.

varying scaled mother wavelets with time. Of importance is the style of mother wavelet chosen. Here and throughout this work we use the Morlet wavelet (see Fig. 2.3). It is necessary to use a wavelet with a shape similar to any expected target oscillation, a criterion which the Morlet wavelet meets (other appropriate wavelets include the Gaussian wavelet). The Morlet wavelet function is created as follows (Morlet et al. 1982; Grinstead et al. 2004):

$$\Psi_0(\eta) = \pi^{-1/4} e^{i\omega_0\eta} e^{-\eta^2/2} \qquad \textbf{(Eq. 2.1)}$$

where, $\Psi_0(\eta)$ is the Morlet wavelet function with associated dimensionless time frequency, with ω_0 also a dimensionless frequency for the wavelet. Following this the CWT can be calculated:

$$W_n(s) = \sqrt{\frac{\delta t}{s}} \sum_{n'=1}^{N} x_{n'} \Psi^* \left[(n'-n)\frac{\delta t}{s}\right] \qquad \textbf{(Eq. 2.2)}$$

where t is the time step, x_n the target signal, N represents the maximum Nyquist defined scale, n the length of the target signal, $*$ the conjugate, and $W_n(s)$ the scale of the wavelet.

The described techniques are used to probe the periodic characteristics of a single dataset only. Often, when investigating links in datasets, particularly in the climatic sciences (e.g. Philander, 1990; Hurrell, 1995; Hurrell et al. 2003; Lockwood, 2012) where climatic oscillations such as the North Atlantic Oscillation and El Niño are frequently cited as influences on local and regional climates, it is necessary to probe links between two datasets. Traditional techniques such as correlation, regression, and t-tests are less successful at extracting information on correlation between inherently noisy natural signals. It is for this reason that wavelet coherence, which takes advantage of the smoothing associated with the wavelet process (i.e. via convolution), is often used (e.g. Grinstead et al. 2004; Cannata et al. 2013a; 2013b). However, the outputs associated with wavelet coherence are unintuitive and hard to interpret as a result. In the following section a new and easy to use technique, based in Matlab® is outlined to enable the easy comparison of two noisy datasets, significantly expediting the comparison of volcanic datasets. The technique is described in detail in section 2.2.2 and implemented on collected volcanic datasets from Mt. Etna in section 2.3.

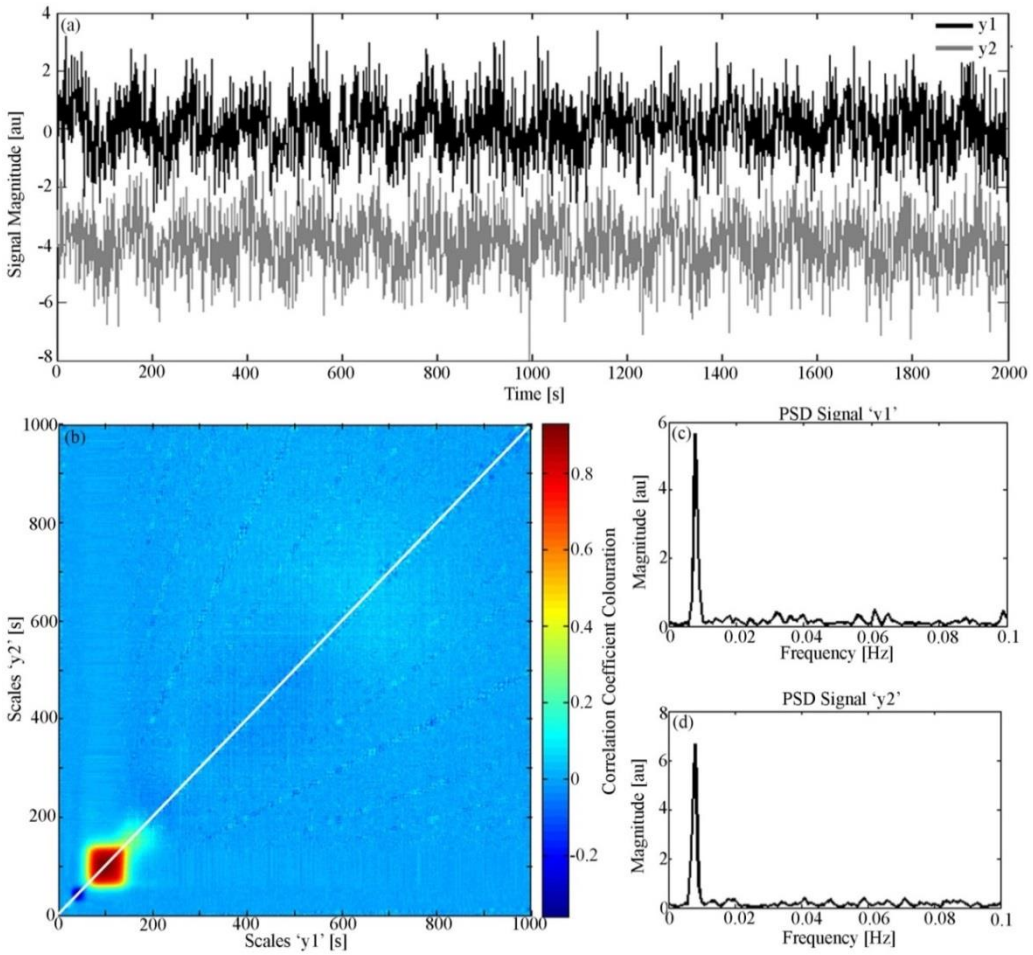

Fig. 2.4: In a) the synthetic signals with no lag and sinusoidal oscillations infused with random noise used for implementing the "corrplot" technique, b) the resulting corrplot image demonstrating period of matching oscillation, and c) and d) which show the PSDS of each separate sinusoidal signal, with dominant frequency at ≈ 125 s (0.008 Hz). Reprinted with permission from Elsevier.

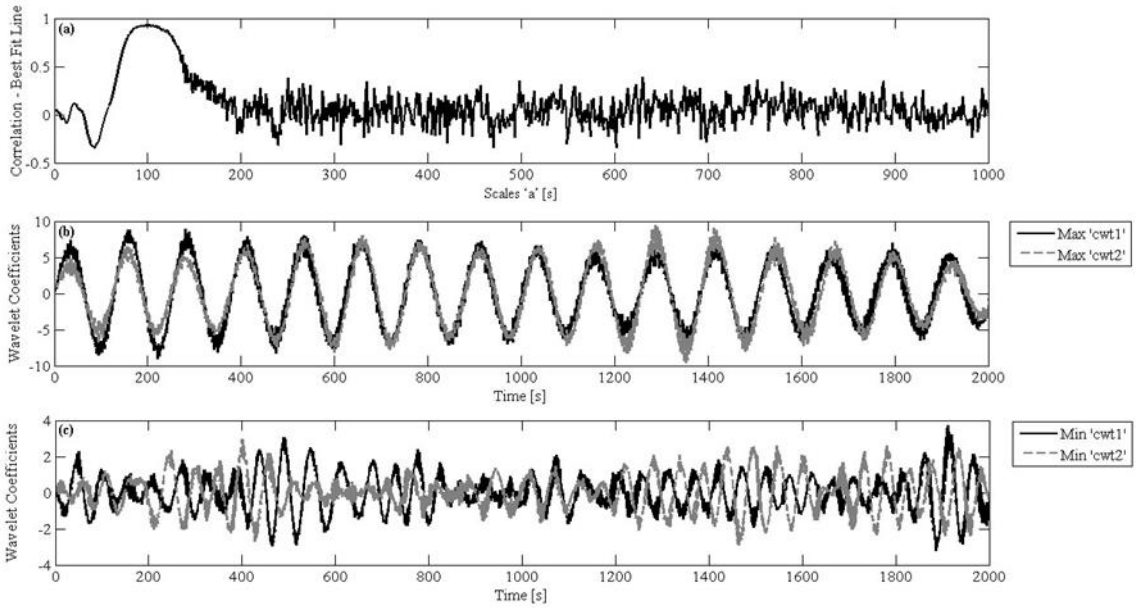

Fig. 2.5: Output from the "corrplot" code: a) the correlation coefficients extracted from the 1:1 line in Fig 2.4b, b) the wavelet coefficients extracted at the scale of maximum correlation, and d) those at minimum correlation. Reprinted with permission from Elsevier.

2.2.2. A new technique for comparing trends in geophysical datasets

By correlating the output of the CWT at each scale for two different signals (normalised prior to processing) of equal length and sampling rate with the Spearman's rank correlation coefficient (r_s; Spearman, 1904; Zar, 1972) a visual representation of correlation in a single plot can be produced:

$$r_s(W_{ni}) = 1 - \frac{6\sum d_i^2(W_{ni})}{n(n^2-1)} \qquad \textbf{(Eq. 2.3)}$$

where d_i^2 is the value associated with the ranked output at each specific CWT scale, and n is the length of the dataset. A code "Corrplot" has been developed in Matlab® (Pering et al. 2014b), and is available in Appendix A. An example application of this technique using associated Matlab® code on synthetic signals is demonstrated in Fig. 2.4 and 2.5, which shows that on artificially generated sinusoidal signals of ≈ 125 s, with added random noise, the developed technique clearly highlights the shared period of within the range of 75 – 150 s. Reassuringly, no further correlations over longer periods appear. Fig. 2.6. shows an example of perfect oscillatory correlation (i.e. essentially identical signals). The code also extracts data along the white 1:1 line, for example in Fig. 2.4b. It is along this line that one would expect that mutual oscillations would best match (i.e. a period of 300 s is unlikely to be related to a period of ~ 10 s). This is illustrated in Fig. 2.5. To aid with oscillatory identification the CWT scales at the points of maximum and minimum correlation are also generated. Similarly, these outputs can be used to aid in identification of any potential lags present in the datasets. A further part of the tool uses cross-correlation over the range of scales to quantify and identify the power

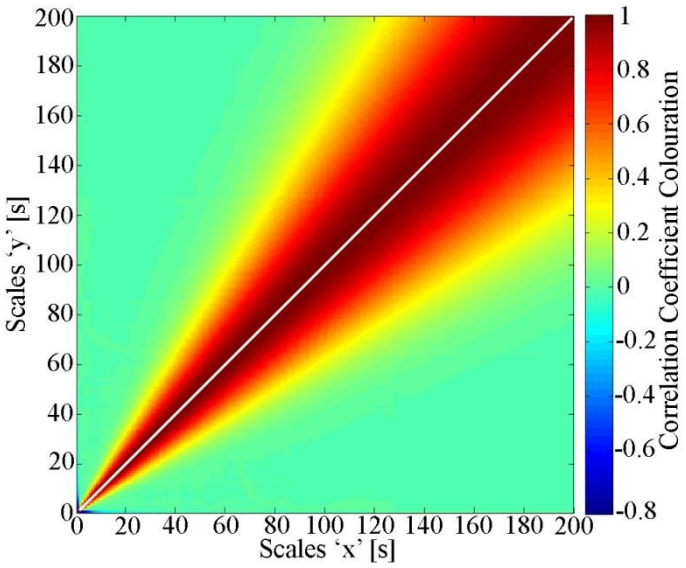

Fig. 2.6: Perfect oscillatory correlation between two identical signals. The white line shows the location of the 1:1 line. Reprinted with permission from Elsevier.

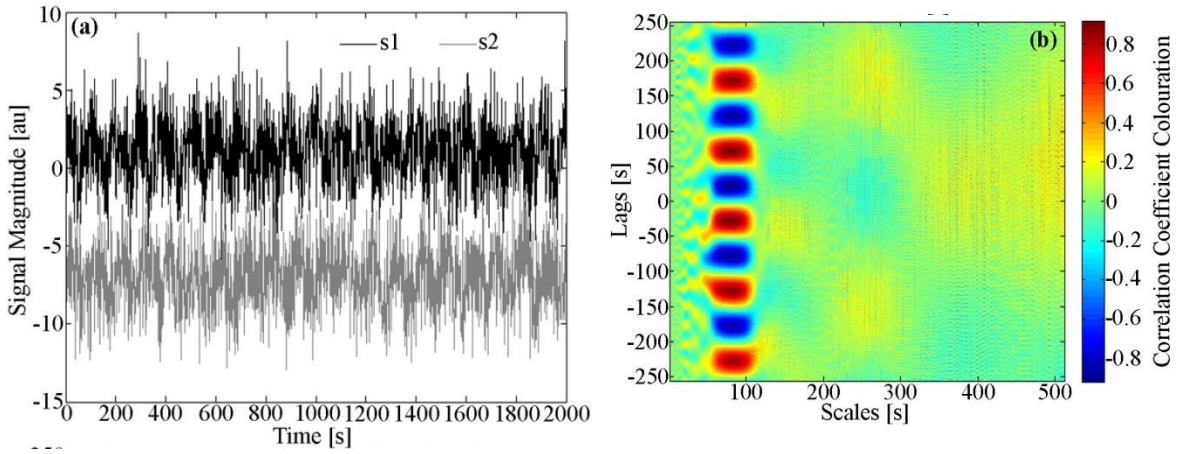

Fig. 2.7: a) example cosinusoidal and sinusoidal signals (i.e. in antiphase), b) a further output of the "corrplot" code which shows the result of cross-correlation of each wavelet coefficient at each scale, this enables the identification of lags. Reprinted with permission from Elsevier.

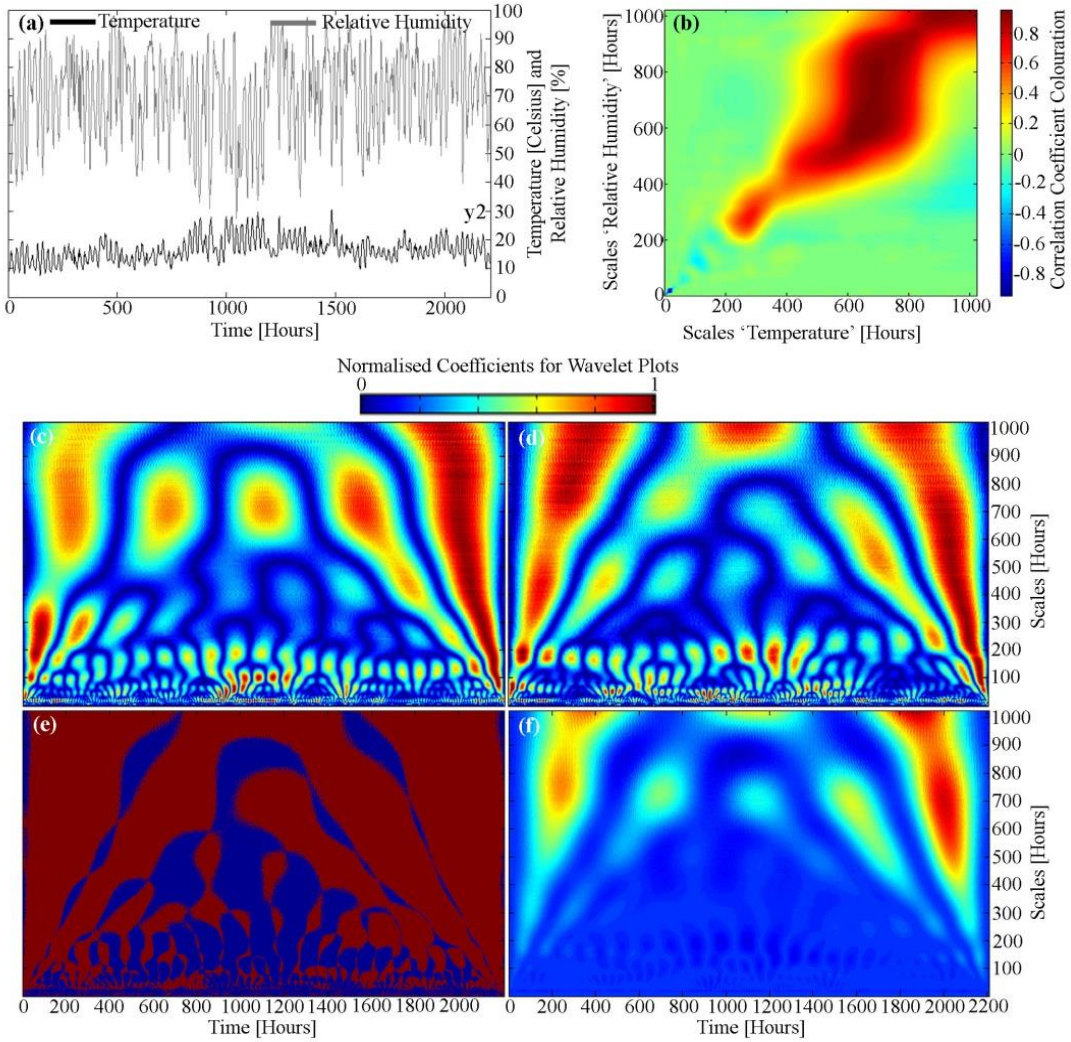

Fig. 2.8: a) temperature and relative humidity data taken from the University of Sheffield, Department of Geography weather station (data courtesy of Edward Hanna, University of Sheffield), in b) the resultant "corrplot" output showing strong links on a timescale of >8 days. In c) and d) are the respective wavelet plots for the raw data, and in e) and f) the wavelet coherence and cross wavelet spectrum respectively, clearly demonstrating that it is easier to identify common periods using the "corrplot" output. Reprinted with permission from Elsevier.

and stability of lags with time. We demonstrate this on two separate artificially generated signals of period 90 s, one a cosinusoid and the other a sinusoid, i.e. in antiphase (Fig. 2.7).

To demonstrate the ease of identifying oscillatory links between two datasets, we applied the code on temperature and relative humidity data from the University of Sheffield, Department of Geography weather station (data courtesy of Edward Hanna, University of Sheffield), the results are illustrated in Fig. 2.8. Here, we also produced plots of wavelet coherence (Fig. 2.8e) and the cross wavelet spectrum (Fig. 2.8f). In Fig. 2.8b it is clearly apparent that there are strong links on periods of ≈ 200 – 8000 hours (i.e. 8 – 33 days), and at ≈ 24 hours there is strong anti-correlation at R^2 = -0.94 (associated with the diurnal cycle). On interrogation of the results of wavelet coherence these links are much more difficult to identify, in contrast to the ready visualisation provided by the corrplot code.

The final demonstration of the developed code is on Multi-GAS data, for CO and H_2S, whilst the Multi-GAS analyser was placed inside the plume of the North-East Crater. Here, we demonstrate links between the two datasets over distinct periods within the range ≈ 300 – 900 s, although the level of correlation is < 0.4 R^2, suggesting some links between the datasets (Fig. 2.9). The benefit of using this technique on Multi-GAS data is that links can still be identified, regardless of the temporal response characteristics of the sensor. Fig. 2.9b also illustrates the results of the corrplot code in 3D, which can give even greater clarity to the relative strength between a range of potentially present oscillatory features.

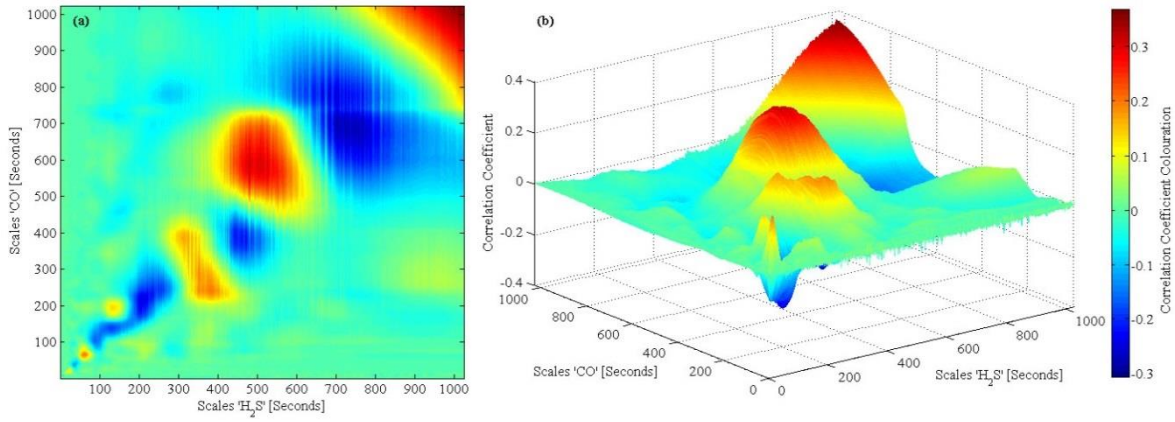

Fig. 2.9: a) Output from the "corrplot" code on H_2S and CO data from a Multi-GAS sensor placed within the NEC of Mt. Etna, b) the same data but output in 3D – this can occasionally enhance clarity and identification of shared periods. Reprinted with permission from Elsevier.

2.3. Results and Analysis

Fig. 2.10a-d show data from the Multi-GAS analyser during the period of acquisition and overlap with collected UV camera data. The background subtracted CO_2 v SO_2 scatter plot in Fig. 2.10a demonstrates a good degree of match, while in Fig. 2.10c CO_2 and SO_2 show a visual degree of match between the gas time series. The exception here is a period highlighted by a grey oval in Fig. 2.11a and a grey bar across Fig 2.10c-f, where two large spikes in CO_2 show a break in the trend. This link between datasets is highlighted further in

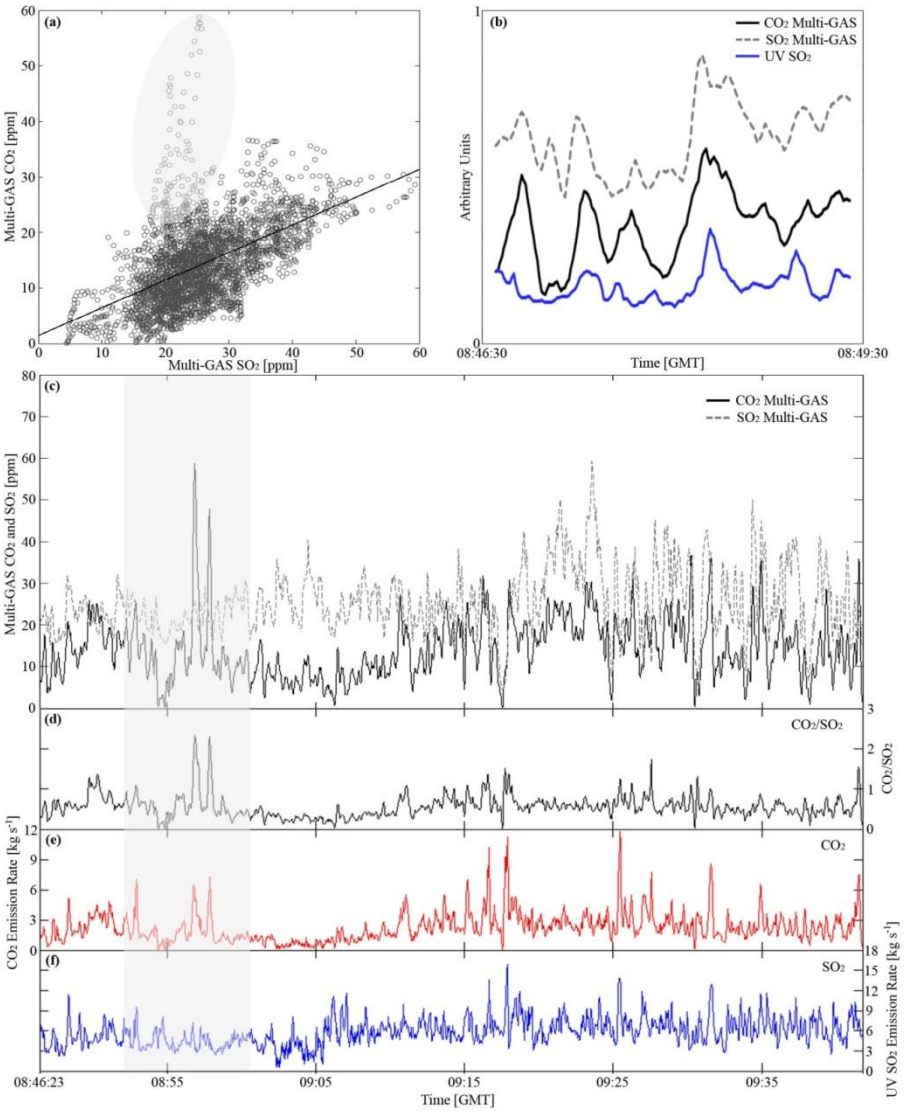

Fig. 2.10: a) scatter plot showing CO_2 against SO_2 (background corrected) collected using the Multi-GAS analyser, the grey oval shows a break in the trend caused by spikes in CO_2, b) a cropped 3 minute period demonstrating the correlation and links between Multi-GAS derived CO_2 and SO_2, with UV camera SO_2 flux, c) Multi-GAS CO_2 and SO_2 during the period of acquisition, similarly in d), e) and f), plotted are temporally coincident CO_2/SO_2 molar ratio, calculated CO_2 flux (through multiplication of SO_2 flux with CO_2/SO_2 mass ratios) and SO_2 flux respectively. Reprinted with permission from Elsevier.

Fig. 2.10b, over a cropped 3 minute period, showing a strong match between peaks and troughs with UV camera data (shifted using determined lag of ≈ 13 s). Given the common time-stamp between Mutli-GAS derived CO_2, SO_2, and the UV camera SO_2 data, it is possible to create an equivalently high temporal resolution and empirical CO_2 flux dataset. This is achieved by converting the CO_2/SO_2 molar ratio to a mass ratio (converted using the molar masses of CO_2 of 44.01 g mol^{-1} and SO_2 of 64.066 g mol^{-1}) and then directly multiplying the new CO_2/SO_2 mass ratio (Fig. 2.10d) by the temporally aligned UV camera SO_2 data (Fig. 2.10f), to produce CO_2 flux in kg s^{-1}. This shows that CO_2 flux experiences order of magnitude variations between ≈ 0.1 – 12 kg s^{-1} over very short timescales, a similar range to the variation observed SO_2 flux (≈ 0.1 – 16 kg s^{-1}). As discussed, we can assign an approximate error of ± 15 % to the calculated CO_2 flux, based on error in Multi-GAS sensor response times.

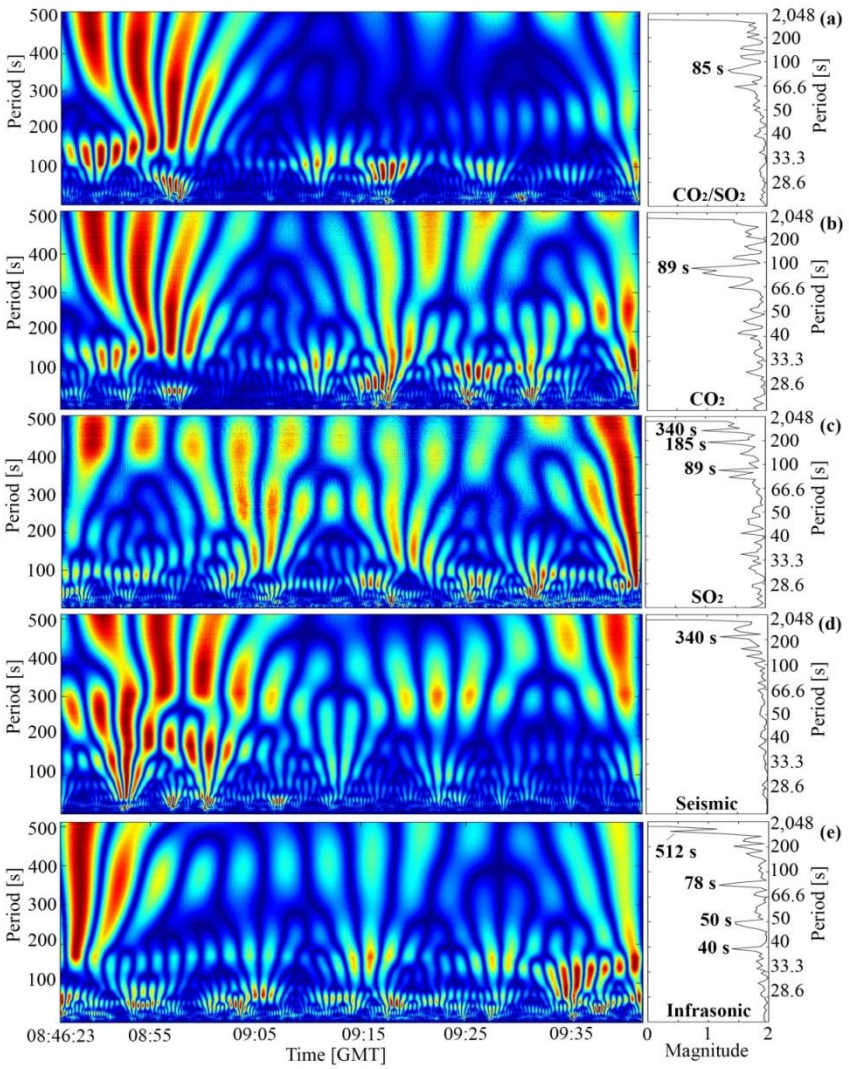

Fig. 2.11: Continuous wavelet transforms using a Morlet wavelet (see Fig. 2.3) for: a) CO_2/SO_2 molar ratio, b) CO_2 flux, c) SO_2 flux, d) seismicity from the EBCN station, and e) infrasound from the EBCN station. Alongside each wavelet plot are the PSDs using Welch's method. Reprinted with permission from Elsevier.

To the author's knowledge, this is the first quantitative estimate of high temporal resolution CO_2 flux for a volcano to date. Previously, high time resolution trends in SO_2 degassing have been identified at a number of volcanoes globally: e.g. Erebus (Boichu et al. 2010; Ilanko et al. 2015a), Kilauea (Poland et al. 2012), and Fuego (Nadeau et al. 2011), amongst others. Indeed, Tamburello et al. (2013) have also identified periodic features in SO_2 degassing, in particular over periods between ≈ 40 – 1200 s. The capture of CO_2/SO_2 ratios, CO_2 flux, and SO_2 flux provides the unique opportunity to probe for potential periodic links between these series and with contemporaneous geophysical datasets e.g. seismicity and infrasound. Geophysical instrumentation were located at the EBCN station (see Fig. 2.1) of the Istituto Nazionale de Geofisica e Vulcanologia (INGV) network (data provided by Andrea Cannata, INGV – Osservatorio Etnea) which was selected as the infrasonic sensor that was the least affected by wind noise of the instrumental network on the volcano (although the signal-to-noise ratio was still relatively high). We performed CWTs on all collected gas based and geophysical datasets (see Fig. 2.11), in addition, we performed PSD analysis using Welch's method (Welch, 1967) to identify the dominant peaks in each series. The results show that all gaseous datasets manifest non-stationary degassing, a feature shared by the geophysical datasets, over periods from ≈ 40 – 512 s. Periods of ≈ 89 s are shared between CO_2 and SO_2, while a similar period of ≈ 85 s is present within the CO_2/SO_2 molar ratio. At ≈ 340 s there is a matching period between seismicity and SO_2.

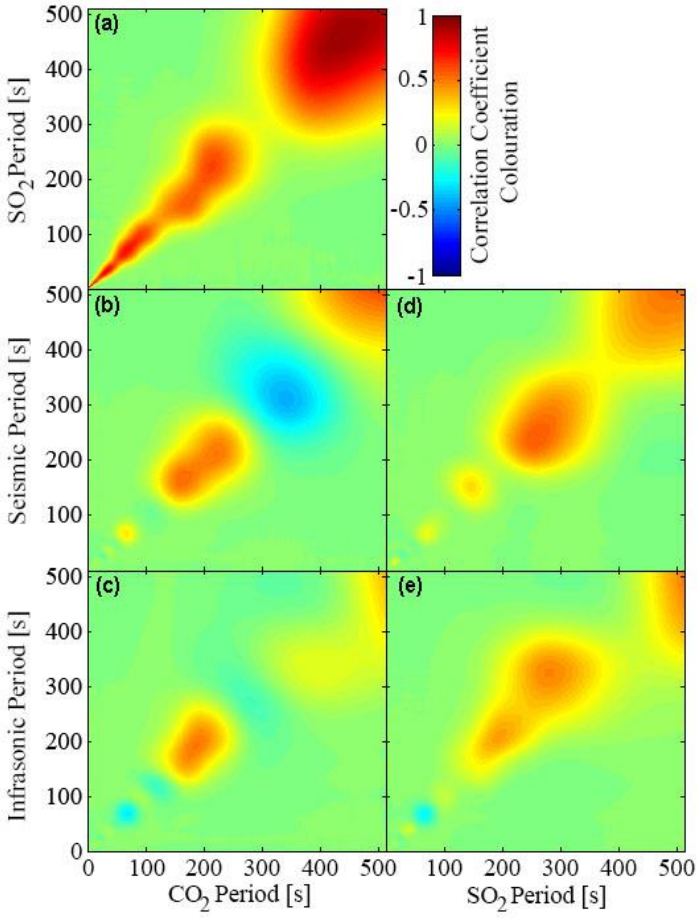

Fig. 2.12: Presented are a series of corrplot images (see section 2.3.2.) to investigate oscillatory links between CO_2, SO_2, seismicity and infrasound. Reprinted with permission from Elsevier.

Using the "corrplot" technique (section 2.2.2.) we investigate whether these periods were shared between the various datasets (see Fig. 2. 12). Firstly, there are strong links (correlation coefficeints > 0.5 on average) between CO_2 and SO_2 flux, particularly between ≈ 1 – 250 s and ≈ 350 – 500 s, with a brief breakdown between these two ranges, i.e. ≈ 250 – 350 s (Fig. 2.12a). Fig. 2.12d confirms the correlation between seismicity and SO_2 flux at ≈ 340 s and also hints at the possibility of links at lower levels ≈ 180 s and ≈ 90 s, although these links are less prominent with low correlation coefficient values of < 0.5. There are suggestions that there may be links between infrasonic and degassing, over periods between ≈ 200 – 400 s. Fig. 2.13b shows some intriguing trends between CO_2 flux and seismicity, primarily that there are links at ≈ 200 – 300 s. However, at ≈ 300 – 400 s this link breaks down and is replaced by negative correlation < -0.5. Intriguingly this is also the period range at which correlation breaks down between the CO_2 and SO_2 fluxes. To investigate this link we extracted the wavelet coefficients between ≈ 300 – 400 s for CO_2, CO_2/SO_2, and seismicity, and integrated over this period range, with the aim of capturing the characteristics of the oscillation. Fig. 2.13 shows that the negative correlation is driven by a lag between the CO_2 and seismic datasets of ≈ 100 – 150 s (with CO_2 release preceding the seismicity), with oscillations most pronounced in the first ≈ 20 minutes of the dataset. Indeed, this is the area where coincident peaks are also present in the CO_2/SO_2 and CO_2 flux records (grey shaded areas (Fig. 2.11), and where wavelet coefficients also show stronger oscillations (Fig. 2.11). By shifting the CO_2 flux dataset forward by ≈ 125 s an R^2 of > 0.9 is achieved.

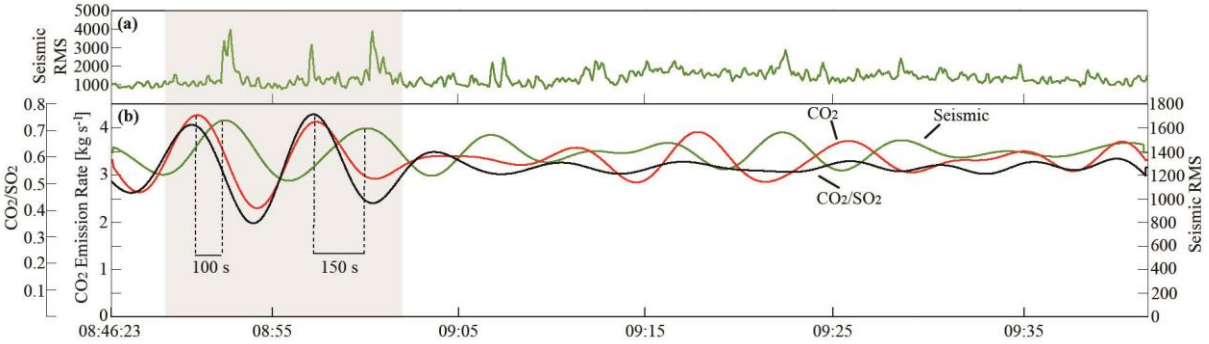

Fig. 2.13: a) seismic RMS during the period of acquisition from the EBCN station of the INGV network, b) wavelet coefficients extracted between 300 – 400 s and integrated for CO_2, CO_2/SO_2, and seismicity. This suggests that the negative correlation observed in Fig. 2.12b is driven by a lag of ≈ 100 – 150 s, with seismicity leading CO_2. The link is strongest in the grey shaded area, which also happens to coincide with CO_2 flux peaks observed in Fig. 2.10e. Reprinted with permission from Elsevier.

2.4. Discussion

The presence of matching periods between CO_2/SO_2, CO_2 and SO_2 (i.e. ≈ 85 – 89 s) suggests that the oscillations present at this level and above are volcanogenic in nature as atmospheric processes (e.g. diffusion, entrainment, and eddy based turbulence or convection) can't modulate oscillations in gas ratios. We rule out possible species and aerosol interaction (e.g. the possibility of chemical modification of the plume in transit) due to the extreme proximity to the vent (i.e. < 200 m) as a cause for this observation. However, atmospheric processes could modulate periods of all gas species simultaneously. For example turbulent diffusion (i.e. a high concentration of gas moving into an area with lower concentration) could smooth observed flux signals. We can calculate the upper period limit of turbulent diffusion (t_d) using Tiesi et al. (2006):

$$t_d = \frac{(2Dt)^{0.5}}{u} \qquad \textbf{(Eq. 2.4)}$$

where t is the time taken for the gas, on emission from the magma, to travel to the point of measurement, u is the plume speed, and D the atmospheric dispersion coefficient (≈ 10^2 m^2 s^{-1}). Instead of taking values of plume speed from this measurement campaign we take a range, typical for the summit of Mt. Etna ≈ 5 – 15 m s^{-1}. In addition, assuming the maximum possible travel distance to the point of gas measurement from the magma surface, potentially ≈ 200 m (personal communication – Alessandro Aiuppa, University of Palermo), this gives t_d values of ≈ 4 – 21 s, clearly below observed values.

Crater geometry can also play a strong role in modulating plume shape as well as periodic gas release. The key process related to crater geometry is the turbulent generation of eddies (e.g. Woods, 2005), which will be related to the diameter of the NEC, i.e. the constraining parameter on where the gas can flow (Pope, 2000; Costa et al. 2005), which is ≈ 100 m. The largest eddies will therefore be generated as the plume leaves the crater and will be equal to approximately half the crater and plume width (i.e. a form of convective cell), ≈ 50 m. Using the same plume speeds, we can estimate the time taken for an eddy of diameter ≈ 50 m to rotate around one circumference as a proxy for the maximum period generated. This gives estimates of ≈ 10 – 31s, again, this is below observed values. This demonstrates that caution needs to be applied when considering periodic links of < 40 s.

This leaves a number of other potential drivers for periodicity, including:

- Magma convection in conduits, magma chambers or storage systems (Koyaguchi et al. 1993; Kazahaya et al. 1994; Boichu et al. 2010; Cassidy et al. 2015), varying rates of convection, or even steady-state convection could help drive periodicity.
- Pulsing of magmas into conduits, chambers or storage systems, for example this has been invoked at Erebus as a cause for a ≈ 10 minute period in degassing (Oppenheimer et al. 2009; Peters et al. 2014a; 2014b).
- Natural arrangement of rising gas into bubble layers associated with bubble coalescence and velocity fields, this has been observed and characterised in basaltic lavas (e.g. Manga, 1996; Herd and Pinkerton, 1997).
- Real changes in gas flux associated with a change in gas supply from depth (Kazahaya et al. 2002).
- Changes in the rheology of a magma (e.g. density and viscosity). In some systems this is proven to be a pivotal component of magma flow within conduits related to convection (i.e. Kazahaya et al. 1994; Boichu et al. 2010). However, changes could be much more local (e.g. associated with crystal growth) and associated with changes in heat flux through the magma. Of course these changes can be short or long term.
- Heterogeneities in plumbing systems, such as conduit wall roughness (Jaupart, 1998), discontinuities which could allow the collection of gas (e.g. James et al. 2006; Palma et al. 2011) or more specifically tied to the collapse of foams which has also been associated with strombolian and Hawaiian type activity (e.g. Jaupart and Vergniolle, 1988; Vergniolle and Brandeis, 1994; Allard et al. 2005).

It is likely that some or all of the above may apply to single volcanic systems, particularly where lower viscosity magmas are involved which allow much more dynamic behaviour particularly where bubbles are concerned. These are illustrated in Fig. 2.14. Each of the above described potential drivers of periodic degassing would likely instigate differing timescales of fluctuations, however, an expanded dataset would be needed to characterise and develop these ideas further.

A number of periods within both CO_2 and SO_2 have been observed from the NEC of Mt. Etna, which are above the minimum limits for volcanically generated phenomena. Given the greater exsolution depth of CO_2 than SO_2 (Giggenbach, 1996), the ability to create datasets of CO_2 flux at high resolution could open up a new avenue for understanding degassing associated at open vent volcanoes globally. Indeed, this also enables the possibility of

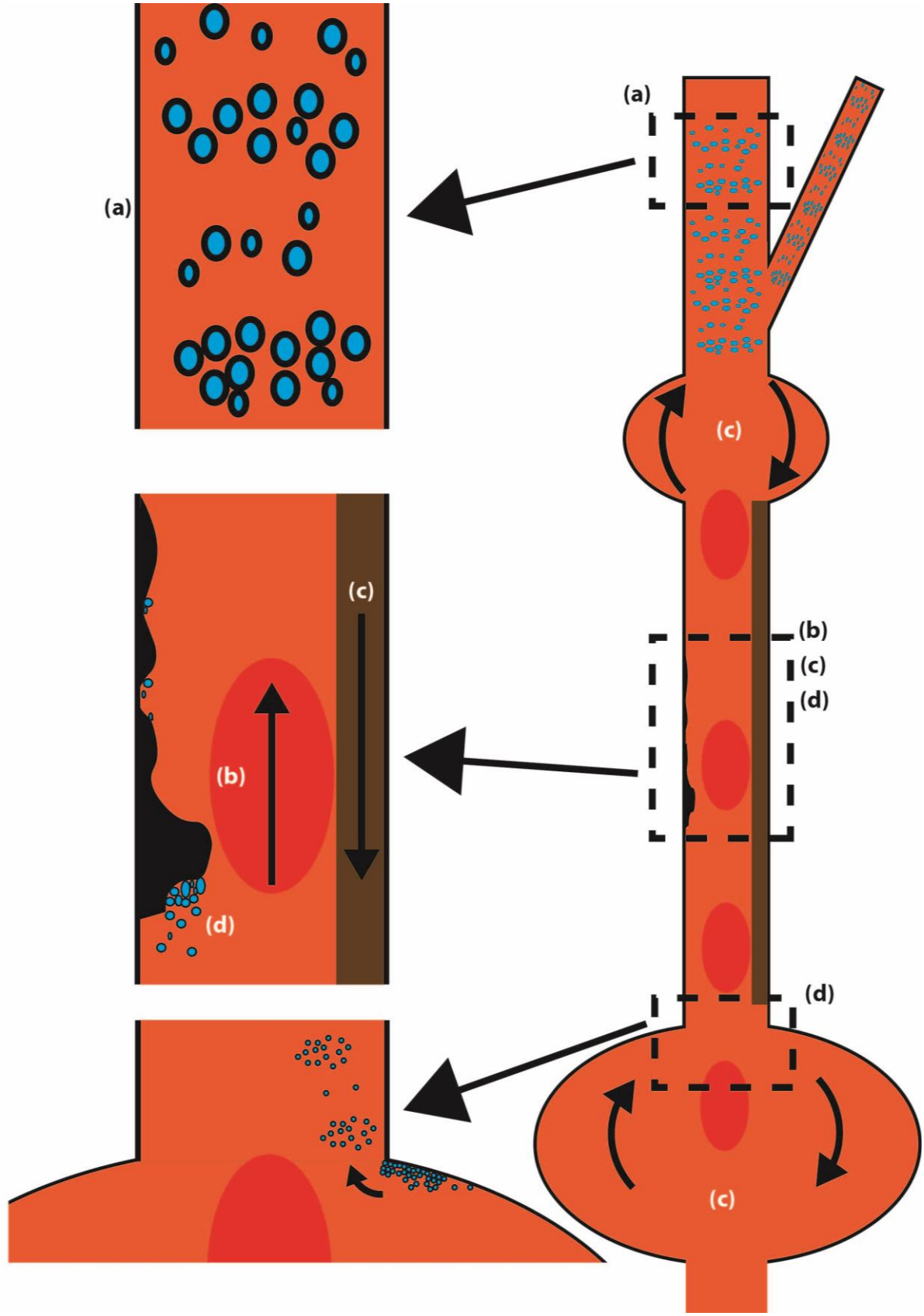

Fig. 2.14: Graphic depicting some of the potential causes for periodicity in volcanic degassing. In a) the periodic structure as a result of the natural arrangement of gas into layers (e.g. Manga, 1996), b) the pulsing of magma in batches (e.g. Oppenheimer et al. 2009; Peters et al. 2014a; 2014b), c) convection in the conduit caused by stratification or variation in magma density (e.g. Kazahaya et al. 1994), and d) the collection of gas at conduit discontinuities which allows the periodic release of bubbles, akin t the foam collapse mechanism (e.g. Jaupart and Vergniolle, 1988).

comparison to contemporary geophysical datasets. We observe strong links between SO_2 and seismicity over periods of ≈ 340 s (also observed over similar timescales by Tamburello et al. (2013) and the negative correlation present with CO_2 and seismicity at ≈ 340 s, caused by the observed lag between datasets (Fig. 2.13). This suggests that the release of CO_2 from the vent is followed by a consequent peak in seismicity some ≈ 150 – 180 s after release (accounting for gas travel time to point of measurement). This process seems to be strongest in the earlier portions of our dataset (between 08:50 and 09:00 GMT). Given the coincident peaks in CO_2/SO_2 ratios at the beginning of the dataset, this is suggestive that gas driving these peaks was sourced from greater depths (i.e. a pulse of magma or gas formed at a greater depth due to a change in heat or pressure allowing the exsolution of CO_2 at a greater depth). This would result in the magma, which contains the newly exsolved CO_2, to reduce in density causing it to rise. During the rise of this pulse local pressure fields following the magma could allow for the exsolution of SO_2 over a similar period, which as SO_2 exsolves at a shallow depth (≈ 3/4 km at Etna: Carroll and Holloway, 1994; Métrich et al., 2004; Métrich and Mandeville, 2010), may be able to generate a stronger seismic signal than the deeper degassed CO_2. The fact that there is a correlation between SO_2 and seismicity, but not directly with CO_2, suggests that the release of CO_2 and SO_2 could become decoupled and migrate largely independent of one another which would back up this hypothesis. Although, it is also plausible that the seismicity could precede the gas release if this is related to a convection based process. It is possible therefore, that the release of gas from the magma causes a readjustment of the magma level, which then generates seismicity.

During the measurement period, at ≈ 09:10 – 09:15 GMT a NW displacement in tremor location, at a depth of ≈ 500 – 1000 m, occurred (i.e. at the location associated with degassing under the NEC – often the main source of seismicity under Mt. Etna – personal communication, Giuseppe Di Grazia, INGV). This is followed by several large peaks in CO_2/SO_2 and CO_2 flux (after ≈ 500 – 900s), which is within a reasonable travel time for bubbles from such depths (e.g. Manga, 1996). This is more consistent with a process based on convection or the exsolution of gases and suggests that movement of magma and gas at depth is more likely to affect gas release and seismicity than magma level realignment, unless the latter is rather dramatic in nature. Again, however, much longer datasets are needed to investigate these processes and links in more detail. in particular, to look for changes during periods leading up to eruptive episodes.

This work also has implications for global volcanic estimates of CO_2 release, of particularly importance for estimating and comparing to anthropogenic emissions (Burton et al. 2013). Given the two order of magnitude variations in CO_2 flux ($\approx$ 0.1 – 12 kg s^{-1}) on rapid timescale of seconds it is conceivable that other estimates at a range of volcanoes could also be subject to similar rapid variations.

2.5. Concluding Remarks

Here, we have demonstrated the combined use of a UV camera and Multi-GAS analyser to produce a high time resolution CO_2 flux dataset. This has identified that rates of CO_2 degassing can fluctuate over two orders of magnitude within seconds. The high temporal resolution has also enabled, for the first time, comparison and analysis with contemporaneously acquired SO_2, and geophysical datasets, including the use of our newly designed technique. Indeed, the intriguing links, including temporal lag, between seismic and CO_2 periods suggest that future campaigns on Mt. Etna using longer datasets would be valuable in improving our understanding of links between degassing and seismicity.

3. Measuring and modelling explosive degassing at Stromboli

Chapter 3 presents the results of a combined UV camera measurement and computational modelling study focussed on degassing at Stromboli volcano. It demonstrates the value of analysing not just the explosive gas mass but that contained within the coda and the relationships between these two degassing modes. Daughter bubble production is suggested to be responsible for the production of the gas flux coda at Stromboli for the first time, with evidence present within the measurements and computational models. This chapter is based on the following presentation: *Pering, T.D., McGonigle, A.J.S., James, M.R., Tamburello, G., Aiuppa, A., 2015a. Comparing computational models of slug rise at Stromboli with UV camera measurements of SO_2 flux. In: EGU General Assembly 2015, Vienna*.

3.1. Stromboli Background

Stromboli, often referred to as the lighthouse of the Mediterranean, has been dominated for centuries by persistent activity associated with frequent explosions (Fig. 3.1) which occur on average every ≈ 5 – 10 minutes (Chouet et al. 1974, GVP, 2015). These explosions, after the name of the island itself, are termed as strombolian. Given the explosive frequency and ease of access to the summit area, Stromboli is one of the most widely studied basaltic volcanoes. These studies include petrological (e.g. Metrich et al. 2001), seismic (e.g. Chouet et al. 1999; 2003), infrasonic (e.g. Ripepe et al. 2002), thermal (e.g. Patrick et al. 2007), explosion dynamics focused (e.g. Taddeucci et al. 2012), the dynamics of slug generation (e.g. Jaupart and Vergniolle, 1988; Wilson, 1980; Parfitt and Wilson, 1995), modelling (e.g. James et al. 2004; 2006; 2008; Suckale et al. 2010b; Del Bello et al. 2012; 2015) and degassing orientated (e.g. McGonigle et al. 2007; 2009; Mori and Burton, 2007; Burton et al. 2007; Tamburello et al. 2012). This is by no means an exhaustive list but gives an overview of the importance of

Fig. 3.1: A strombolian explosion occurring from the a summit crater at the summit of Stromboli, photo taken by the author.

Stromboli as a volcanic target of study. Within this chapter the focus is two-fold, on measurements of degassing events using UV cameras and modelling slug flow using computational fluid dynamics, all in a bid to understand the dynamics of slug flow and the generation of slugs at Stromboli.

The introduction to this thesis has already provided an overview of the development of the UV camera technique; the reader is therefore referred to that chapter for further methodolgical information. Previous studies on gas emissions at Stromboli have mostly focussed on the explosive aspects (e.g. Mori and Burton, 2006; McGonigle et al. 2009; Tamburello et al. 2012). Burton et al. (2007) specifically looked at gas ratios for a range of degassing types, while Tamburello et al. (2012) as a result of improvements in UV camera technology began to be able to identify gas masses from puffing in addition to characterising explosive gas release. Tamburello et al. (2012) were also the first to note the presence of an extended gas coda following on from strombolian explosions. This is an aspect which is investigated further in this chapter.

Strombolian events are generally accepted to be caused by the ascent and bursting of a gas slug (Chouet et al. 1974; Blackburn et al. 1976), also referred to in the non-volcanic literature as Taylor bubbles (e.g. Taha and Cui, 2006). Hence, understanding how these bubbles behave within the conduit and how they emit gas when they reach the surface is vital. Strombolian events occur from the summit craters at Stromboli, while smaller hornito degassing events sometimes referred to as puffing (e.g., Tamburello et al. 2012), occur from smaller hornito features on the sides of the main crater. It is important to note here that there are differences in the use of the word "puffing" at Stromboli and even globally. Some authors (e.g. Taddeucci et al. 2012) refer to puffing as the constant rapid pulsing (every ≈ 0.5 s) of small clouds of gas released from smaller vent openings (e.g. hornitos). Here, however, we refer to puffing as events which occur without the ejection of explosive material (e.g. Tamburello et al. 2012), which can be accompanied by an infrasonic signal (although are not always so) and occur over longer repose periods. These puffing events are also associated with the bursting of larger gas bubbles.

3.2. UV Camera Measurements

Data was collected using the UV camera network operated by the Palermo and Firenze Universities. The UV camera network allows the calculation of entire crater terrace SO_2 fluxes, which, in turn also allows the calculation of explosive SO_2 mass for events occurring from individual craters and from a hornito (see Fig. 3.2a for example images of a hornito event). For further details on the UV camera procedure and data collection the reader is referred to sections 1.3.1, 2.2, and 4.2. Each event is typified by an initial rapid increase in SO_2 flux, followed by a coda of varying length before returning to background flux levels.

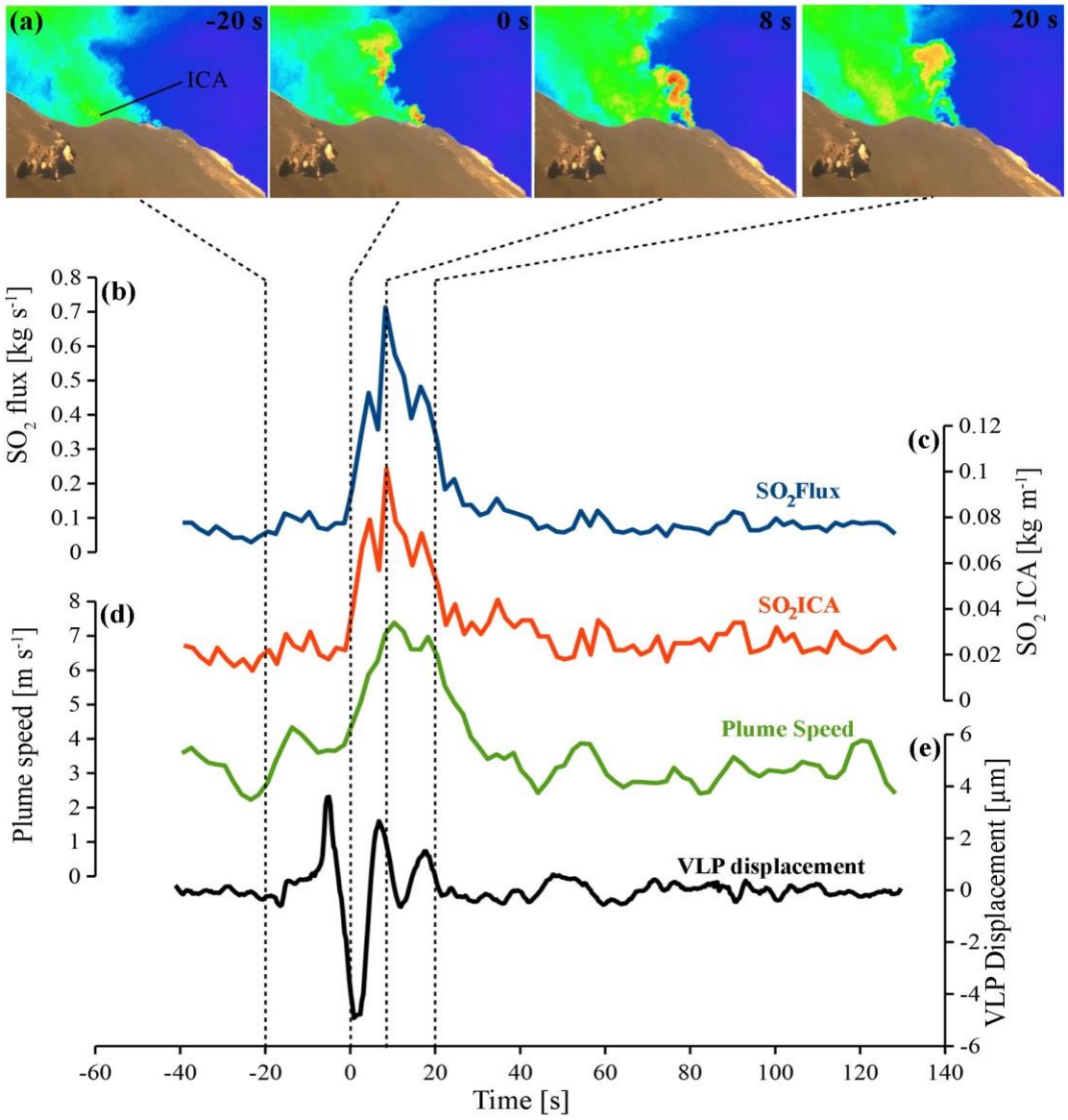

Fig. 3.2: Here, an example sequence of UV camera SO_2 absorption images during a hornito degassing event is presented (a) along with associated parameters used for the calculation of flux (b); including SO_2 ICA (c), plume speed determined using optical flow algorithms, the resultant SO_2 flux (b), and VLP displacement (d). Data and graph provided by Giancarlo Tamburello (Palermo University).

Fig. 3.2 illustrates this process for a single hornito event including example SO_2 ICA, plume speed (calculated using optical flow algorithms – e.g. Horn and Schunk, 1981; Peters et al. 2015), and VLP (very-long-period) displacement which is often associated with strombolian events (Chouet et al. 2003) but only sporadically for hornito events (data and figure courtesy of Giancarlo Tamburello, Palermo University). This process was repeated for 120 strombolian events and 80 hornito events.

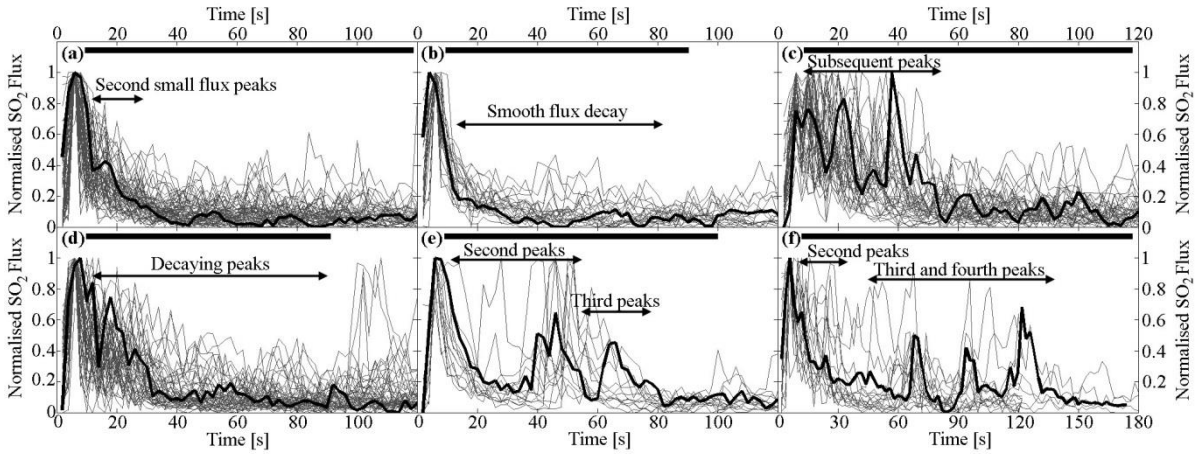

Fig. 3.3: Here, every single measured strombolian and hornito event is displayed within our dataset, after subtraction of the minimum value and dividing by the maximum. From (a) through to (e) the typically degassing regimes observed have been split and categorised together. In each subplot the event in bold denotes a typical event style, although this is by no means a hard and fast rule, while the black bar at the top of each subplot represents the maximum observed event time during the observation period, where an event is deemed to cease on return of flux to background levels. For a full description of how the events have been characterised, see Table 3.1 and the text.

Fig. 3.3 shows all of these analysed events. To enable comparison of strombolian and hornito events, which are of varying magnitude both intra and inter explosion, the minimum value was subtracted (i.e. approximately the background flux level) then all the events' time series were divided by their respective maximum value (usually the initial flux peak). This process highlighted a certain array of events which appeared to share similar patterns following the initial flux peak associated with the initial bursting of the slug (e.g. see Tamburello et al. 2012). These have been split up and are illustrated in Fig. 3.3. The dominant styles of post-explosive degassing are associated with those in Fig. 3.3a and Fig. 3.3d. In Fig. 3.3a events are associated with an initial flux peak in magnitude followed by a small secondary peak, not exceeding the first flux peak but occurring within ≈ 20 – 30 s of the initial explosion. The maximum event time (calculated as the point that flux returns to levels seen prior to the explosion) is ≈ 120 s. The events in Fig. 3.3b have an initial flux peak and then a smooth

coda not exceeding ≈ 90 s in length. The events in Fig. 3.3c are significantly more prominant with initial peaks followed by multiple subsequent peaks up to a maximum ≈ 60 s after the initial event. The subsequent peaks are occasionally observed (as in the black characteristic event of Fig. 3.3c) to be of a larger magnitude (but not necessarily a larger mass). Fig. 3.3d events, the second most common class of events, are associated with multiple peaks following the initial burst; however, each peak is lower in magnitude than the previous peak (i.e. decaying peaks) until they return to background flux levels. Fig. 3.3e events experience two peaks following from the initial flux peak. These are of varying magnitude with second peaks occurring in the first ≈ 20 – 50 s, and the third peaks occurring between ≈ 50 – 80 s. Finally, events in Fig. 3.3f have multiple peaks, up to a total of 4, with the second peaks occurring in the first ≈ 30 s and third and fourth peaks occurring between ≈ 50 – 140 s. These events are also the longest lived with maximum coda of ≈ 180 s. Table 3.1 summarises the selection and characterisation of these degassing patterns following from events. All descriptions and duration estimates are relevant to the collected data only. Stromboli is a highly dynamic degassing system (Taddeucchi et al. 2012; Tamburello et al. 2012; Burton et al. 2007), as such, significant variability in patterns, timescales and magnitude is expected.

Table 3.1: A summary of the degassing regimes identified following on from strombolian explosions. The raw data is presented in Fig. 3.3.

Event Type	Description	Event Time (s)
Type a	An initial flux peak with a small flux peak within ≈ 20 – 30 s of the initial peak. Coda can experience smaller rapid fluctuations.	30 – 120 s
Type b	A smooth flux decay over 30 – 90 s	30 – 90 s
Type c	3 or more peaks of a similar size within 60 s of burst, superimposed over a coda with length 50 – 120 s	50 – 120 s
Type d	An initial burst followed by decaying peaks, superimposed over a coda with length 30 – 90 s	30 – 60 s
Type e	An initial burst with a small coda < 30 s, followed by a secondary flux peak of varying magnitude after 20 – 60 s, a similar small coda and/or a tertiary peak may also be present	60 – 100 s
Type f	An initial burst, followed rapidly by a secondary flux peak within 40 s of a similar or greater magnitude, these can be followed by tertiary and quaternary peaks between 60 – 140 s, a small coda < 30 s is present following each peak	120 – 180 s

From this data it is then possible to calculate explosion mass and coda mass for each strombolian and hornito event. Explosion mass is calculated as per the procedure of Tamburello et al. 2012 and Pering et al. (2015b), by integrating underneath the initial flux peak. Here, we reasonably assume that the initial flux peak is associated with the impulsive

burst event when a gas slug arrives at the surface and vigorously bursts, releasing gas rapidly towards the point of integration (i.e. the ICA). An event is deemed to have ceased on returning to background flux levels, calculated as the flux prior to the initiation of an individual event. The coda mass can then be calculated as the explosion mass subtracted from the event mass. This process is illustrated for three strombolian events in Fig. 3.4.

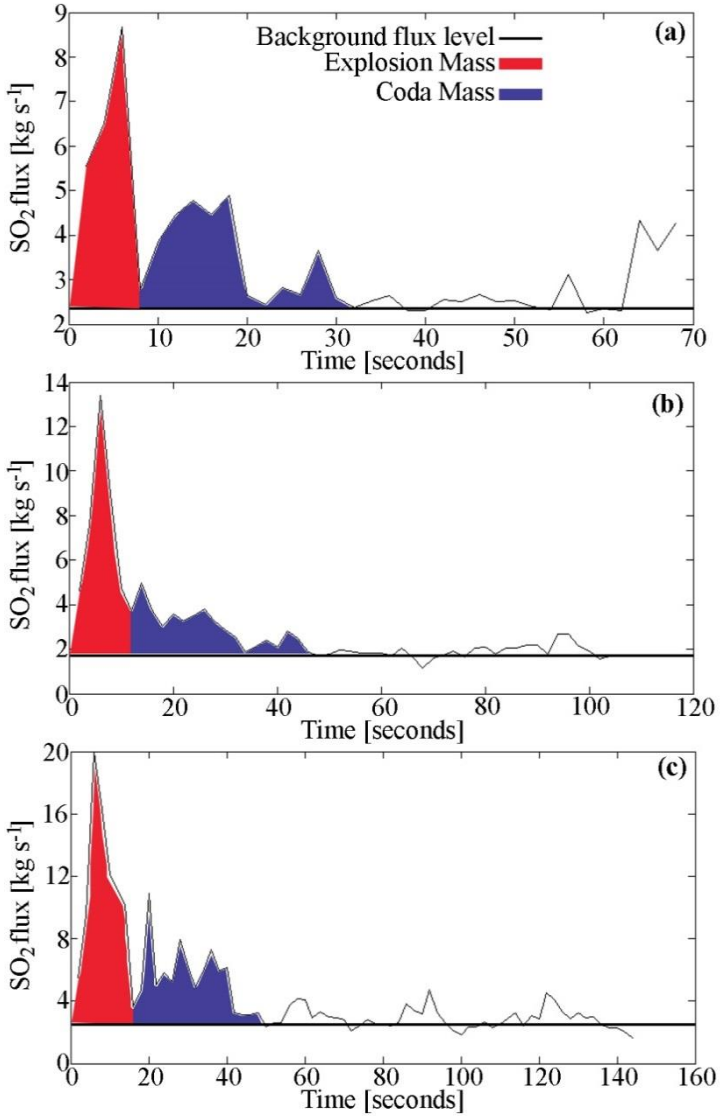

Fig. 3.4: Three examples (a, b, and c) of determined explosion and coda mass by integrating underneath the initial flux peak to determine the explosion mass and integrating beneath the rest of the flux peak until flux has returned to background levels seen prior to the explosion (black line).

Strombolian explosion SO_2 masses ranged from ≈ 8 – 82 kg, with total event SO_2 mass between ≈ 18 – 225 kg. Hornito explosion SO_2 masses ranged ≈ 0.2 – 5.3 kg, with total event SO_2 mass between ≈ 2 – 19.6 kg. By combining these values with gas ratios (CO_2/SO_2 and

H_2O/SO_2) determined by Burton et al. (2008) it is possible to approximate the total gas mass released from strombolian and hornito events. The results of this process are summarised in Table 3.2. This demonstrates the magnitude difference between strombolian and hornito events.

Table 3.2: A summary of determined explosive and event SO_2 masses, with equivalent total gas masses calculated using the Burton et al. (2007) gas ratios.

	Minimum	Mean	Maximum
Strombolian Explosion [kg SO_2]	8	30	82
Strombolian Event [kg SO_2]	18	87	225
Strombolian Explosion Total Gas Mass [kg]	181	708	1,949
Strombolian Event Total Gas Mass [kg]	428	2,072	5,360
Hornito Explosion [kg SO_2]	0.2	1.9	5.3
Hornito Event [kg SO_2]	2	7.5	19.6
Hornito Explosion Total Gas Mass [kg]	5	46	125
Hornito Event Total Gas Mass [kg]	47	179	467

Prior to this work the amount of gas released passively after an explosion has received relatively little focus. Tamburello et al. (2012) briefly remark on the length and presence of a gas coda. In Fig. 3.5 the range of determined coda masses is illustrated, highlighting the range of coda for both hornito (Fig. 3.5a) and strombolian events (Fig. 3.5b). Again, the magnitude difference between style is evident; however, some overlap in the upper ranges of hornito coda and lower ranges of strombolian coda is present. The majority of coda (i.e. between the 1st and 3rd quartiles) for hornito coda are located between ≈ 96 – 148 kg (median = 125 kg), and for strombolian coda ≈ 865 – 1,750 kg (median = 1,120 kg). A much smaller range of coda masses is apparent for hornitos than for strombolian events. In percentage terms, the majority of gas is contained within the coda for hornito events, at ≈ 70 – 84 %, while, for strombolian events this is ≈ 53 – 75 %.

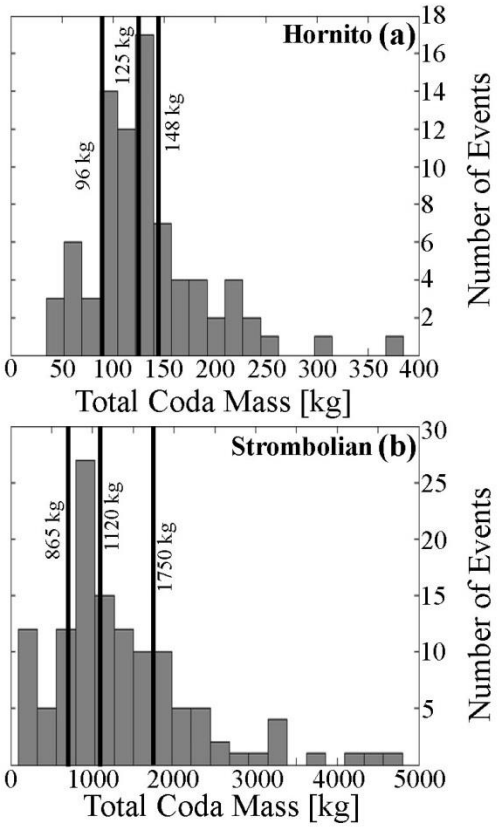

Fig. 3.5: The distribution of total gas masses contained in hornito (a) and strombolian events (b). The black lines show the minimum, median and maximum coda masses respectively.

In Fig. 3.6 the potential relationships between explosive SO_2 mass and varying parameters is investigated. Fig. 3.6a shows a lack of correlation between explosive and coda mass for all the measured events. There is also no clear correlation of this nature for either of the event styles (both producing $R^2 \approx 0$). Fig. 3.6b shows a general relationship ($R^2 = 0.84$) for the strombolian and hornito events between explosive mass and total event mass (explosion plus coda), highlighting, that as explosion mass increases so does the total event mass. Finally, in part (c) of Fig. 3.6, explosive mass is compared to the coda:explosion mass ratio. Here the hornito ratio shows a strong $R^2 = 0.79$, demonstrating that as explosion mass increases the proportion of gas contained within the coda decreases. This is a trend which may also be present with strombolian ratios, however, there are a significant number of events with low explosive mass and lower coda:explosion mass ratios < 1. Overall, the data here show that there are clear differences between the masses of the explosive and coda portions of strombolian and hornito events. Within this analysis there appears to be little evidence of significant relationships associated with the different event categories of Fig. 3.3 (described in Table 3.1), i.e. events seem to be interspersed with each other with little clustering.

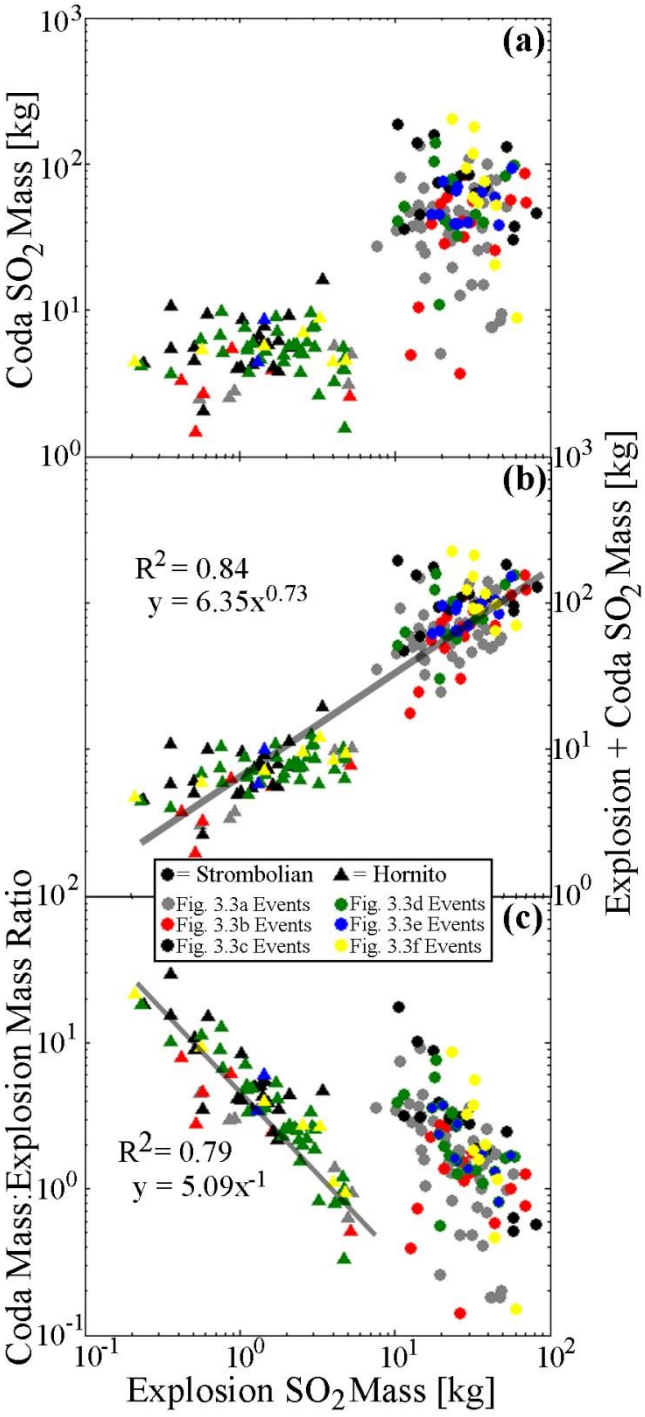

Fig. 3.6: The relationship between explosion mass and a) coda mass, b) explosion plus coda mass (i.e. event mass), and c) coda to explosion mass ratio. No clear relationship is apparent in a), as explosion mass increases so does explosion plus coda mass in b), while in c) hornito events demonstrate a decreasing portion of gas within the coda as explosion mass increases. This relationship is clouded with strombolian events.

3.3. Behaviour of bubbles at Stromboli

To understand and begin to probe possible physical causes of the observed coda it is first essential to understand how rising bubbles behave within the conduit at Stromboli. A large number of studies, have demonstrated that gas slugs are the parsimonious explanation for the cause of strombolian eruptions (e.g. Chouet et al. 1974; Blackburn et al. 1976, Seyfried and Freundt, 2000 and references therein). As such, the behaviour of gas slugs has received considerable attention (e.g. James et al. 2008; Del Bello et al. 2012, 2015; and references therein). Indeed, the behaviour of gas slugs is predictable based on the media in which they flow, according to: magma density, conduit radius, and magma viscosity (conduit inclination also plays a part). A gas slug rising in a vertical cylinder has a hemispherical nose and a gap between the edges of a slug and the cylinder (or conduit) wall which is called the falling film. A slug is considered to be a slug when it is at least as long as it can be wide, i.e. around the conduit diameter (Wallis, 1969; Clift, et al. 1978). As the slug ascends the base of a slug rises at a constant velocity (Viana et al. 2003), while the nose (as it approaches the surface) will accelerate, due to depressurisation increasing the volume of the slug prior to burst at the surface of the liquid (Seyfried and Freundt, 2000; James et al. 2008). During this process the falling film is pulled down the sides of the slug. The falling film thickness can be estimated based on the relation of Llewellin et al. (2012):

$$\lambda' = 0.204 + 0.123\tanh(2.66 - 1.15\log_{10} N_f) \qquad \textbf{(Eq. 3.1)}$$

where N_f is the dimensionless inverse viscosity, a term which is used to characterise the system (Wallis, 1969):

$$N_f = \frac{\rho_m}{\mu}\sqrt{g(2r_c)^3}. \qquad \textbf{(Eq. 3.2)}$$

Here ρ_m is the magma density, μ is magma viscosity, g is the acceleration due to gravity and r_c is the conduit radius. N_f can also be used in predicting the rise speed of the base of a slug, here the Froude number (Fr) is calculated (Viana et al. 2003; Llewellin et al. 2012):

$$Fr = 0.34\left[1 + \left(\frac{31.08}{N_f}\right)^{1.45}\right]^{-0.71} \qquad \textbf{(Eq. 3.3)}$$

which then allows the calculation of the rise speed of the base of the slug, u_{sl}, as follows:

$$u_{sl} = Fr\sqrt{2gr_c} \qquad \textbf{(Eq. 3.4)}$$

Another important feature of a slug is the form of the slug base, termed the wake. Here, N_f has been used in a series of studies (e.g. Campos and Guedes de Carvalho, 1988; Noguiera et al. 2006) to categorise the form of the slug wake. A slug wake can be completely closed and axisymmetric, with little or no interaction with the surrounding medium, or can be open and actively turbulent. Noguiera et al. (2006) demonstrated that for N_f < 500 the wake of a slug is closed and interaction decreases as N_f decreases. However, for an N_f of > 500 a wake can open and become increasingly turbulent. This turbulence, if severe enough, can even involve the shearing of small bubbles from the gas slug itself. These bubbles are termed 'daughter bubbles' and can either be reincorporated into the slug (Campos and Guedes de Carvalho, 1988) or ejected from the influence of the slug and of the wake to rise as separate trains of bubbles (Bouche et al. 2010).

By using parameters appropriate to Stromboli we can begin to probe how these slugs, particularly from a turbulence perspective, may start to behave within the conduit. By using a magma density of 2700 kg m^3 (Vergniolle and Brandeis, 1996; Métrich et al. 2001), a magma viscosity range of 200 – 500 Pa s^{-1} (Vergniolle et al. 1996; James et al. 2008), and values for conduit radius of 1 – 3 m (Harris and Stevenson, 1997; Donne and Ripepe, 2012), the N_f relation gives a broad range of values of N_f values = 47 – 621. This demonstrates that there may well be some turbulence and daughter bubble production within the volcanic regime at Stromboli. As such, it is entirely plausible that the gas coda of section 3.2 are caused by the production of daughter bubbles from the base of an ascending slug. The possibility of daughter bubble production in a volcanic environment has been discussed previously (James et al. 2006; Bouche et al. 2010; Llewellin et al. 2014a) and in the next section the importance of slug mass loss during bubble ascent will be assessed using computational fluid dynamics (CFD) in comparison to the observations of section 3.2.

3.4. CFD modelling of slug flow at Stromboli

Models of volcanic gas slugs were implemented in the commercially available CFD software package Ansys Fluent®. To simplify the model and reduce run-time a 2D axisymmetric simulation was used, which effectively simulates a small wedge of a vertical cylinder (i.e. the volcanic conduit). A small quadrilateral gridded mesh (mapped face meshing) of 0.1 m by 0.1 m was used (see Fig. 3.8b). Here we use the in-built volume-of-fluid solver within Ansys Fluent ®, with the implicit body force option enabled which allows the sharper definition of

boundaries between magma and slug gas. The model is pressure-based (as opposed to density based) as this allows the full scaling of a model to a volcanic situation involving slug expansion and includes thermal effects (which effects the expansion of the slug). All equations defining the models, which are based on the solution of the compressible Navier-Stokes equations are available from the software suppliers website at http://www.ansys.com/, where the reader can find further details. The timing scheme was explicit, i.e. the solution of the Navier-Stokes equations was performed for a defined future time-step. A fixed time-step of 10^{-3} s was used during slug rise and 10^{-5} s when the slug is approaching burst, this is to allow the maximum Courant number to remain below 0.25. The setting of the Courant number allows the correct solution of the partial differential equations and is based on the velocity of every grid-cell within the simulation (Courant et al. 1967). Data was outputted from the model at a resolution of 10 Hz. The simulated conduit has a closed base (i.e. no free flow of magma or gas) and an open top set at a constant atmospheric pressure of 101,325 Pa. In contrast to previous models (e.g. James et al. 2008), three fluids are simulated, these include: the magma, dry air for the atmosphere above the magma column, and water vapour for the slug. Water vapour is chosen as Burton et al. (2007) demonstrated that 83% of a slugs molar mass at Stromboli is indeed water vapour (this is a common feature of most volcanic gas slugs). The magma and dry air phases are simulated as incompressible fluids, with water vapour the only compressible fluid (i.e. behaving as an ideal gas in accordance with the ideal gas law – $PV = nRT$, where P is pressure, V is volume, n the number of moles, R the universal gas constant, and T temperature).

Ansys Fluent® has been used by Taha and Cui (2006) and Araujo et al. (2012; 2013) to simulate slug flow. However, in each instance this was for smaller conduits and markedly different fluids. To investigate the applicability of the Ansys Fluent® volume-of-fluid method to a volcanic situation a number of validation models were run. These were implemented with a conduit radius of 1m, all with single slugs at a magma depth of ≈ 400 m, a magma density of 2700 kg m^3, but with varying magma viscosities (between 50 – 2000 Pa s^{-1}). This is to simulate a range of N_f numbers (≈ 12 – 478) and hence a range of slugs with differing wakes. All other model parameters are as described in the previous paragraph. For a summary of validation model runs (V1 – V27) see Table 3.3. I can then compare the results of these validation simulations with theoretical values for film thickness (Llewellin et al. 2012) and slug base rise speed (Viana et al. 2003; Llewellin et al. 2012). Within the models the film thickness was taken as the distance between the conduit wall and the point that the

density of the material within a cell (on a horizontal transect through the conduit), on filled density contour plots, is < 2700 kg m^3, i.e. transitioning to water vapour and the slug gas. The distance between pure magma density and that of pure slug gas is ≈ ± 0.13 m in each model simulation; this is therefore taken as model error in film thickness. The in-model slug base rise speed is taken at two different model simulation times (10 s apart) and as the distance travelled by the base of the slug. With slug base rise speed the error is ≈ ± 0.1 m s^{-1}, i.e. this is taken to be equal to the time step of the model simulation and the cell size (of 0.1 m).

Table 3.3: A summary of model validation runs, modelled, and theoretical film and slug base speeds. Italicised rows are those simulations which produced daughter bubbles.

Name	Nf	Viscosity (Pa s^{-1})	Th. Film (m)	Th. Speed (m s^{-1})	M. Film (m)	M. Speed (m s^{-1})
V1	*478*	*50*	*0.16*	*1.49*	*0.1*	*1.19*
V2	*435*	*55*	*0.16*	*1.48*	*0.1*	*1.18*
V3	*399*	*60*	*0.16*	*1.48*	*0.1*	*1.16*
V4	*342*	*70*	*0.17*	*1.47*	*0.12*	*1.13*
V5	*299*	*80*	*0.18*	*1.47*	*0.15*	*1.15*
V6	*266*	*90*	*0.19*	*1.46*	*0.15*	*1.10*
V7	*240*	*100*	*0.19*	*1.45*	*0.18*	*1.07*
V8	*199*	*120*	*0.21*	*1.44*	*0.19*	*1.06*
V9	120	200	0.24	1.37	0.19	1.05
V10	80	300	0.26	1.28	0.20	0.95
V11	60	400	0.27	1.19	0.22	0.94
V12	48	500	0.28	1.11	0.24	0.93
V13	40	600	0.29	1.03	0.26	0.90
V14	34	700	0.29	0.97	0.26	0.89
V15	30	800	0.30	0.90	0.27	0.86
V16	27	900	0.30	0.85	0.28	0.84
V17	24	1000	0.30	0.79	0.28	0.80
V18	22	1100	0.30	0.75	0.28	0.75
V19	20	1200	0.31	0.71	0.29	0.72
V20	18	1300	0.31	0.67	0.29	0.67
V21	17	1400	0.31	0.63	0.29	0.63
V22	16	1500	0.31	0.60	0.29	0.60
V23	15	1600	0.31	0.57	0.29	0.58
V24	14	1700	0.31	0.55	0.29	0.55
V25	13	1800	0.31	0.52	0.29	0.53
V26	13	1900	0.31	0.50	0.30	0.50
V27	12	2000	0.31	0.48	0.30	0.48

Fig. 3.7 shows the results of these validation model runs, while Fig. 3.8a gives a snapshot of slugs at the same time-step but at differing viscosities. An excellent degree of match is demonstrated for CFD modelled slugs at viscosities of ≥ 900 Pa s^{-1}, with errors of < 1% or ≈ 0.01 m s^{-1}. At values of < 900 Pa s^{-1} modelled slug speed is slower than the theoretical values, with errors of ≈ 2 – 25%, or ≈ 0.03 – 0.38 m s^{-1}. This error is non-linear, with a rapid increase in modelled speeds at viscosities < 200 Pa s^{-1}. A large amount of this disparity is likely a result of converging values of cell size, film thickness and simulation time-step. Meanwhile, a similar degree of match is seen for film thicknesses but at lower viscosities of ≥ 600 Pa s^{-1}. The difference between modelled and theoretical film thickness values diverge slightly below this. The average difference between modelled and theoretical film thicknesses is ≈ 0.03 m or ≈ 12%. In a similar manner modelled film thickness is noted to rapidly change at < 200 Pa s^{-1}. To the author's knowledge, this is the first open determination and display of the accuracy of CFD for simulating volcanic gas slugs in comparison to theoretical values.

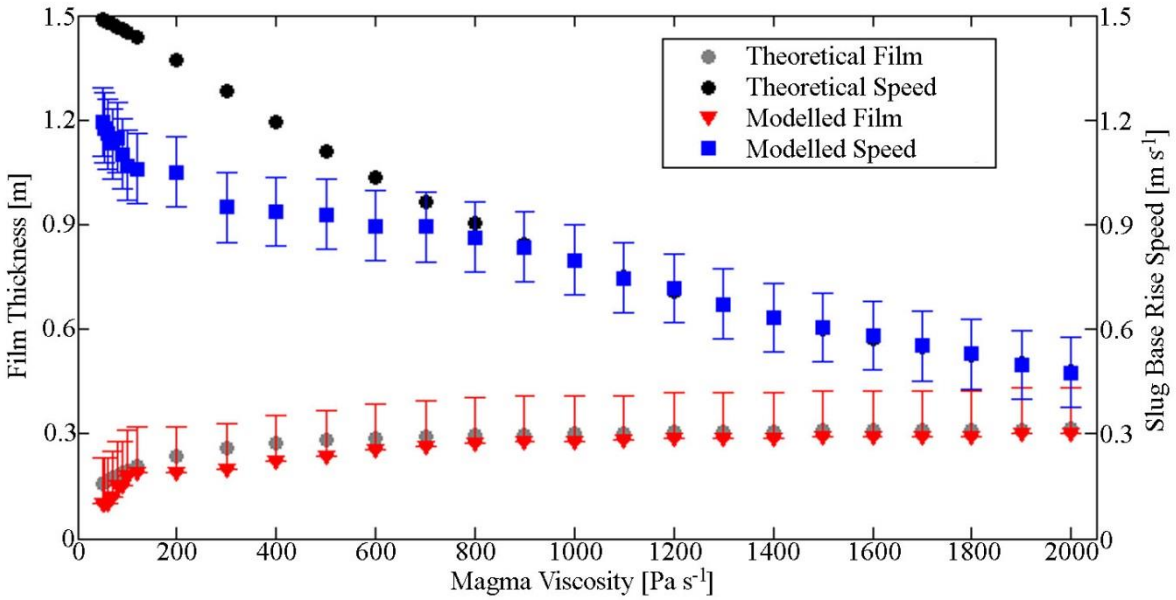

Fig. 3.7: Figure showing the performance of Ansys Fluent® against theoretical values. For details on error bars see section 3.3 and for details on calculation of theoretical film thicknesses and rise speed see equations 3.1 to 3.4 in section 3.3.

Overall, these results demonstrate the ability to model a volcanic system well at higher viscosities with lower N_f values, with slightly more divergence at higher N_f values. This is potentially caused by the production of daughter bubbles from the base of slugs (which are not considered in the theoretical estimates). Daughter bubbles are indeed seen as a common feature at N_f values ≤ 120 Pa s^{-1}. It is also important to restate here that while the simulations are 2D and axisymmetric the underlying features and physics will be broadly the same as a

full 3D simulation, although, a certain amount of model error is likely. An important aspect in all volume-of-fluid simulations is the conservation of volume, particularly of the incompressible phase, in this case the magma (dry air can be released from the open top of the conduit, and the slug gas is compressible). Results show that the volume of the magma is conserved to a value of < 1 %, this gives further confidence in our models. Average mass loss rate from each validation model run which produced daughter bubbles was also calculated (see italicised model runs in Table 3.3), this was then plotted against N_f (see Fig. 3.9). This shows a non-linear relationship between N_f and mass loss rate worthy of further investigation in a lab or CFD setting.

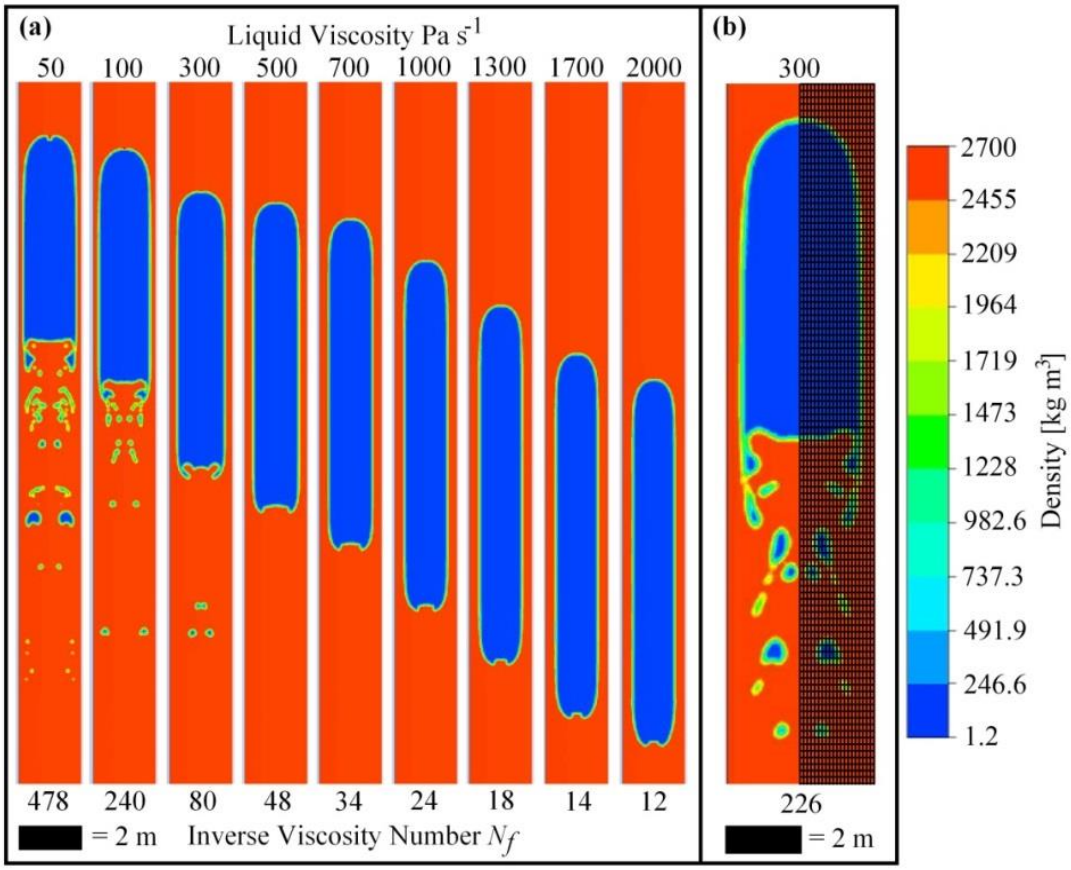

Fig. 3.8: In a) a snapshot of slugs from a series of validation model runs showing the production and non-production of daughter bubbles. All models images were captured at 12 s after model initiation. In b) an example slug from the Stromboli specific model runs with mesh density displayed.

This validation then allows us to have a degree of confidence in our Stromboli specific model runs. In total four Stromboli specific model runs (S1 – S4) were chosen over a range of slug masses and two initial slug depths. The first three model runs (S1 – S3) were initiated with an initial slug depth of ≈ 300 m, and a range of appropriate slug masses, S1 = 1537 kg, S2 = 3303 kg, S3 = 5096 kg. This initial depth was chosen as this corresponds to the source of

VLP as determined by Chouet et al. (1999). The final run (S4) was initiated with a slug depth of ≈ 900 m and slug mass = 3515 kg, with the purpose of investigating slug behaviour over a longer ascent distance. This information is summarised in Table 3.4.

Table 3.4: A summary of Stromboli specific model runs from S1 – S4, including final results for slug length, final exploded mass, and percentage of mass lost into the coda.

Name	Mass (kg)	Depth (m)	Final Length (m)	Final Mass (kg)	% Mass Lost
S1	1537	300	28.3	477	69
S2	3303	300	72.8	1576	53
S3	5096	300	95.7	2932	43
S4	3515	900	5.0	26	>99

For these Stromboli specific models the following model parameters are used: a magma density of 2700 kg m^3 (Vergniolle and Brandeis, 1996; Métrich et al. 2001), a magma viscosity of 300 Pa s^{-1} (Vergniolle et al. 1996), a magma surface tension, σ, of 0.4 N m^2 (Seyfried and Freundt, 2000; James et al. 2008), and a conduit radius of 2 m (Harris and Stevenson, 1997; Donne and Ripepe, 2012). The magma is set at a temperature of 1000°C, with the dry air at 20°C. The slug water vapour is initialised at the same temperature as the magma, with a thermal conductivity = 0.0261 W m^{-1} K^{-1} (in-built Ansys Fluent® value) and a ratio of specific heats of 1.4 (James et al. 2008). These values are summarised in Table 3.5.

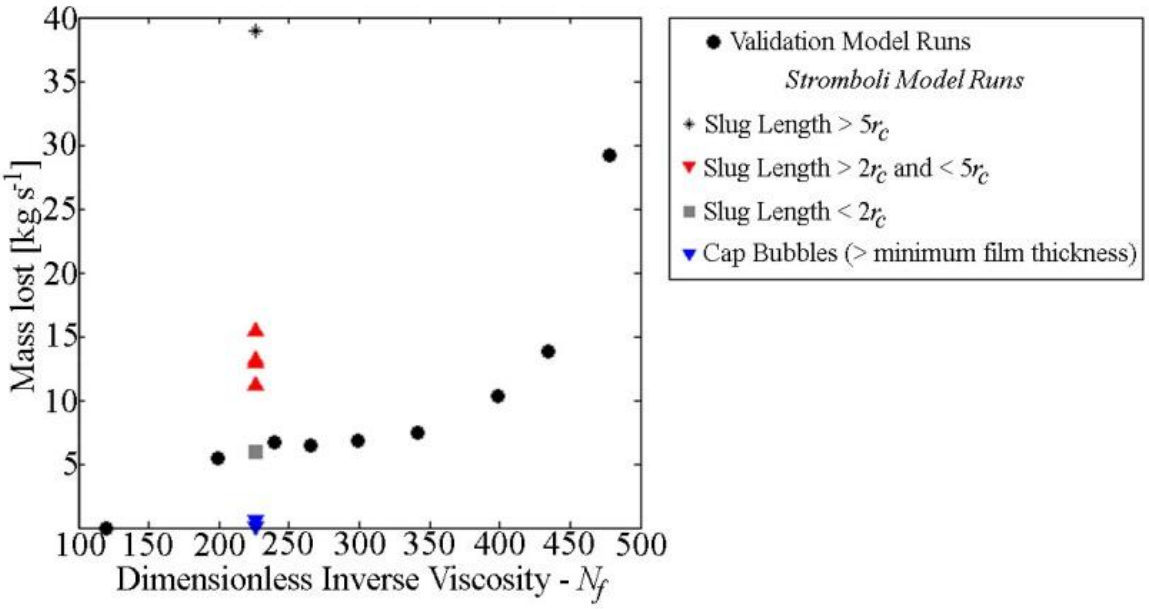

Fig. 3.9: This plot shows the relationship between N_f and mass lost per second for both validation and Stromboli specific model runs. The non-circular coloured points refer to different gradients, which are illustrated and annotated in Fig. 3.10.

The first observation from all Stromboli runs is that they all demonstrate the production of daughter bubbles (see Fig. 3.8b and Appendix B). The overwhelming majority of these daughter bubbles, which range in mass between ≈ 0.2 – 14.4 kg (mean ≈ 2.7 kg), are fully released from the influence of the slugs, which leads to a subsequent large reduction in the mass of each slug. From each model; slug mass, magma surface level, and the position of the slug nose and base as a function of time was outputted. Model S4 shows bubble length instead of slug base and nose position due to length of the bubble and total distance travelled. Fig. 3.10 demonstrates mass loss rates (kg s^{-1}) and it quickly becomes clear that the mass loss rate is not constant during each slugs ascent. In S1 the slug loses 69 % of its initial mass and has three dominant mass loss rates: 13 kg s^{-1}, 5.9 kg s-1 and 0.6 kg s^{-1}. At some points during ascent, the slug dips below the minimum criteria for categorisation as a slug. In S2 the slug loses 53 % of its initial mass, but sustains a constant mass loss rate of 11.2 kg s^{-1}. In S3, the largest massed of the slugs injected at 300 m, in the initial ≈ 30 s of slug ascent, slug gas is lost at 38.9 kg s^{-1} before reverting to 15.4 kg s^{-1} for the remainder of the simulation prior to burst, resulting in a loss of 43% of its mass. In these simulations (S1 to S3) more rapid variability is seen with S1 and S2 than with S3. S4, initiated from a depth of 900 m, loses almost all of its mass (e.g., > 99%). There are also two dominant mass loss rates 13.2 kg s^{-1} for the first ≈ 200 s of the simulation and 0.1 kg s^{-1} for the remaining ≈ 250 s. This large reduction reduces the bubble's mass to such an extent that it reverts to a more primitive cap bubble morphology with very little daughter bubble production (see Fig. 3.10d for illustrations). Indeed, at ≈ 200 – 250 s the rising bubble gains mass from previously emitted daughter bubbles which have caught up with the rising bubble (see videos of simulations described in Appendix B).

Table 3.5: A summary of parameters used in the Stromboli specific model runs, selected according to the current understanding of the magmatic system at Stromboli: [a,f] Vergniolle and Brandeis (1996), Métrich et al., (2001); [b] Vergniolle et al. (1996); [c] Harris and Stevenson (2007); [d] Harris et al. (1997), Donne and Ripepe (2012); [e] Chouet et al. (1999), [f] James et al. (2008).

Parameter	Value
Magma Density[a]	2700 kg m^3
Magma Viscosity[b]	300 Pa s^{-1}
Magma Temperature[c]	1000 °C
Conduit Radius[d]	2 m
Atmospheric Pressure	101325 Pa
Initial Slug Depth[e]	300 m
Ratio of Specific Heats[f]	1.4

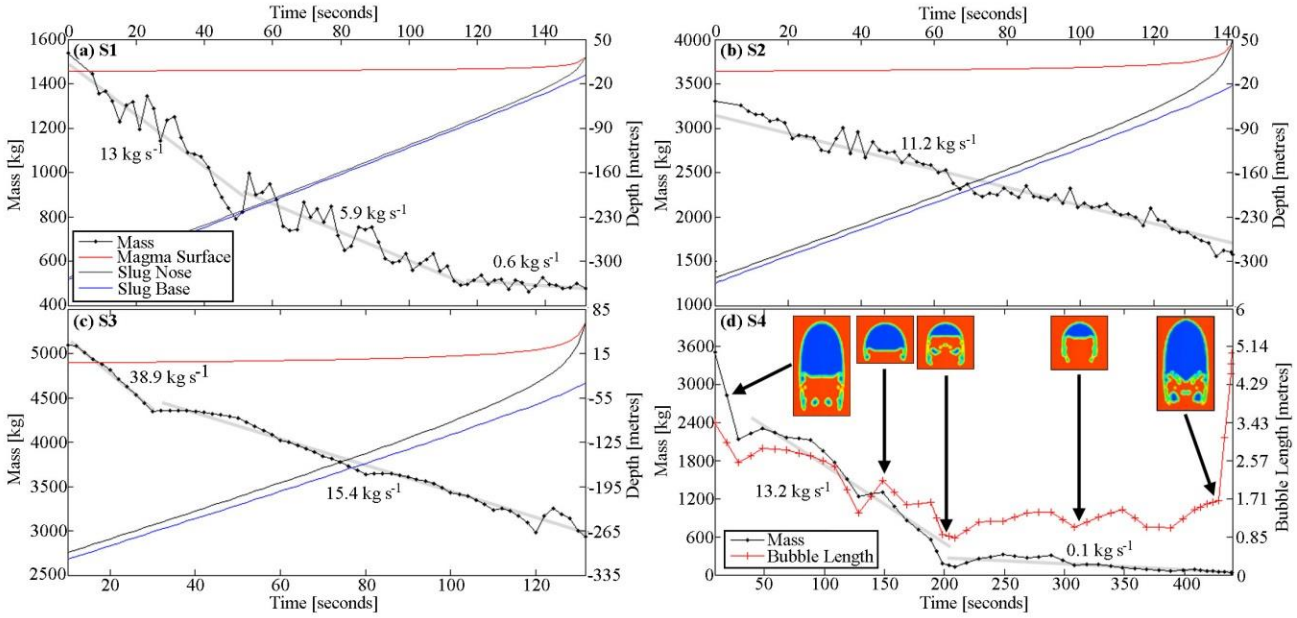

Fig. 3.10: These plots show the mass of a slug as a function of time for all Stromboli specific model runs. The trend lines with determined mass loss rates are also displayed. For runs S1 – S3 the change in magma surface height, and positions of the slug nose and slug base are also displayed. In S4 bubble length is displayed alongside mass. Increased variability is evident in S1 and S2 compared to S3, largely associated with the larger mass of the rising slug. In S4 images of a slug which eventually transitions to a cap bubble are displayed along with their associated times.

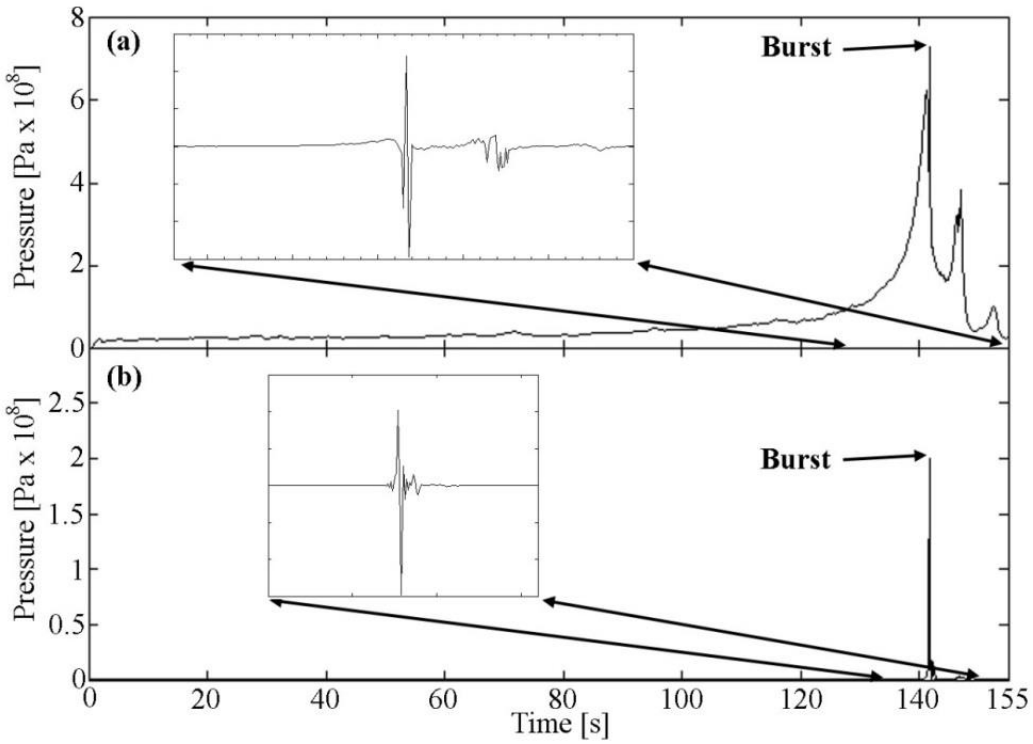

Fig. 3.11: Example artificial geophysical signals generated during Stromboli specific model run S1. In a) a proxy seismic signal showing general pressure increase and peak at burst, with inset differentiated pressure pulse. In b) a proxy infrasonic signal with inset differentiated pressure trace showing the characteristic N-wave of a volcanic infrasonic pulse.

3.4.1. Proxy geophysical signals

The Ansys Fluent® software package also allows the extraction of geophysical signals generated during the ascent of a gas slug. By integrating pressure at a point ≈ 10 – 20 m above the magma (at point of burst) in the conduit, at a time resolution equal to the model-time-step (well above geophysical data collection rates), the passage of an infrasonic pressure wave can be detected. As a proxy for seismicity the pressure in the entire magma column is summed at each time-step, this takes into account the changes in pressure associated with gas flow and movement of the magma. This fits with the general theory that seismicity is caused by resonance of the magma-gas mixture as it moves within the conduit (e.g. O'Brien and Bean, 2008). By differentiating each signal one can extract a proxy of how this signal would appear in the raw geophysical data.

Fig. 3.11 shows example geophysical signals for the S1 model. In Fig. 3.11a a slow increase in pressure within the magma is observed, associated with the increasing length and passage of the slug through the magma. This occurs over a similar time period to the VLP observed at Stromboli. After the burst (indicated in Fig. 3.11a), a few oscillations appear which are likely associated with the readjustment of the magma level and the ascent of trailing daughter bubbles. Inset in Fig. 3.11b is the characteristic N-wave shape associated with a volcanic infrasonic pulse (Ripepe et al. 2002). Whilst not a focus of the study discussed here, this has potential for the future application of models in combining gas flux measurements with both geophysical signals as well as models of gas flow with accompanying modelled geophysical signals.

3.5. Discussion and Implications

A variety of degassing regimes are identified, as expected for such a dynamic degassing environment. However, a degree of repeatability is demonstrated over the various event types which leads to a number of possible root causes. There are four main potential drivers of variable degassing following a burst event: (1) atmospheric generation, (2) conduit geometry heterogeneities, (3) magma rheology heterogeneities, and (4) physically varying flux from the conduit (e.g. generated by the slug). Each of these will now be discussed in turn.

Atmospherically generated flux variations can occur through the entrainment of ambient air into the hot rising volcanic gas (Costa et al. 2005; Kaminski et al. 2005), additionally

diffusion, dispersion and turbulent eddy generation can play a role, while crater geometry can be key to the latter (Woods, 2005; Tamburello et al. 2013). These will all act to smooth the flux signal on exit from the conduit and will affect all the identified degassing regimes.

A volcanic conduit will rarely be perfectly cylindrical (e.g. Seyfried and Freundt, 2000), indeed at Stromboli there is strong evidence for a kinked conduit (Chouet et al. 2008), while observations at other volcanoes suggest that conduits can be tapered towards the surface (Walker, 1993). Varying conduit wall roughness could also allow the collection and release of gas intermittently (Jaupart and Vergniolle, 1988, 1999; Gilbert and Lane, 2008). For example these could change the way that a slug behaves within the conduit and even the stability of a slug. The opening of the conduit closer to the surface would increase the turbulence of the slug wake (i.e., increasing the N_f number) and could lead to increased daughter bubble production.

Closer to the magma surface, fall-back of ejected pyroclasts and radiative cooling of the upper portions of the magma could induce a viscosity contrast, which would have a resultant effect on how a slug interacts with and eventually emits gas at the surface (e.g. Capponi et al., 2014; Gaudin et al. 2014a). One of these effects is the pinching of a gas slug, in effect creating two (or perhaps more) separate gas pockets which could emit as distinctly separate entities (Del Bello et al. 2015). Indeed, within the flux measurements this is the case with the most common events (Type a, from Fig. 3.3) and events with large peaks in quick succession following a burst (Types c, d, e, and f from Fig. 3.3). This also fits well with visual observations which demonstrate two distinct gas thrust phases (Tadduecci et al. 2012).

Evidently, a physically varying flux issuing from the magma can be generated via mechanism (2) or (3), equally though it is plausible that gas directly generated by the rise of a gas slug (i.e. including daughter bubbles) could rise and burst to be observed in the flux records at the surface. In particular, the most common event types a and b (from Fig. 3.3), which are also the least peaky events, with flux codas of ≈ 30 – 120 s, and similar in length to those reported in Tamburello et al. (2012), could be generated by the initial burst of a slug and bubble chain. It is possible that pressure variations in the magma caused by the passage of the gas slug could allow the exsolution of additional gas from the melt, which could also account for the coda observed when the gas reaches the surface. Hypothetically, c, e, and f (from Fig. 3.3), which have secondary, tertiary and even quaternary peaks between ≈ 40 – 140 s after initial burst could be generated by the bursting of larger daughter bubbles created by coalescence

and eventual expansion prior to bursting at the magma surface (see videos described in Appendix B) and could even provide a causal mechanism for puffing activity.

Fig. 3.6, which colour codes the different categories of degassing regimes, doesn't identify any clear separation of different styles of events. This suggests that the degassing patterns could be a result of variability or a combination of a number of the discussed drivers. For example, hornito events regardless of degassing pattern all lie on the same trend line (particularly in Fig. 3.6c).

Overall, measurements in the field show a relatively tight range for mass loss from slugs with ≈ 53 – 75% and 70 – 84% of the slugs' gas lost from strombolian and hornito events respectively. In comparison, for models initiated from a depth of ≈ 300 m, this range is ≈ 43 – 69%; which is a particularly close match with the measured strombolian events. A degree of caution with direct comparison is necessary however, due to the simplification of our models and the complexity of the system at Stromboli. Furthermore, as previously mentioned the shallow portion of the conduit is likely inclined at 40° from the vertical. This will have implications for the behaviour of the gas bubble both in rise speed and with the generation of daughter bubbles (Clift et al. 1978). A slug rising in an inclined conduit will rise with an increased base velocity, with inclined conduits even promoting slug flow (James et al. 2004). This will have an as yet unknown effect on the production of daughter bubbles, although if this behaviour remains, as is likely, linked to the parameter N_f then daughter bubble production may remain somewhat consistent. Although this study has certainly demonstrated the high variability of daughter bubble production rate even with constant magma and conduit parameters. A further uncertainty in our models is in the use of the 2D axisymmetric environment, a necessity for allowing a quick model solution with manageable data amounts. The calculation of mass released from daughter bubbles is therefore the sum of a series of tori released from the base of the slug. Whilst, the variations seen between differing regimes will be preserved, the estimates for mass loss rate will likely be over-estimates and represent upper-limits for potential mass lost. Fig. 3.9 and Fig. 3.10, demonstrate this further complexity associated with differing conduit widths and bubble shapes. All this suggests that further investigation using more sophisticated 3D models is necessary to enable the full characterisation of both daughter bubble loss and the effect of inclined conduits.

Total gas masses of created daughter bubbles observed within the models ≈ 0.2 – 14.4 kg (mean ≈ 2.7 kg) fit relatively well with total measured gas masses of puffing events at

Stromboli, estimated at ≈ 3.33 – 10.72 kg (mean of 6.67 kg), using Burton et al. (2007) gas ratios and Tamburello et al. (2012) measurements of SO_2 mass for individual puffs (0.14 – 0.45, mean 0.28 kg). The slight disparity between modelled and measured puffing event averages could be a result of the inability of the UV camera to measure the smallest events (Tamburello et al. 2012). Alternatively the physics and model mesh size could also be contributing factors.

Based on our determined gas coda for hornito and strombolian events and our average gas mass loss rate from slugs, ≈ 13.2 kg s^{-1} (this is calculated using the dominant mass loss rate seen for medium lengths of slugs – see red triangles of Fig. 3.9). We can estimate the time that it would take for a slug to rise to produce the observed coda. Using the 1st and 3rd interquartile values for total slug mass this gives results of ≈ 130 – 270 m, with a median of ≈ 190 m, and a maximum of ≈ 740 m (i.e. using the maximum observed coda mass). For hornito events this is much shallower at ≈ 15 – 23 m for the 1st and 3rd interquartile, and for the maximum hornito coda mass ≈ 60 m. The larger range in observed strombolian rise depths is certainly consistent with the variability observed in the coda:explosion mass ratio. The clustering of depths at < 300 m implies a possible change in conduit geometry in the initiation of daughter bubble production; as this is also around the depth of VLP generation (Chouet et al. 1999) this is a reasonable possibility. Fig. 3.6c shows a greater degree of hornito trend strength and event repeatability. Given the obvious differences in gas mass (see Fig. 3.6) between strombolian and hornito events, this suggests that there is a different generation mechanism and/or a shallower source depth for the slugs. The largest coda and maximum ascent depth of ≈ 740 m suggests that, if the daughter bubble model is in operation throughout the conduit, slug flow can only be sustained above this level, i.e. during our measurement period no larger coda were observed. In addition smaller massed gas slugs would destroy themselves, as in simulation S4. All of the above data are illustrated in Fig. 3.12.

Our models also have other implications, particularly associated with the modelling of gas slugs. In the case of the deepest modelled slug, daughter bubble production appears constant for the initial ≈ 450 m until the length of the slug has decreased to such an extent (≈ 2 m), that it is probably better termed a spherical cap bubble (e.g. Wallis, 1969). At this stage, daughter bubble production visually slows (see videos described in Appendix B). This will induce a disparity when using single slug models to predict slug length prior to and at burst. For example the model of James et al. (2008) predicts a length of ≈ 5 m, contrary to the observed

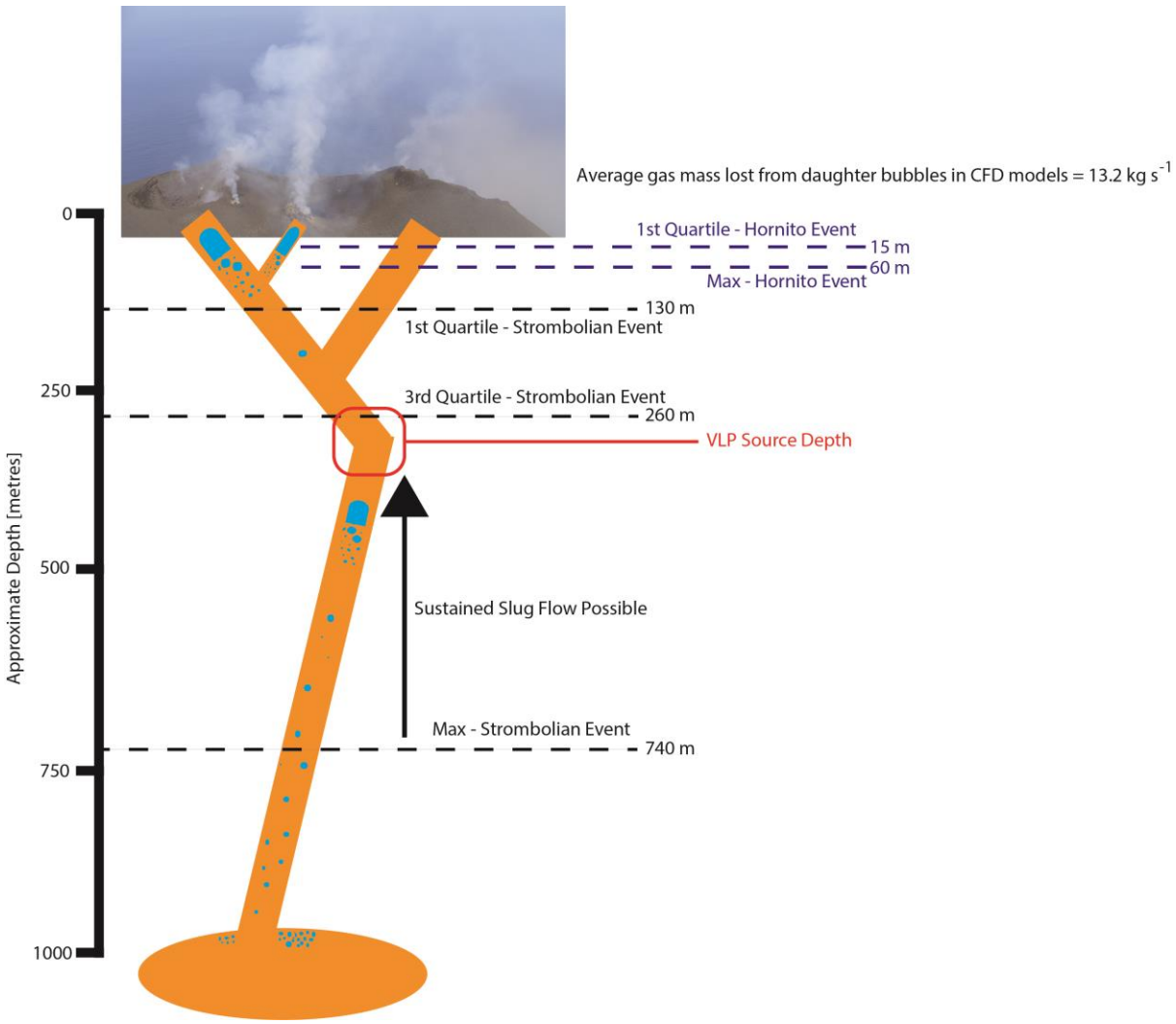

Fig. 3.12: A graphic summarising the hypothesis presented for stable slug flow based on the daughter bubble model presented in this chapter. The ranges of distance needed to generate strombolian and hornito coda is indicated along with approximate VLP source depth.

≈ 2 m. These observations, associated with the deepest modelled slug, are not observed to the same extent, with those of the shallower counterparts. This suggests that existing single slug models (e.g. James et al. 2008; Del Bello et al. 2012) may only be applicable where: viscosity and applicable magma parameters (e.g. magma density, conduit radius etc.) are above or below certain critical values (i.e. below an appropriate N_f number); where daughter bubble production and full release of these bubbles from the influence of the slug wake does not occur, and in the area dominated by the greatest decompressive expansion of the slug length.

This highlights the importance of considering the volume loss from a rising slug. Using the ideal gas law, in combination with the average gas mass loss rate, 13.2 kg s^{-1}, we can approximate the depth at which volumetric expansion of the slug would begin to dominate over daughter bubble loss. We estimate this using three reasonable sized events, appropriate

for our measurements: 500 kg, 2,000 kg, and 5,000 kg of gas. This suggests that volumetric expansion begins to dominate at ≈ 350 m, ≈ 1,500 m, and > 2000 m for the small, medium, and large massed events. However, over these ascent ranges no consideration is given to the time period of ascent and release. The model merely demonstrates the point above which volumetric expansion would dominate. If a slug of ≈ 5,000 kg rose from a depth of ≈ 2,000 m it would lose more than the mass it originally contained, at around 13,200 kg s^{-1} (calculated using ascent speed of ≈ 2 m s^{-1}). Note then that this is hypothetical and is not meant to override the previous results discovered by mass loss, but does serve to illustrate that large enough slugs could flow at depth.

The possibility of daughter bubble production highlights the complexity of the magma system at Stromboli and also presents questions about the slug formation mechanism at Stromboli (i.e. foam collapse [Vergniolle and Jaupart, 1986] or bubble coalescence [Parfitt, 2004]). It is already clear that there are larger centimetre to metre sized bubbles (other than and including slugs) contained within the conduit which cause hornito and puffing events. Any slug rising in such a mixture will pick up and lose gas mass during ascent. If a rising slug is losing mass through daughter bubble production during ascent, initial conduit injection mass will be larger than measured at the surface. In short, given the dynamic regular nature of activity, pinning slug generation at Stromboli to arise from a single formation mechanism is likely a significant over-simplification of the system.

3.6. Concluding Remarks

In this chapter, the value of combining measurements of degassing with computational models is clearly demonstrated. Further to this, the key need to investigate trends in passive degassing (in this case associated with coda) after an explosive event is identified. Using this it is hypothesised that daughter bubbles produced by the rising slugs themselves could be implicated in the production of the gas flux coda. The models demonstrate that daughter bubble production at Stromboli could be prolific, to the extent that if a slug was to rise from depths of > 740 m, slug flow may not be able to sustain itself. Indeed, the attrition of mass can even cause reversion to more basic bubble forms such as cap bubbles. The complexity of daughter bubble production in a volcanic environment is also demonstrated, where the parameter N_f is clearly not the only control on daughter bubble production. This should lead

to more in-depth studies using 3D computational models to understand and characterise this behaviour.

The detailed characterisation of coda and their explosions is the first such study, building on the original work of Tamburello et al. (2012). Significantly more information could be gleaned from data such as this with combined geophysical analysis. In addition knowledge of changes in gas ratios for each individual event (through the use of an FTIR [Fourier Transform Infrared Spectrometer]) could unlock information about where the rising gas completely decoupled from the melt (e.g. using the technique of Burton et al. [2007]). Equally this could demonstrate whether there are any changes in ratio between the initial explosion and subsequent coda. Stable ratios during the explosion and coda could indicate that the gas is sourced from the same location – i.e. the slug itself.

This work highlights the need for care when using existing slug models such as James et al. (2008) and Del Bello et al. (2012) for predicting overpressures and final slug lengths, particularly where the input parameters could be within the daughter bubble producing regime. Further work will help to produce a universally applicable combined model.

4. Measuring and modelling rapid strombolian activity

Chapter 4 focuses on UV camera measurements during a rare period of Strombolian activity at the Bocca Nuova crater on Mt. Etna. The mass of strombolian events from this target is estimated for the first time. Basic modelling is applied with a view to understanding more about the dynamics of the system and investigating the cause behind an intriguing trend observed, whereby larger slugs are followed by longer repose times before the following explosion. This chapter is based on the work: *Pering, T.D. Tamburello, G., McGonigle, A.J.S., Aiuppa, A., James, M.R., Lane, S.J., Sciotto, M., Cannata, A., Patanè, D., 2015b. Dynamics of mild strombolian activity on Mt. Etna. Journal of Volcanology and Geothermal Research* 300, 103-111.

4.1. Introduction

The previous chapter discussed activity related to the bursting of single slugs at Stromboli (Fig. 4.1). Here, the focus is on much more rapid strombolian activity occurring on timescales of seconds instead of minutes. An important distinction for this chapter is the difference between the behaviour of slugs during strombolian activity in a single slug environment (e.g. Davies and Taylor, 1950; Wallis; 1969, Clift et al. 1978; James et al. 2008;2009; Llewellin et al. 2012; Del Bello et al. 2012; 2015) and those in a multi-slug environment (Seyfried and Freundt, 2000; James et al. 2004; Pioli et al. 2012). A slug is considered to be operating in a single slug environment when it is travelling at a sufficient distance from the adjacent slugs, such that it is not impeded or affected in any way by the progress of neighbouring slugs. Defining this distance and exploring inter-slug relationships in much more detail (e.g., investigating the potential timing of bursts) is the focus of Chapter 5. Given the inherent complexities surrounding slug behaviour in a multi-slug environment, much of our current understanding is derived and extrapolated from the single slug literature, particularly in a volcanic context (e.g. James et al. 2008; 2009; Llewellin et al. 2012; Del Bello et al. 2012; 2015). However, a number of fluid dynamical studies, e.g., Pinto and Campos, (1996); Pinto et al. (1998, 2001); Krishna et al. (1999) do focus on the interaction between multiple bubbles. In particular, these studies identify the most important features of a slug, which are

the wake interaction length (e.g., Pinto and Campos, 1996) and the wake length (Campos and Guedes de Carvalho, 1988; Noguiera et al. 2006). Fig. 4.1 illustrates these features.

The wake length is defined using the N_f criterion (described fully in Chapter 3, with the mathematical definition repeated here):

$$N_f = \frac{\rho_m}{\mu}\sqrt{g(2r_c)^3}. \qquad \textbf{(Eq. 4.1)}$$

From this we can use Campos and Guedes de Carvalho (1988) to calculate the wake length (l_{wake}):

$$l_{wake} = 2r_c\left(0.30 + 1.22 \times 10^{-3}N_f\right). \qquad \textbf{(Eq. 4.2)}$$

We can also use Pinto and Campos (1996) to calculate the wake interaction length (l_{min}):

$$l_{min} = 2r_c(1.46 + 4.75 \times 10^{-3}N_f). \qquad \textbf{(Eq. 4.3)}$$

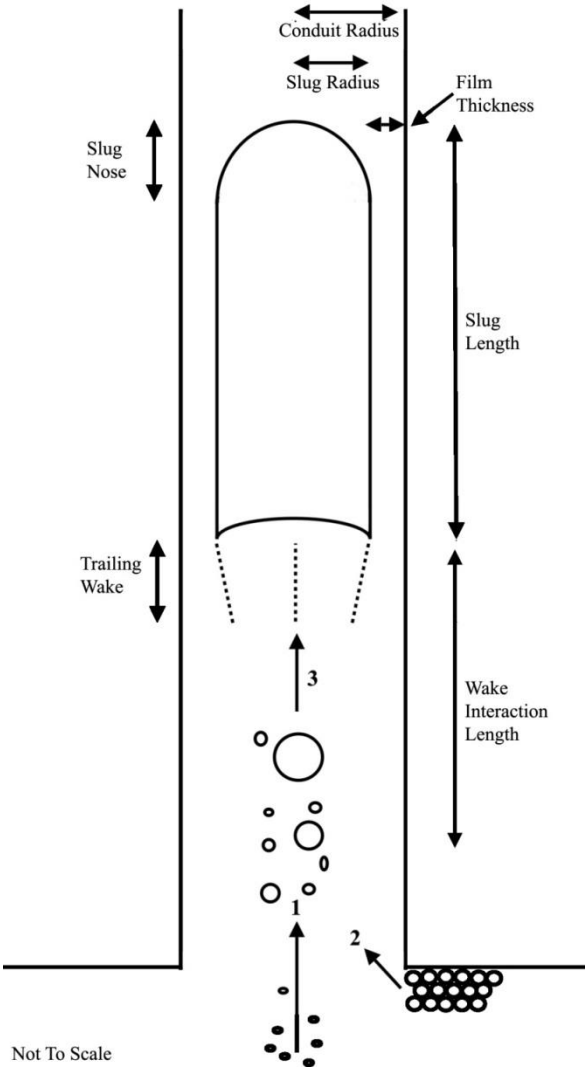

Fig. 4.1: A diagram of the important features of a rising gas slug. Of particular relevance for this chapter are the wake interaction length and trailing wake length. Point 1 illustrates the basic concept of the rise-speed dependent model (Wilson, 1980; Parfitt and Wilson, 1995), point 2 the foam collapse model (Jaupart and Vergniolle, 1988; Vergniolle and Brandeis, 1994), and point 3 the eventual transition to slug morphology. Reprinted with permission from Elsevier.

If we consider two slugs rising in a conduit, the one closest to the surface (termed the leading slug) and a slug behind this (termed the trailing slug) the effect of the wake length and wake interaction length, can be determined (this terminology will be used throughout this chapter). The wake interaction length is longer than the wake length by approximately a factor of 4. As a trailing slug begins to volumetrically expand (i.e. due to decompression) it may begin to enter the wake interaction length of the leading lsug. Normally a slug will rise with a constant base velocity (e.g. Viana et al. 2003), however, on entering the wake interaction length the whole of the trailing slug, including the base, will begin to accelerate (see videos described and explained in Appendix

C). This process shortens the gap between the trailing and leading slugs and begins the coalescence process (Pinto and Campos, 1996). The trailing slug will then undergo a further rapid acceleration, leading to complete capture into the base of the leading slug (Pinto et al. 1998; 2001), thereby ending the coalescence process (see Chapter 5 for further discussion and Appendix C for animations of the coalescence process in action).

Another important factor in driving the behaviour of multiple slugs, in addition to the coalescence process, is the overall gas volume fraction of the magma. At higher gas volume fractions (i.e. where there are many slugs), it is possible for the bases of slugs to rise at velocities far above (up to 6 times) those predicted for single slug systems, even when slugs do not fall within one another's wake interaction length (Krishna et al. 1999). This is important when considering travel times of gas slugs from potential source depths.

Within this chapter the focus is on measurement of rapid slug driven strombolian activity observed with UV cameras on Mt. Etna and on application of the above models to understand the dynamics of the observed activity.

4.2. UV Camera measurements of rapid strombolian activity at Mt. Etna

UV camera theory and the experimental configuration have already been discussed in depth in Chapters 1 and 2. Here, the same equipment set-up was used at the summit of Mt. Etna during a rare period of strombolian activity originating from a vent in the Bocca Nuova (BN) crater (N 37.7503°, E 14.9936°, also see Fig. 4.2) on the 27th July 2012. On this particular day, the strombolian activity had been occurring from this vent from

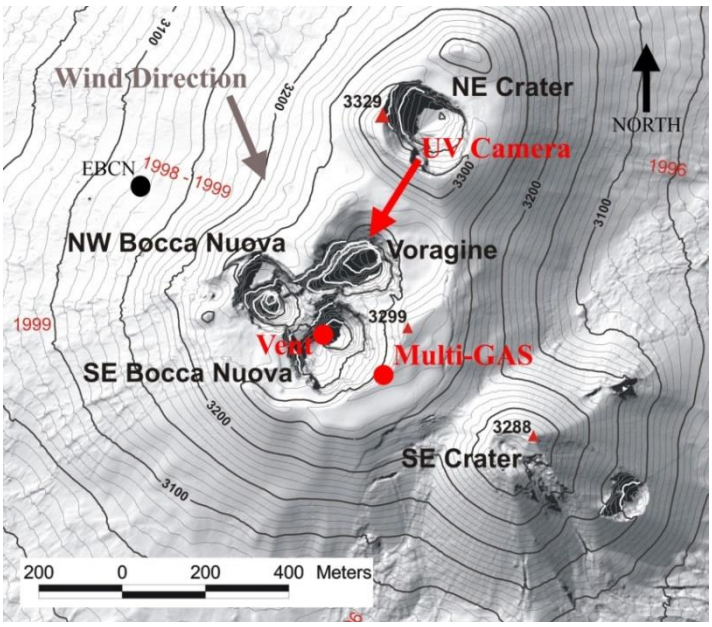

Fig. 4.2: Map of the summit of Mt. Etna including location and orientation of the UV camera, Multi-GAS unit, the vent, EBCN seismic station and wind direction. For locations of other seismic sites used in this study the reader is referred to the google maps file available, see Appendix C. Reprinted with permission from Elsevier.

around midnight. Prior to our observation period the activity was more vigorous and more frequent, as evidenced in the seismic record (Fig. 4.3d). This vent had been active for the majority of July, indeed on the 25th we observed the same vent producing sporadic ash-rich plumes. During the measurement period (09:32:58 to 09:59:58 GMT) the activity was rapid with explosive events occurring with separation of a few seconds to tens of seconds (the measurement resolution was ≈ 1Hz). Each explosion was accompanied by an audible bang and the ejection of ductile pyroclasts, which could be seen to glow. There was no visible evidence of ash production at the surface of the vent. Prior to our measurements (approximately an hour before) there was a small lava flow protruding from the edge of the cone built up around the vent (personal communication Sonia Calvari, INGV). This overflow was not being fed at time of measurement. This period of activity is described in depth through the INGV bulletins (http://www.ct.ingv.it/en/rapporti.html) and Spampinato et al. (2015). During the UV camera measurements a Multi-GAS instrument (Aiuppa et al. 2007) operated by the Palermo Unviersity was recording gas ratios.

Calibration of the system required more investigation due to our use of rock as a background source of light. The UV camera was located at N 27.7525°, E 14.9950° which was ≈ 250 m away from the active vent. This proximity to the vent minimised the light dilution effect; indeed the effect can be negligible at these distances (Kern et al. 2010a; 2010b; 2013, Campion et al. 2015). In addition, as the only visible source of gas within the crater was the vent itself, we can therefore be confident that the measured gas was that from the strombolian explosions. However, the basaltic rock face of the BN (see Fig. 4.3a for example background rock) might potentially introduce error as it differs from the conventionally applied method of using a clear sky background (e.g. Kantzas et al. 2010). All procedures described in Kantzas et al. (2010) for the calibration and capture of vignette images were therefore performed over a clear basaltic rock background, within the crater, adjacent to the strombolian activity, yet on the opposite side to the direction of gas travel (see Fig. 4.3c for illustration). An important aspect of calibration is that absorption must be uniform within the image, regardless of where within the SO_2 gas cells, the absorption value is determined. This angular aspect was investigated in an area at the summit of Etna, with negligible SO_2. Using four calibration cells of 100, 200, 400, and 1600 ppm SO_2 (the same cells used during the measurement), it was demonstrated that a strongly correlated (R^2 = 0.99) calibration line was generated regardless of where in the image this was determined. The location used for the test calibration and the resulting calibration line is shown in Fig. 4.3b. This gives confidence in

our method of calibration. The amount of light reflected from the background rock was 40 % of the background sky value (a small strip of skylight is visible in each UV image above the horizon), such that a sufficient amount of light was incident on the UV cameras. Furthermore, the use of light reflected from rocky surfaces is not uncommon in the planetary sciences to investigate surface properties (e.g. Hendrix et al. 2003).

An example absorption image is displayed in Fig. 4.3c, where the vent degassing is clearly visible. Also visible is a ring effect which is evident towards the top right corner of the image. This isn't a result of vignetting but is likely associated with the collection of vent gases along the walls of the crater.

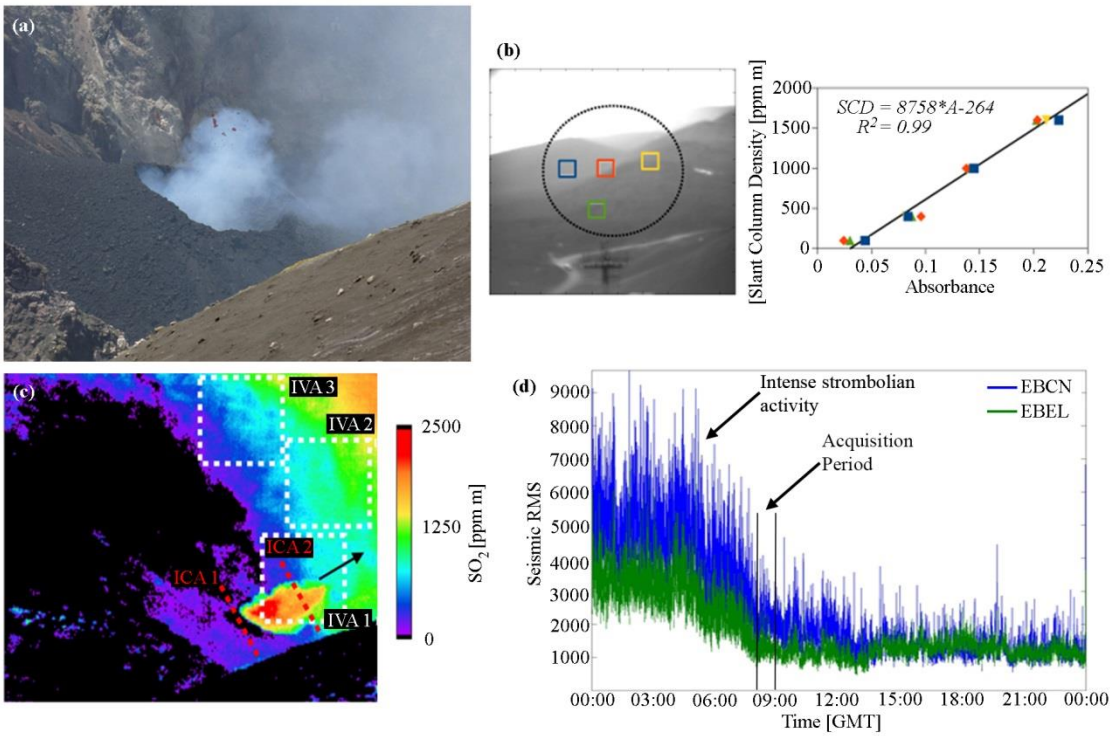

Fig. 4.3: In a) a visible image showing a typical explosion during our period of observations with ejection of limited incandescent material. In b) a test calibration performed at the summit of Mt. Etna where SO_2 is known to be negligible, this test demonstrated that the linear calibration is possible over a rock background regardless of where within the SO_2 cell the absorption value is derived (black circle and coloured boxes represent the outline of the SO_2 cell and points used for the calibration line on the right). In c) an example absorption image showing the locations of IVAs for determining slug SO_2 mass (IVA1) and for background correction (IVA2 and IVA3). Also depicted is ICA1 for determining gas flux and ICA2 to calculate background fluctuations. In d) the intense strombolian activity prior to our acquisition period, which is indicated between black lines is demonstrated. Reprinted with permission from Elsevier.

The first process in calculating the masses of individual strombolian explosions was to determine when each explosion occurred. This was achieved in two ways: by identifying in the UV camera imagery where solid ejecta were visible, and by identifying marked increases

in gas velocity from the vent. Following this the SO_2 mass of each explosion was calculated using the technique of Tamburello et al. (2012) which involves integrating within an area of the UV camera image to calculate the integrated volume amount (IVA). This is illustrated in Fig. 4.3c. The identification of an explosive gas mass appearing from the vent and subsequent images showing the transit of this explosive cloud is illustrated in Fig. 4.4. From (a) to (e) in Fig. 4.4 the propagation and shape of the explosive cloud is tracked, demonstrating the ability to measure the mass of the entire explosive event and also calculation of the initial velocity of each explosive cloud on a frame by frame basis. Given the relatively high background SO_2 concentration, a correction procedure was employed by taking two additional IVAs (IVA 2 and IVA 3) in the area of high background SO_2 concentration similar to that behind the explosion masses but completely away from potential contamination by the explosive masses themselves (see Fig 4.3c). To correct IVA1 (that used for the explosions) the average of IVA2 and IVA3 was subtracted from IVA1. IVA2 and IVA3 were separated by only ≈ 6 %. A supplementary video showing the activity in visible wavelengths and two periods of UV camera imagery is described in Appendix C.

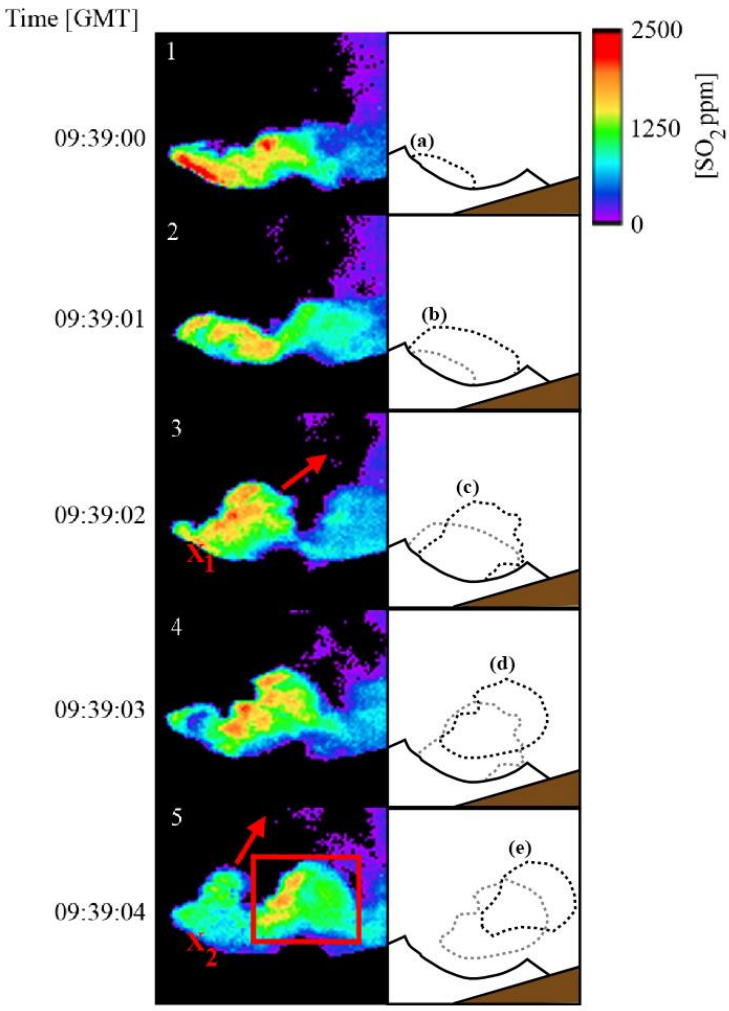

Fig. 4.4: From 1 to 5 at 1 second intervals the explosion and wireframes (a – e) of explosive cloud are illustrated. The red arrow illustrate the direction of the explosive cloud, with red x's showing where the cloud first appears from the vent. The red box is the approximate equivalent of IVA1 in Fig. 4.3c which is used for determining explosive SO_2 gas mass Reprinted with permission from Elsevier.

To enable comparison with seismicity, gas flux time series were also calculated using the ICA procedure described in Chapters 1 and 2. The location used to calculate the ICA is shown in Fig. 4.3c. The cross-correlation technique was used to determine plume rise speed (e.g. McGonigle et al. 2005; Williams-Jones et al. 2006). The plume rise speed was determined at a significant distance away from the vent and between explosions, with a result of ≈ 5 m s^{-1}.

These data allowed the SO_2 mass to be determined for 195 strombolian events. However, to be of use for modelling the observed activity the total gas masses need to be estimated. This was achieved with a Multi-GAS analyser, which was located on the south-east crater edge of the BN crater (N 37.7409°, E 14.9953°), see Fig. 4.2, ≈ 200 m from the vent. During acquisition winds were E-SE, with wind speed of 10 – 14 m s^{-1}. Due to given the distance from the vent to Multi-GAS unit, it was not possible to constrain gas ratios on an explosion by explosion basis. We therefore used the time average for the period, with molar gas ratios of: $CO_2/SO_2 = 2.8$, $H_2O/SO_2 = 8.5$, and $H_2O/CO_2 = 3$. There was little variation in the ratios during acquisition with errors of between 4 – 15 %, the reader is referred to Chapter 2 for further discussion on Multi-GAS error quantification. From these data we can infer that the proportion of molar mass contained within the slug is as follows: SO_2 = 8%, CO_2 = 22 %, H_2O 70 %. We base this on the assumption that the majority of gas released at Etna is via these three species (e.g. Aiuppa et al. 2007). These molar ratio values were then be converted to mass ratios and multiplied by the determined SO_2 slug masses to give a rough estimate of the total slug mass.

Three seismometers belonging to the INGV (Osservatorio Etneo) were used to investigate seismicity during and preceding the period of acquisition, these included: EBCN (N 37.752365°, E 14.986281°), EBEL (N 37.740238°, E 15.008239°), and ETFI (N 37.738195°, E 15.000649°). The location of the closest of these is in Fig. 4.2. Infrasound was also measured but on the day of question, the microphones were too polluted by wind noise to pick up any signal from the BN crater. Fig. 4.3d demonstrates the more intense strombolian activity in the early hours, associated with more intense seismicity, displayed as seismic RMS (Root-Mean-Square). During the acquisition period, seismicity waned in tandem with a reduction in explosivity of the vents activity. Detailed investigation into potential links between seismicity and gas flux was performed by Andrea Cannata and Mariangela Sciotto (INGV, Osservatoria Etneo – sezione di Catania), with techniques described fully in Martini et al. (2009); Cannata et al. (2013b); and Zuccarello et al. (2013).

4.3. Results and analysis

The strombolian explosions ranged ≈ 0.1 – 14 kg of SO_2 in gas release. When applying the determined mass ratios, to these values, the range of total gas masses becomes ≈ 0.1 – 74 kg. Using the gas flux record it is also possible to calculate the combined explosive and passive SO_2 release by integrating over the entire gas flux record, with a result of ≈ 360 kg SO_2 passively released (calculated by subtracting the ≈ 183 kg released explosively, from the overall value). Combining these values demonstrates that the dominant mode of degassing from the vent was still passive, with a ratio of 67:33% passive to explosive. Fig. 4.5a shows the distribution of these gas masses. There is a distinct skew in the data towards smaller events between ≈ 0.2 – 20 kg, with > 150 events in this range. In Fig. 4.5b the delay time between events, termed here the inter-event duration, shows a similar skew towards shorter inter-event durations between ≈ 1 – 46 s. The dominant inter-event duration is ≈ 4 s (the modal value), with a median of ≈ 5 s, demonstrating the rapidity of the

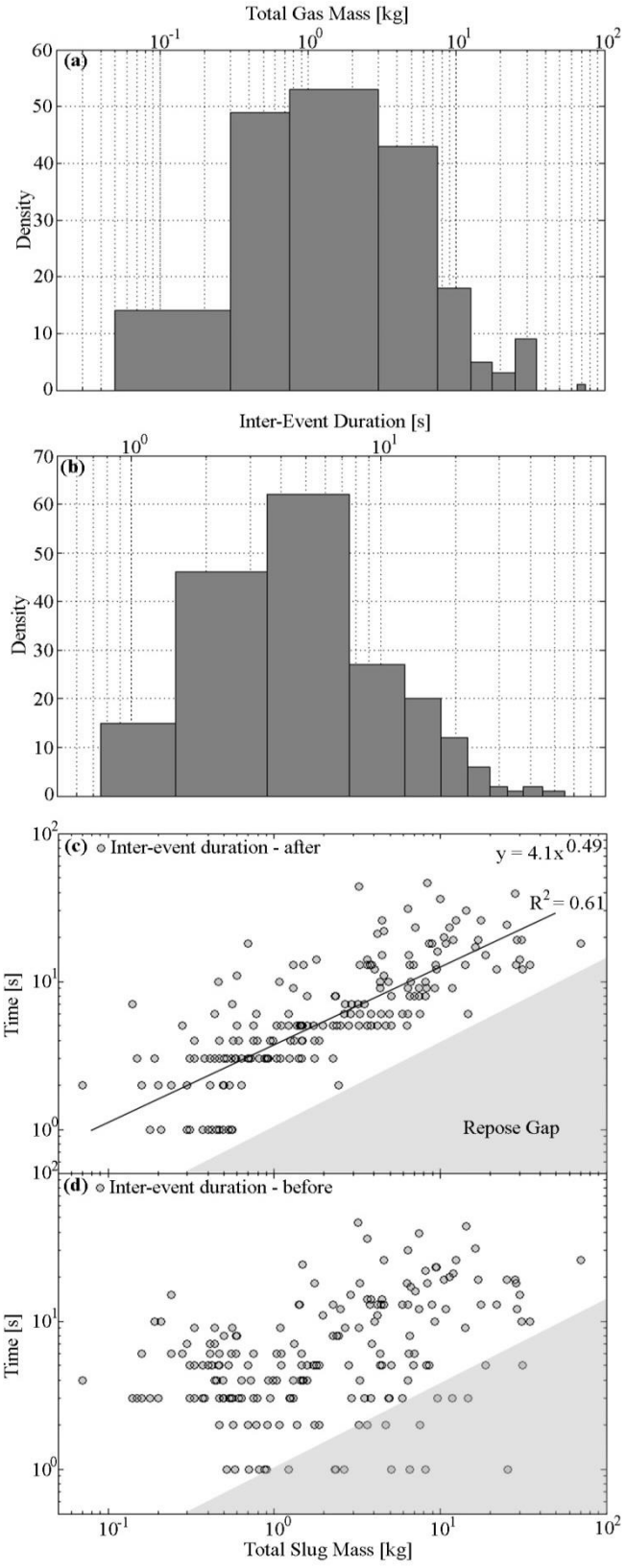

Fig. 4.5: a) a histogram showing the spread of total gas masses, b) a histogram of inter-event durations, c) a scatter graph showing a general trend between time after a burst and total slug mass, also shaded in grey is the repose gap where larger bursts are followed by longer wait times before another can occur, d) a graph of time duration before a burst showing no such relationship. Reprinted with permission from Elsevier.

activity.

In Fig. 4.5c and d the relationship between total slug mass and inter-event duration is investigated. Here there are two separate plots referring to the inter-event duration *after* a burst before the next one occurs (event onset is determined as the time when the explosive gas cloud is first obscured within the vent) and the inter-event duration *before* a burst (i.e. comparing burst masses with delays before, Fig. 4.5d, and after, Fig. 4.5c, each burst). Fig. 4.5c, illustrates that for the larger bursts there is a relatively long delay before the following burst of any magnitude can occur. The smaller mass events have smaller post-explosive inter-event durations. This is illustrated by the grey shaded area in Fig. 4.5c, which termed henceforth the repose gap area. There is also a mild correlation of $R^2 = 0.61$, giving a best-fit line with equation of $y = 4.1x^{0.49}$. This area is not present within the plot of inter-event durations before an event (Fig. 4.5d).

Fig. 4.6 shows the results of burst vectors, where the base of the arrow (at the edge of the vent, see red crosses in Fig. 4.4) denotes where the centre of the cloud is first visible, and the arrow tip the direction and distance travelled between two separate UV camera images. A dominant orientation of gas release from the vent is apparent in Fig. 4.6. However, a varying array of directions is presented. Indeed the supplementary video (see 09:55:33 in video described in Appendix C) show that bursts can occur from markedly different directions in rapid succession. Fig. 4.7a shows a time series of burst trajectories such that no relationship is evident from burst to burst. The average vector angle is ≈ 57° from the vertical (grey line on Fig. 4.7a). In Fig. 4.7b the relationship between emission speed and total slug mass shows a similar trend to the earlier described repose gap behaviour, such that there were no large slug mass - low emission speed events. This is likely linked to the fact that the largest mass slugs will experience more expansion and therefore explode with an initial higher velocity.

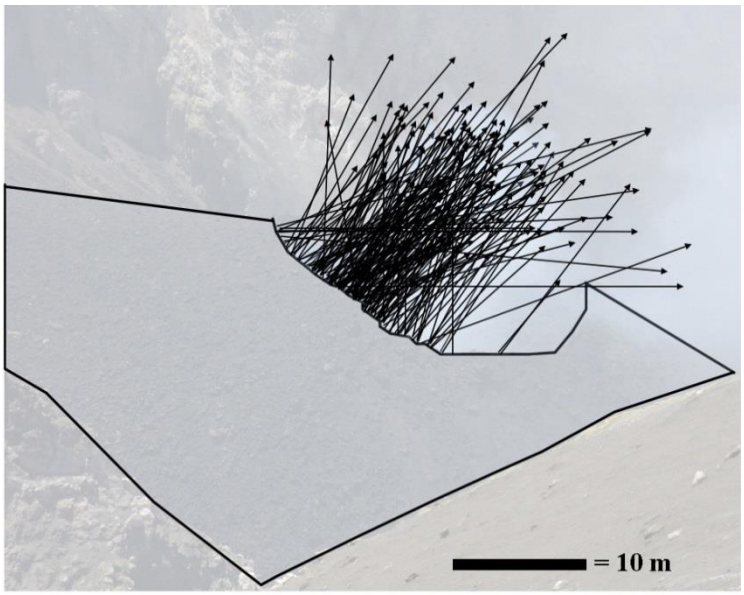

Fig. 4.6: An illustration of burst vectors for all 195 bursts during the period of acquisition. For a plot of this data see Fig. 4.7.

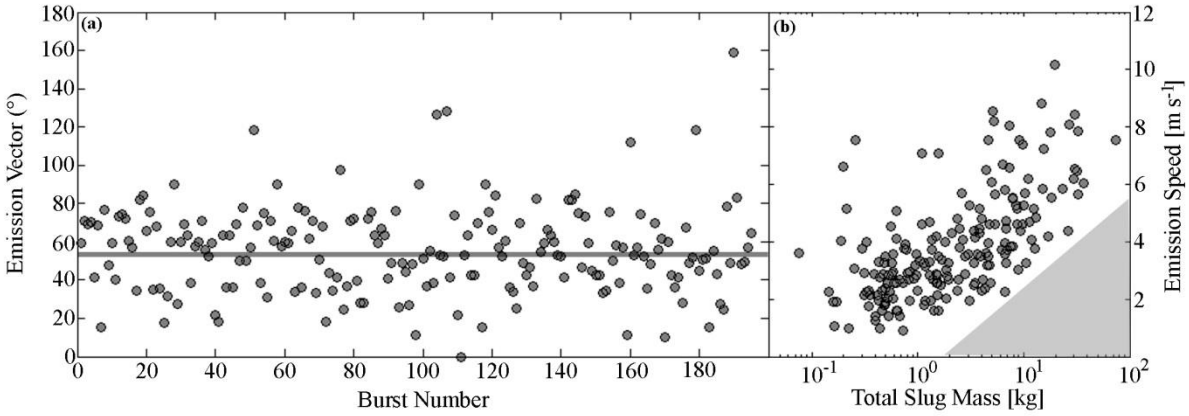

Fig. 4.7: a) The emission vector for all bursts, plotted in degrees from vertical, with the average vector illustrated. In b) the relationship between total slug mass and emission speed shows a similar area without bursts (shaded) as the repose gap feature seen in Fig. 4.5c suggesting that larger bursts have a higher minimum emission speeds.

An analysis by Andrea Cannata and Mariangela Sciotto (personal communication) discovered that there were no definitive links discovered between any of the analysed data series, including gas flux and a varying array of seismic RMS signals which were averaged over different windows (from 30 s to 5 minutes, with lags of up to ± 10 mins). Fig. 4.8 shows the raw data associated with the acquisition period: in a) frequency characteristics, b) seismic RMS, and c) the raw pre-processed seismic signal. From these data, power spectral density analysis was performed, using Welch's method (Welch, 1967), on the seismic (Fig. 4.8d and e) and infrasonic (Fig. 4.8f and g) signals from the EBCN and EBEL seismic stations (the

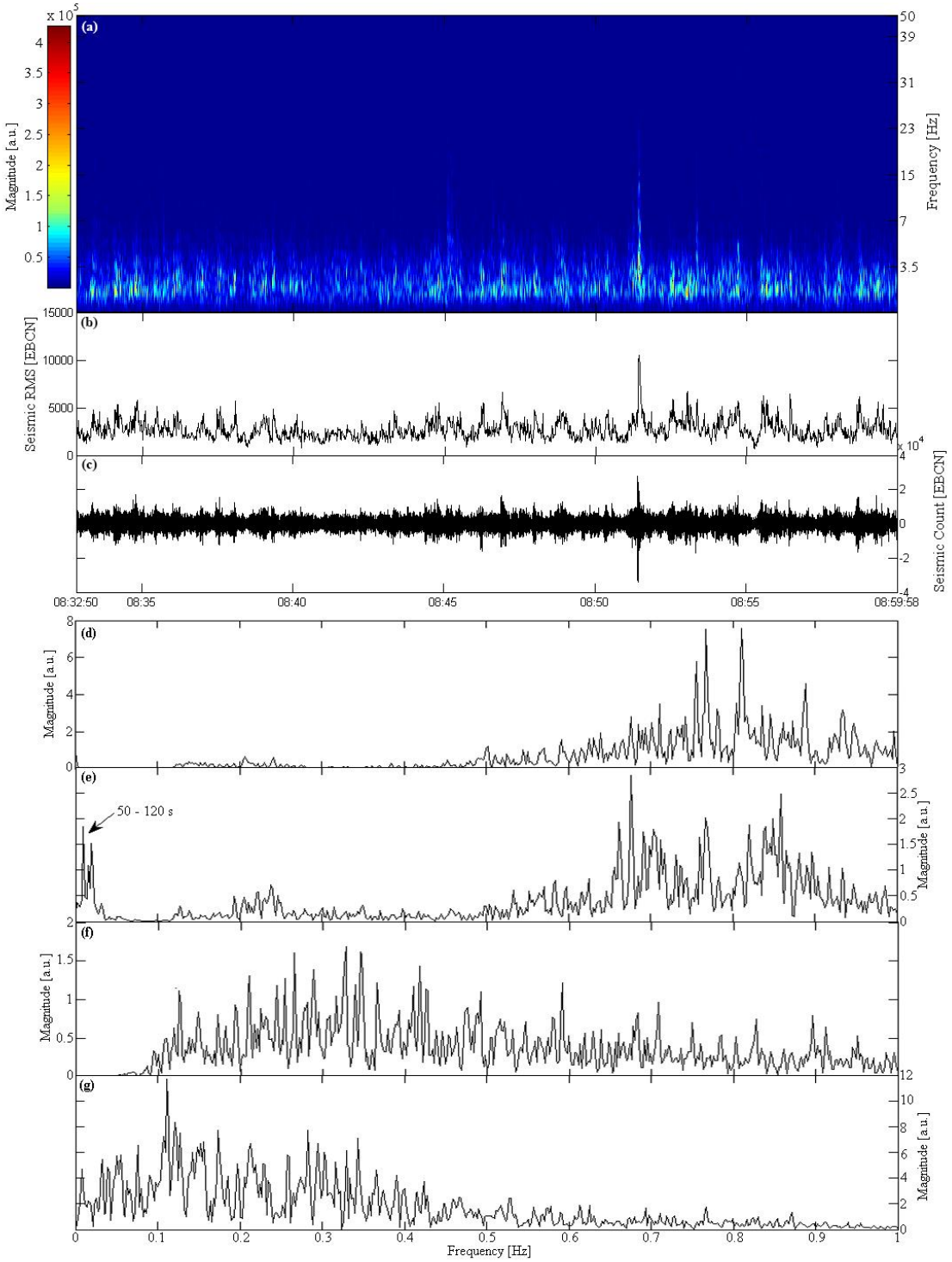

Fig. 4.8: a) frequency characteristics of the seismic signal at the EBCN stations, b) RMS, and c) the raw unprocessed seismic signal. In d) and e) PSDs showing dominant periods present at the EBCN and EBEL stations respectively, with oscillations at 50 – 120 s present at EBEL. In f) and g) for EBCN and EBEL the dominant oscillations show that wind noise occludes any potential infrasonic signal.

.kmz Google Earth file showing these locations is available in Appendix C). Here, one can observe the high frequency characteristics at the EBCN seismic station between ≈ 0.5 – 1 Hz. Similar frequency behaviour is also presented at EBEL, but there are also some longer period oscillations between 50 – 120 s, which are likely related to activity beneath the NEC (see

Chapter 2, Tamburello et al. 2013). The infrasonic PSDs demonstrate the dominance of wind noise.

4.4. Basic modelling of the activity

In an effort to understand the dynamics of the measured activity, one must first constrain the bubble morphology and hence the gas regime in operation. This has been achieved in a number of ways. Firstly, using the ideal gas law:

$$PV = nRT, \qquad \textbf{(Eq. 4.4)}$$

where P = pressure, V = volume, n = number of moles (per gas slug), R = 8.314 J K^{-1} mol^{-1} (i.e. the universal gas constant), and T = the temperature in Kelvin. At the summit of Mt. Etna (≈ 3,350 m) atmospheric pressure is ≈ 69 kPa, while the magma temperature is likely ≈ 1,273.15 K (e.g., Armienti et al. 2012), which will give a similar temperature just above the vent. Given our knowledge of total gas mass and the approximate proportions of CO_2, SO_2, and H_2O, the molar mass of each explosion can therefore be calculated, which, when applied to the ideal gas law gives gas volume ranges of ≈ 0.4 – 411 m^3. If we take a conduit radius of ≈ 1 m (with the assumption that the bubble is almost as wide as this), we can estimate, using the equation for the volume of a cylinder:

$$V = \pi r^2 h, \qquad \textbf{(Eq. 4.5)}$$

the length of the slugs (e.g., h in equation 4.5), as ≈ 0.1 – 53 m. A bubble can be classified as a slug when its length reaches or exceeds approximately the width of the conduit (Davies and Taylor, 1950; Wallis, 1969), minus the film thickness, which reaches a minimum value during the slug flow regime (Llewellin et al. 2012). For a full discussion of slug behaviour see section 4.1. Part of the complexity arising from modelling this activity is the prior non-existence of any developed model for multiple rising slugs. For the purposes of the remainder of this section, I implement the only volcanic slug models available, which apply to slugs rising without any neighbour interactions, i.e. single slug models (e.g. James et al. 2008; Del Bello et al. 2012).

This initial basic analysis suggests that some of the explosive events may be being driven by slugs bursting at the surface. However, the key parameter conduit radius, is a relative unknown. Reliance must be placed upon literature estimates of similar activity (e.g. Seyfried

and Freundt, 2000; James et al. 2008). The Del Bello et al. (2012) static pressure model can be applied *en masse* to all of the measured explosive events in an effort to estimate a range of conduit and magma parameters. The Del Bello et al. (2012) model allows the calculation of burst overpressure with information on gas mass or volume (see above calculation), magma viscosity, and conduit radius. Given that each burst was accompanied by an audible bang it is reasonable to assume that each explosion had an overpressure. The model output gives positive values where overpressure is present and meaningless negative values in the absence of overpressure. For a range of magma viscosities between 10 – 5,000 Pa s^{-1} and conduit radii 0.5 – 5 m the model can estimate the number of bursts that burst with overpressure (see Fig. 4.9). Fig. 4.9 demonstrates that overpressure is favoured for smaller conduit radii and magma viscosities of > 500 Pa s^{-1}, although at the smallest conduit radii of 0.5 m lower viscosities of 100 Pa s^{-1} do also produce a strong percentage of bursts with overpressure (at these lower conduit radii gas masses are also more likely to be slugs). Regardless of whether any rising gas bubble has a slug morphology the model will provide a reasonable estimate of the likelihood of explosivity.

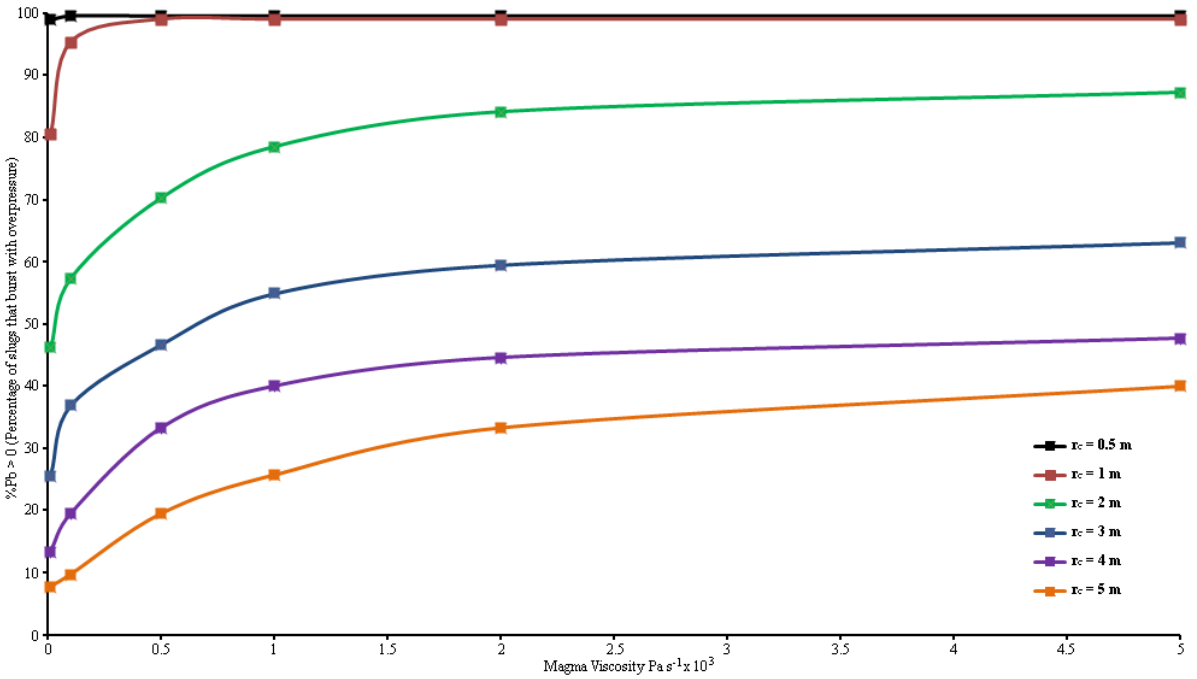

Fig. 4.9: Here the Del Bello et al. (2012) static pressure model is used to estimate values for magma viscosity and conduit radius, based on the assumption that all bursting slugs must have some form of overpressure, given the audible bang accompanying each burst. The percentage of bursts with overpressure is plotted on the y-axis. This plot demonstrates that smaller radii and/or higher magma viscosities expedite overpressure.

By considering the morphology of the vent (using visual images of the vent geometry – e.g. Fig.4.3a) an upper estimate for conduit radius of ~ 3.5 m is assigned (see Fig. 4.10), based on

the inclination of the interior angle of the cone and an estimate for magma level change. This corroborates the Del Bello et al. (2012) analysis.

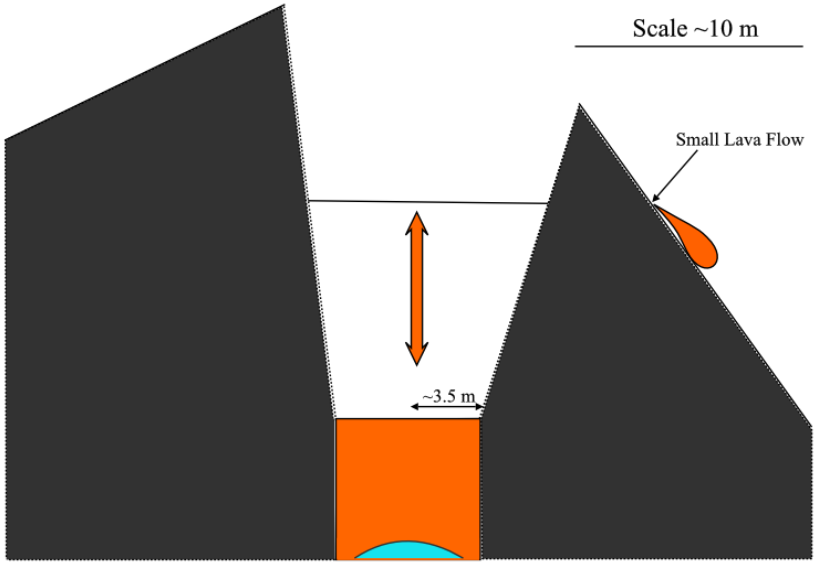

Fig. 4.10: An approximation of possible maximum conduit geometry based on visual images of the vent. Also indicated is the position of the small lava flow which had ceased prior to the UV camera acquisition period.

A number of previously introduced dimensionless parameters, including N_f can be used to estimate the form of gas slugs (see Chapter 3) and hence turbulence and stability within the operating regime. Based on this initial analysis, magma viscosity is taken to range 100 – 1000 Pa s^{-1}, and conduit radii 0.5 – 1.5 m. A magma density of ≈ 2600 kg m^3 is used, in keeping with other literature estimates of basaltic magmas (e.g. James et al. 2008) given limited knowledge of magma vesicularity at depth. This gives an N_f range of ≈ 8 – 423 (see equation 4.1), with lower values generated by larger viscosities (as is more likely for Etnean magmas – e.g. Pinkerton and Norton, 1995; Giordano and Dingwell, 2003). This suggests that there is little turbulence within the regime. All current single slug models assume a negligible magma velocity (i.e. a stagnant magma column). This will affect the turbulence and interaction of individual bubbles and slugs. Given the small amounts of material released (see supplementary video and Fig. 4.3a) it is likely that the upward velocity of the magma is low, affirming the applicability of the single slug models to some extent.

To probe the behaviour of the observed activity in greater detail the model of James et al. (2008) is used to estimate final slug lengths, and the depth at which rising gas masses transition to slug flow. According to this model, the following allows the calculation of the time, position, and length of a slug:

$$\frac{1}{2}\rho_m(1+A')\ddot{L} = P_0 L_0^{\gamma} L^{-\gamma} h^{-1} - \rho g - P h^{-1} - 8\mu \dot{L} r_c^{-2}, \qquad \textbf{(Eq. 4.6)}$$

where ρ_m is the density of the magma, A' is:

$$A' = \left(\frac{r_{sl}}{r_c}\right)^2, \qquad \textbf{(Eq. 4.7)}$$

and other parameters include: λ the ratio of specific heats using the same value of 1.4 as in Chapter 3, L the length of the slug, P_0 is the initial pressure of the slug added to atomspheric pressure (≈ 69 kPa). The slug radius is taken as conduit radius minus the film thickness value determined using Llewellin et al. (2012), see equation 3.1. The model also requires initial estimates for slug base rise speed, which are calculated using equations 3.2 (see also 4.1), 3.3 and 3.4 (see section 3.3). Estimates for film thickness over the N_f range 8 – 424 are therefore ≈ 0.13 to 0.43 m, while slug base rise speed is ≈ 0.24 – 1.82 m s^{-1}.

To estimate potential slug transition depth, single values for the following parameters are taken, including: 1 m for conduit radius, 500 Pa s^{-1} for magma visocsity, which gives an N_f = 46, film thickness of 0.28 m and slug base rise speeds of 1.1 m s^{-1}. The James et al. (2008) model (equation 4.6) is initialised at depths known to be greater than the transition depth (i.e. through a simple estimate using the ideal gas law), and the point at which the rising gas masses reaches lengths equal to the conduit diameter is taken to indicate slug transition. For the majority of bursts this occurs at very shallow depths of ≈ 5 m, whilst the largest slug could transition at a depth of ≈ 170 m. This leads to final burst lengths of ≈ 3 – 27 m. On combining these estimates with the range of slug base rise speeds, rise times could range ≈ 93 – 708 s from a depth of 170 m. An example of a series of model runs using the model of James et al. (2008) is illustrated in Fig. 4.11, showing the potential position and transition depths of four of the measured slugs.

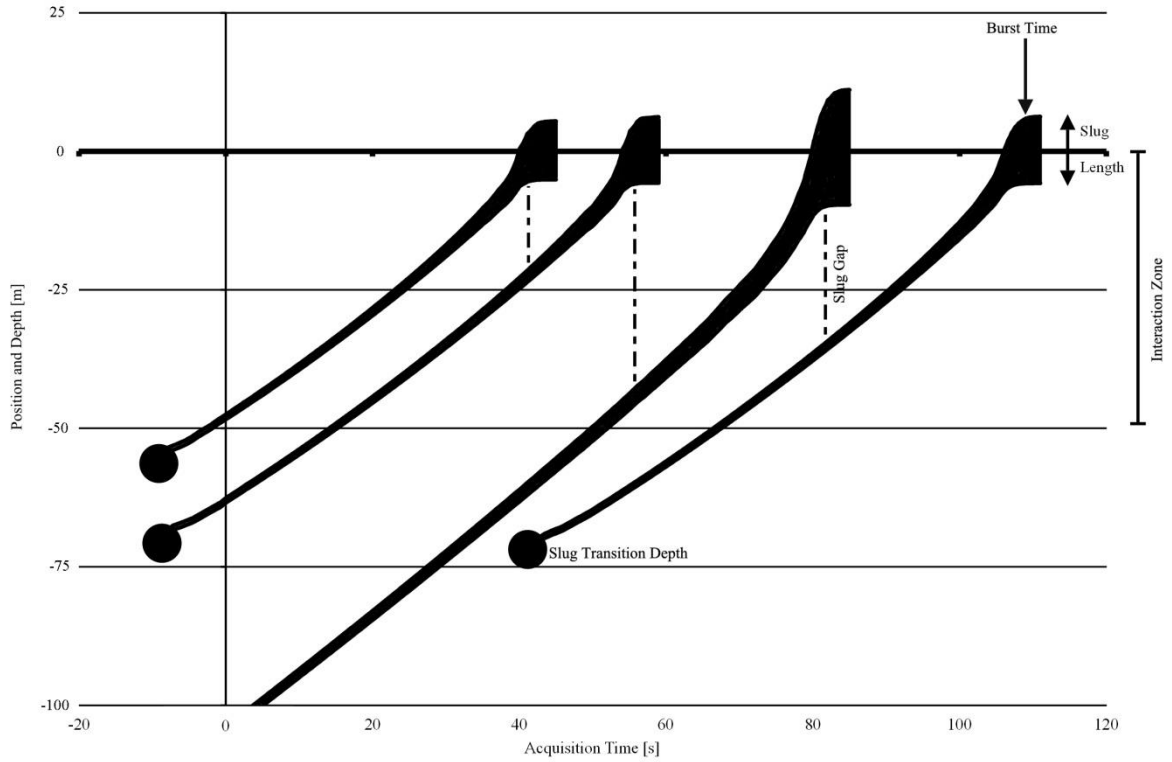

Fig. 4.11: Example output from the James et al. (2008) slug model (equation 4.6). Here, the results of four of the largest sequential bursts and their potential separation distances and burst lengths as a function of time are plotted. See the main text for further details on calculation.

Using equations 4.2 and 4.3, the wake length and wake interaction length can be calculated over the N_f range 8 – 423 as: ≈ 0.3 – 2.4 m and ≈ 1.5 - 10.4 m respectively. These values are particularly important in determining the possibility of coalescence between rising slugs (Pinto and Campos, 1996). This implies that with stability and a lack of turbulence in the magma, frequent explosive activity could occur with rising slugs separated by little fluid in between bursts. During slug rise the whole of the slug will decompress which will allow the slug to expand, increasing the probability of a trailing slug entering the wake ineteraction length (see Fig. 4.1 and 4.11) and hence increasing the likelihood of coalescence. With wake interaction lengths of ≈ 1.5 – 10.4 m, the base rise speed of slugs ≈ 0.24 – 1.82 m s^{-1}, and the modal temporal explosion separation of ≈ 4 s, it is possible that rising slugs could be separated by as little as ≈ 0.96 – 2.2 m of melt, suggesting that there could be significant interaction between slugs, both within slug wakes and wake interaction lengths.

The estimated slug transition depths of ≤≈ 170 m strongly suggests that rising gas masses transition to full slug flow late on during the rise process. This implies that bubbles will be rising in a non-slug morphology form for the majority of travel inside the conduit. Section 1.1

outlines the transitions of bubble forms. The precursor to a slug is the cap bubble (Davies and Taylor, 1950; Wallis, 1969; White and Beardmore, 1962). Cap bubbles share many features of a slug including: a more variable film thickness, wake and interaction lengths (and hence the same coalescence mechanism), and a constant base speed whilst the bubble retains a constant shape (Davies and Taylor, 1950; White and Beardmore, 1962; Wallis, 1969; Viana et al. 2003). The dimensionless Reynolds bubble number (Re_b), which is an approximate measure of bubble morphology (Suckale et al. 2010b; James et al. 2011), suggests that, for values of 0.3 a bubble will behave as a spherical particle (i.e. stokes law can be applied). Re_b can be calculated as follows:

$$Re_b = N_f Fr. \qquad \textbf{(Eq. 4.8)}$$

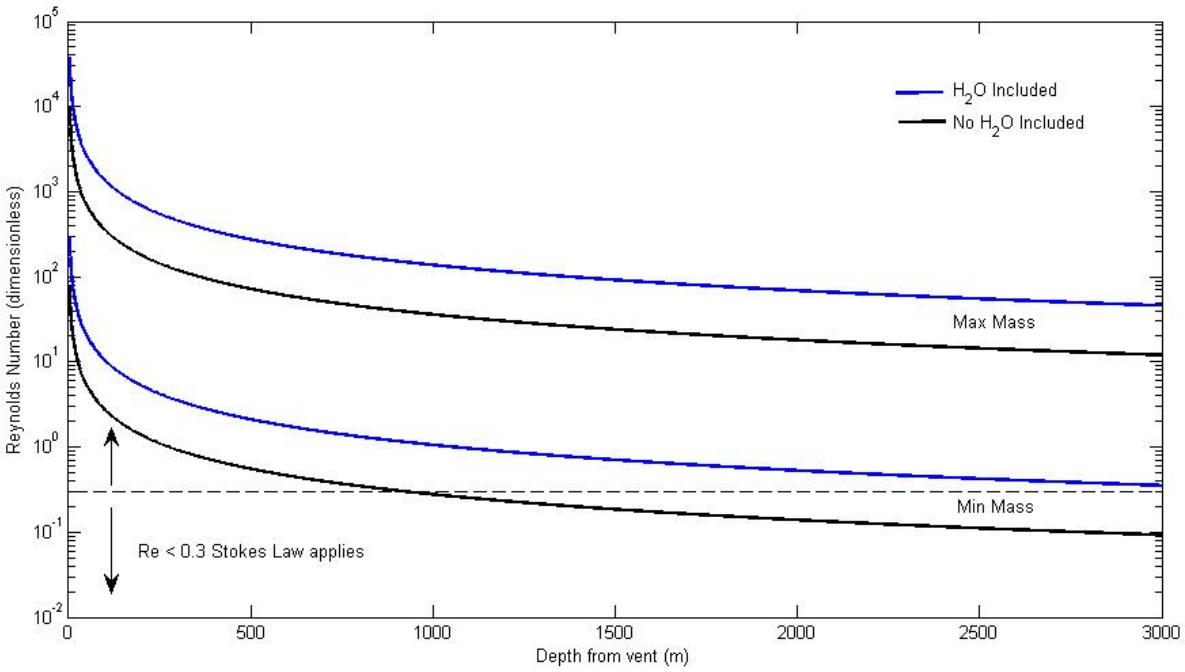

Fig. 4.12: Here the Reynolds bubble number (equation 4.8) is applied to our measured gas masses to approximate bubble morphology during rising from depth. The blue line shows results with water mass of the slug included and black without, this is done because of the shallow exsolution depth of H_2O.

By applying this equation (see equations 3.2 (also 4.1) and 3.3 for N_f and Fr) to the collected Etnean data for all the bursts, the rising bubbles (assuming no interaction whatsoever) would be non-spherical from depths < 3000 m (see Fig. 4.12, for the moment ignoring potential source depth – see section 4.4.1.). This has important consequences for the gas flow regime, which initiates and drives the activity (James et al. 2013; Vergniolle and Gaudemer, 2015).

4.4.1. Activity Source Depth

In Burton et al. (2007), a method was detailed to determine the source depth of slug driven explosions at Stromboli. Here, a similar method is applied to the explosions detected on Etna. Given the knowledge of relative concentrations (discussed below), ratios of slug mass ($H_2O/SO_2 \approx 2.8$, $H_2O/SO_2 \approx 8.5$ and $H_2O/CO_2 \approx 3$) and rock composition (SiO_2 value of ≈ 49 wt% [e.g. Métrich and Clocchiatti, 1989]), the VolatileCalc software (Newman and Lowenstern, 2002) can be used to calculate: the solubility (the amount of a volatile which can be dissolved within a magma at a certain pressure) versus pressure of CO_2 (ppm) and H_2O in wt % (this was also completed in Collins et al. [2009] Fig. 1A), and the degassing pathway and saturation pressure of these volatiles. To date there has been only a limited amount of work on volatile content of H_2O and CO_2 in Etnean magmas. According to Corsaro and Pompilio (2004) the average H_2O content of Etnean magmas ranges between $\approx 0.5 – 1.3$ wt%, whilst Métrich and Rutherford (1998) determined as much as ≈ 2.5 wt% for primitive basaltic-hawaiitic magmas. Together, Del Carlo and Pompilio (2004) and Metrich et al. (1993), determined a range of $\approx 1– 3$ %. Meanwhile, determined CO_2 contents range from $\approx$ 200 – 1500 ppm, with the upper limit derived from the large sub-plinian eruption of $\approx$ 3930 BP (Del Carlo and Pompilio, 2004). In this analysis it was decided to take the more realistic ranges for this type of activity: 1 – 2.5 wt % H_2O and 200 – 1000 ppm CO_2, for the determination of degassing path of these volatiles. Due to the nature of the BN activity it was also assumed that an open-vent system was operating. The VolatileCalc software (Newman and Lowernstern, 2002) computes on this basis the molar volumes of H_2O and CO_2. The point at which the derived ratios match a slug H_2O/CO_2 ratio of ≈ 3 can be taken as a proxy for approximate slug source depth, with results shown in Fig. 4.13. Depending on the volatile content, the source depth of slugs could range $\approx 0.5 – 3.3$ km.

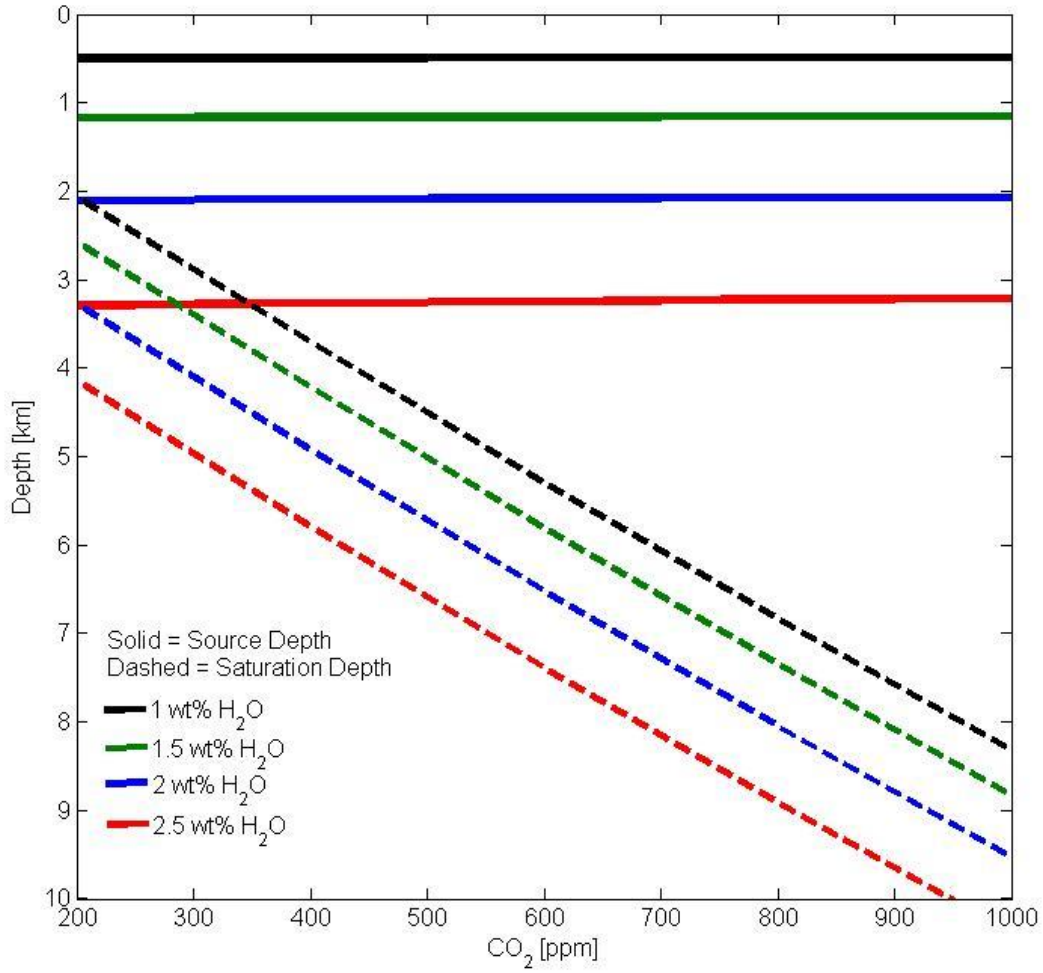

Fig. 4.13: The results of VolatileCalc (Newman and Lowernstern (2002), showing the source depth based on matched ratios and a range of water weight percentages. The dashed lines show the saturation depth and hence when water will begin to exsolve from the melt.

Given a source depth between ≈ 0.5 – 3.3 km, which is a similar range to activity seen at Stromboli of ≈ 0.8 – 3.3 km (Burton et al. 2007), information about the shallow magma pathway can be inferred and the original source processes could be similar. As with the conclusions of Burton et al. (2007), there is no discernible way of differentiating between the foam collapse and slug coalescence model for slug formation. This said, potential evidence of late coalescence and slug formation in the conduit could give credence to the coalescence model for this activity. As Fig. 4.13 shows, the water content of the basaltic magma is the main control on the source depth of the slugs, indicating that the driving magmatic gas in this case is likely H_2O. The source depth of slugs also fits within the general upper 4 km area of the volcano where the majority of exsolution of volatiles from the melt occurs, leading to the consequent formation of bubbles, and the shallow storage area which is thought to occupy a

space between the summit and sea level base (Corsaro and Pompilio, 2004; Alparone et al. 2004; De Barros et al. 2009; Corsaro et al. 2013).

4.5. Discussion and Implications

4.5.1. Considerations on activity dynamics

The above modelling considerations have demonstrated that the slugs could rise separated by relatively little melt and that interaction between rising gas masses could be commonplace. This interaction would likely include the coalescence of bubbles and slugs (Pinto and Campos, 1996). This coalescence process will be enhanced as slugs reach the surface as this is the region of greatest decompression (James et al. 2008; 2009) and hence an increase in slug length will encourage interaction within wake interaction lengths. Estimated N_f numbers suggests that turbulence within the system could be low, i.e. restricted by an increasingly closed wake, which reduces turbulent transference of the slug wake to the melt (Campos and Guedes de Carvalho, 1988). This would allow rapid and stable slug activity. However, as mentioned previously, these are single slug models, applied to the much more complex behaviour associated with the ascent of multiple slugs. It is entirely possible that fluid disturbance could be extended beyond wake interaction lengths, remaining interaction even more likely (e.g. Krishna et al. 1999; Llewellin et al. 2014). The relatively short lengths of the modelled Etnean slugs (≈ 3 – 27 m; in comparison to slugs at Stromboli which can be an order of magnitude longer [e.g. James et al. 2008; Del Bello et al. 2012]), at burst, imply that the transition to slug flow occurs relatively high in the conduit, and hence turbulent interaction multi-slug based activity could be limited to the upper ≈ 170 m of the conduit, where coalescence would be expedited.

During multi slug activity it is important to consider the combined volumetric effects of the magma and gas mixture as this will effect changes in magma level and the point at which a slug bursts at the surface (James et al. 2013; Vergniolle and Gaudemer, 2015). Each explosion was accompanied by the visible ejection of material, which suggests that the magma level was relatively constant during the acquisition (i.e. only varying by estimated slug lengths). At Stromboli a viscous cap at the top of the magma column may impede a slugs progress prior to burst (e.g. Capponi et al. 2014; Del Bello et al. 2015). Given the rapid activity, it is possible that the magma surface could rupture and accumulate both ejecta fall-

back and unsteady magma drainage along the conduit walls, which could lead to instability in the bursting slugs (e.g. Pering et al. 2014c and Chapter 5). Despite the rapidity of the activity, turbulence and instability of the activity seemed to be limited, as all other portents also suggest. Fig. 4.4 demonstrated that gas clouds can be emitted in drastically different orientations in quick succession (e.g., see also 09:55:33 GMT in video described in Appendix C, and Fig. 4.7). It has already been suggested that slugs could be rising within interaction lengths, when a slug enters into this area its nose and shape can be deformed and altered (Nogueira et al. 2006; Figuera-Espinoza and Fabre, 2011). The propelling of eruptive gas in different directions in rapid succession could be evidence of this. Of course there are significant caveats to this which include other potential influences including gaseous transport effects through the atmosphere (e.g. Woods, 2005; Pope, 2000), conduit inclination and general geometrical heterogeneities (James et al. 2004), and as discussed the state of the magma surface.

4.5.2. The Repose Gap

The presence of the repose gap (see Fig. 4.5c) is a unique observation. Indeed, it is possible that the trend whereby the largest slugs are followed by longer wait periods, is driven by the fluid dynamic processes inherent with multi slug activity e.g., coalescence. During the coalescence process the whole of a slug, including the trailing slug base, is accelerated into the base of the leading slug. Larger slugs formed by coalescence would therefore leave longer fluid lengths behind the newly formed slug and hence a longer repose period prior to the onset of the following burst. Equally, larger slugs will be more prone to coalescence such that volumetric expansion will encourage interaction with leading slugs (Pinto et al. 1998; 2001). Both these processes would not affect any slug ahead of a leading slug which is involved in coalescence. This is shown to be the case in Fig. 4.5d. The frequency of observed activity is therefore a function of potential interaction between rising slugs and gas masses.

Fig. 4.6c (emission speed vs. slug size) demonstrates that a similar trend occurs, indicating that a slug of a certain mass must be released at a certain minimum speed. This is likely to be related to the repose gap and behaviour of multiple slugs. This could also be explained by a larger explosion creating a delay (i.e. the slug coalescence explanation) or an alternative third mechanism could be implied, whereby larger slug bursts create a bigger drop in magma level following the explosion such that subsequent gas from bursts would then take longer to travel

to the surface. Although the presence of visible ejecta at the surface consistently throughout the acquisition period suggests that this mechanism is improbable and further suggests that the magma level was relatively stable and close to the surface (see visible video in Appendix C).

Evidently other processes could be implicated in the formation of the repose gap, including the rise speed dependent model of Wilson (1980) and Parfitt and Wilson, (1995). This model is also dominated by coalescence and the speed of rising masses, which are volumetrically controlled, i.e. a larger volume rises at a faster rate. Fig. 4.12 suggests that this ceases to be the case at significant depths and certainly within the interaction area of ≈ 170 m (i.e. Re_b numbers are > 0.3). Unless the arrival time of slugs at the surface is determined at depth by individual rising bubbles prior to the development of morphologies such as cap bubbles or slugs, with rise speeds that are largely dependent on conduit radius, the repose gap is unlikely to be caused by this model.

Finally, the collapsing foam model as discussed in Jaupart and Vergniolle (1988) and Vergniolle and Brandeis (1994), could lead to the repose gap. This model suggests that bubbles can accumulate at the top of shallow storage areas or at discontinuities within conduits, and is often implicated in the formation of slugs (e.g., at Stromboli). The release of a larger gas mass from a foam could lead to an increase in the stability of a foam, which would increase the delay before another gas mass could be released, hence creating the repose gap. However, it is also easy to see that this should also lead to a similar pattern appearing before bursts, i.e. larger bursts should also be accompanied by a longer delay preceding an event as well as that following, however, this already been demonstrated not to be the case (see Fig. 4.5d). In short, whilst the intriguing repose gap observed here is likely steeped in complexity, it is continuously suggested that the potential driving mechanism is the coalescence of gas slugs.

4.5.3. Observations on explosive masses

It is important to note at the beginning of this section that strombolian activity is common at Etna as a whole (see GVP, 2013 and INGV bulletins), particularly from the NSEC. Within this chapter the focus has been on the somewhat rarer activity at the BN crater, over the relatively short observation duration. However, 195 explosions is a sizeable dataset particularly given this constituted the first observations of gas mass for strombolian events at

Etna (Burton et al. 2015a). Here a somewhat low range of explosive SO_2 masses was determined between ≈ 0.1 – 14 kg. This is likely associated with the measurements occuring during the waning period of activity (e.g. as backed up by seismicity). At Pacaya an overlapping range of SO_2 masses was observed, 3 – 29 kg (Dalton et al. 2010). At Stromboli however, Mori and Burton (2009) determined values of ≈ 15 – 40 kg, while Tamburello et al. (2012) suggest values of ≈ 2 – 55 kg, which are somewhat higher than the Etnean values. This is likely related to the style of manifest activity, which at Stromboli is associated with explosions spaced on the order of minutes (Ripepe et al. 2008), while Etna often exhibits more frequent explosions separated by seconds (e.g. GVP, 2013). This suggests that there may be different source mechanisms driving the observed activity. The measured ratio for active to passive degassing is 67:33%, lower than the 77:23% and 92-97:8-3% determined by Tamburello et al. (2012) and Mori and Burton (2009) respectively for Stromboli. If the activity is considered in relation to overall Etnean degassing, the measured activity represents < 1% of the total degassing budget of Etna (Burton et al. 2015a). Burton et al. (2007) demonstrated that ratios between active and passive degassing can vary significantly. Here, out of necessity, average gas ratios were used, the estimate for active to passive degassing at the BN is therefore the best possible on the basis of the data available.

The presence of explosive activity with such low explosive masses (i.e. ≈ 0.2 kg) also raises questions about how the explosivity is generated, far beyond considerations of differences in atmospheric pressure (i.e. the lower pressure at the summit of Etna, i.e. ≈ 3,350 m, allows more expansion compared to targets such as Stromboli, i.e. ≈ 900 m)). If one were to consider the activity at Etna, not as the rise and bursting of individual gas slugs, but as the ascent of a swarm of gas bubbles this could also explain the mass deficiency of some bursts which eject material containing little gas mass. A swarm of gas bubbles has a higher velocity, up to 3-6 times faster than a single Taylor bubble, and can be determined by Krishna et al. (1999):

$$u_{slsw} = 0.71\sqrt{g2r_{sl}(SF)(AF)} \qquad \textbf{(Eq. 4.9)}$$

where (SF) and (AF) are scaling correction and acceleration factors respectively (see Krishna et al. 1999) for *Eo* >40 (*Eo* is the Eotvos number, at appropriate levels for volcanic activity – e.g. Del Bello et al. 2012). As the bubbles rise, overpressure could be generated in bubbles which have not yet fully developed into slug flow.

Low gas masses also explain and are potentially linked to the lack of any link between seismicity and either gas flux or erupted masses. Fig. 4.14 shows the location of tremor at the time of acquisition, which was actually dominated below the NEC. Other studies have demonstrated a clear relationship between seismicity and eruptive masses (e.g. McGonigle et al. [2009] at Stromboli and Kazahaya et al. [2011] at Asama), the lack of a correlation here is again the combined result of explosive frequency and low gas mass, in contrast to Zuccarello et al. (2013), who did discover a link. It is likely therefore that the overall strength of the activity is related to seismicity, e.g. linked to the resonance of the conduit (O'Brien and Bean, 2008). Indeed, during the more vigorous activity, seismicity associated with the BN crater was higher (see Fig. 4.3d).

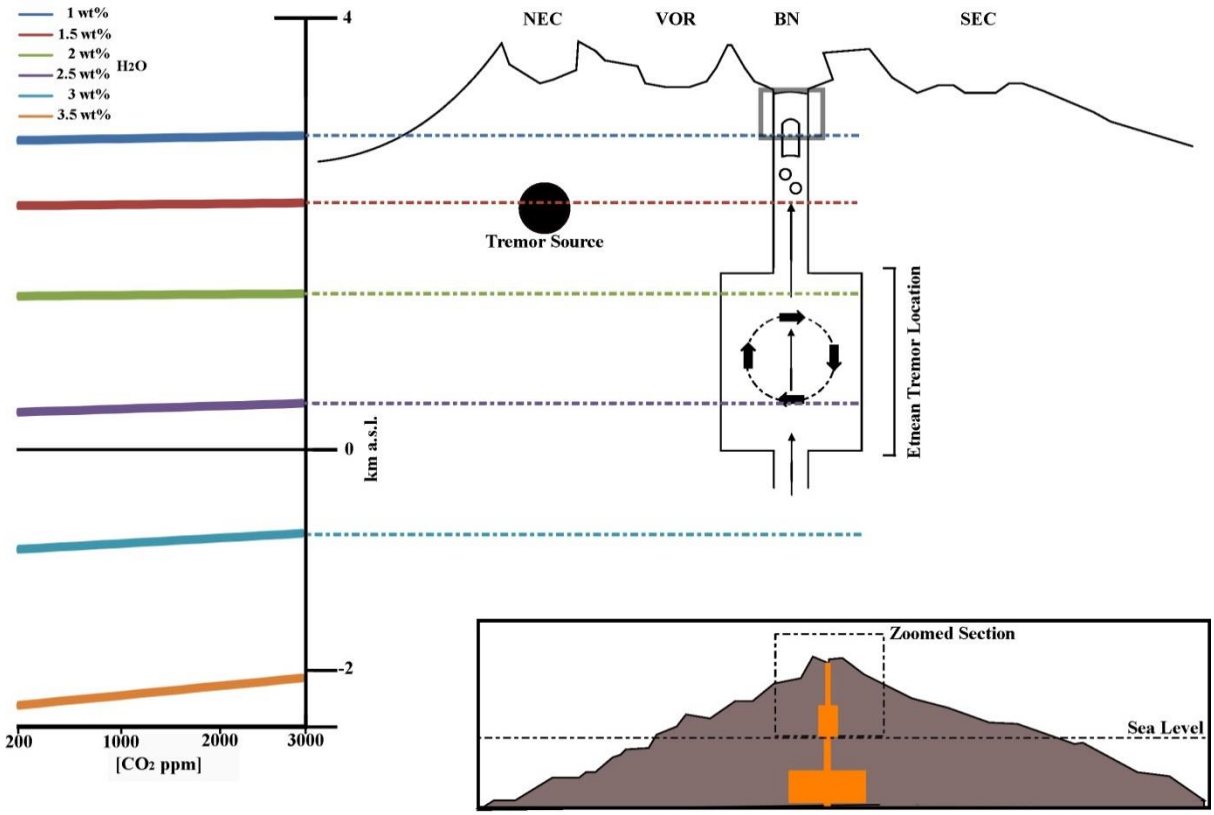

Fig. 4.14: This schematic illustrates the ranges of bubble source depths using the Burton et al. (2007) method over an approximation of the magma system at Etna. The tremor source is located (black solid circle) and the usual location of tremor at Etna. The grey box at the top of the conduit illustrates where the transition to slug based activity could occur.

The Burton et al. (2007) source depth model, which identifies where rising gas masses decouple from the melt – i.e. the point that they stop incorporating freshly exsolved gasses from the melt, suggests a depth range of ≈ 0.5 – 3.3 km. A H_2O gas rich magma batch finding its way to the surface via the BN crater could be the driver behind the observed strombolian activity, with the strombolian activity driven by shallow exsolution. Gas ratio data for

individual bursts would provide invaluable information. Fig. 4.14 provides this information in context at Etna.

4.6. Concluding Remarks

This chapter has illustrated through the use of UV cameras at the BN crater of Mt. Etna, relatively low gas masses of explosive activity ≈ 0.2 – 74 kg, compared to other volcanoes. These are the first such estimates for light strombolian activity at Mt. Etna. One of the main features of the observed activity is the discovery of a repose gap whereby larger explosions are followed by longer wait times before another explosion can occur. Amongst the possible causes of this feature, the most probable involves the coalescence of rising gas slugs which lead to the creation of larger distances in the melt between rising bubbles and hence longer delay times before the onset of the following explosion. The next chapter investigates this process in more detail.

This chapter has also highlighted the value in applying single slug models, despite the potential inapplicability to multi slug activity, to investigate parameters such as transition depths to slug flow, with results suggesting shallow transitions of ≈ ≤ 170 m. In addition by estimating wake interaction lengths in combination with slug rise speeds, it was demonstrated that slugs could rise in close proximity to one another and could indeed interact and coalesce, a process which is likely expedited during slug expansion close to the surface.

5. Investigating multi-slug behaviour

In the previous chapter, measurements of rapid slug driven strombolian activity were presented, along with a repose gap feature. This chapter combines laboratory analogue analysis of slug flow to probe slug interactions with computational analysis of this behaviour. The laboratory analysis reveals that coalescence can occur between rising slugs, even when the leading slug base is ascending at a faster velocity than the trailing slug base, an observation which has not previously been reported on. A relationship between gas volume fraction and slug rise speed is also demonstrated. The analysis also shows that the repose gap behaviour can be clearly defined using existing fluid dynamical relations, as successful tested using laboratory and field data. This is based on work presented at AGU, 2014: *Pering, T. D. McGonigle, A. J. S., James, M.R., Lane, S.J., Capponi, A., Tamburello, G., Aiuppa, A., 2014c. Observations on Multi-Slug Activity – Implications for Volcanic Processes. In: AGU Fall Meeting 2014 San Francisco.* The laboratory experiments were conducted at Lancaster University using the equipment described in James et al. (2013), Lane et al. (2013), and Del Bello et al. (2015).

5.1. Introduction

A large proportion of the material relevant for this chapter has already been introduced in Chapters 3 and 4. Here, the focus is on experimental and fluid dynamical studies into rising and expanding gas slugs with a view to investigating and observing rapid strombolian activity. However, a number of non-volcanic slug based studies do focus on the interaction of two bubbles in both stagnant (Pinto and Campos, 1996) and co-current flow (Pinto et al. 1998, 2001; Serizawa et al. 2002). With only two slugs in a pipe or conduit, given a sufficient distance between the two (i.e. beyond the disturbance created by the wake interaction length and expansions of the trailing slug) slugs should behave as they would in a single slug system (Taitel et al. 1980; Pinto et al. 2001). As additional slugs are added this relationship will break down as the trailing slugs begin to exert an influence on those above, hence influencing the speed and dynamics of the rising slugs, especially in bulk (Wallis, 1969; Llewellin et al. 2014).

In this chapter, the behaviour of multiple rising slugs is investigated utilising a scaled laboratory environment in addition to computational fluid dynamics (CFD). Apart from very

brief considerations by Seyfried and Freundt (2000), James et al. (2004), and Pioli et al. (2012), there has been little consideration of a multi-slug regime in a volcanic setting, an issue which this chapter addresses.

5.2. Laboratory Set-Up

To simulate a varied rate of slug flow a bubble injector was installed at the base of an ≈ 1.8 m borosilicate glass tube of diameter ≈ 0.025 m (see Fig. 5.1). The bubble injector was equipped with a flow rate meter and was set to inject single bubbles of various volumes. The tube was kept at a constant pressure (during experiments) via a vacuum pump connected to the top of the tube, to allow a range of slug expansions rates to be investigated, in essence simulating volcanic slug flow at a variety of depths prior to burst. Mechanical vacuum pump oil was chosen as the liquid, which has a density of 862 ± 2 kg m^3, and a viscosity of 0.162 ± 0.004 Pa s^{-1}. A similar equipment set up was used in Corder (2008), James et al. (2013), Lane et al. (2013), and Del Bello et al. (2015). With this equipment set up and fluid parameters, the dimensionless parameters were scaled to volcanic levels (see also Lane et al. 2013 supplementary material for scaling arguments in more detail). An N_f value of ≈ 66 is well within a reasonable volcanic range (see Del Bello et al. 2012). It should be noted here however, that there is a large difference in surface tension between lab (0.03 ± 0.002 N m^2) and volcanic environments (between 0.3 – 0.4 N m^2, e.g. Sparks, 1978), which effects the scaling of the experiments. Surface tension will be important in the lab setting, while surface tension effects can largely be neglected in a basaltic magma (Seyfried and Freundt, 2000; James et al. 2008; Del Bello et al. 2012; Lane et al. 2013).

A series of experiments were designed to investigate a range of volcanic situations from low flow rates with little expansion, to simulate slug flow at depth with low overall gas volume fractions, to high flow rates with greater bubble expansion rate to simulate near-surface slug flow with high gas volume fractions. These experiments are summarised in Table 5.1. All experiments were recorded for ≈ 30 s with a slow motion ≈ 300 fps camera (Basler A602f, see Lane et al. 2013; Capponi et al. 2014) and a conventional Digital Single-Lens Reflex camera (DSLR, a Canon EOS 1100D) at ≈ 25 fps for a longer duration of ≈ 180 – 360 s. Slow motion video was necessary to track the coalescence process of individual bubbles in detail, which occurred at such a rapid rate (largely in < 3 s) that it could not be captured in enough detail using conventional recording methods. All tracks (of slug features) were made

manually using the software package ImageJ® and the plugin MTrackJ (http://www.imagescience.org/meijering/software/mtrackj/), this manual tracking process leads to a certain amount of rapid variability in slug base and nose positions associated with the pixel size. Despite this, this method is preferred over automated processes, which are unreliable during bubble coalescence. The tracks and signals were not filtered (e.g., via averaging or filtering) to preserve existing information and oscillations which would be removed otherwise. The longer duration DSLR data, which has a wider field of view, captures the full length of the tube, following the bubbles from injection to burst, which enabled the determination of bubble length and burst time with an accuracy of ± 0.01 m and ± 0.04 s respectively. Additional measurements were made using transducers at the base and the top of the tube, which recorded pressure at 1,000 Hz; a displacement transducer was also placed at the base. Pressure was measured using Honeywell 163PC01D75 differential pressure transducers.

Table 5.1: Summary of the laboratory experiments, their set-up parameters, average slug length and average gas volume fraction of each regime observed.

Code	Av. Flow Rate (cm^3 s^{-1})	Surface Pressure (Pa)	Av. Slug Length (mm)	Gas VF (%)
Lab 1	9.38	1	16.98	8
Lab 2	49.71	1	50.34	27
Lab 3	174.92	1	208.71	58
Lab 4	9.38	0.5	23.91	9
Lab 5	49.71	0.5	56.75	29
Lab 6	174.92	0.5	223.81	63
Lab 7	9.38	3	10.46	6
Lab 8	49.71	3	27.29	18
Lab 9	174.92	3	115.88	50
Lab 10	9.38	5	8.27	7
Lab 11	49.71	5	18	16
Lab 12	174.92	5	73.47	40

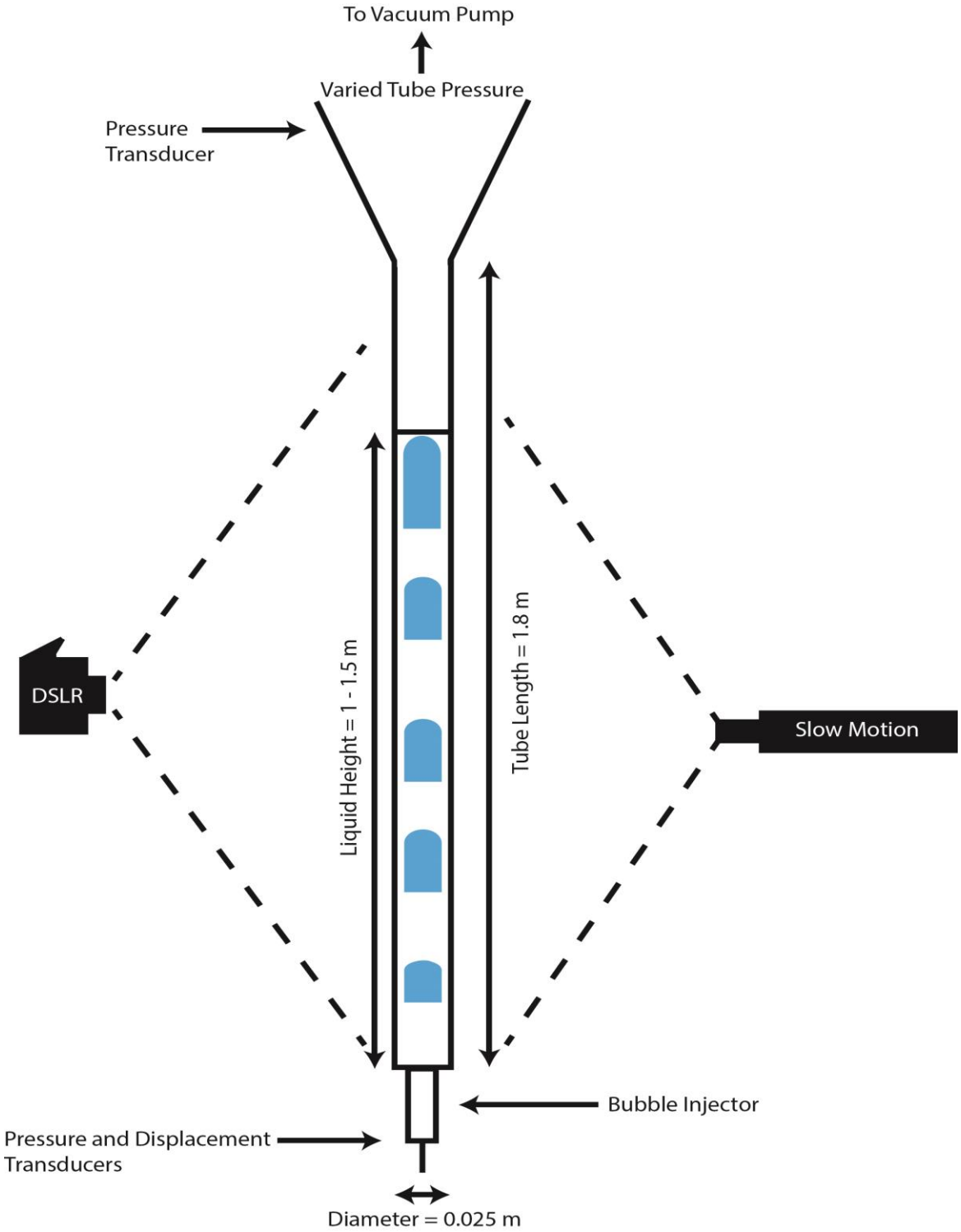

Fig. 5.1: The experimental set-up included a vertical tube with a bubble injector attached to the base to simulate a range of flow rates. Tube pressure was varied via connection to a vacuum pump at the top of the tube, but was kept constant during experiments. Two cameras, a DSLR (Canon EOS 1100D), and a slow motion camera (Basler A602f), were aligned to image the rising slugs in the tube. Pressure transducers were placed at the top and the base of the tube.

5.3. Lab Results

Here, the results of the laboratory experiments are presented. Firstly a number of example image stills of all bubbles within the column are shown in Fig. 5.2 during the coalescence process to illustrate the different flow regimes. This is the first such analysis of its kind, in particular in the lab using parameters scaled to match volcanic dimensionless parameters (e.g., N_f, see Chapters 3 and 4). Following this, the bulk behaviour of slugs was considered, in particular focussing on burst rates, rise speeds, and lengths (and volume) of the slugs with a view to investigating the repose gap behaviour of Chapter 4. Finally, data recorded by pressure and displacement transducers were analysed and compared to the burst data.

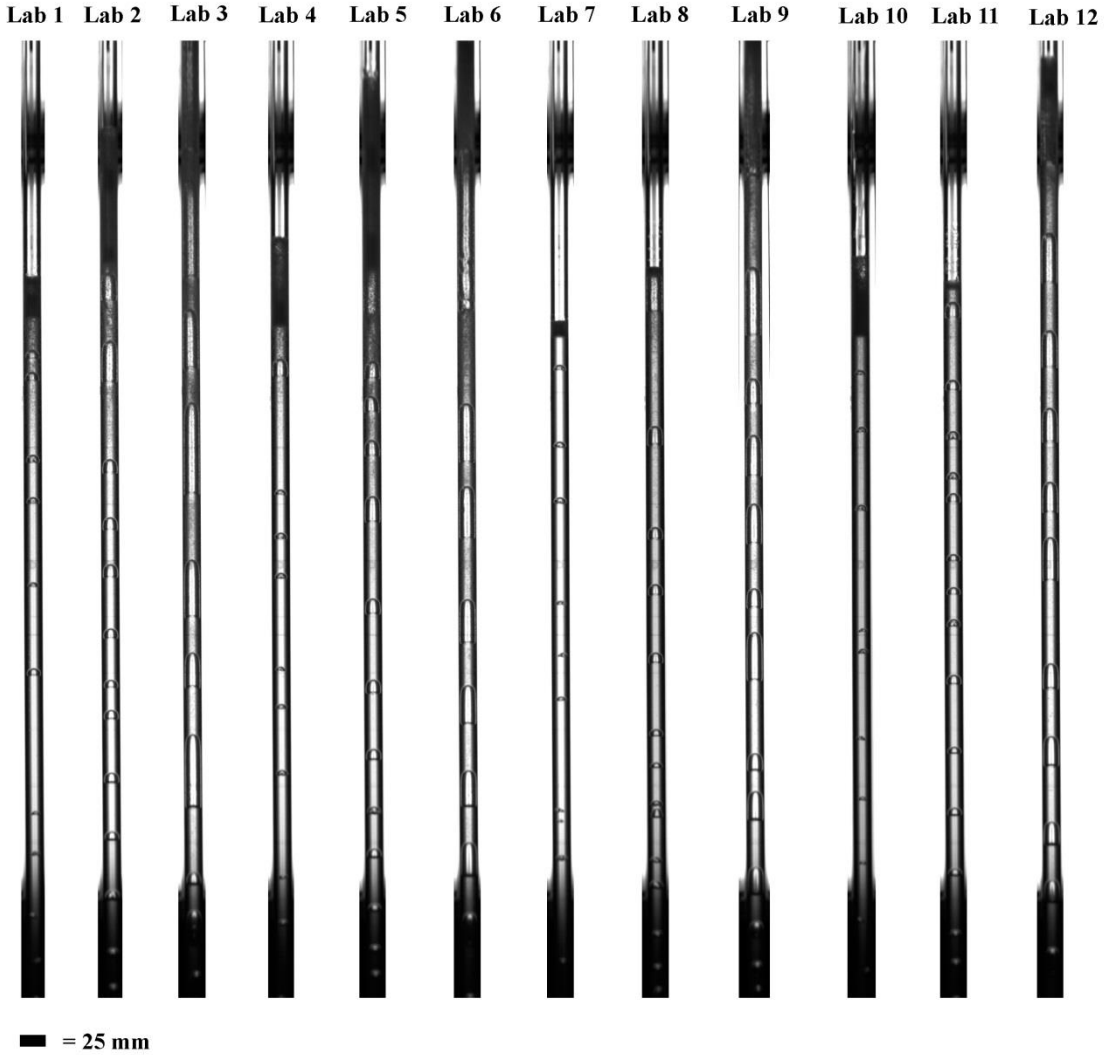

Fig. 5.2: Example images from each lab experiment demonstrating slug length and overall gas volume fraction of the simulated regimes (see Table 1.1 for information on each flow regime).

5.3.1. Tracking slug interaction

Fig. 5.3 shows an example of coalescence within the laboratory regimes. In Figs. 5.4 to 5.7 the coalescence process of two bubbles was tracked on a frame by frame basis. In each figure a number of features are plotted, including: the lengths of the trailing and leading slug, the distance between the trailing and leading slug (termed the gap length), the wake interaction length (see equation 4.3), the wake length (see equation 4.2), the trailing and leading slug base speeds, the predicted slug base speed in a single slug environment according to Viana et al. (2003), and the gap length plus the trailing length. Theoretically the latter parameter should be constant, until the trailing slug begins to interact with the leading slug, as it is at this point, assuming that the whole of the slug including its base begins to accelerate (Pinto and Campos, 1996; Kawaji et al. 1997; Pinto et al. 1998), that this gap plus trailing length should begin to decline. A summary of information surrounding the plots in Figs. 5.4 to 5.7 is given in Table 5.2.

In all plots there are number of different observations:

- At lower volume fractions (< ~10 %) the coalescence process occurs as expected, with a decreasing gap length plus trailing length, leading to coalescence (see Figs. 5.4c, 5.5a, 5.5e, and 5.5f). The rise speed of the base of the slugs in these situations is close to, or at the predicted value (Viana et al. 2003; Llewellin et al. 2012).
- At moderate volume fractions (> ~ 10 %) the rise speed of slugs is above predicted values a single slug system (Viana et al. 2003; Llewellin et al. 2012) but within the Krishna et al. (1999) estimate, see Figs. 5.5b, 5.5c, 5.5d, 5.6b, and 5.6c. This could be related to turbulence or a measurable effect of expansion from lower slugs.
- At still higher volume fractions (> ~ 20 %) the rise speed of slugs reacts to bulk changes in fluid movement resulting from the burst of larger slugs at the top of the liquid column. This is illustrated in rapid fluctuations in rise speeds (see Figs. 5.4a, 5.4b, 5.4d, and 5.4e).
- Slugs begin to interact at the wake interaction length (or within this limit), as evidenced by a reduction of the gap length plus trailing length in several figures (see Figs 5.4c, 5.5a, 5.5e, 5.5f, 5.6a) within this limit. Rapid capture occurs on entering the slug wake (a more rapid acceleration of the trailing slug base into the leading slug) in the final ≈ 0.2 s of the coalescence process.

- At a relatively constant base speed for both trailing and leading slugs, regardless of whether the rise speed is above or at the predicted speed for single slugs the coalescence process occurs “normally” (see Figs. 5.4c, 5.5a, 5.5e, and 5.5f), i.e. the gap plus trailing length decreases before rapid capture on entering the slug wake. In these cases, the slugs are behaving as though they are rising in a stagnant fluid.
- In certain circumstances the gap plus trailing length actually increases before coalescence (see Figs. 5.4a, 5.4b, 5.4d, 5.4e, 5.5b, 5.5c, 5.5d, 5.6b, 5.6c). In these cases the base of the leading slug begins to move at a faster speed than the trailing slug, however, the length of the trailing slug, begins to increase (i.e. the nose accelerates, in tandem with an increase with the leading slug base speed) which allows the whole of the trailing slug to be, in essence, stretched into the wake of the leading slug resulting in coalescence, (see Fig. 5.7a, 5.7b, 5.7c for an example of the tracks). This is a similar observation as that associated with coalescence in a co-current environment (Pinto et al. 1998), who also show that the leading slug can travel at a faster speed than the one below. Here, the results show that coalescence can still occur even in these cases, which Pinto et al. (1998) suggest cannot (see Table 5.2 for examples).

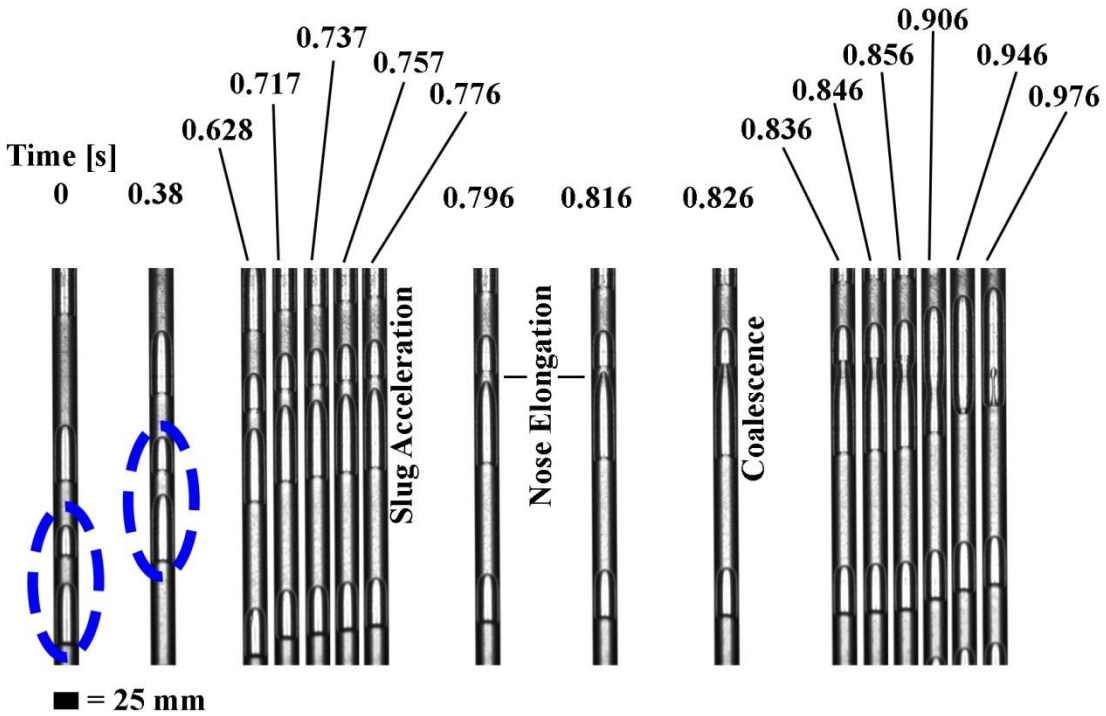

Fig. 5.3: Stills showing the coalescence process for two ascending gas slugs (circled in blue at time 0 and 0.38 s). As the trailing slug expands it begins to enter the area of influence and the whole of the slug begins to accelerate, on entering the slug wake, the nose elongates, ending in coalescence.

- The coalescence process takes longer in the regimes where expansion is less dominant (see Fig. 5.6). Indeed, in some instances, the tube may not be long enough to capture the entire coalescence process. In addition, the probability of coalescence is increased if the trailing slug has a higher mass/volume than the leading slug, i.e. the trailing slug is inserted into the areas of influence by a higher rate of slug expansion, making coalescence more likely.
- During all experiments a foam layer is generated at the air-liquid surface interface, however, this is most pronounced in the higher gas volume fraction experiments, of > 40%. This foam layer has a resultant effect on how the slugs arrive and burst at the surface in those experiments (Lab 3, Lab 6, and Lab 9) as in effect, the viscosity of the upper portion of the conduit will have been changed (Del Bello et al. 2015). This includes the slowing of slugs on entering this layer and hence how they interact. Although separation distances between slugs are preserved. These foam layers are visible in the videos contained in Appendix D.

Table 5.2: A summary of the rise speeds of the bases of the trailing and leading slugs during a number of coalescence events. The speeds were calculated during the whole sequence, during coalescence (defined by the last < 1 s before coalescence), and pre coalescence. All italicised rows refer to coalescence events where the leading slug base is travelling at a faster speed than the trailing slug base. *Slug 1 refers to the leading slug and slug 2 to the trailing slug, all values are in m s^{-1}. Refer to Table 5.1 for experimental conditions, error on these values is ± 4 x 10^{-4} m s^{-1} (i.e. length error of ± 0.01 m multiplied by time error of ± 0.04 s).

	Pre Coalescence		During Coalescence		Whole Sequence	
Experiment	**Slug 1***	**Slug 2***	**Slug 1***	**Slug 2***	**Slug 1***	**Slug 2***
Lab 1	0.12	0.13	0.13	0.17	0.12	0.14
Lab 2	0.16	0.16	0.20	0.23	0.18	0.20
Lab 3	*0.25*	*0.24*	*0.33*	*0.31*	*0.28*	*0.27*
Lab 3	*0.23*	*0.22*	*0.31*	*0.27*	*0.26*	*0.24*
Lab 3	*0.25*	*0.24*	*0.27*	*0.26*	*0.26*	*0.25*
Lab 4	*0.13*	*0.13*	*0.17*	*0.15*	*0.15*	*0.14*
Lab 5	0.14	0.15	0.14	0.21	0.14	0.18
Lab 5	0.14	0.15	0.15	0.17	0.14	0.16
Lab 5	0.14	0.14	0.15	0.16	0.15	0.15
Lab 6	*0.23*	*0.22*	*0.43*	*0.36*	*0.36*	*0.31*
Lab 6	*0.24*	*0.23*	*0.37*	*0.33*	*0.28*	*0.26*
Lab 6	0.24	0.24	0.22	0.22	0.23	0.23
Lab 6	0.25	0.24	0.27	0.27	0.26	0.26
Lab 6	0.23	0.23	0.28	0.28	0.25	0.25
Lab 7	0.12	0.13	0.13	0.15	0.12	0.13
Lab 8	0.14	0.14	0.14	0.15	0.14	0.15
Lab 9	0.21	0.22	0.23	0.24	0.22	0.22
Lab 9	*0.22*	*0.22*	*0.24*	*0.23*	*0.23*	*0.22*
Lab 9	0.21	0.21	0.24	0.24	0.22	0.22
Lab 9	*0.22*	*0.21*	*0.26*	*0.23*	*0.24*	*0.22*
Lab 9	0.21	0.20	0.23	0.23	0.23	0.22
Lab 9	0.21	0.21	0.22	0.24	0.21	0.22
Lab 11	0.14	0.14	0.14	0.15	0.14	0.15
Lab 11	0.14	0.14	0.15	0.15	0.14	0.15
Lab 12	0.20	0.20	0.23	0.24	0.21	0.21
Lab 12	0.18	0.20	0.20	0.21	0.19	0.21
Lab 12	0.20	0.20	0.24	0.24	0.22	0.22
Lab 12	*0.20*	*0.19*	*0.23*	*0.22*	*0.22*	*0.21*

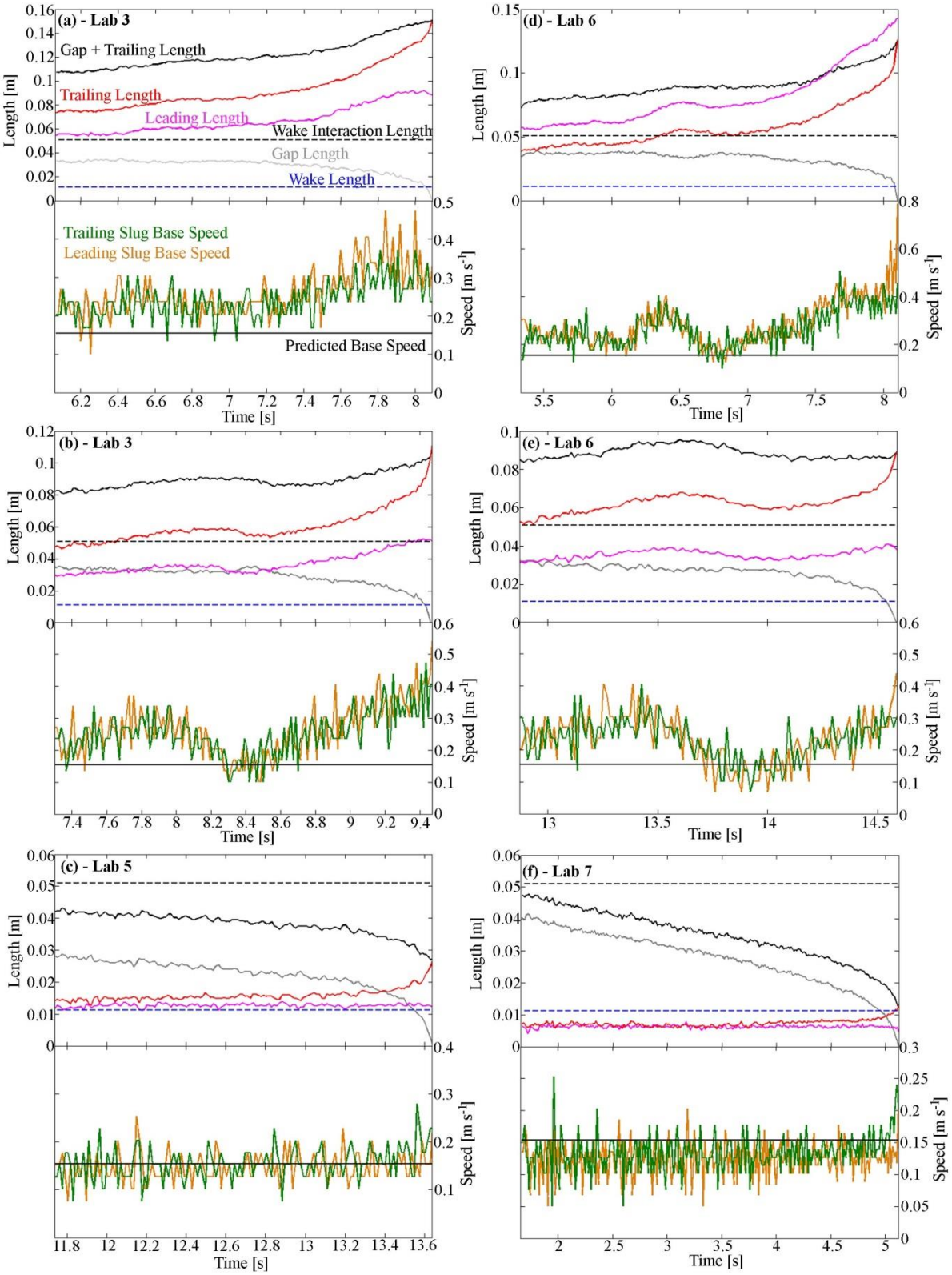

Fig. 5.4: Example tracks and speeds of a selection of coalescence events (continued in Figs. 5.5 and 5.6). The gap length is the distance between the leading slug base and the trailing slug nose. In (a), (b), (d), and (e), slugs are rising at a rate faster than the predicted theoretical rise speed, in (c) they are rising at that speed, and in (f) below the speed. Rapid oscillations in rise speed, obvious in (a), (b), (d), and (e) are related to the bursting and drain back of liquid from the burst of a slug at the surface affecting the whole magma column. (c) represents expected behaviour of coalescing slugs in a normal single slug regime, whilst in (f), the rising bubble has yet to transition to a full slug. For a detailed discussion of features see the text at section 5.3.1.

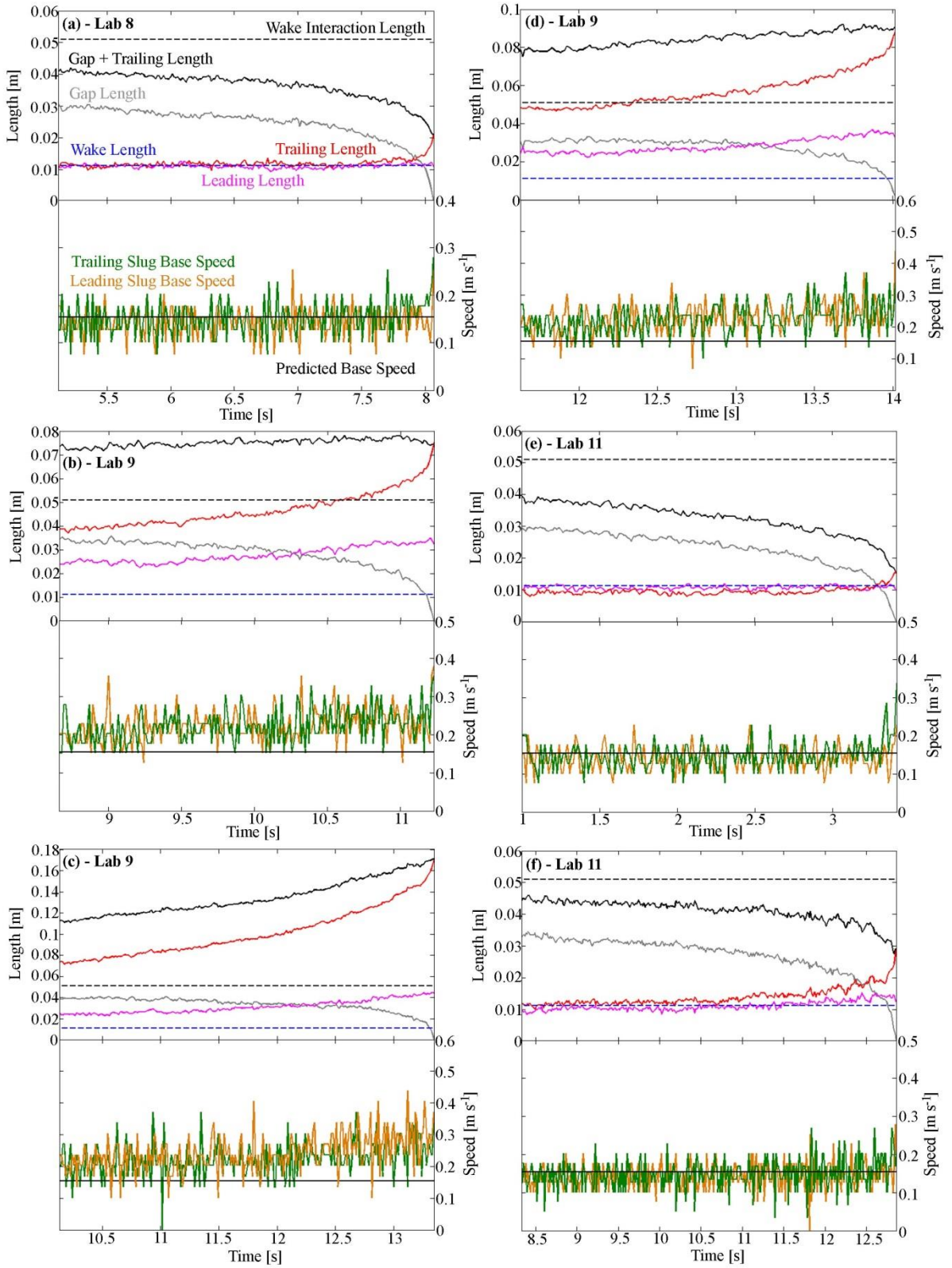

Fig. 5.5: A continuation of Fig. 5.4. In (a) the rising slugs are behaving as though they are in a single slug system. In (b), (c), and (d), both slugs are rising above the theoretical speed, and demonstrate a generally increasing gap plus trailing length before coalescence. For a detailed discussion of features see the text at section 5.3.1.

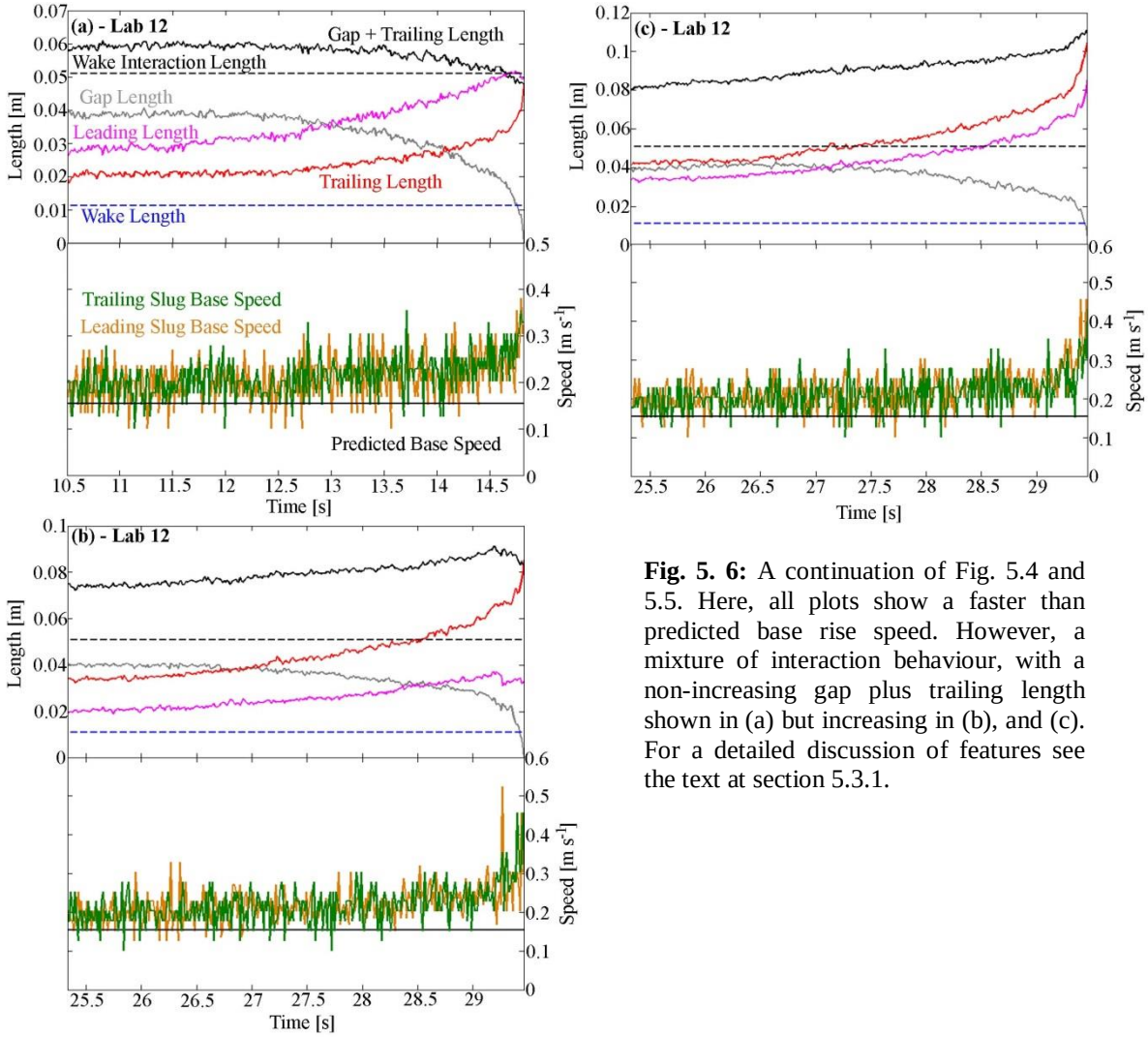

Fig. 5. 6: A continuation of Fig. 5.4 and 5.5. Here, all plots show a faster than predicted base rise speed. However, a mixture of interaction behaviour, with a non-increasing gap plus trailing length shown in (a) but increasing in (b), and (c). For a detailed discussion of features see the text at section 5.3.1.

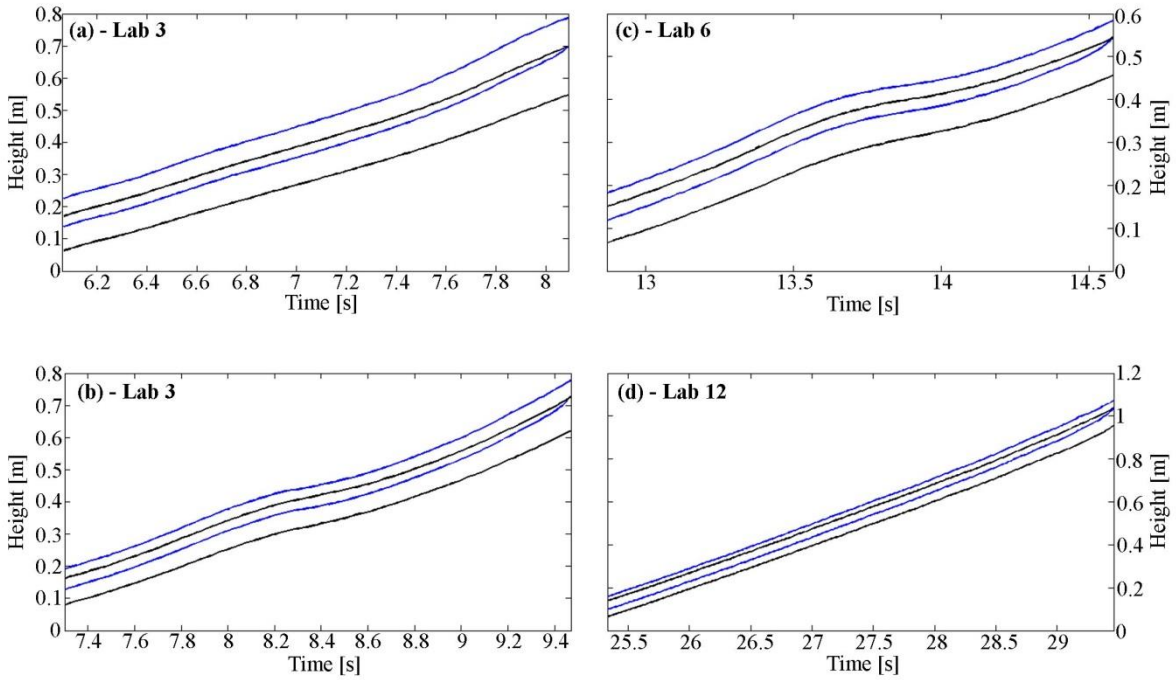

Fig. 5. 7: Example positional tracks of four sets of coalescing slugs. In (d) the coalescence event demonstrated in Fig. 5.6a shows a constant trailing base speed until acceleration and eventual coalescence. In (a), (b), and (c) the bulk behaviour of rising slugs is demonstrated.

Table 5.3: A summary of slug base speeds calculated for non-coalescing slugs only.

Exp #	Speed (m s^{-1})	Exp #	Speed (m s^{-1})	Exp #	Speed (m s^{-1})	Exp #	Speed (m s^{-1})
Lab 1	0.126	**Lab 4**	0.165	**Lab 7**	0.126	**Lab 10**	0.125
Lab 1	0.126	**Lab 4**	0.162	**Lab 7**	0.125	**Lab 10**	0.122
Lab 1	0.127	**Lab 4**	0.159	**Lab 7**	0.128	**Lab 10**	0.124
Lab 1	0.127	**Lab 4**	0.144	**Lab 7**	0.125	**Lab 10**	0.122
Lab 1	0.127	**Lab 4**	0.132	**Lab 7**	0.126	**Lab 10**	0.120
Lab 1	0.130	**Lab 4**	0.126	**Lab 7**	0.124	**Lab 10**	0.122
Lab 1	0.126	**Lab 4**	0.134	**Lab 7**	0.126	**Lab 10**	0.121
Lab 1	0.123	**Lab 4**	0.130	**Lab 7**	0.122	**Lab 10**	0.126
Lab 1	0.128	**Lab 4**	0.127	**Lab 7**	0.122	**Lab 10**	0.119
Lab 1	0.131	**Lab 4**	0.129	**Lab 8**	0.145	**Lab 11**	0.139
Lab 2	0.161	**Lab 5**	0.161	**Lab 8**	0.142	**Lab 11**	0.140
Lab 2	0.158	**Lab 5**	0.152	**Lab 8**	0.140	**Lab 11**	0.138
Lab 2	0.152	**Lab 5**	0.146	**Lab 8**	0.137	**Lab 11**	0.135
Lab 2	0.147	**Lab 5**	0.144	**Lab 8**	0.144	**Lab 11**	0.135
Lab 2	0.146	**Lab 5**	0.161	**Lab 8**	0.142	**Lab 11**	0.134
Lab 2	0.146	**Lab 5**	0.157	**Lab 8**	0.145	**Lab 11**	0.139
Lab 2	0.142	**Lab 5**	0.151	**Lab 8**	0.141	**Lab 11**	0.138
Lab 2	0.139	**Lab 5**	0.149	**Lab 8**	0.142	**Lab 11**	0.137
Lab 2	0.166	**Lab 5**	0.145	**Lab 8**	0.147	**Lab 11**	0.136
Lab 2	0.153	**Lab 5**	0.143	**Lab 8**	0.147	**Lab 11**	0.141
Lab 2	0.153	**Lab 5**	0.143	**Lab 8**	0.145	**Lab 11**	0.141
Lab 2	0.146	**Lab 5**	0.146	**Lab 8**	0.141	**Lab 11**	0.139
Lab 2	0.145	**Lab 5**	0.144	**Lab 8**	0.138	**Lab 11**	0.136
Lab 2	0.144	**Lab 5**	0.142	**Lab 8**	0.139	**Lab 11**	0.136
Lab 2	0.139	**Lab 6**	0.319	**Lab 9**	0.264	**Lab 12**	0.221
Lab 3	0.283	**Lab 6**	0.272	**Lab 9**	0.255	**Lab 12**	0.215
Lab 3	0.258	**Lab 6**	0.250	**Lab 9**	0.242	**Lab 12**	0.208
Lab 3	0.220	**Lab 6**	0.240	**Lab 9**	0.229	**Lab 12**	0.200
Lab 3	0.215	**Lab 6**	0.223	**Lab 9**	0.224	**Lab 12**	0.194
Lab 3	0.206	**Lab 6**	0.324	**Lab 9**	0.213	**Lab 12**	0.189
Lab 3	0.201	**Lab 6**	0.284	**Lab 9**	0.207	**Lab 12**	0.186
Lab 3	0.298	**Lab 6**	0.261	**Lab 9**	0.207	**Lab 12**	0.217
Lab 3	0.274	**Lab 6**	0.239	**Lab 9**	0.250	**Lab 12**	0.209
Lab 3	0.244	**Lab 6**	0.303	**Lab 9**	0.228	**Lab 12**	0.197
Lab 3	0.230	**Lab 6**	0.280	**Lab 9**	0.220	**Lab 12**	0.192
Lab 3	0.227	**Lab 6**	0.262	**Lab 9**	0.211	**Lab 12**	0.189
Lab 3	0.317	**Lab 6**	0.248	**Lab 9**	0.208	**Lab 12**	0.202
Lab 3	0.292	**Lab 6**	0.239	**Lab 9**	0.197	**Lab 12**	0.201
Lab 3	0.276	**Lab 6**	0.258	**Lab 9**	0.194	**Lab 12**	0.195
Lab 3	0.255	**Lab 7**	0.128	**Lab 10**	0.122		

5.3.2. Bulk behaviour of slugs

The average velocity of slugs in each regime was calculated using the slugs visible in the slow motion camera videos (see Table 5.3 for all values, and Appendix D for videos). This was then compared to the calculated volume fraction for each laboratory experiment (see Table 5.1). Volume fraction was calculated using a series of images stills for each experimental regime (in 30 s intervals using DSLR data), by summing the gaseous component and hence calculating the proportion of the liquid column occupied by gas. A summary of calculated speeds is available in Table 5.4, with the relationship between volume fraction and speed displayed in Fig. 5.8.

Table 5.4: Table summarising the calculated average slug base rise speeds of slugs (see Table 5.3 for all values) in each laboratory experiment (calculated using the slow motion camera images).

Experiment	VF (%)	Speed (m s^{-1})
Lab 1	8	0.127
Lab 2	27	0.149
Lab 3	58	0.253
Lab 4	9	0.140
Lab 5	29	0.148
Lab 6	63	0.266
Lab 7	6	0.125
Lab 8	18	0.142
Lab 9	50	0.223
Lab 10	7	0.122
Lab 11	16	0.137
Lab 12	40	0.201
Theory	N/A	0.153

Fig. 5.8 shows that there is a general relationship between the overall average gas volume fraction and observed rise speeds of the base of slugs, suggesting that the approximate speed of a rising slug in a multi-slug regime can be estimated. A number of the experimental regimes lie below the predicted line, which relate to experiments with < 20% gas volume fraction, and those which have yet to transition to full slug flow. A number of correlative relationships can be obtained, the following linear relationship has an $R^2 = 0.9474$:

$$y = 0.245x + 0.102, \quad \textbf{(Eq. 5.1)}$$

the following exponential has an $R^2 = 0.9615$:

$$y = 0.112e^{1.388x}, \quad \textbf{(Eq. 5.2)}$$

and the following 5th order polynomial has an $R^2 = 0.9921$:

$$y = 40.99x^5 - 74.65x^4 + 49.35x^3 - 13.99x^2 + 1.77x + 0.056. \quad \textbf{(Eq. 5.3)}$$

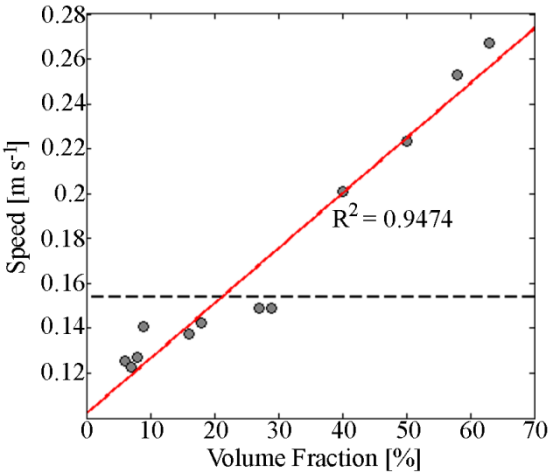

Fig. 5.8: Relationship between base rise speed (Table 5.2) and volume fraction of each lab experiment. Here a linear relationship is demonstrated (red line). The black dashed line represents the theoretical rise speed for a slug in a single system. Rising bubbles below this have yet to transition to a full slug flow regime.

For each laboratory simulation the average slug length (at burst) was also calculated (see Table 5.1), indeed when compared with gas volume fraction a relationship is similarly identified (see Fig. 5.9). This is largely a result of the controlled laboratory conditions, however, this may be of use in estimating average slug lengths during rapid activity if slug masses or volumes are known.

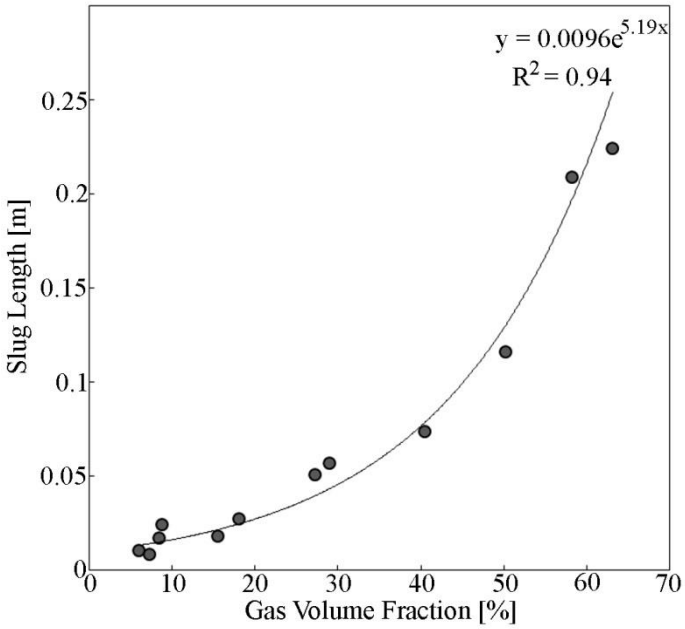

Fig. 5.9: The exponential relationship between slug length and gas volume fraction using averages of slug length at burst.

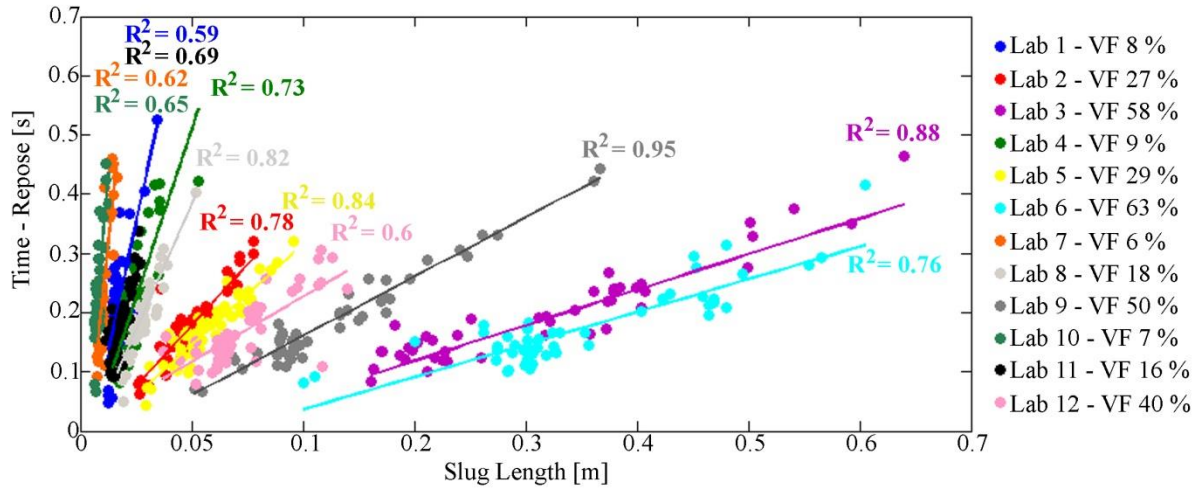

Fig. 5.10: Plot showing the repose time and lengths of slugs (or cap bubbles) at burst for each laboratory regime. The data for producing this plot were taken from DSLR videos (see Appendix D for description and videos). Each set of experiments is given its own colour code and is associated with a linear trend, with a gradient that decreases in regimes with higher gas volume fraction.

5.3.3. Investigating the repose gap behaviour

Here, the slug lengths and burst times of all bursts within all lab runs observed in the DSLR videos are calculated and illustrated. In Fig. 5.10 the slug lengths of all observed slugs are plotted against repose time (following a burst before the next occurs, as with the repose gap of Chapter 4). The results show a number of linear trends associated with repose time and slug length, with the majority possessing R^2 relationships of > 0.59. The gradients of these lines, which do not all go through the origin decrease with increasing volume fraction.

Using the best fit lines we can compare these gradients with the volume fraction of each experiment. This shows a strong relationship of R^2 = 0.95 with equation $y = 17.6x^{-0.66}$, indicating that the gradient increases for smaller gas volume fractions as is evident in Fig. 5.11.

In Fig. 5.10, there also appears to be a graduated increase in repose time with slug length. To investigate this area in more detail all slug lengths were converted to slug volume, using the equation for a volume of a cylinder ($V = \pi r^2 l_s$, the latter term is slug length). Fig. 5.12 shows the results of this conversion, with the repose gap clearly visible. Here, the black repose gap line is drawn using the following equation:

$$Rep_{min} = \frac{L+L_{wake}}{u_{sl}} \quad \textbf{(Eq. 5.4)}$$

where the minimum repose time, the Rep_{min}, is equal to the length of a slug, L, added to the length of the wake, l_{wake} (see equation 4.3), all divided by the predicted rise speed of the base of a single slug (see equations 3.3. and 3.4). In essence, this is a measure of the time taken for a trailing slug to travel through the length of the leading slug and its wake. A larger slug will make a larger disturbance at the surface with falling film and trailing liquid, therefore restricting the rise of a trailing slug (e.g. as evidenced in Figs 5.4 and 5.5). This process is also related to the amount of time taken for the turbulence contained within the liquid to return to background levels (Taitel et al. 1980). The result is a convincing match (black line in Fig. 5.12) with the lower slug bursts associated with the limits of burst frequency. Additionally, if l_w, is replaced with the wake interaction length, l_{min} (see equation 4.2), then any bursts occurring between the repose gap line and the repose transition line (red dashed line in Fig. 12) could potentially begin to interact with one another, i.e. the time delay between bursts is rapid enough such that the slugs should be separated by a small amount of liquid, around the wake interaction length:

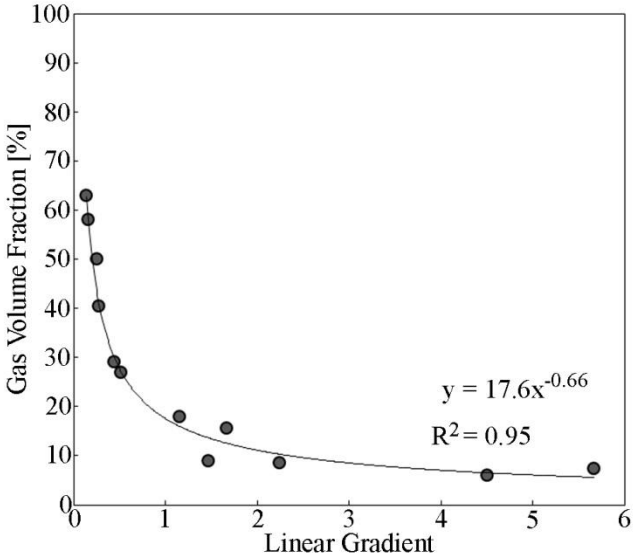

Fig. 5.11: The relationship between linear gradient of each laboratory regime and associated gas volume fraction, shows a strong trend.

$$Rep_{transition} = \frac{L+L_{min}}{u_{sl}}. \qquad \textbf{(Eq. 5.5)}$$

All slugs lying above the red dashed line in Fig. 5.12, are more likely to behave as though they are in a single slug system.

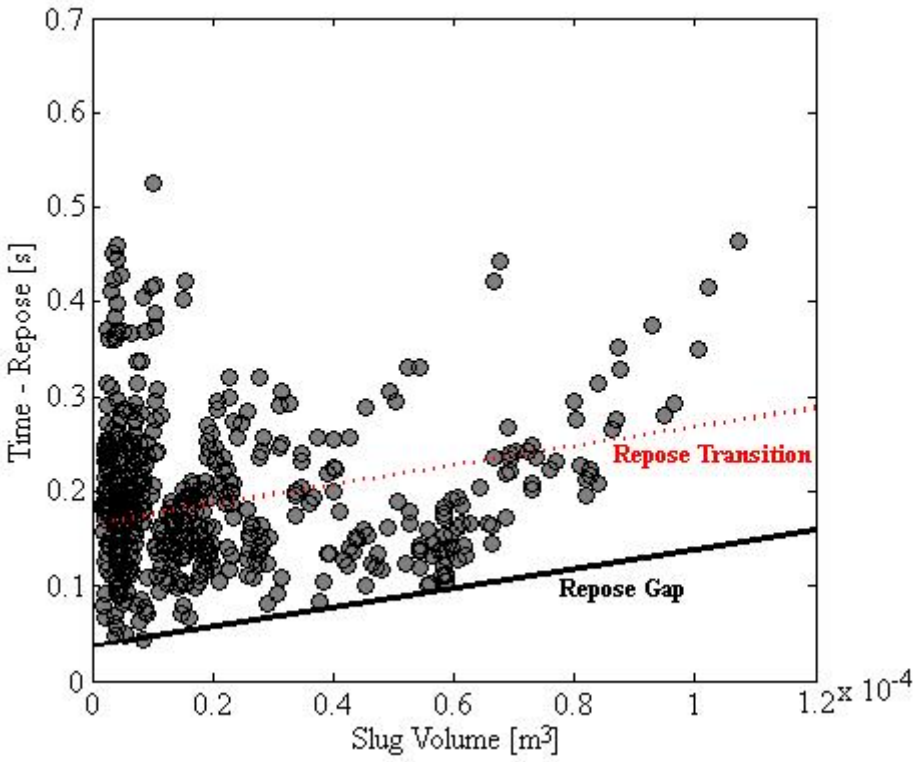

Fig. 5.12: In this plot each slug has been converted to volume at burst. This reveals a similar repose gap type behaviour as described in Chapter 4. Here, the repose gap (black line) has been defined using equation 5.4 in the text. Also displayed is the repose transition line (dashed red line). Between the transition and repose gap line, slugs may begin to interact with one another. Above the transition line slugs may behave as though they are in a single slug environment, at least in so far as rise speed is concerned.

5.3.4. Proxy Geophysical signals

Geophysical signals associated with each laboratory regime were also investigated. In each case the possibility of correlations with acoustic pressure (see Fig. 5.13 for example acoustic traces) and slug volume/length were investigated, but in each case a link between the two was elusive. Matching bursts with pressure traces were performed on a temporally coincident basis, but, there was not always a coincident acoustic pressure trace for each burst. Fig. 5.14 shows an example relationship between slug length and pressure, where it can be seen that there is no correlation suggesting an underlying complexity to links between acoustic pressure and slug mass (e.g. Lane et al. 2013; Matoza et al. 2013). Fig. 5.15 shows example traces for three of the lab experiments (Lab 1, 2, and 3), these which show that for regimes with elevated flow rates, the associated acoustic oscillations over timescales of seconds become larger.

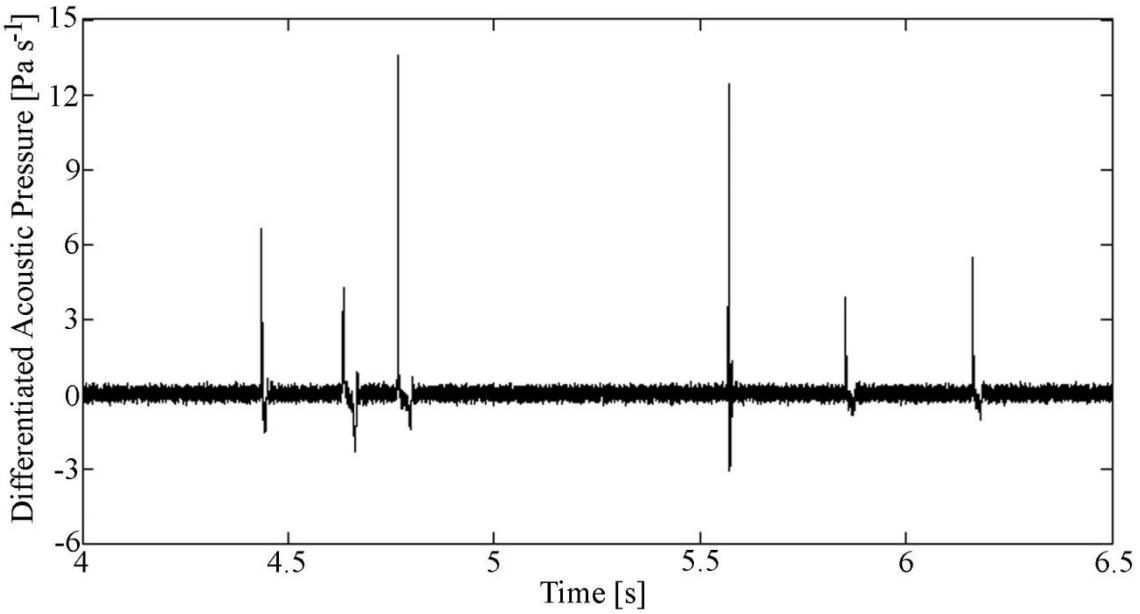

Fig. 5.13: A plot demonstrating the differentiated acoustic pressure trace from six slug bursts during experiment Lab 3. Here we see the characteristic *N-wave* of a volcanic infrasonic pressure wave is evident. Here, the larger acoustic signals don't correspond to the largest volume of bursts.

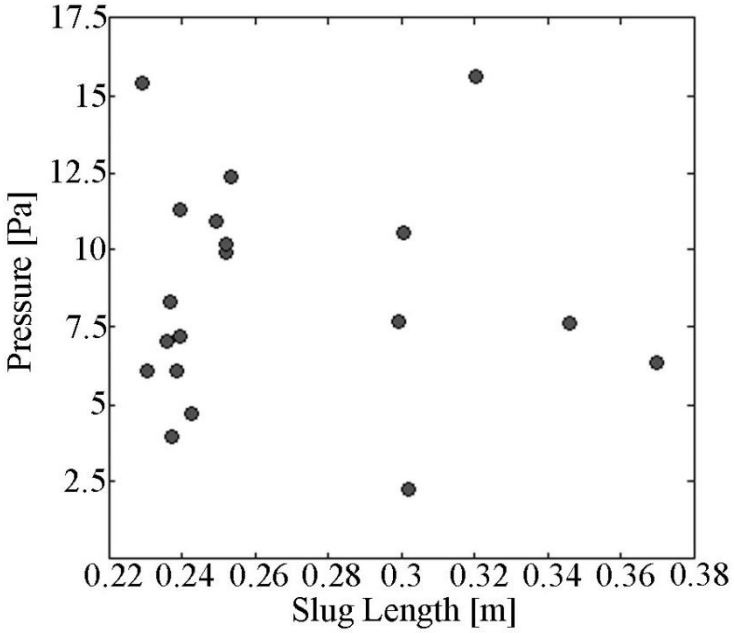

Fig. 5.14: An attempt at finding a correlation between slug lengths and the acoustic pressure generated by the bursting of slugs. Here, there is little relationship evident.

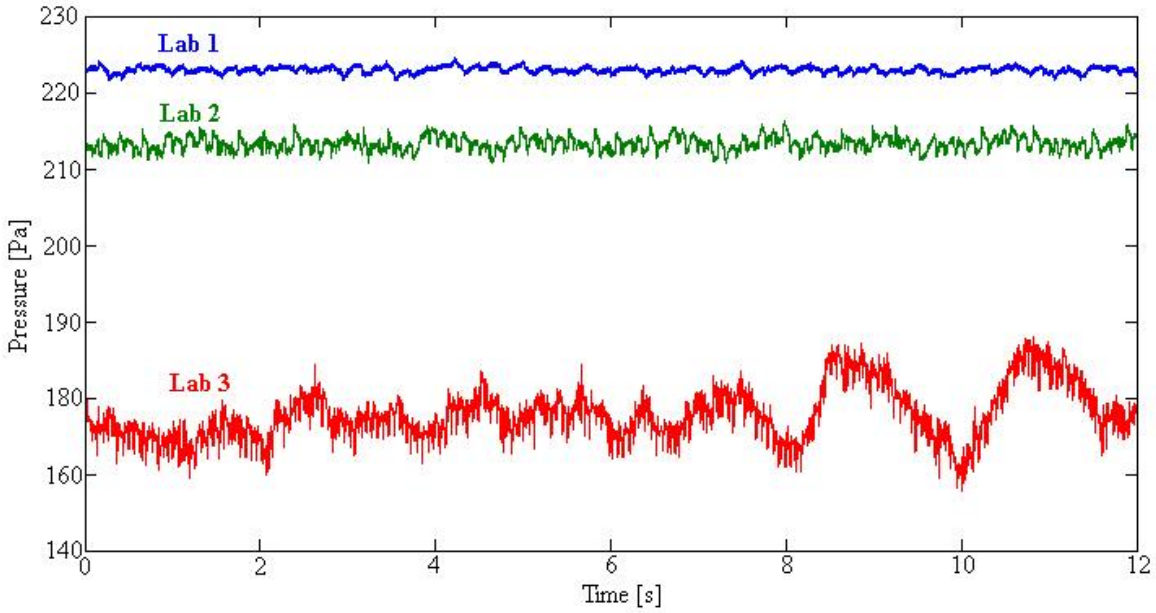

Fig. 5.15: Example base pressure of the experimental tube for three laboratory experiments: Lab 1, 2 and 3. A higher variability and oscillation range is evident for the larger volume fractioned experiments. The lower pressure at higher volume fraction is associated with the higher proportion of lower density gas within the column.

5.4. CFD Set-Up

The CFD package Ansys Fluent® with almost the same model parameters as described in Chapter 4 were used. The reader is referred to section 3.4 for the full model set-up details. Here the differences are magma density, which was set to 2500 kg m^3, and magma viscosity to 1000 Pa s^{-1}. A conduit radius and length of 1.5 m and 250 m, were used respectively, with each model initialised with 150 m of magma below 100 m of dry air at an atmospheric pressure of 101,325 Pa. During model testing, models with low viscosity magmas produced low model stability and run time was too long to allow a large number of runs. Hence, higher viscosity values were chosen, as appropriate for basaltic magmas (e.g. Shaw et al. 1968; Sparks, 1978; Llewellin et al. 2014b). As with Chapter 4, the composition of the volcanic slug was set to water vapour. In this chapter, the behaviour of multiple slugs in a volcanic setting is of interest. A number of experiments with identical mass slugs added at different depths and different separation distances were performed, to probe the interactive behaviour of the bubbles. A summary of model runs is available in Table 5.5 with the initial model conditions displayed in Fig. 5.16. A number of slugs in a volcanic system from one (as a control) to four were simulated at varying separation distances, ranging between 0.8 and 5 the wake interaction lengths. The additional slugs were added below the initial slug, to allow comparison with the (control) single slug.

Table 5.5: Summary of computational experiments.

Exp #	# of Slugs	Slug Separation Distance [m]	Coalescence?
C1	1	N/A	
C2	2	25	
C3	2	20	
C4	2	15	
C5	2	10	
C6	2	5	
C7	2	4	Y
C8	3	25	
C9	3	20	
C10	3	15	
C11	3	10	
C12	3	5	
C13	3	4	Y
C14	4	25	
C15	4	20	
C16	4	15	
C17	4	10	
C18	4	5	
C19	4	4	Y

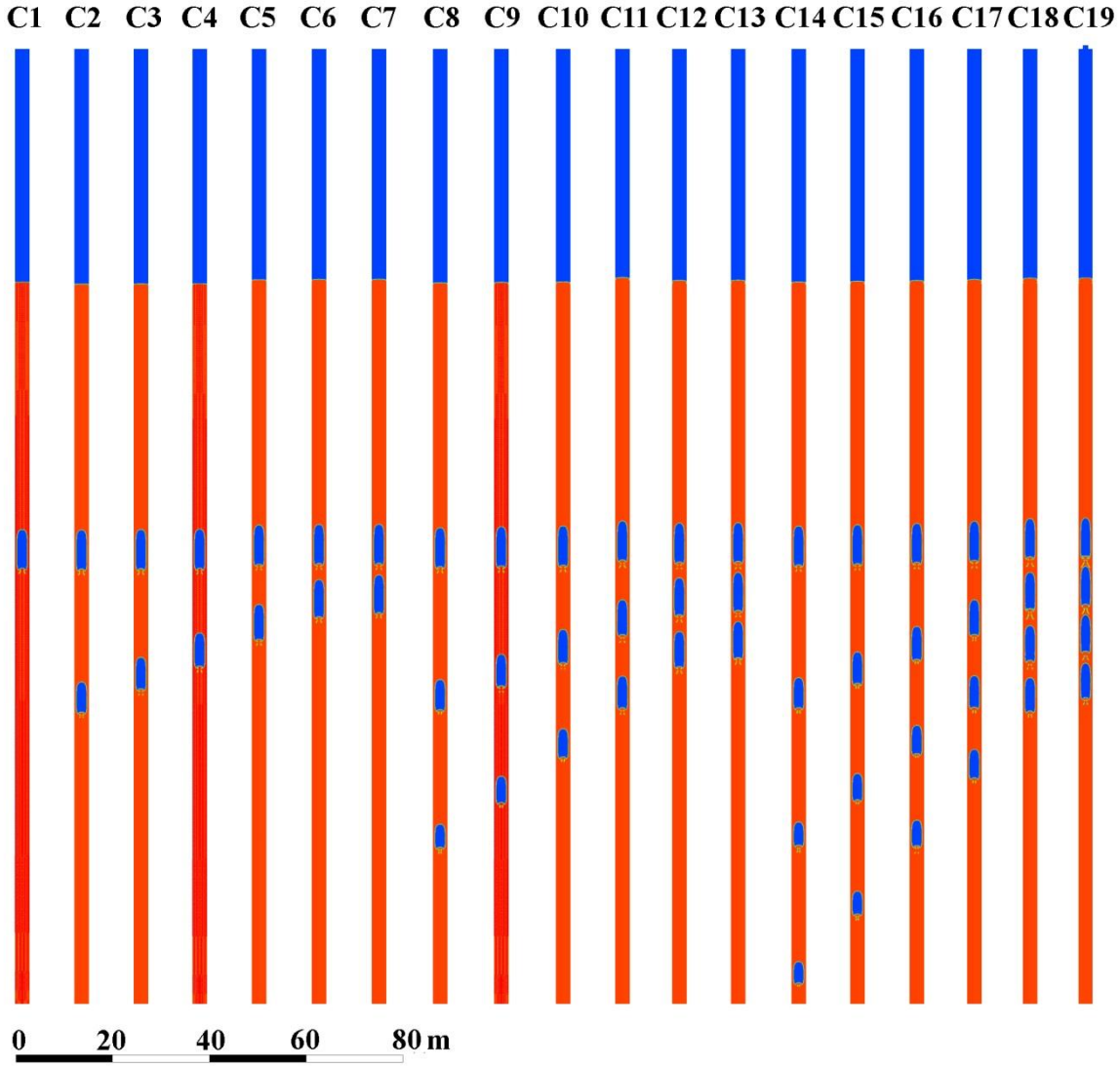

Fig. 5.16: Initial model parameters for each computational experiment listed in Table 5.5. The blue colours represent gas, and the red, magma. Models C7, C13, and C19 all produced coalescence..

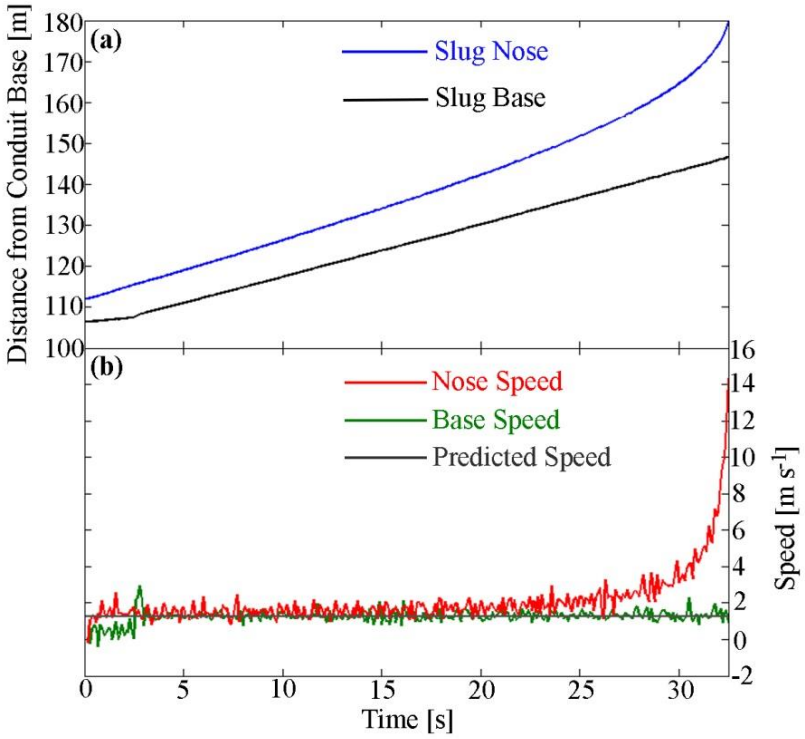

Fig. 5.17: Plot showing the results of the "control" computational run C1. In (a) the position of the slug nose and base prior to burst is displayed, while in (b) the speed of the nose and base are displayed alongside the predicted theoretical speed of 1.27 m s^{-1}. Here the predicted speed is seen to match well with that modelled, as the model validation suggests in Chapter 3. Slug burst occurs at the far right hand side of the plot.

5.5. CFD Results and Analysis

Fig. 5.17 shows, for reference, a single slug rising to the magma surface, expanding and bursting. The tracks of the slug clearly show a constant base velocity (apart from the first ≈ 2.5 s of the simulation, which are associated with bubble equilibration). This is also demonstrated in Fig. 5.17b, which shows that the slug base rises at the predicted speed of ≈ 1.29 m s^{-1}. Fig. 5.18 shows stills from simulation C7, where coalescence of two slugs occurs. The following Figs 5.19 – 5.22 are associated with the tracks of two to four slugs during a coalescence event (Figs. 5.20; 5.22a-e) and those where a coalescence event doesn't occur (Figs. 5.19; 5.21; 5.22f). A large amount of variability in the data is again associated with the manual tracking process, which is preferred due to the dynamic nature of the bubble during coalescence events, and the inability of automated computational or other tracking methods to differentiate between a single and a newly coalesced bubble.

The two slug simulations are illustrated in Figs 5.19 and 5.20, while Fig 5.18 shows stills of the coalescence process. It is not until the slugs are initiated within the interaction length (≈ 5 m) that coalescence occurs. With sufficient distance between the two slugs, outside of the region of greatest volumetric expansion, both slug bases appear to rise at or very near to the theoretical speed (Viana et al. 2003), as is clear in Fig. 5.19a, b, c. As the rising slugs ascend in closer proximity to each other, the expansion of the trailing slug begins to have an influence on the leading slug, due to an increase in base velocity. This is achieved by giving an upward velocity to the magma column, over its stagnant initial conditions. The slug rise speed increase is more pronounced closer to the magma surface (see the last 5 s before burst in Fig. 5.19d) suggesting that slug coalescence will also be more pronounced, closer to the surface, particularly in volcanic regimes.

In Fig. 5.20 the coalescence process of two volcanic slugs is displayed. In the first three seconds of the simulation the model equilibrates (as with all models, see section 3.4). Following this there is a period between 3 and 8 s where the distance between the two rising slugs reduces slightly. At ≈ 8 s this length continues to reduce but at an increased rate, until coalescence occurs. This more rapid increase at ≈ 8 s is accompanied by a rapid increase in slug length from ≈ 9 to 11 m, whereas the leading length remains at ≈ 9 m, indicating that this rapid increase is a result of the coalescence process and not normal expansion. In effect, the trailing slug nose seems to be accelerated (or stretched) into the leading slug (see videos in Appendix D), with little acceleration of the slug base until the trailing slug nose has entered the leading slug base, where the momentum of the slug nose acceleration is passed on to the slug base.

Fig. 5.21 shows three slugs of identical mass, which don't coalesce. Again, this shows that the closer slugs are to each other and the closer they are to the surface, the greater the effect they have on each other. In all cases the distance between the rising slugs noses and bases (the gap lengths) remains constant. The coalescence of the two leading slugs in the three slug regime (see Fig. 5.22a, and b) follows a similar process to that described in the previous paragraph. This also has an effect on the length of the third slug, which oscillates with the changes in magma movement as a result of the coalescence event. The gap between the newly created slug and the originally third slug then returns to the original gap length between the original third slug and the original second slug. Fig. 5.22f shows an example

four slug regime where coalescence doesn't occur. Here as with the three slug regimes, the slugs rise at a slower speed (see Table 5.6 for summary of rise speeds) the further down they are in the conduit. Indeed, through the simulations, a significant observation is the rapidity at which co-current flow becomes a major influence, or at least the slug behaviour associated with it (see Pinto et al. 1998, 2001; Liu et al. 2005).

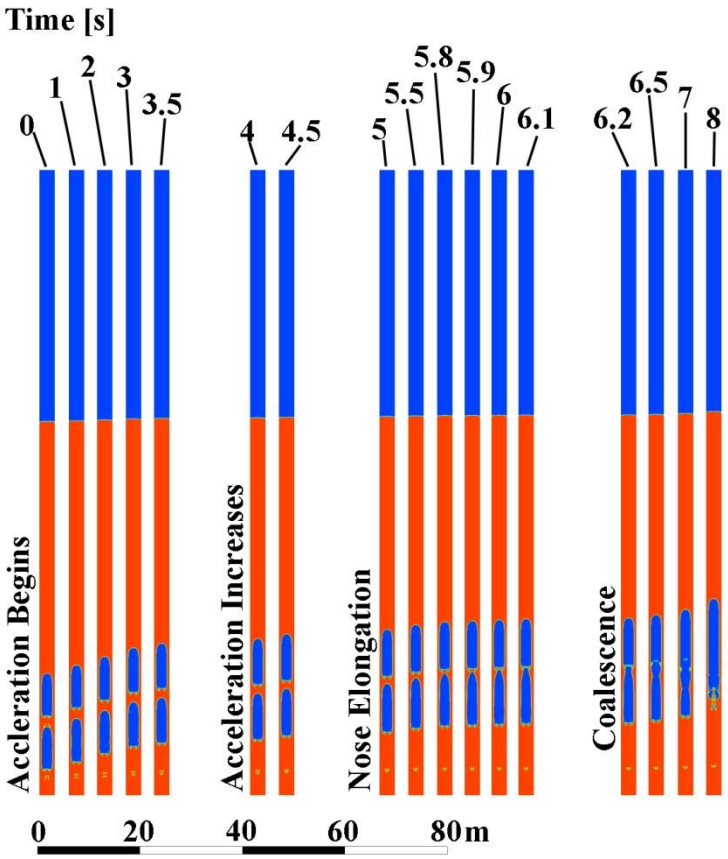

Fig. 5.18: Stills showing the coalescence process of two ascending gas slugs within volcanic regime C7. Here similar features are observed as with Fig. 5.3, slug acceleration increases within the wake area, causing nose elongation and eventual coalescence. The tracks for this slug coalescence can be seen in Fig. 5.20.

Table 5.6: The average rise speeds of the base of all slugs within the computational simulations. The slugs are numbered according to their depth with Slug 1 being the closest to the surface.

Exp #	Slug 1 (m s^{-1})	Slug 2 (m s^{-1})	Slug 3 (m s^{-1})	Slug 4 (m s^{-1})
C1	1.23	N/A	N/A	N/A
C2	1.46	1.24	N/A	N/A
C3	1.50	1.24	N/A	N/A
C4	1.55	1.24	N/A	N/A
C5	1.53	1.24	N/A	N/A
C6	1.75	1.24	N/A	N/A
C7	1.42	1.20	N/A	N/A
C8	1.57	1.36	1.24	N/A
C9	1.65	1.39	1.24	N/A
C10	1.78	1.44	1.23	N/A
C11	1.91	1.51	1.23	N/A
C12	2.20	1.66	1.24	N/A
C13	1.70	1.47	1.34	N/A
C14	1.66	1.44	1.33	1.25
C15	1.76	1.5	1.35	1.23
C16	1.93	1.59	1.37	1.23
C17	2.15	1.75	1.46	1.25
C18	2.63	2.05	1.62	1.26
C19	1.73	1.74	1.66	1.07

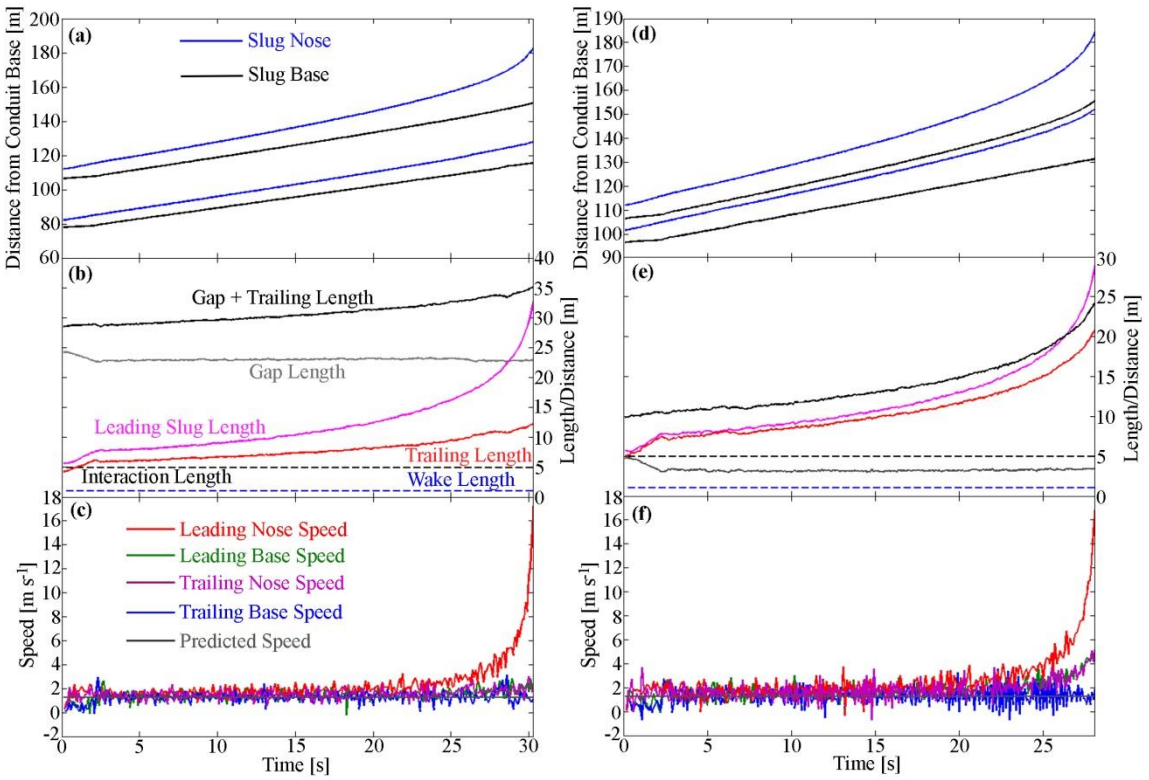

Fig. 5.19: Here, tracks for experiment C2 (left hand side) and C6 (right hand side) are shown. In addition to the speed traces for all slugs (c) and (f), in (b) and (e) plots containing identical information to those in the laboratory regimes demonstrate the distances between slugs, and their relationship with regards to wake length and trailing length. In each computational simulation the gap plus trailing length increases where coalescence isn't observed. The theoretical speed is shown in gray (c, f) for reference.

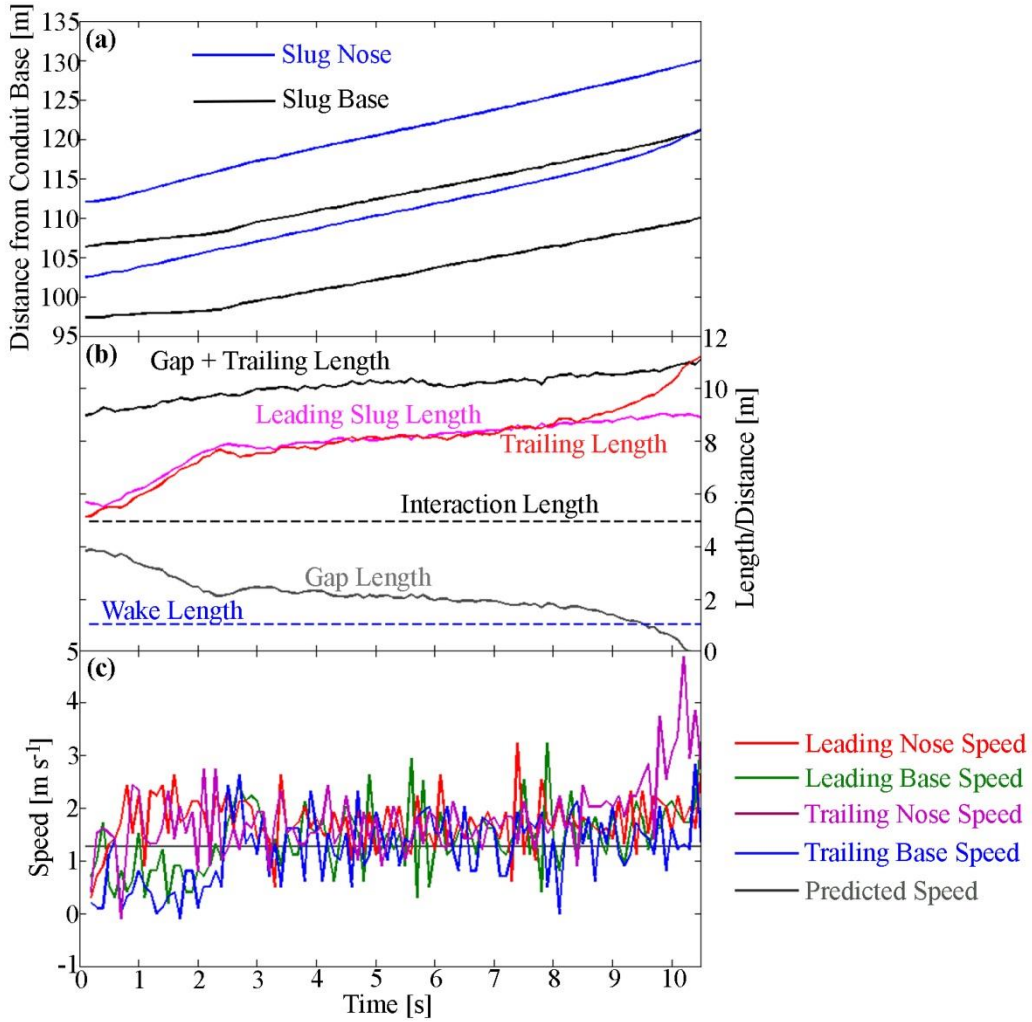

Fig. 5.20: A continuation of Figs. 5.18 and 5.19. Here the first pair of coalescence slugs are analysed. Given that both slugs are of identically mass, it takes model initiation of the two slugs within the interaction length for coalescence to occur. Rapid variability of slug rise speeds is caused by the manual tracking process. Here the trailing length is seen to increase rapidly into the leading slug, suggesting that the trailing slug is stretched into the leading slug. Indeed, the base of the trailing slug (a) seems to accelerate little prior to the point of coalescence. The theoretical speed is shown in gray (c) for reference.

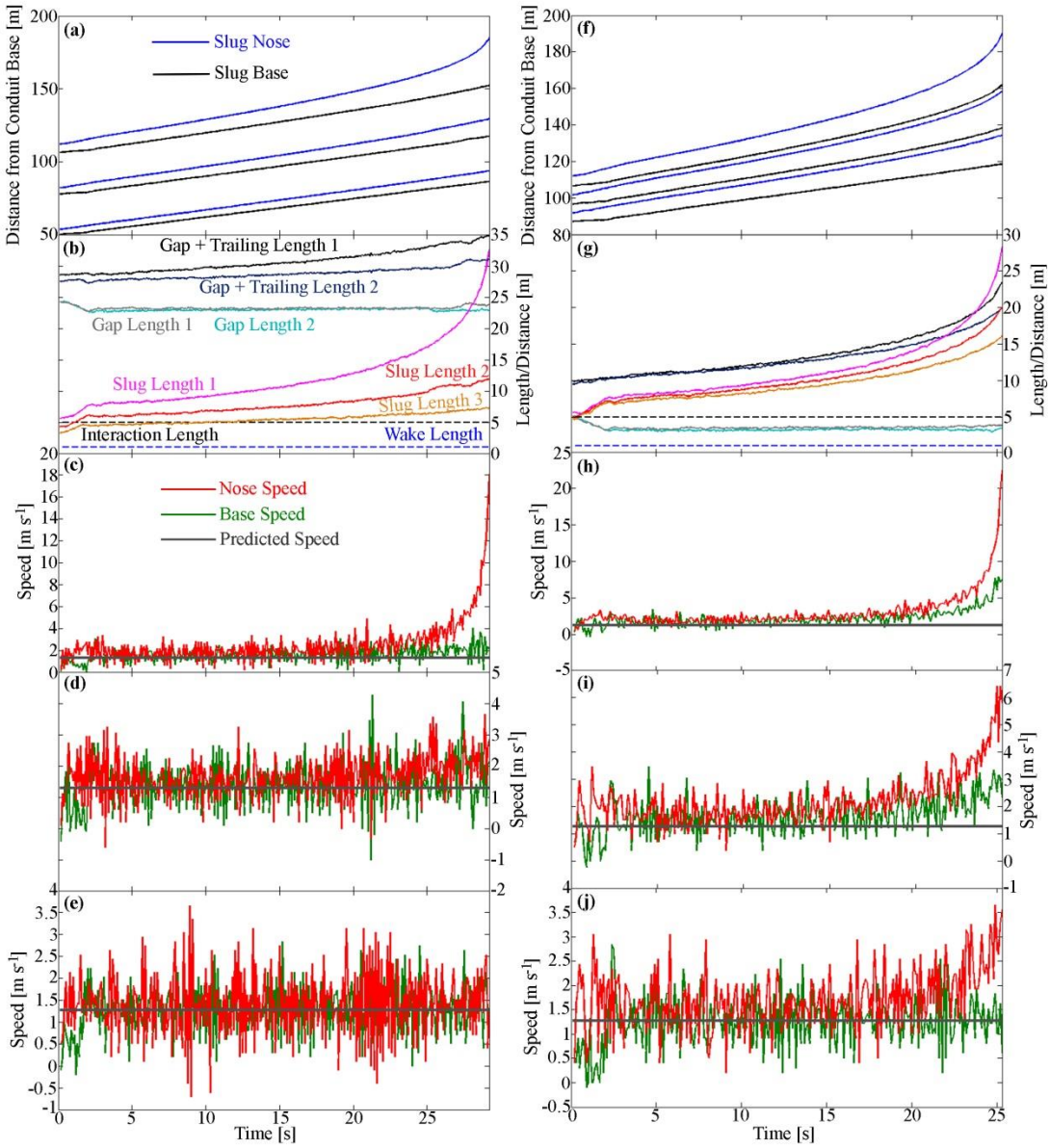

Fig. 5.21: Here, tracks for experiments C9 (left hand column) and C15 (right hand column) are presented, (c), (d), and (e) display the rise speeds of the leading, middle and lower slugs respectively for C9 and (h), (i), and (j) for C15. The closer the slugs are to one another, the greater the effect of slug expansion on rise speed. This is particular clear in (f), where slug expansion appears to push the slug above it at a faster pace. The gap plus trailing length in each instance is observed to increase, indicating that the leading slug is indeed rising at a faster pace than the trailing slug. The theoretical speed is shown in gray (c, d, e ,h, i, j) for reference.

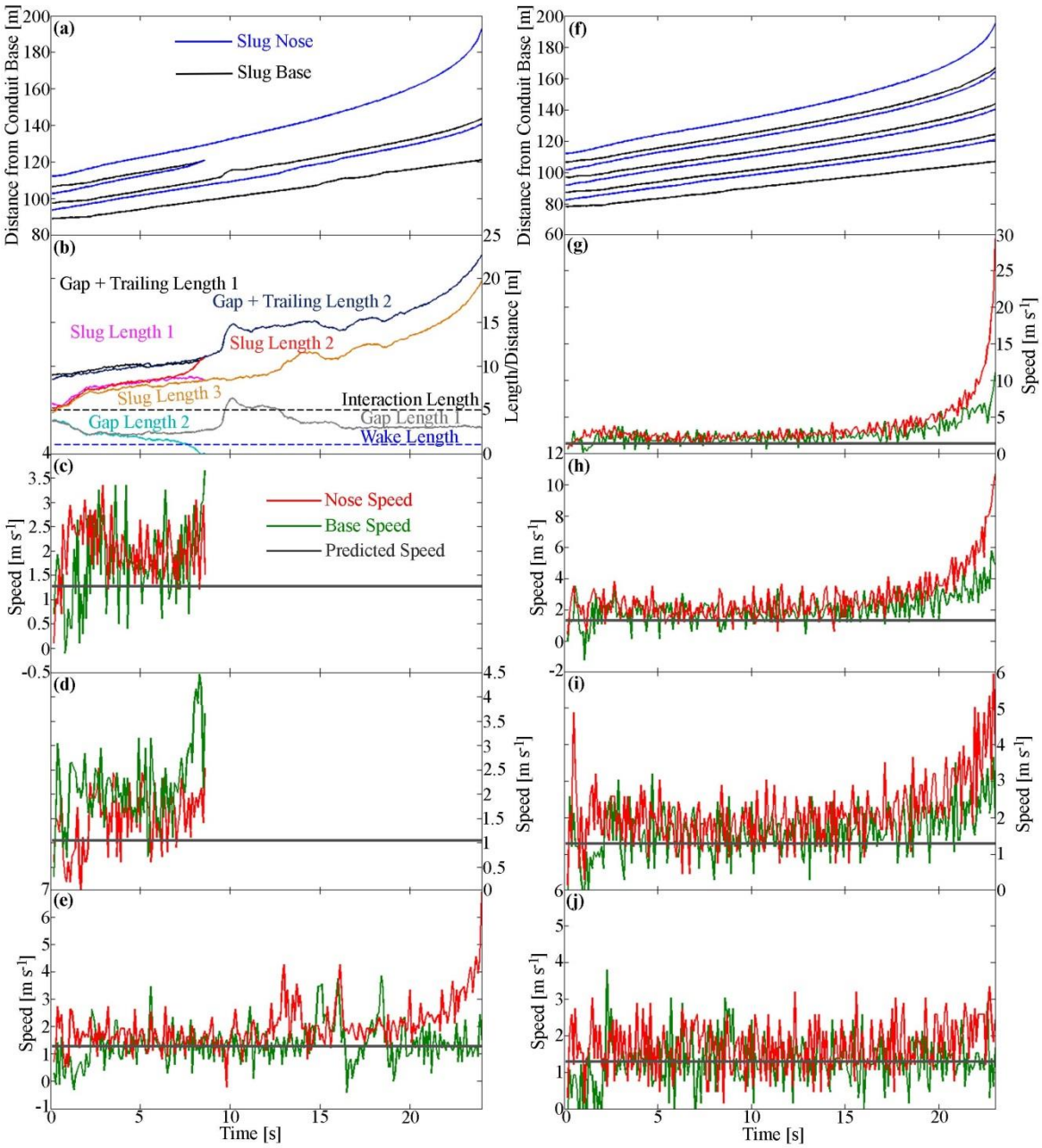

Fig. 5.22: Here, tracks for experiments C13 (left hand column) and C18 (right hand column) are presented. As per Fig. 5.21, (c), (d), and (e) refer to the leading, middle and trailing slug speeds, and speeds for the four slugs are depicted in (g), (h), (i), and (j). For experiment C13 one coalescence event occurs, the middle slug into the upper slug. Following on from this the gap plus trailing length is seen to increase again demonstrating that this can increase even when coalescence occurs. C18 again demonstrates this increase in slug rise speed, influenced by the slug below. The theoretical speed is shown in gray (c, d, e, g, h, i, j) for reference.

5.6. Application of repose theory to Etna Data

By using equations 5.4 and 5.5 to enable determination of bubble/slug volumes the repose gap model can be applied to the collected Etna data during rapid strombolian activity as described in Chapter 4. Here, using parameters appropriate for Etnean magma: density = 2600 kg m^3, viscosity = 2000 Pa s^{-1}, and a conduit radius of 1.5 m, the theoretical repose and transition times can be added to the Etna data. Fig. 5.23 shows that the repose gap relation also characterises this volcanic situation well. Fig. 5.23b demonstrates that there are six bursts which fall below the repose gap boundary. There could be a number of reasons behind this: inappropriate magma or conduit parameters, bursts are inappropriately timestamped due

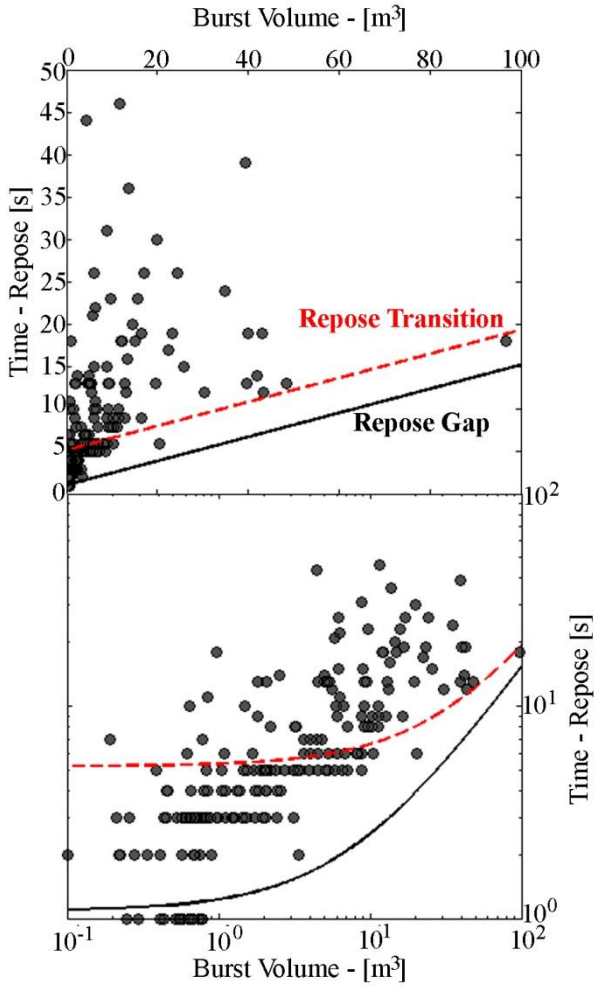

Fig. 5.23: Here, burst data pertaining to data collected during Etnean activity at the Bocca Nuova crater (described in full in Chapter 4) are presented. All data have been converted to burst volumes. Above the data plotted on a normal plot, below the data plotted on a log-log plot. Also added to both plots is the repose gap line (equation 5.4) and the repose transition line (equation 5.5). For a magma density of 2600 kg m^3, viscosity of 2000 Pa s^{-1} and conduit radius 1.5 m these parameters seem to match well with the observed activity, with the exception of a number of bursts less than 1 m^3 in volume.

to limited temporal resolution of the UV camera and the bursts which are of the lowest volumes may not involve slugs.

Fig. 5.24 shows infrasonic data collected from rapid strombolian activity at the base of the NEC on the 17th July 2014. A total of 34,229 events were captured using a seismo-acoustic recorder at a distance of ≈ 5 km (data courtesy of Andrea Cannata, INGV - Osservatorio Etneo). Given that only one recorder was used for the study it is not possible to convert acoustic pressure to bubble volume (e.g. Matoza et al. 2013). However, the relative acoustic pressure and hence burst amplitude from each slug burst should be preserved. Highlighted in

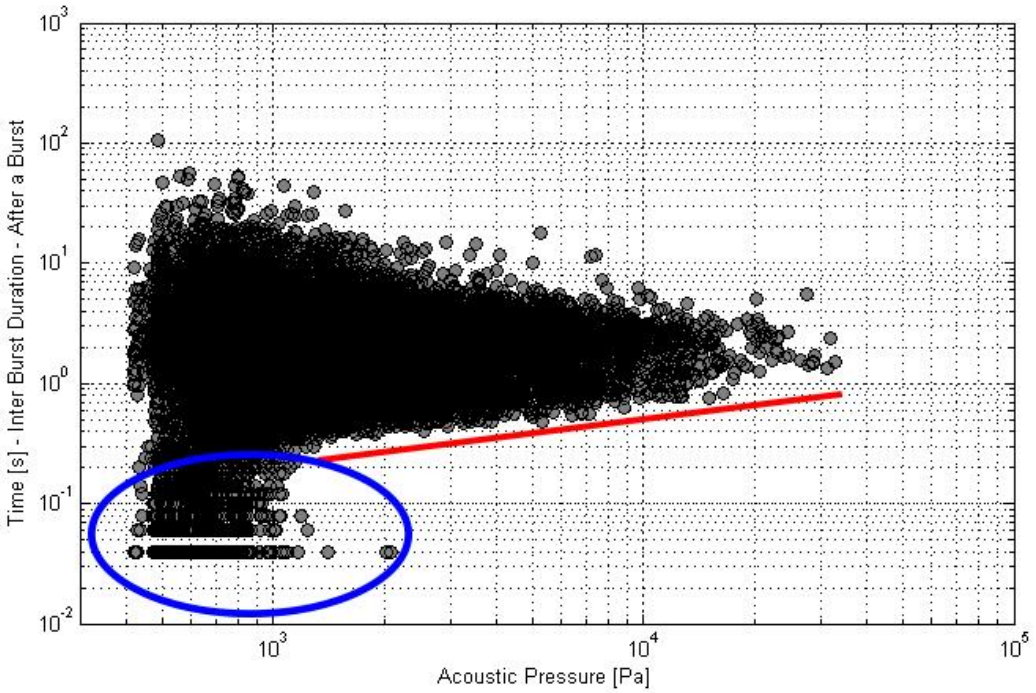

Fig. 5.24: Over 34,000 strombolian events from activity on the NEC on the 17th July 2014, which generated an infrasonic pressure pulse, are plotted here. Two areas of interest are identified, the first red line indicates a repose gap type feature, while the blue circled area appears to indicate an area which may break this feature. It is possible that the red line is related to the repose gap behaviour, while smaller bursts, associated with lower acoustic pressures can disrupt this trend. Data courtesy of Andrea Cannata (INGV, Osservatoria Etneo).

Fig. 5.24 are two areas of importance. The red line highlights a repose gap like feature whereby there is a minimum wait time before another burst can occur. This line effectively stretches from ≈ 0.2 s, at an acoustic pressure of 10^3, to ≈ 1 s. Within the blue circle of Fig. 5.24 there are a number of bursts which would fall below the red line if it was extended. It is possible that the bursts which fall within this zone are not full slugs and can burst at an increased rapidity, perhaps due to a change in burst regime (James et al. 2009). It is equally possible that the rapid nature of the activity could vary the acoustic pressure generated by bursts, which would be expected of a single bursting slug (Matoza et al. 2013).

5.7. Application to Yasur

There is a significant shortage of field data relating to high frequency volcanic slug bursting, specifically with time information attached. One of the exceptions involves data contained within Kremers et al. (2013) for strombolian explosions at Mt. Yasur, Vanuatu. The explosions at Yasur are also thought to be caused by the rise and bursting of gas slugs (e.g. Nabyl et al. 1997; Kremers et al. 2012; Gaudin et al. 2014b). For the purposes of applying the repose relations (equations 5.4 and 5.5) to Yasur, slug lengths contained within Kremers et al. (2013) Tables 2 and 3 are converted to volume (not all data could be used due to a lack of slug length information or events without subsequent time stamps), see Table 5.7 for a summary of bursts used. Here, appropriate parameters for the system at Yasur were used to convert slugs to volume and for application of equations 5.4 and 5.5: magma density 2600 kg m^3, viscosity 1000 Pa s^{-1}, and conduit radius 1.5 m (at the atmospheric standard pressure). The results are displayed in Fig. 5.25. All bursts lie above the repose gap line (black line), with all but one above the transition line (red dashed line), indicating that most bursting slugs have little influence on one another in this case.

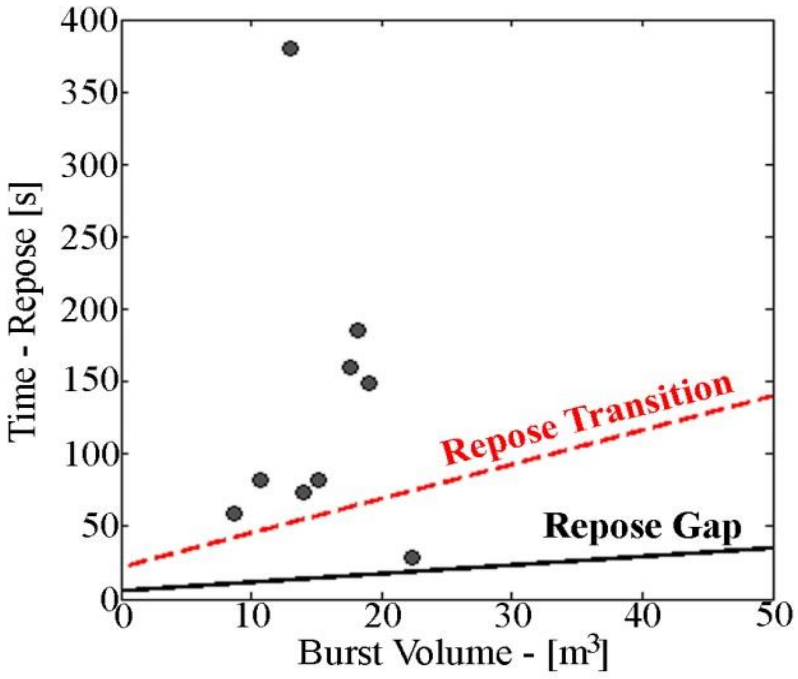

Fig. 5.25: Here, the repose gap and transition equations are applied to data from Kremers et al. (2013) relating to strombolian activity from Yasur volcano. Again the criteria seem to hold up well, given parameters for magma density of 2600 kg m^3, viscosity of 1000 Pa s^{-1} and conduit radius of 1.5 m (this is also the dimension used to convert length data to volume data). Only one burst may have been influenced by those preceding it, while all others can be considered to be "single" bursts.

Table 5.7: A summary of burst data used from Kremers et al. (2013).

Slug Length (m)	Volume (m^3)	Repose (s)
118.5	15.10	82
174.9	22.29	29
138.5	17.65	160
68.6	8.74	59
109.7	13.98	73
149.5	19.05	149
142.1	18.11	185
102.6	13.07	380
83.7	10.67	82

5.8. Discussion

This chapter identified the behaviour of slugs in a volcanic context using laboratory analogues and computational models. This work highlights several important differences between existing studies into slug coalescence in stagnant flow (e.g. Pinto and Campos, 1996), primarily that it is possible for the leading slug to travel at a faster speed than the trailing slug, confirming an observation in Pinto et al. (1998) for co-current flows. However, in these cases Pinto et al. (1998) observe that coalescence *does not* occur, which is contrary to the observations of this chapter, where coalescence is observed on several occasions (see Table 5.2 for slug rise speed values), although Pinto et al. (2001) do state that the bubbles should interact in some way. This is likely due to the increased importance of slug expansion on the observed regimes and has not been explored previously in the literature (Taitel, 1987). It is important to note here, that the literature on slug coalescence, which is quite spartan (e.g., limited to Pinto and Campos, 1996; Pinto et al. 1998, 2001), focuses only on the coalescence of two slugs. Here the focus, particularly in the laboratory regimes, is on the significantly more complex behaviour associated with multiple rising slugs in a continuous regime. Llewellin et al. (2014a) also identified behaviour associated with multiple slugs, however, that study focussed on the formation of much larger slugs via the coalescence mechanism also observed in this study. Llewellin et al. (2014a) suggest that coalescence could be the cause behind the formation of much larger slugs which can cause very large strombolian explosions. The work in this chapter also supports this conclusion.

The discovery of a relationship between gas volume fraction and slug base rise speed is not entirely unexpected. However, the fact that this relationship can be defined is promising (see Fig. 5.8), building on the conclusions of Krishna et al. (1999), who suggest that the value

could be up to six times the theoretical limit. Within this work, the slug bases rise at no more than twice times the theoretical values. Of course, as demonstrated, there will be significant fluctuations caused by the burst of larger slugs at the surface and interacting slugs. The discovery of a relationship between slug length and volume fraction could also be useful in a volcanic setting, providing a way of estimating the length of slugs based on gas emissions. Relationships between slug length and flow regime have been identified previously for horizontal slug flow (e.g. Barnea and Taitel, 1993; Cook and Behnia, 2000). Significantly more work is needed to define these with more accuracy in vertical slug flow.

A brief investigation into the proxy geophysical signals demonstrated a lack of correlation between acoustic pressure generated by slug bursts in the laboratory and slug lengths; the rising slug did not always produce an acoustic pressure trace. Lane et al. (2013) demonstrated that the burst mechanism of the slug (i.e. how the meniscus behaves) plays a key role in the strength of acoustic signals (Matoza et al. 2013; Giancarlo Tamburello, personal communication). With the presence of multiple slugs creating a non-stagnant, potentially co-current liquid, this will effect the way that the bubble overpressurises and bursts (e.g. Krueger, 2005; James et al. 2009; Lane et al. 2013). In addition, in a number of the experiments a foam layer developed, which effected the way the slugs interacted with the liquid-air interface, influencing the results. The increase in base pressure alongside increasingly rapid flow regimes is logical given assumptions on gas flow generating seismicity, particularly in basaltic systems (O'Brien and Bean, 2008). Indeed, much more detailed studies combining seismicity during rapid strombolian activity and gas flux measurements, could begin to confirm this relationship, if present.

The computational work suggests that, with slugs of identical mass, it is incredibly difficult for coalescence to occur, unless the models are initialised within the interaction area. In a novel observation, the gap between a trailing slugs' nose and the leading slugs' base is observed to remain constant (see Figs. 5.19 – 5.22). This has significant implications for the bulk behaviour of slugs in a column of magma, particularly in the upper regions of a conduit, where the slugs rapidly expand, and ascend at much faster rates than those below, perhaps approaching the limits on slug rise speed proposed by Krishna et al. (1999). Within the four slug regime, at the burst time of the leading slug, slug bases were rising at 1.66 – 2.63 m s^{-1}, above the theoretical $\approx$ 1.29 m s^{-1} value. This observation paves the way for further experiments, investigating a range of slug masses and potential interactions with each other. This also ties in with Llewellin et al. (2014a), who suggest that smaller bubbles, which are

not limited by the speed-limit controlled by the conduit width (Viana et al. 2003; Llewellin et al. 2012), are the cause behind slug growth to form larger bubbles. If these two phenomena are combined, they would expedite the explosivity of the manifest strombolian activity.

5.8.1. Repose Gap Discussion

Unfortunately, given the sparsity of data available for high frequency strombolian activity, particularly related to the mass and volume of bubbles there is little possibility to test the developed repose gap relation (equations 5.4 and 5.5). However, the relation does appear to hold well when tested against laboratory and available field data using estimated magmatic and conduit parameters (it also holds for the computational models). From Fig. 5.2 it is clear that some of the regimes contain bubbles which have yet to transition to slugs. even in these situations the relation holds as the factors which cause coalescence, the wake and interaction lengths remain a similar length (Clift et al. 1978). If this relation can be validated in the field using collected data and known magma and conduit parameters then a further degree of certainty could be added beyond that of the controlled conditions within a laboratory. Notwithstanding this, the repose gap relationship could be a valuable tool when applied to rapid basaltic degassing. By observing stable single to multiple slug regimes, it is possible to hone estimates of magma viscosity and conduit radius etc., useful for understanding more about shallow magma pathways and eruption transitioning.

The observations within this chapter, particularly those associated with relationships discovered in the laboratory regimes, allow a further inference to be made concerning the Etnean activity discussed in Chapter 4. There is a lack of a strong correlation between slug mass and repose time (see Fig. 5.23a – the non-log-log plot), which is present with a relatively constant volume fraction. This suggests that the gas supply into the conduit at Etna was highly variable at the time of measurement, playing a key role in both the mass of slugs generated, their interactions with one another, and ultimate explosivity at the surface.

The concepts discovered here could also have value outside of volcanic environments, for example, in oil pipelines, and nuclear reactors (when rapid rod cooling is needed), where slugging is also a major area of study (e.g. Costigan and Whalley, 1997; Masella et al. 1998; and references therein).

5.9. Conclusions

This chapter covers a range of behaviours some previously identified and others not in association with the behaviour of multiple rising slugs in a vertical conduit. In particular, a minimum repose period between rising slugs before another eruption can occur has been mathematically defined (equations 5.4 and 5.5). When tested against laboratory data the relation holds well, with data from Etna (Chapter 4), and Yasur (Kremers et al. 2013) also demonstrating some agreement. The discovery of a statistically strong (> 0.94 R^2) relationship between gas volume fraction and slug rise speed, suggests that, with further work this can be constrained in more detail.

A significant gap in the volcanic and fluid dynamical literature concerning the behaviour of multiple rising and coalescing slugs has been identified and addressed. This has demonstrated that previously developed models for the interaction of two bubbles, specifically where coalescence is involved are lacking in important detail, especially in the slug expansion regimes which were investigated here. For instance it is reported in this these that, even with expansion, volcanic slugs with identical mass will not coalesce and just force the slugs above to rise at a faster speed. Additionally, even where a leading slug base is travelling at a faster speed than a trailing one, coalescence can still occur. In these instances the nose accelerates or stretches into the base of the leading slug.

6. Investigating transitions between different styles of basaltic degassing

This Chapter builds on the research detailed in the previous two Chapters. Here, the development and application of a unifying theory of basaltic degassing is outlined. The work is based on combining the observational results and repose gap model documented in Chapters 4 and 5 with additional models within the volcanic and fluid dynamical literature. This provides unprecedented insights into fluid dynamics within basaltic systems and could provide significant future research potential when combined with additional gas measurements. This is based on work presented at AGU, 2014: *Pering, T. D. McGonigle, A. J. S., James, M.R., Lane, S.J., Capponi, A., Tamburello, G., Aiuppa, A., 2014c. Observations on Multi-Slug Activity – Implications for Volcanic Processes. In: AGU Fall Meeting 2014 San Francisco* and currently in preparation: *Pering, T.D., McGonigle, A.J.S., In Prep. A unifying theory of basaltic degassing.*

6.1. Introduction

Basaltic volcanism is the most common form of volcanic activity both on Earth and in an extra-terrestrial context (Wilson and Head,1981). A key feature of basaltic eruptions, compared with more silicic activity, is the emission of low viscosity magmas ranging: 10^1 – 10^4 Pa s^{-1}(Shaw et al. 1968). This allows bubbles to travel independently of the melt which is an important characteristic of basaltic volcanism (Parfitt, 2004), playing a key role in exsolution and bubble expansion (Sparks, 1978), and in eruption style (Parfitt and Wilson, 1995; Parfitt, 2004). Indeed, of particular interest are the transitions between different styles of activity (Jaupart and Vergniolle, 1988; Parfitt and Wilson, 1994; 1995). However, as the dates of these publications suggests, there has been little recent consideration of this topic, in particular in so far as the full range of explosive and passive styles of activity is concerned. During the past decade or so there has been a concerted focus on specific eruptions styles and the associated degassing styles. This is particularly evident for strombolian (e.g. Blackburn et al. 1974; James et al. 2004, 2008, 2009; Del Bello et al. 2012; 2015; Llewellin et al. 2012, 2013, 2014a; Taddeucci et al. 2012 and references therein) and hawaiian (also referred to as lava fountaining) volcanism (e.g. Parfitt and Wilson, 1995; Elias et al. 1998; Poland et al. 2008; Carbone et al. 2013).

This chapter concerns the development of a model spanning the breadth of basaltic volcanism (excluding the rarer and rather distinct mechanism driving basaltic plinian activity). It draws on the analysis of the previous two chapters, but also upon diverse literature sources to probe the behaviour of bubbles across various flow regimes. Here, Fig. 6.1, reprinted from the introduction to this thesis, highlights the various flow regimes which may exist in a basaltic magma. In particular, transitions between strombolian activity and lava fountaining are of particular interest. This chapter, through the use of theoretically developed models aims to shed light on the driver of lava fountaining. It is clear from the sheer volumes of gas vented during these events, for example the recent Holuhraun fissure activity released ≈ 370 – 1200 kg s^{-1} of SO_2 (Burton et al. 2015b; Galle et al. 2015), that a highly efficient gas flow regime must exist to drive the activity, yet little work has been performed to date to characterise this.

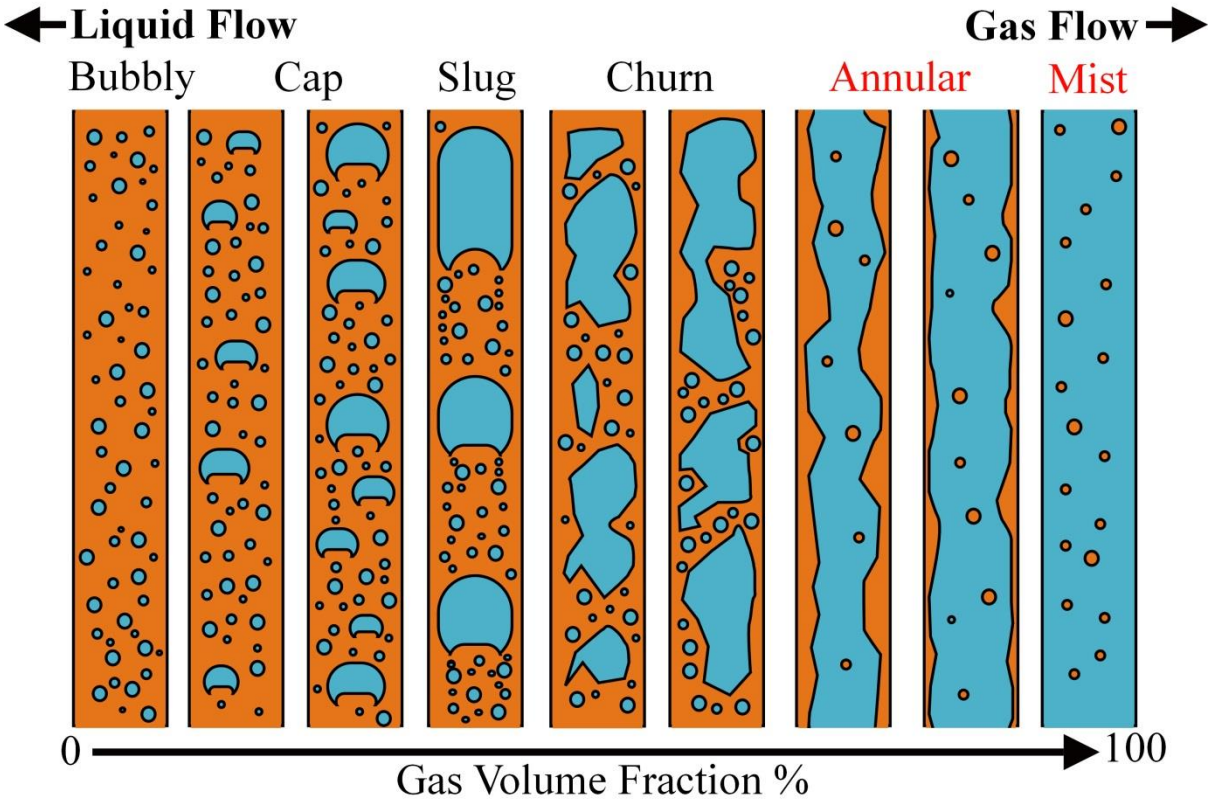

Fig. 6.1: Reproduced from Chapter 1 to illustrate the flow regimes which drive basaltic volcanic activity. The flow regimes highlighted with red text, particularly mist flow, indicate flow regimes with no direct field analogue evidence or quantification.

6.2. Developing a unifying theory applicable to basaltic degassing

There are two distinct aspects to this theory to enable characterisation of demarcations between the range of potential basaltic degassing models. The first component (section 6.2.1)

applies the discovered and tested repose gap relationship from Chapter 5, with existing slug models and studies into bubble dynamics (e.g. Clift et al. 1978; Campos and Guedes de Carvalho, 1988; Viana et al. 2003; Noguiera et al. 2006; James et al. 2009; Suckale et al. 2010b; James et al. 2011; Llewellin et al. 2012), in a bid to combine magmatic and gaseous parameters with a view to predicting the style of activity at certain thresholds. This is applied dimensionally, although it can easily be converted to non-dimensional parameters, i.e. with the former being particularly relevant on a specific volcano-by-volcano basis and the latter useful for comparing across volcanic systems. This first model is specifically related to the delay between events (i.e. connected to the repose gap behaviour of Chapter 4 and section 5.3.3) and the length of slugs or bubbles. This is limited to stable bubbles only and only considers sub lava fountaining styles of activity (i.e. passive through to rapid strombolian activity).

The second (section 6.2.2) is specifically related to gas volume fraction, which also builds on the behaviour and relationships detailed in Chapter 5. This model uses the gas volume fraction relationships in combination with the repose gap, to highlight the style of activity likely to dominate in particular regimes, including potential transitioning to hawaiian type activity, the pinnacle of common basaltic activities.

By combining all of these models one can begin to understand how, when and why volcanoes transition to different styles of activity, and to understand the fluid dynamics inherent at the sub-surface. In the following sections the development (section 6.2.1 and 6.2.2) and application of the theory to real systems (section 6.3) is outlined. For the purposes of clarity a number of previously listed equations are reprinted here (including symbol definitions). However, for a full outline and description, the reader is referred to the original listing of the equation.

6.2.1. Developing a unifying theory applicable to bubble lengths

In this model it is reasonably assumed that as bubble length $\rightarrow \infty$ burst frequency must increase. This premise is then backed up by our defined criteria. A stagnant or near-stagnant magma is also assumed. This initial section is accompanied by an annotated model (Fig. 6.2), which clearly outlines the areas discussed, with arbitrary x and y axes. As per section 5.3.3,

the repose gap line (Rep_{min}) defines an area where, theoretically, no burst should be present. This can be directly applied to the combined model:

$$Rep_{min} = \frac{L+L_{wake}}{u_{sl}}. \qquad \textbf{(Eq. 6.1)}$$

In addition the $Rep_{transition}$ can also be applied:

$$Rep_{transition} = \frac{L+L_{min}}{u_{sl}}. \qquad \textbf{(Eq. 6.2)}$$

In these two equations, the L parameter can be applied to a set of arbitrary slug lengths to obtain both Rep_{min} and $Rep\ _{transition}$ temporal values. All slugs which lie above the repose line but below the transition line will behave as though they are in a multi-slug environment (Fig. 6.2e). All slugs above the transition line will behave as though they are in a single slug environment (Fig. 6.2c and 6.2d).

The P^*_{slim} value is a dimensional measure of burst vigour, where a value of ≥ 1 equates to a vigorous explosive eruption, while values of < 1 correspond to passive degassing (James et al. 2009). This can therefore be applied to our model, whereby: $A' = 1 - (\frac{r_s}{r_c})^2$, L_0 is the same set of arbitrary slug lengths used in equations 6.1 and 6.2, P_0 is an initial pressure condition, and P_{surf} is atmospheric pressure at the surface. Reprinted in the equations original form from James et al. (2009), this can be expressed as:

$$P^*_{slim} = \frac{\sqrt{\rho g A\prime L_0 P_0}}{P_{surf}}. \qquad \textbf{(Eq. 6.3)}$$

However, this equation is not directly applicable to the model developed here. To enable the application of 6.3 here I first reasonably assume that P_0 is equal to surface pressure (i.e. the model is specifically applicable to the bursting of bubbles at the surface). The important parameter under investigation is the ability of P^*_{slim} to predict burst vigour, which is intuitively related to final gas mass (i.e. not to some initial condition at depth). Equation 6.3 can be recast, as follows, therefore:

$$P^*_{slim}(L_0) = \frac{\sqrt{\rho g A\prime L_0 P_{surf}}}{P_{surf}}. \qquad \textbf{(Eq. 6.4)}$$

The generated data will give a range of values indicating the potential for explosivity. Here, the point of interest is where $P^*_{slim} < 1$, indicating non-explosive behaviour. Applying this to

the range of arbitrary bubble/slug lengths which satisfy slug criteria (i.e. those with lengths above the width of the conduit) and plotting it against the results of equation 6.2 (the repose transition line for defining single slug behaviour), this line will fall on the same trend as the single slug line (Fig. 6.2c). Hence, all slugs of these lengths which burst above the line will do so without explosions. These slugs will have lower masses and are therefore likely associated with puffing events such as those manifested at Stromboli (Ripepe et al. 2002; Taddeucci et al. 2012; Tamburello et al. 2012). This area is therefore assigned as corresponding to puffing behaviour. The slugs which burst above the transition line with a $P^*_{slim} > 1$ will be explosive; this area is therefore termed explosive strombolian (Fig. 6.2d).

Following this there are two further important definitions included in the model: under what conditions precisely can a bubble be considered a slug, and when does a bubble behave spherically. Clearly in a stagnant magma a perfectly spherical bubble will not produce an explosion and will likely be released passively at the surface. Indeed, if a basaltic magma cannot efficiently degas, this could lead to lava effusion (Harris et al. 2007), and numerous studies of lava show sufficiently small bubble radii for this to be the case (Herd and Pinkerton, 1997). Consistently throughout this thesis a bubble is considered to be a slug when its length exceeds the diameter of the conduit, up to its minimum film thickness. This is applied as a straight line on the model, termed the non-slug line (see Fig. 6.2b). To the right of this line a bubble is a slug (and is part of the puffing area – Fig. 6.2b or the rapid strombolian area – Fig. 6.2e) and to the left of the line a bubble ceases to be slug. At (g) in Fig. 6.2 the frequency that bubbles can bursts in succession will increase.

A bubble will begin behaving in a spherical manner at $Re_b < 0.3$ (the Reynolds bubble number). Here, the adapted bubble Reynolds number for non-slug flow is used (James et al. 2013):

$$Re_b = \frac{2\rho_m u_b r_b}{\mu} \qquad \textbf{(Eq. 6.5)}$$

where $r_b$is the bubble radius which is equal to $l_{arb}/2$ (arbitrary lengths used in all equations), and where u is the bubble rise speed according to Stokes law:

$$u_b = \frac{2(\rho_m - \rho_g) g {r_b}^2}{\mu} \qquad \textbf{(Eq. 6.6)}$$

where ρ_m and ρ_g are the magma and gas density respectively. The length at which a bubble stops behaving spherical is easily found. This is then applied to the model (see Fig. 6.2a). At (h) in Fig. 6.2 the frequency of bubble bursts will increase again.

The work of Suckale et al. (2010b) suggested that there is a maximum possible bubble radius for a given magma viscosity and density (Bellman and Pennington, 1954; Plesset and Whipple, 1974; Clift et al. 1978; Grace et al. 1978). These values are reproduced in Table 6.1 from James et al. (2011). When a bubble exceeds this radius, slug driven activity will cease to be possible as can be calculated using:

$$a_{cr} = 2\sqrt{\frac{\sigma}{g\Delta\rho}} \qquad \textbf{(Eq. 6.7)}$$

where a_{cr} is the maximum bubble radius. For example, for a magma viscosity of 100 Pa s^{-1} (towards the lower range of basaltic magmas) and a magma density of 2600 kg m^3, this suggests a maximum conduit radius of ≈ 1.3 m (Suckale et al. 2010b; James et al. 2011), when taking into account slug film thickness (Llewellin et al. 2012). On increasing the magma viscosity, the maximum stable bubble radius increases and hence so does the width of a conduit which can carry stable basaltic slug-driven activity. The accompanying code used to generate this model is detailed within Appendix E.

Table 6.1: Taken from Table 1 in James et al. (2011), based on the original Table 1 in Suckale et al. (2010b). These values show the maximum stable bubble radii for given magma density and viscosity values.

	Maximum Bubble Radius	
Magma Viscosity (Pa s^{-1})	**Density 3500 kg m^3**	**Density 2600 kg m^3**
10	0.11	0.13
25	0.19	0.23
50	0.30	0.37
75	0.39	0.48
100	0.48	0.58
250	0.88	1.07
500	1.39	1.70
750	1.82	2.22
1000	2.20	2.70

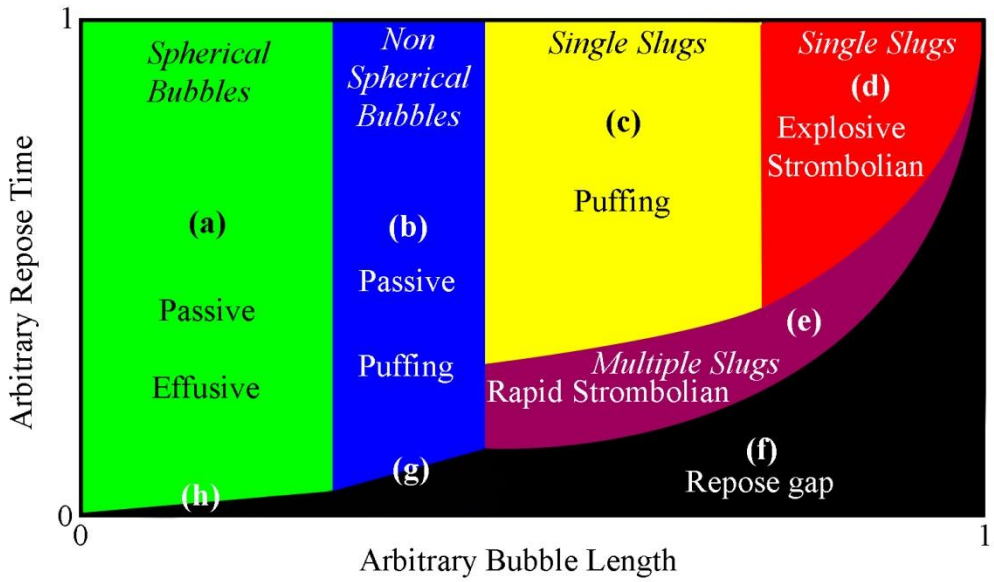

Fig. 6.2: Idealised bubble length model indicating the areas which are defined by the equations 6.1 to 6.6 in the text. In (a) a passive or effusive area where bubbles are near to spherical. In (b) bubbles sized between spherical transition and before a bubble becomes a slug. In (c) an area defined using equation 6.4 which indicates the burst of slugs in a non-explosive manner – i.e. puffing. In (d) all slugs with lengths above the puffing area in (c) will be explosive, while in (e) slug bursts occur so rapidly that they can begin to interact, the rapid strombolian area. The repose gap, where no bursts can occur is shown in (f). In (g) and (h) it is assumed that as bubbles get smaller they can burst more rapidly.

6.2.2. Developing a unifying theory applicable to gas volume fraction

The concepts described in the last Chapter and section 6.2.1 can now be applied to a model which includes gas volume fraction on the x axis instead of bubble length, potentially a more accessible parameter for volcanologists to use. This also allows the inclusion of lava fountaining activity and transitions towards and away from this. This model draws on material from the previous chapter, particularly pertaining to the discovered relationships between gas volume fraction, the linear gradient of an idealised multi-slug system, and slug length. This model draws on aspects already defined in the previous model, including: the repose gap (equation 6.1), the repose transition (equation 6.2), and explosive transition (equations 6.3 and 6.4) areas.

To initialise this model, one additional parameter is required: conduit length. Conduit length is needed to allow conversion of the model to gas volume fraction. Given that the model is specifically tailored to differing flow regimes, this is ideally the length of the conduit feeding the surface (alternatively the exsolution depth of the dominant volatile could be used, e.g.

Jaupart and Vergniolle [1989]). For example, this allows for the conversion of slug length to overall conduit gas volume fraction. Whilst there is a resident gaseous component within the melt, here, the focus is only on the decoupled gaseous phase, which is rising independently of the magma. This allows the repose gap and explosive transition relations to be converted to volume fraction, by dividing slug lengths by the conduit length. The passive and puffing area (see Fig. 6.5) is defined as everything below the explosive transition slug length as defined in equations 6.3 and 6.4. Using the relationship between slug length and gas volume fraction from section 5.3.2, a series of expected slug lengths based on volume fractions between 0 – 100 % can be derived. This is achieved by converting the following equation:

$$y = 0.0096e^{5.19x}, \qquad \textbf{(Eq. 6.8)}$$

to a slug length based on the conduit length (in the lab) and volume fraction:

$$\frac{L}{1.8} = 0.0096e^{5.19gvf}. \qquad \textbf{(Eq. 6.9)}$$

This is the first such suggested relationship based on overall gas volume fraction, instead of conduit length for vertical conduits (e.g. Fernandes et al. 1983; Dukler et al. 1985; Taitel et al. 1987, van Hout and Shemer, 2001). The slug lengths calculated using equation 6.9 can then be converted to volume fraction. These lengths (and equivalent volume fractions) can then be used in the repose gap and transition relations (equations 6.1 and 6.2). Fig. 5.8 and section 5.3.2 demonstrated that there is a general relationship between the gas volume fraction and rise speed of the base of a slug:

$$y = 0.245x + 0.102, \qquad \textbf{(Eq. 6.10)}$$

which can be converted based on the theoretical slug speed (u_{th}) and the slug base rise speed in the lab (0.1537 m s^{-1}) to an equation which will apply in a volcanic situation:

$$\frac{u_{sl}}{0.1537} = (0.245\text{gvf} + 0.102) \times u_{th}. \qquad \textbf{(Eq. 6.11)}$$

These speeds are used in equations 6.1 and 6.2 to produce the repose gap and transition lines. The next important definition is the transition between rapid strombolian activity and lava fountaining.

The transition will begin to occur around the maximum suggested length of slugs in vertical flows, which is suggested to be ≈ 25 times the conduit diameter (Moissis and Griffith, 1962; Fitremann, 1977; Fernandes, 1981; Fréhou, 1986; Fabre and Line, 1992). The volume

fraction at which this will occur can then be derived based on the slug lengths determined with equation 6.9, which will vary with conduit lengths input into the model. Fig. 6.3 shows the results of this process for a variety of conduit lengths. It shows that as conduit length increases the activity will transition towards lava fountaining at smaller gas volume fractions. The same is achieved by decreasing the conduit radius. At these volume fractions, which will be termed the critical volume fraction (*CVF*), the repose time between individual events can begin to decrease, with events falling below the repose gap area. This area is illustrated on Fig. 6.5 and can be termed as transitional and progressing towards a lava fountaining regime.

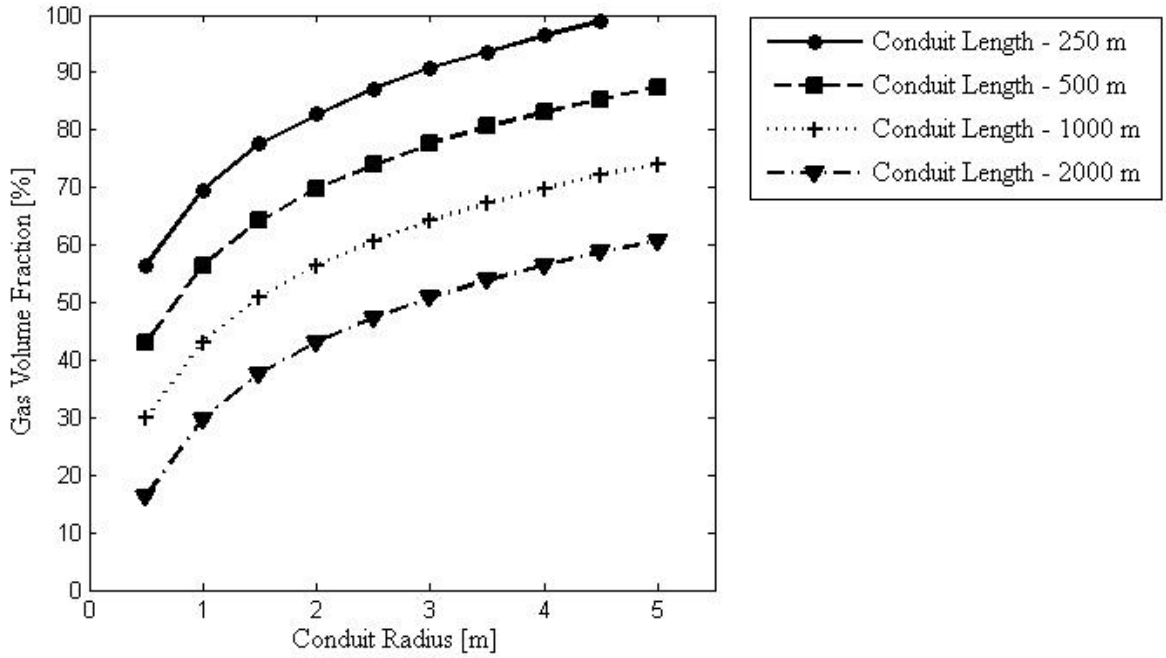

Fig. 6.3: Critical volume fractions (*CVF*), for a range of conduit radii, conduit lengths, and gas volume fractions. This demonstrates that by increasing the conduit length the *CVF* for transitioning towards lava fountaining decreases, while decreasing the conduit radius achieves the same result.

During lava fountaining episodes, which can last from minutes to months (e.g. Allard et al. 2005; Ganci et al. 2012), the fountain height is not constant (Parfitt et al. 1995) and discrete pulses can be observed (e.g. Witt and Walter, 2015). It is the time delay between the arrival of these pulses at the vent exit that is of interest here, i.e. each pulse represents the ascent and burst of a discrete but deformed bubble.

The final transition occurs when the individual pulse events are spaced closely enough to permit full lava fountaining activity. This transition represents a flow regime transition to churn or annular flow. It is possible to calculate the gas speed at which transition to churn and annular flow will occur (Hinze, 1955; Pushkin and Sorokin, 1959; Turner et al. 1969; Taitel

et al. 1980). The following equation taken from Taitel et al. (1980) equation 27, defines the transition between slug flow and churn flow:

$$\frac{l_E}{D} = 40.6\left(\frac{U_m}{\sqrt{gD}} + 0.22\right) \qquad \textbf{(Eq. 6.12)}$$

where, u_m is the combined rise speed of the liquid and gas, which in this case is taken as broadly representative of the gas rise speed during lava fountaining (i.e. the gas and magma are essentially moving in concert in this regime). l_E is the entry length of the bubble or slug which is taken here to be the length of a bubble at the *CVF*. Fig. 6.4a shows the example churn transition speed for a range of conduit diameters and slug lengths. The following equation, also taken from Taitel et al. (1980), equation 32, defines the point of transition to annular flow from churn flow, in this case, directly in terms of gas rise speed:

$$\frac{U_{gs}\rho_g^{\frac{1}{2}}}{[\sigma g(\rho_l - \rho_g)]^{\frac{1}{4}}} = 3.1 \qquad \textbf{(Eq. 6.13)}$$

where equation 6.13 is solved for U_{gs} the gas rise speed. This equation can be solved for different liquid densities (ρ_l), assuming a constant gas density (1.22 kg m^3) and surface tension of 0.4 N m^2. Fig. 6.4b shows the results for a range of appropriate magma densities. The calculated gas rise speeds are then used in equation 6.1 (using the transitional slug length and the original wake length together as a proxy for where bubbles may or may not interact) to determine the time delay below which activity may transition towards churn or annular flow. The final transition to lava fountaining will occur when the repose period between

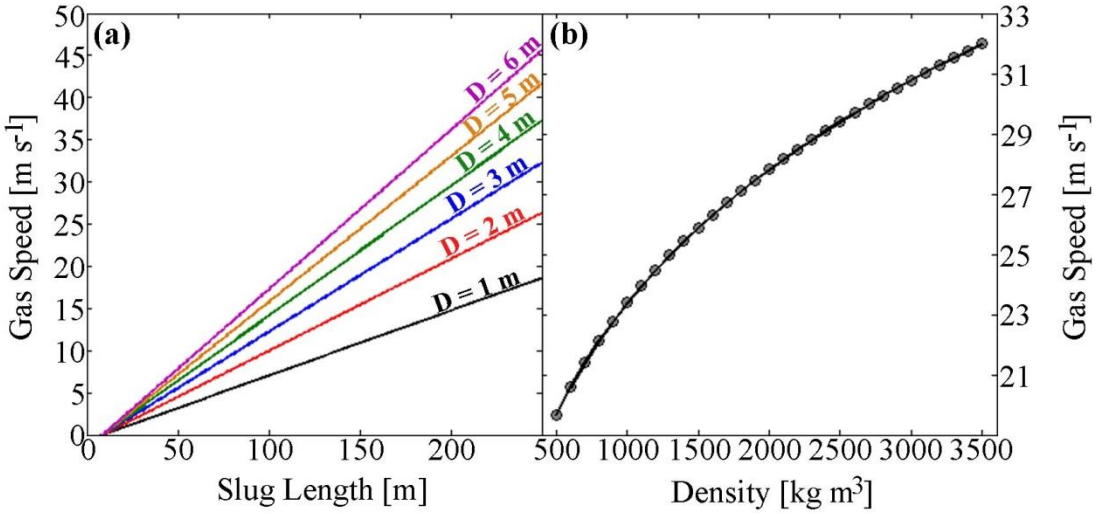

Fig. 6.4: In (a) the gas transition speeds to churn flow are displayed for a range of slug lengths and conduit diameters (D). These are calculated using equation 6.12. In (b) the gas at which transition speed to annular flow occurs is displayed for a range of magma densities. These speeds were calculated with equation 6.13.

events drops below this threshold. Both equation 6.12 and 6.13 suggest different speeds for the transition to lava fountaining. In some instances the churn transition speed is higher than the annular transition speed. The lower of the two speeds is used as the transition speed when applied to equation 6.1 (the lower speed is chosen, for the moment, given our current lack of knowledge surrounding potential flow regime, churn or annular, which drives fountaining). Fig. 6.5 shows an idealised and exaggerated model based on the definitions described in this section. Also included in this idealised model is a grey shaded area which is labelled as improbable terrestrially. In this area, the gas volume fraction would be insensibly high for terrestrial eruptions, particularly for lava fountaining. See Appendix E for Excel spreadsheet used to generate the gas volume fraction model.

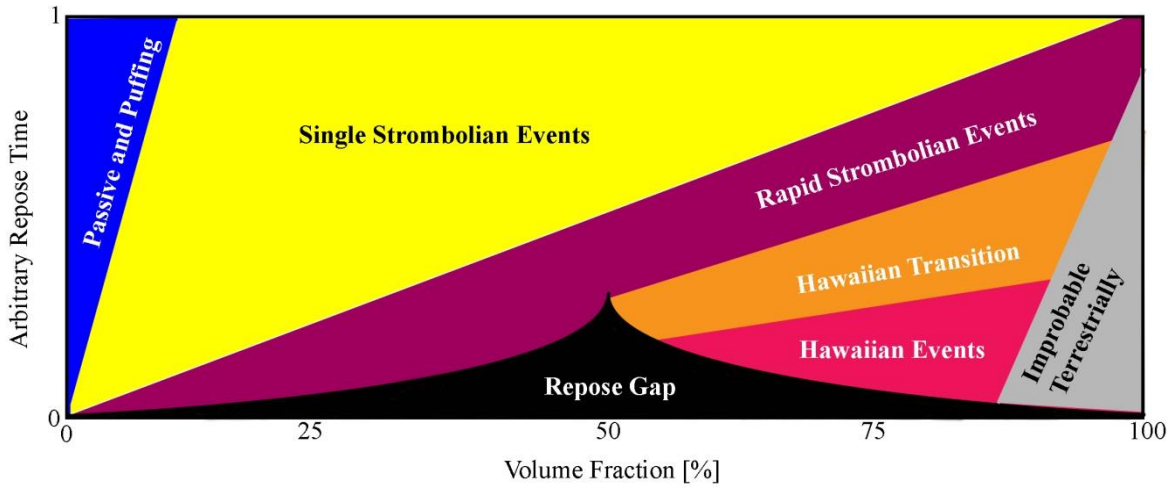

Fig. 6.5: Demonstrating the idealised volume fraction model. Here the colours represent the different areas which the model defines, similar to the areas in Fig. 6.2. The blue passive and puffing area refers to all single bubbles and slugs which do not burst explosively. The yellow area represents all slugs which burst as though they are in a single slug regime, and the purple area those in a rapid environment. The orange and pink areas show the volume fractions and repose times where activity can be assumed to transition towards hawaiian lava fountaining activity. At the same time the repose gap area reduces allowing individual bubbles or pulses to burst more rapidly. Also shown on this plot is a grey shaded area where only non-terrestrial activity could exist on the plot.

6.3. Applying the unifying theory to understand basaltic systems

This section briefly summarises, in graphical form, the results of the models described in sections 6.2.1 and 6.2.2, similar to the idealised models displayed in Figs. 6.2 and 6.5. Fig. 6.6 shows an example bubble length model (section 6.2.1) using appropriate parameters for Stromboli (density = 2700 kg m^3, viscosity = 300 Pa s^{-1}, radius = 1.5 m). Also plotted on Fig.

6.6 are total slug mass values converted to slug length from Tamburello et al. (2012) and Chapter 3. Given that the time delay between events is unknown nor is day to day variation in this, typical values for activity at Stromboli were used (e.g. Ripepe et al. 2002). The results demonstrate that the developed model characterises well the variations between the different types of events. For strombolian activity, all of the events defined in Chapter 3 (with explosion masses ranging ≈ 428 to 5,360 kg, mean of 2,072 kg) fit well within the explosive area, above the repose gap, and also above the rapid strombolian region. For the Tamburello et al. (2012) explosion data (massed ≈ 50 to 1,310 kg) the mean and upper values are within the explosive area, while the minimum is within the "puffing" area. Hornito events from Chapter 3 fall within the puffing area, with the smallest events likely not being of slug form. More rapid puffing events which occurred with repose periods of ≈ 0.5 – 2 s (of mass ≈ 0.6 to 9 kg), here plotted with a repose of ≈ 2 s, and which have been associated with the bursting of decimetre sized bubbles (Ripepe and Gordeev, 1999; Tamburello et al. 2012), fit within the rapid puffing area. The largest mass events fall within the repose gap area. If the repose is reduced to 0.5 s all events are within the repose area, suggesting that the events here may be more applicable to different parameters, particularly a smaller conduit radius.

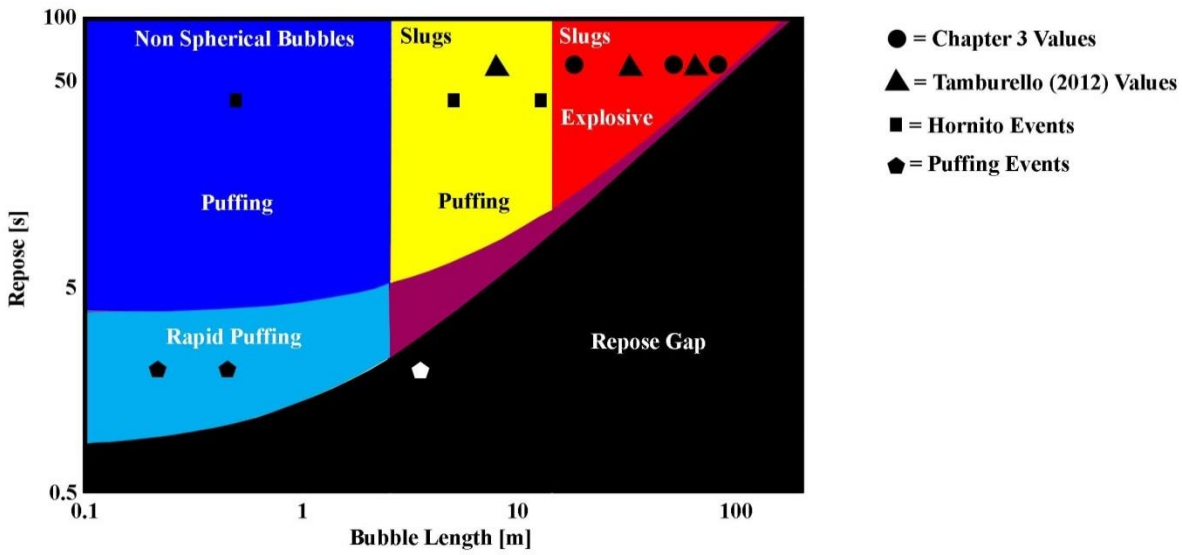

Fig. 6.6 The bubble length model applied to data from Stromboli demonstrating that the model works well for activity at Stromboli. Data for slug lengths were taken from Tamburello et al. (2012) and Chapter 3.

Fig 6.7 and 6.8 show a further series of example repose plots for the bubble length model (section 6.2.1) over a range of basaltic parameters. In Figs. 6.7a and b, a constant conduit radius of 0.5 m and magma density of 2600 kg m^3, are applied with magma viscosities of 100 Pa s^{-1} (Fig. 6.7a) and 2000 Pa s^{-1} (Fig. 6.7b). With the higher magma viscosities the repose

area is larger, with explosive activity with a minimum repose period of ≈ 50 s in comparison to ≈ 8 s at the lower viscosity. In essence, in the lower viscosity magma there is a quicker transition to explosive activity. Fig. 6.8a shows a low density magma of 900 kg m^3 (e.g., in the region that estimated for Kilauea by Carbone et al. [2013]) estimated a low density magma for the lava lake at Kilauea), a mid-range viscosity of 1000 Pa s^{-1}, and conduit radius of 2 m. Fig. 6.8b shows the same magma viscosity, but with a larger magma density and conduit radius of 2600 kg m^3 and 3 m, respectively. In this case, explosive activity in the lower density magma is more difficult to realise without larger slugs of ≈ >50 m in contrast to the smaller conduits of Fig. 6.7. By increasing the conduit radius and the magma density, explosive activity can begin at bubble lengths of ≈ 30 m, and slug bursting can occur more frequently.

Fig. 6.9 and 6.10 show example model outputs for the volume fraction model of section 6.2.2. With a small conduit length of 250 m, lava fountain transitioning only occurs with gas volume fractions of > 90% (Fig. 6.9a). Increasing the conduit length to 2000 m and decreasing the viscosity also decreases the volume fraction at which lava fountain transitioning can occur (volume fraction of ≈ 52%). While lava fountaining activity proper occurs above volume fractions of 60%, but only at very short periods between waves of ≈ 1 – 5 s. In Fig. 6.10 the model is presented using a log scale for repose on the y axis. Both of these plots have a conduit length of 500 m. A large conduit radius of 3 m and low density of 900 kg m^3 mean a much higher gas volume fraction of ≈ 78% is required for transition, with fully fledged lava fountaining occurring at maximum repose times of ≈ 8 to 14 s (Fig. 6.10a). By decreasing the conduit radius to 0.5 m the transition volume fraction drops to ≈ 43%. In addition, for stable single strombolian events, at high gas volume fractions, bursts must occur at repose periods of ≈ 75 s at a volume fraction of 50%, and ≈ 500 s for volume fractions of > 90%. The areas defining rapid strombolian activity, passive degassing, and puffing are often the smallest area of all plots. However, by decreasing the conduit length and conduit radius the passive and puffing areas are increased.

Finally Fig. 6.11 shows the volume fraction model for three planetary scenarios: Io (Fig. 6.11a), Mars (Fig. 6.11b), and Venus (Fig. 6.11c). It should be noted here that these only represent one typical or probable set of example parameters for each planet/moon. For Io (Fig. 6.11a) the *CVF* is around 58%, and with the low associated gravity and atmospheric pressure there is a quick transition to explosive activity, which is already known to be a strong control on the large observed eruptive plumes (Davies, 2007). The parameters for Io

were taken from Davies (2007). For Mars and Venus the *CVF*s are similar at ≈ 52%, however the time period associated with transitions to lava fountaining activity are halved for Venus in comparison to Mars.

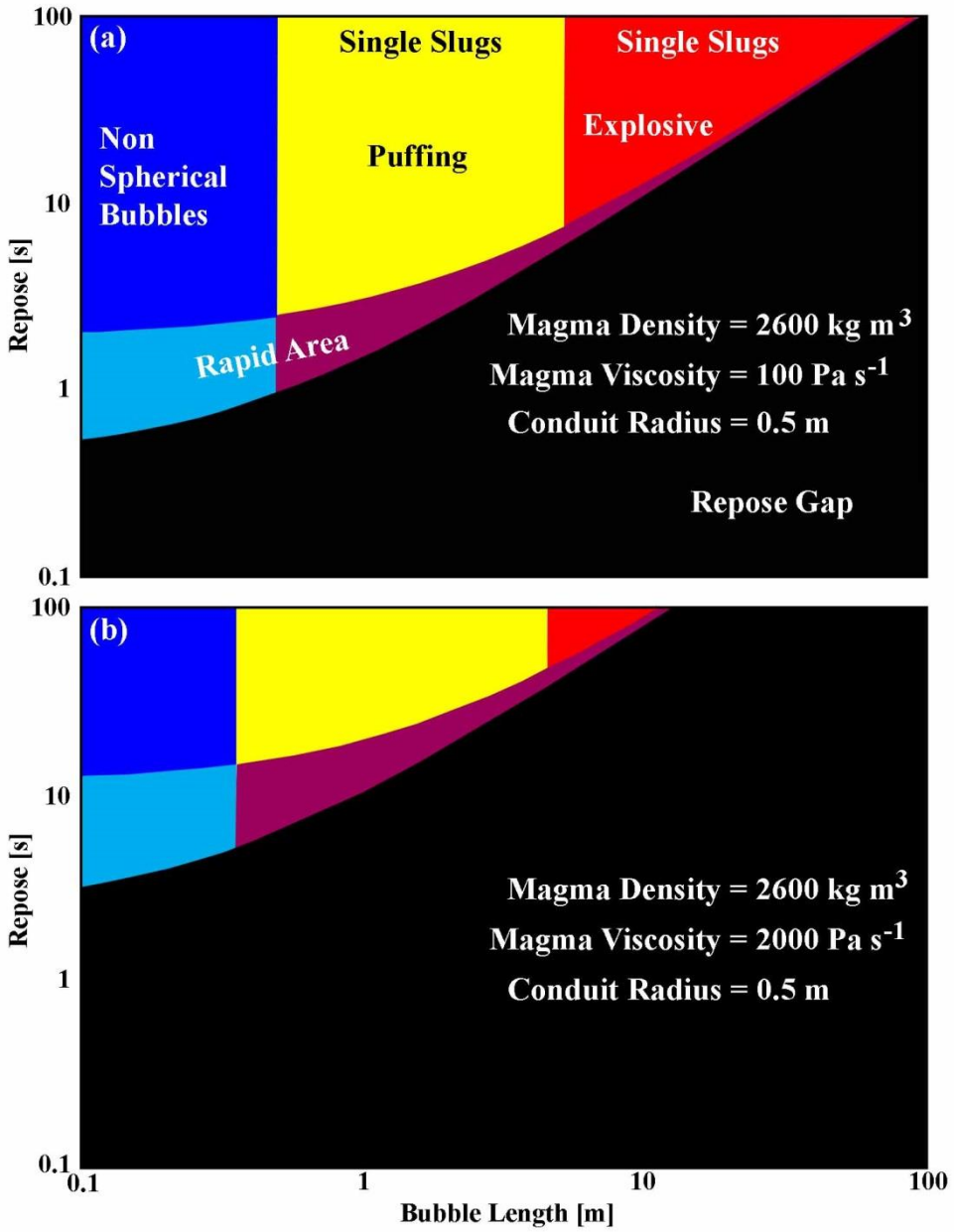

Fig. 6.7: Example bubble length models with two different sets of parameters (a) and (b), where the viscosity is higher in (b).

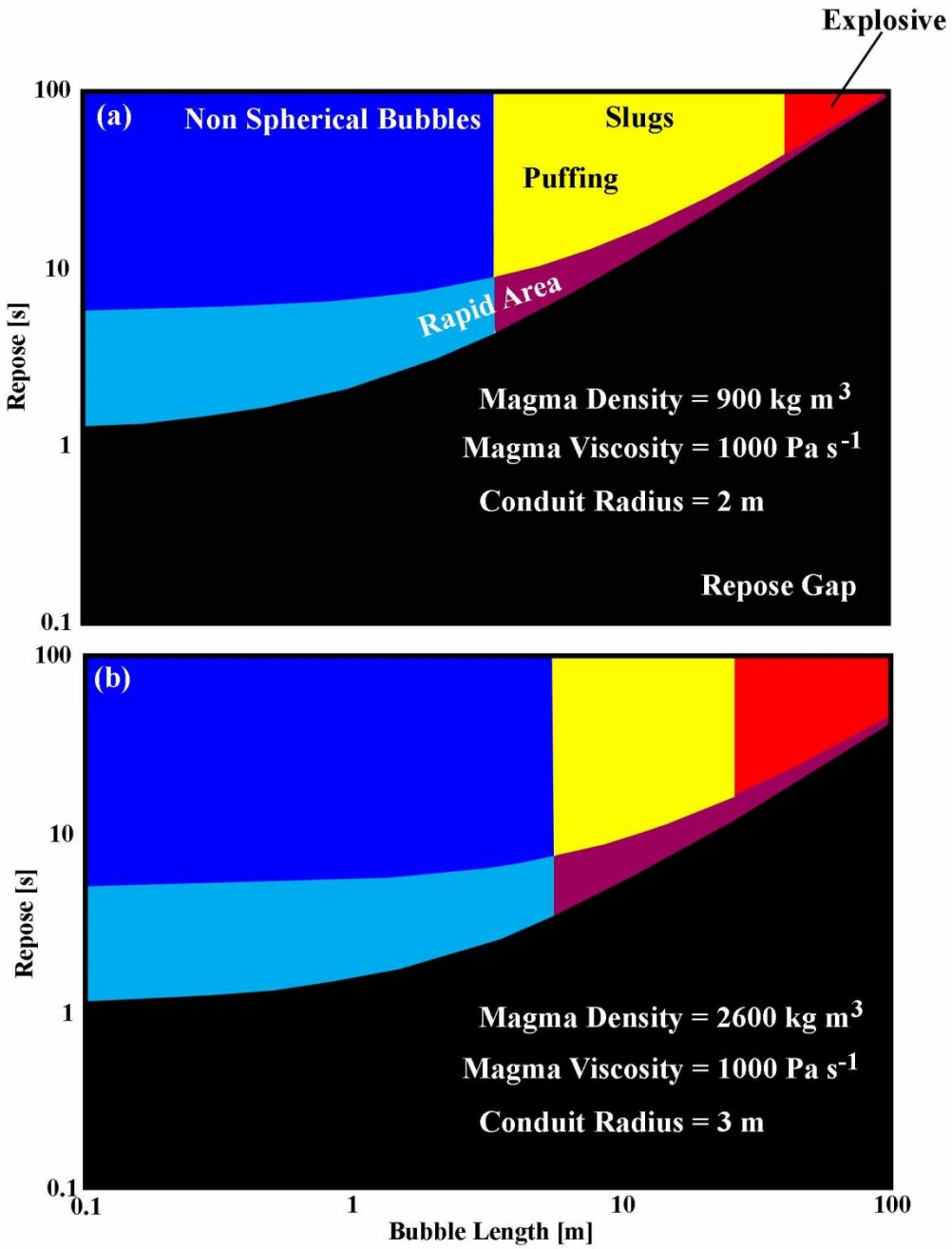

Fig. 6.8: Example bubble length model for another two sets of basaltic parameters (a) and (b). Here the data are demonstrated using a log plot on the y axis.

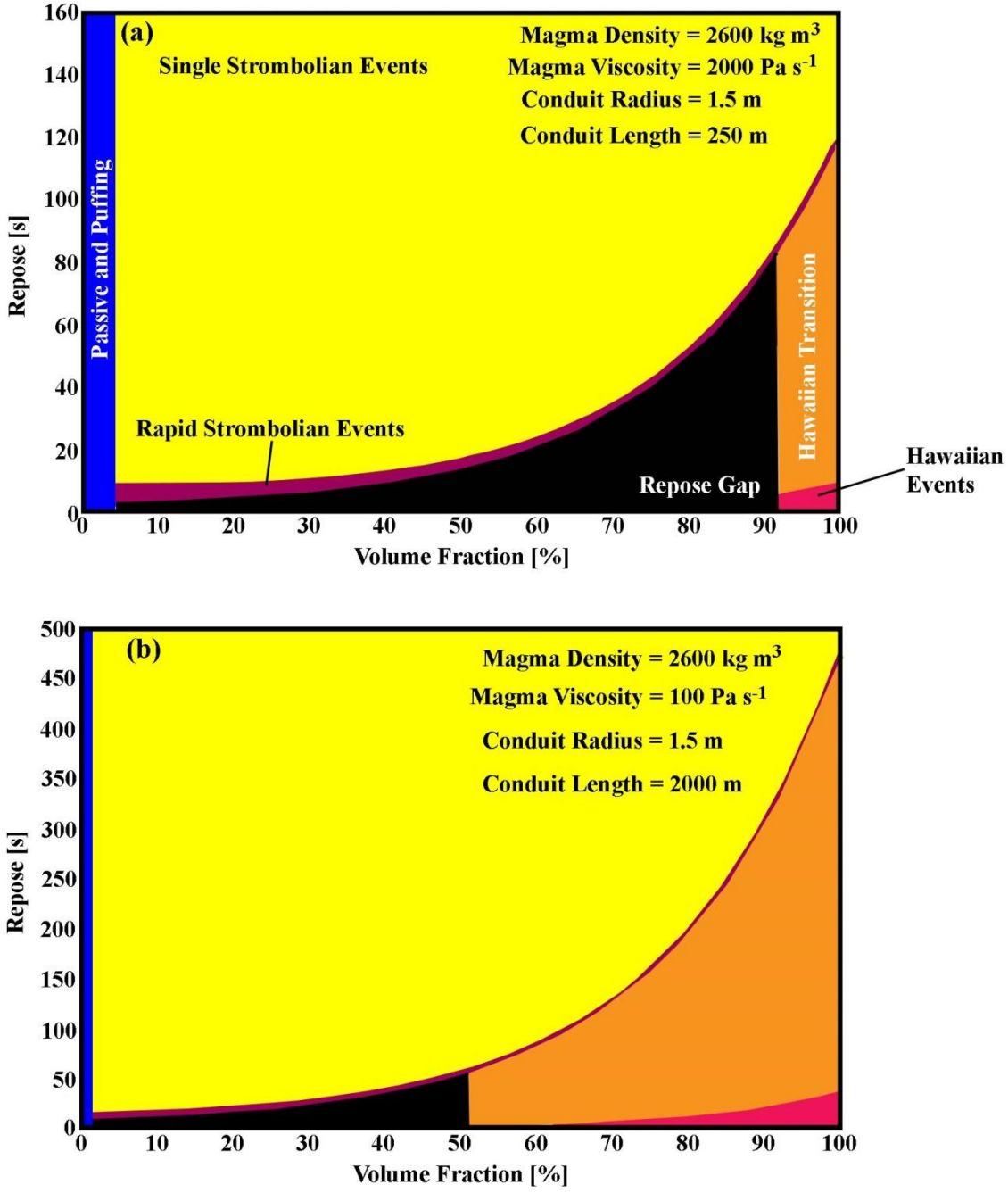

Fig. 6.9: Example volume fraction model for two sample basaltic magmas. With a small conduit length of ≈ 250 m the lava fountaining transition (hawaiian activity) occurs at very high volume fractions of > 90 %. For the longer conduit of 2,000 m this transition occurs for lower gas volume fraction.

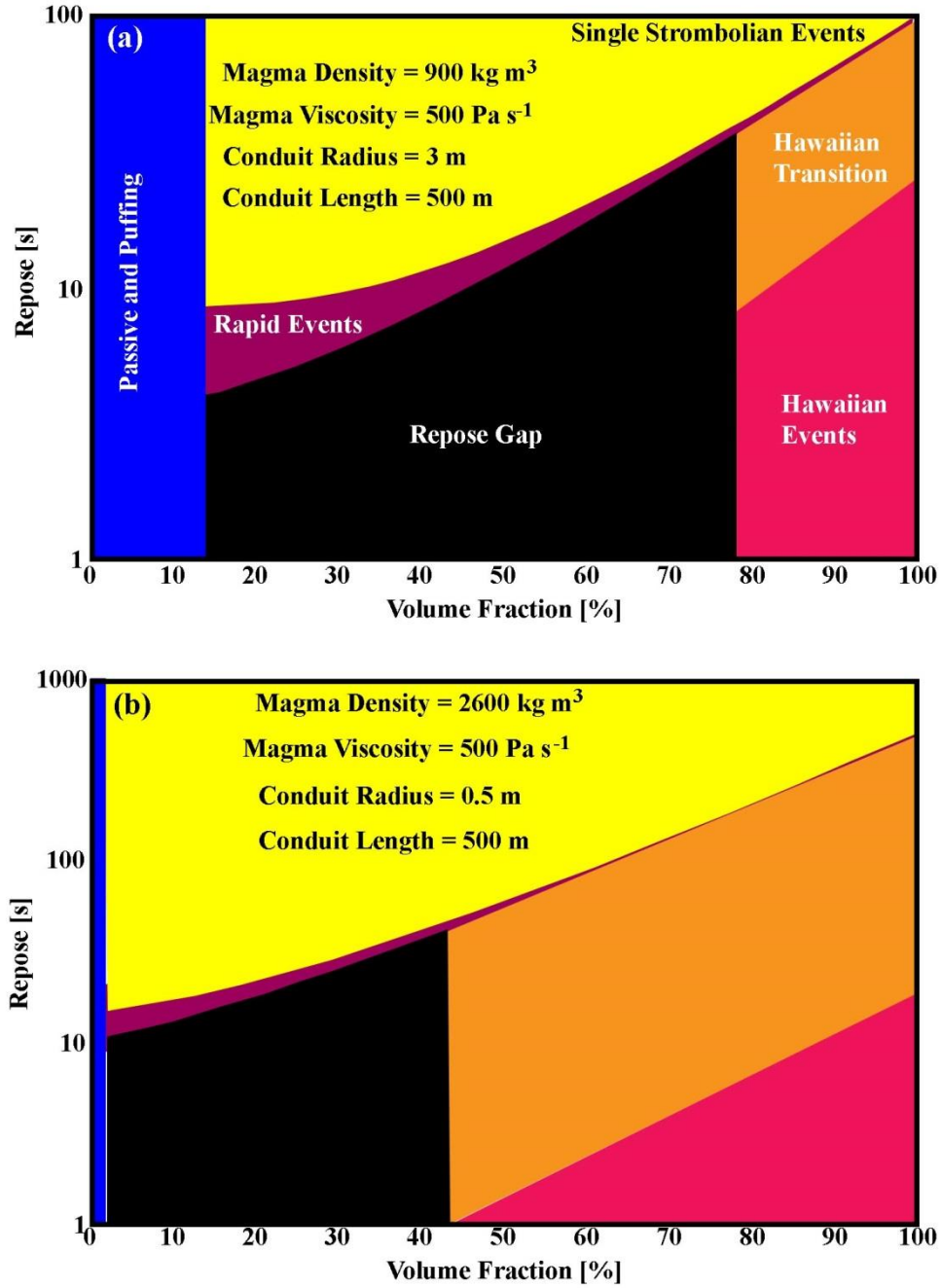

Fig. 6.10: Example volume fraction model for another two sets of basaltic degassing parameters. Here the repose (y) axis is displayed on a log scale. The wider conduit and lower magma density in (a) demonstrates that lava fountaining (hawaiian) occurs for low repose intervals and high gas volume fractions. In (b) the smaller conduit radius allows for transition to lava fountaining at rather lower gas volume fractions.

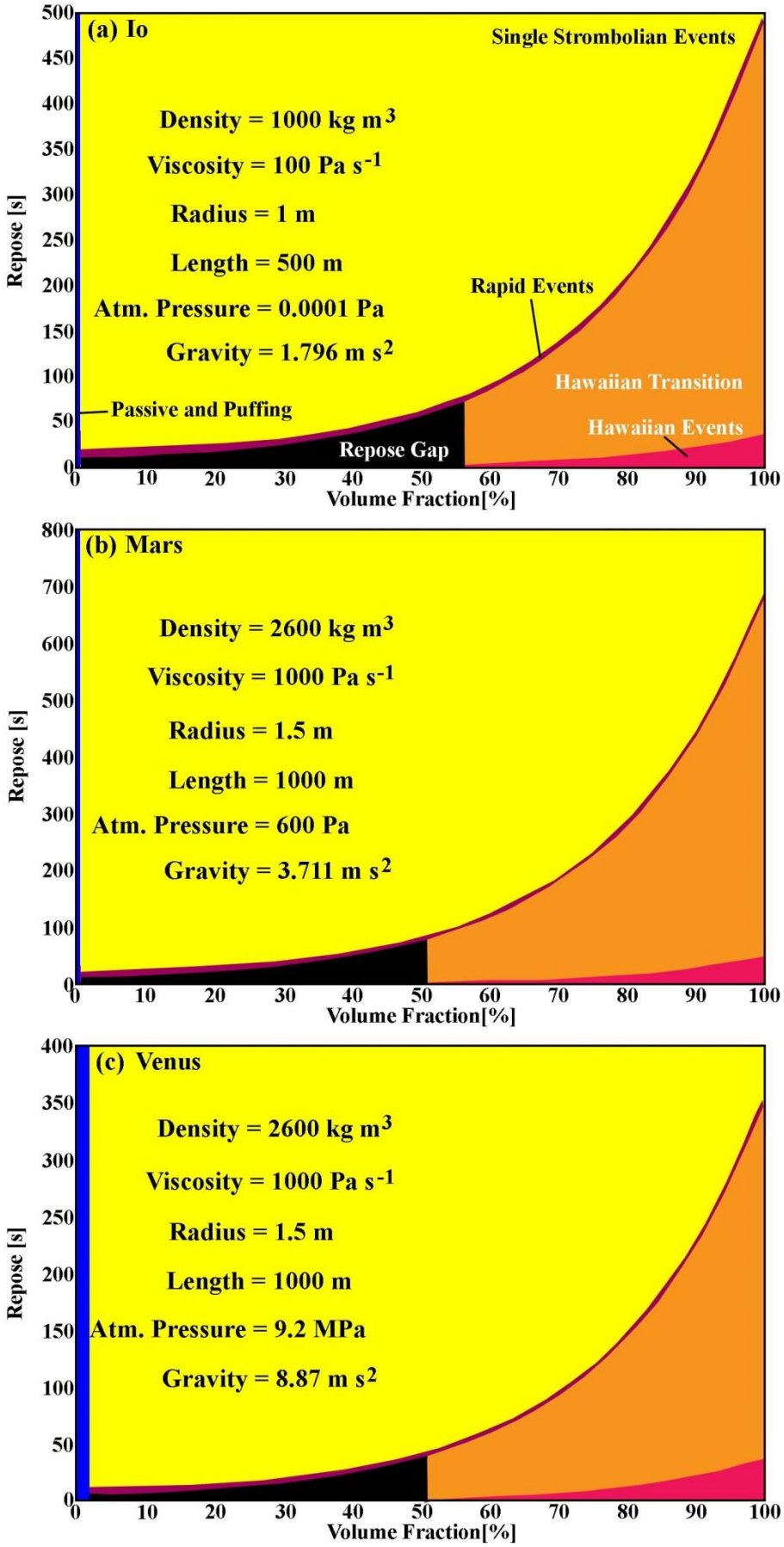

Fig. 6.11: The volume fraction model applied to three extra-terrestrial cases: (a) Io, (b) Mars and (c) Venus.

6.4. Investigating links between gas emissions and seismicity

In Chapter 5, the laboratory proxy geophysical signals suggested that for higher gas content within a conduit, there ought to be elevated seismicity. Here, using studies which identify a correlation between seismicity and SO_2 flux, the possibility of a correlation across multiple volcanoes is investigated. Due to the lack of standard measurements of gas emissions and seismicity cited in the literature, it was necessary to convert all identified data into comparable values, to enable the combination of all information onto a single plot.

For the purpose of this study, SO_2 emissions, were converted to kg s^{-1}. Where values were quoted in t d^{-1} (tonnes a day) these were converted into the average equivalent emitted per second (i.e. by dividing by 86,400). In the study of Palma et al. (2008) only the SO_2 data from Fig. 15a (those which were collected by Palma et al. [2008]) were used, which represented daily averages. In the case of McGonigle et al. (2009), SO_2 emission values were not corrected as the ejection of gases following the bursting slugs occurred rapidly, on the order of ≈1 s.

Table 6.2: Summary of parameters used in equations 6.11 and 6.12, the overall flux ranges, and references used for the study.

Volcano	Radius (m)	Vent Distance (m)	Flux (kg s^{-1})	Reference
Stromboli	2	500	≈ 0.2 – 3.2	McGonigle et al. (2009)
Asama	19	320	≈ 8 – 430	Kazahaya et al. (2011)
Villarica	2.7	3900	≈ 1.4 – 15.6	Palma et al. (2008)
Santa Ana	3	2000	≈ 1.6 – 49.8	Olmos et al. (2007)

Likewise, a standard is required for seismic values. This involved the conversion of RSAM (Endo and Murray, 1991; Olmos et al. 2007), VLP moment (Kazahaya et al. 2011) and RMS values, by reversing the mathematical procedures used in their creation, into a dimensional value, namely displacement in m s^{-1}. Where values are quoted as VLP moment (e.g. Kazahaya et al. 2011) or displacement (e.g. McGonigle et al. 2009), these were converted to one second time averaged values by dividing by the width of the original VLP filter.

Following on from this conversion procedure, datasets were generated for the four at the listed volcanoes, with identical and easily comparable parameters, although, in each instance, seismic measurements were made at different distances from the source. Any multi volcano

correlation between gas emission and displacement, therefore, needs to be corrected for this difference. A theoretical correction was applied based on the attenuation of seismic waves, whereby the measured displacement, d_r was scaled up to that theoretically occurring at the 'source' d_{th}, which was reasonably assumed to be co-located with the point of gas emission from the volcano, according to the following relationship modified from Chapman (2004):

$$d_{th} = \frac{d_r}{(\cos(k)t - wr_{source})^{ar_{source}}}, \qquad \textbf{(Eq. 6.14)}$$

where t is the time taken for a seismic p-wave travelling at (v) 3000 m s^{-1} to travel from the source to receiver, the radius of the source r_{source} for each volcano (i.e. the conduit width), a the absorption coefficient of 0.05 for granite (Lavergne, 1989), k is the wave number, here taken to be 0, as the correction concerns *theoretical* displacement, at the vent, at an event time = 0, w is the angular frequency (e.g. $k \times v$), given these values (i.e. $\cos 0 = 1$). One can therefore simplify and rewrite as follows:

$$d_{th} = \frac{d_r}{t^{ar}}. \qquad \textbf{(Eq. 6.15)}$$

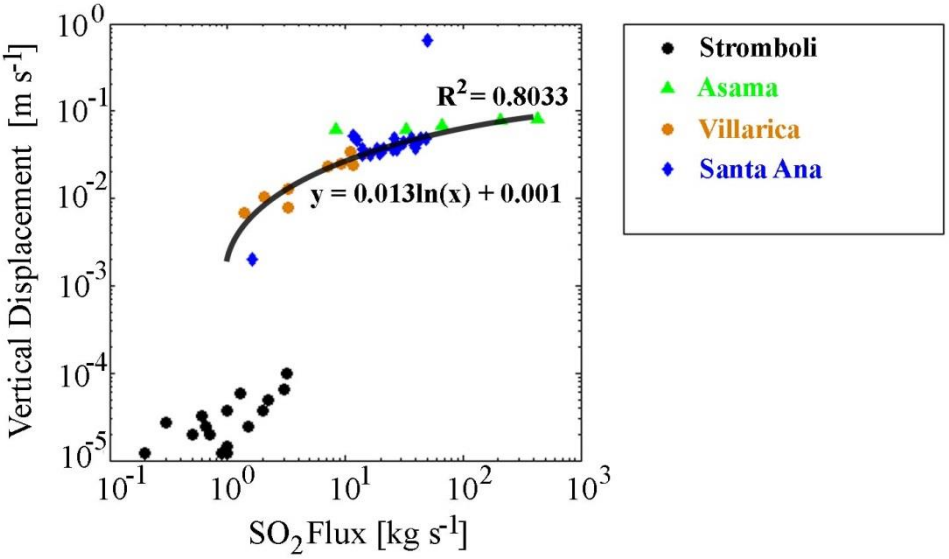

Fig. 6.12: The relationship between SO_2 flux and theoretical vertical displacement for four volcanoes. For details see the text in section 6.4.

The following values for r_{source} were used at each volcano (see also Table 6.2):

- Villarica – 2.7 m (Witter et al. 2004),
- Asama – 19 m (Ohwada et al. 2013), taking the lower value of 19 m associated with more quiescent activity,

- Stromboli – 2 m (Ripepe et al. 2007),
- Santa Ana – 3 m (Olmos et al. (2007)

Fig. 6.12 shows the results of this procedure which demonstrates the following log relationship:

$$y = 0.013 \ln(x) + 0.001 \qquad \textbf{(Eq. 6.16)}$$

with an $R^2 = 0.8033$.

6.5. Discussion

The potential of using the patterns in gas release to unlock conduit and magma viscosity parameters associated with activity is a unique possibility (and *vice versa* of course*)*. This could open up the ability to estimate gas release from explosive activity, based solely on intervals between events, potentially assisting in eruption forecasting, and by complementing existing approaches (e.g. Voight, 1988; Sparks, 2003; Aiuppa et al. 2007). This builds on the models of Parfitt and Wilson, (1995), which investigate basic transitions between styles of activity based on bubble rise speed. In this chapter, an effort has been made to combine volcanological and fluid dynamical studies on bubble flow and transitions between different styles of activity. While the lines drawn on the graph are inherently and necessarily sharp and defined, real boundaries will likely be 'fuzzy', particularly in a volcanic environment where non-Newtonian magmas and significant heterogeneities will be present (Gonnermann and Manga, 2003). On a basic level the models suggest that developing "true" rapid slug driven activity where slugs begin to influence each other, yet can still rise and burst independently, is difficult. It is therefore likely that, by combining high volumes of gas with a rapid release rate, lava fountaining is inherently more likely. Additionally, if it is known how much magma is released during the activity one can begin to estimate the range of expelled gas volumes which would be required to generate the observed activity, creating an estimate of gas release without the need for examining the ejected rocks themselves (e.g. Greenland et al. 1985).

Stromboli probably represents the best target for study of slug flow, as such it is the focus of the overwhelming literature on volcanic slug flow (e.g. Ripepe et al. 2002; James et al. 2008, 2009; Tamburello et al. 2012). This also makes it the ideal target to test the developed models. Unfortunately, exact timings between individual bursts are unknown, making the estimates included for repose time somewhat crude. This said the repose times applied here,

of between ≈ 3 – 10 minutes broadly represent the time-averaged activity at Stromboli (Ripepe et al. 2002). Literature estimates for strombolian eruptive masses, and hence volumes and approximate slug lengths, are well constrained (e.g. Mori and Burton, 2006; Tamburello et al. 2012; this thesis – Chapter 3, although the data collected here were not for sequential events – i.e. not all burst times can be reliably constrained). Application of these slug lengths with repose estimates fits well with both models presented here, offering a form of validation. In addition, estimates of lengths of slugs which generate puffing (e.g. Ripepe and Gordeev, 1999; Tamburello et al. 2012) also agree well with the model, falling well within the non-explosive area. This reinforces the stability of the system at Stromboli; e.g., each rising slug, according to this model, has little to no impact on the bursts which follow, i.e. fluid disturbances will have been damped by the time another slug passes then erupts at the surface. This of course assumes that each gas slug that forms erupts at the surface, and that slugs don't destroy themselves on ascent (see Chapter 3). Of course, the bubble length model is only directly applicable to stagnant magmas, as is likely or assumed to be the case at Stromboli (James et al. 2008) and vertical conduits. However, for magmas with non-negligible momentum and/or inclined conduits, the fluid dynamics would be modified (Hasan and Kabir, 1992; Pinto et al. 1998, 2001; Nogueira et al. 2006). Whilst the developed model could be adapted to these changes, the literature body is rather limited in comparison to cases of stagnant magmas and zero conduit inclination making data validation of such cases rather unfeasible at this stage.

Strombolian masses for eruptive activity at Etna are more poorly constrained, with the only current estimates, being those within this thesis (Chapter 3; Burton et al. 2015a). Validation of the repose gap model was performed with relative success in section 5.3.3 (see Fig. 5.10). Given the large variety of eruptive styles manifested at Etna: passive (e.g. Aiuppa et al. 2007; Tamburello et al. 2013), effusive (e.g. Andronico and Lodato, 2005; Burton et al. 2005), single event and high temporal resolution strombolian activity (e.g. this work, Chapter 4, and Andronico et al. 2005; Behncke et al. 2014), lava fountains (e.g. Allard et al. 2005), and even basaltic plinian (Coltelli et al. 1998), a variety of flow regimes can clearly be implicated in their generation. In combination with constant measurements of degassing at the summit of Etna, the application of this model could begin to provide warning of an impending change in activity style, i.e. a decreasing repose gap between strombolian events, could presage a transition to lava fountaining. Indeed, during a so-called Etnean paroxysm, events are seen to

be quite cyclic (Bertagnini et al. 1990; Behncke and Neri, 2003; personal communication Alessandro Aiuppa, Palermo University).

What makes volcanoes such as Kilauea more prone to produce lava fountains? Why is strombolian activity rare or even non-existent on this target? Much of this will be related to the bubble formation mechanism and activity flow regime. Vergniolle and Jaupart (1990) propose that a collapsing foam, via the collection of bubbles at the roof of a chamber injects a "gas pocket" which resembles a gas slug, which then generates the typical hawaiian lava fountaining activity. However, there are a number of problems with the assumption that gas pockets or slugs generate lava fountaining activity, which are fluid dynamic in nature, i.e. what flow regime (see Fig. 6.1) generates lava fountaining activity? It is clear that compared to lava ejection, the volume of gas in this case is clearly dominant, occasionally in excess of 90% gas. For that gas content in the conduit, at the viscosities suggested by Vergniolle and Jaupart (1990) of 30 Pa s^{-1}, strombolian activity, could not occur according to the model developed in this thesis; this also extends to stable slug flow (see also Suckale et al. 2010b; James et al. 2011, 2013). Significant bubble deformation and interaction will therefore occur, leading to a further question: given the proposed rapid injection/collapse of foams, what flow regime is responsible for lava fountaining at Kilauea? Does the conduit develop a form of annular flow or is there a more turbulent churn type flow (see Fig. 6.1)? Unfortunately the model developed here cannot differentiate between the two types of flow within the conduit clearly, future study into flow regimes using a variety of magma parameters would help identify this. This said, the application of this model does open up new avenues for research. Toramaru (1988) suggested that waves/instabilities in two-phase churn or transitional annular flow could be evidence of these flow regimes in lava fountaining activity. Indeed, recent work has identified distinct pulses in lava fountaining, occurring seconds apart at the recent Holuhraun lava fountain activity (e.g. Witt and Walter, 2015). If these pulses follow some form of fluid dynamic relation (as Toramaru [1988] suggests) then it stands to reason that this can be used to predict exact gas volume fraction and magma parameters, which could then be applied to constrain the observed activity.

There are a large number of studies into the size of bubbles at depth (e.g. Sparks, 1978; Mangan et al. 1993; Proussevitch and Sahagian, 1988; and references therein) and bubbles contained within ejected lava (e.g. Manga, 1996; Herd and Pinkerton, 1997), which are largely unrelated to the flow regimes and hence the major gas phase driving explosive activity. Kilauea is dominated by lava flows and lava fountaining, but could Kilauea produce

strombolian activity? The short answer is yes. However, this would likely involve large bulk changes to both conduit geometry, and magma rheology. Stable gas pockets will only begin to form at certain viscosities, it is at these values that the rapidity of foam collapse will define the type of activity present, be it single strombolian events or a more rapid strombolian activity. For example, the rapid injection of a large amount of gas via a collapsing foam is the only conceivable way to rapidly increase the volume fraction of gas in the conduit. The coalescence mechanism is an obvious way of driving cyclicity in observed activity, with generation of larger slugs leading to impulsive events (e.g. Llewellin et al. 2013; 2014a) which are unlikely to last hours to weeks.

The lava lake at Marum Crater (Ambrym Volcano, Vanuatu) is a turbulent environment (Carniel et al. 2003; Allard et al. 2009) and the bursting or rise of individual bubbles to the surface can be clearly seen here. It is likely here, considering the frequency of bursting events (every ≈ 1 – 10 s), well below the typical repose gap boundary (see Figs. 6.7 and 6.8), that a form of churn flow is prevalent. In the absence of a sustained jet, annular flow is improbable as the cause (Triplett et al. 1999). A more detailed survey of potential sub-surface structures and gas release at high time resolution would be needed to unlock more information about the flow regime in this instance. For example it would be possible for slug flow to be present at depth, where the fluid dynamics allow stability, but as the conduit opens out, instability could be generated (Campos and Guedes de Carvalho, 1988; Suckale et al. 2010b) with a transition to a more complex flow regime. Marum is in direct contrast to a lava lake such as Erebus where viscosities are so high, on the order of ≈ 10^4 Pa s^{-1} (Moussallam et al. 2013), that any form of activity other than single strombolian events would be very rare.

The easily adaptable nature of the equations in sections 6.1 and 6.2 mean that it is not only terrestrial volcanism that could be investigated. For example, the most active body in the solar system, other than the Earth, is Io (Davies, 2007). Applying these relationships to estimates of activity on Io could identify important aspects about activity pathways in the sub-surface and the ability of this moon to produce certain styles of activity. Here, however, there is also the possibility of more exotic flow regimes, such as mist flow (see Fig. 6.1), which is dominated by the gas phase (Matsui, 1984).

Section 6.4 suggested that there is a direct relationship between gas release and seismicity generated. This information, which corroborates an observation in Chapter 5, that an increased gas flow could increase conduit pressure and hence seismicity, could be important

in defining the amount of gas present at depth before an eruption has occurred, or while it is ongoing. This could be of benefit when combined with the model developed in this chapter, as estimates of gas release can enable constraint on slug length which can then be directly applied to the models in this chapter. This relationship, however, has only been defined on four volcanoes. A significant increase in the number of volcanoes covered is required to enable further confidence in the relationship.

6.6. Conclusions

Through the combined use of existing volcanic studies on slug flow in the literature (e.g. James et al. 2009, 2013; Suckale et al. 2010b), the work of Chapter 5, fluid dynamical studies on flow transitions (e.g. Taitel et al. 1980, Dukler et al. 1985), and characteristics of bubbles (e.g. Viana et al. 2003; Llewellin et al. 2012), I have developed a model to characterise activity observed based on flow regimes, defined by their respective gas volume fractions, slug lengths, and repose times between events. The model demonstrates that certain magma parameters are more likely to produce particular eruptive styles, however, the formation mechanisms of slugs also remains a key parameter. It is clear that the developed models show promise, however, given the sparsity of current available data, validation is far from complete. Although, application of the model on targets where data are presently available, particularly for Stromboli, does show that the model is applicable in these contexts. Through the combination and use of this with model with real time gas emissions estimates, the models could be of use for eruption forecasting at volcanoes such as Etna, where activity can rapidly cycle between styles.

7. Concluding Remarks

7.1. Unifying the study of degassing: A brief discussion and conclusions

The overall aim of this thesis was trifold: to measure basaltic volcanic degassing (both passive and explosive), to model computationally, and to model in the lab then process the collected data. It is only through this combined approach that one can fully understand the inner workings and resultant styles of activity observed at the surface. This has been aided by the new found ability to measure gas emissions at temporal resolutions of ≈ 1 Hz appropriate to the dynamic nature of explosive basaltic volcanism (Mori and Burton, 2006; Bluth et al. 2007), and has opened up, for the first time, the ability to compare measured gas emissions with laboratory analogue models, and computational fluid dynamical simulations (this thesis). This is an essential aspect in understanding the processes driving basaltic activity given the inherent difficulties of directly observing sub-surface magma and gas flow, arguably though this study could be taken much further with a thorough incorporation of aspects of petrology.

Prior to this study a large number of UV camera studies, which are valuable in their own right, have offered an improvement in our estimation of volcanic degassing budgets of SO_2 (e.g. Tamburello et al. 2011a; McCormick et al. 2013, 2014; Burton et al. 2015a and references therein) or CO_2 (Allard et al. 1991; Burton et al. 2000; Burton et al. 2013). Some papers have gone further and have investigated correlations between SO_2 release and seismicity (e.g. McGonigle et al. 2009; Kazahaya et al. 2011; Nadeau et al. 2011; this thesis). A large body of UV camera literature is still focused on narrowing uncertainty and quantifying error (Kantzas et al. 2010 Kern et al. 2010a, 2010b, 2013, 2014; Lübcke e tal. 2013), again an essential part of providing confidence in the measurements. Necessary improvements in plume speed estimation have been made (Peters et al. 2015), as have attempts at quantifying light dilution related errors (Campion et al. 2015). However, UV cameras are now at the stage where they can be used to begin to answer scientific questions concerning impulsive and passive gas release. It is hoped that this thesis goes some way to demonstrating this.

Understanding the fluid dynamics of magma flow in the sub-surface is a key aspect in defining the activity which will be prevalent at the surface (Parfitt, 2004), and how sustainable this may be (Chapter 3). This furthermore highlights the increased need to

consider total gas emissions and not just the release of single species (Pering et al. 2015c). Whilst there is substantial focus on SO_2 for obvious reasons, it is only by considering all the major gas components (SO_2, CO_2, and H_2O) that flow regime behaviour can be properly investigated. This unification then allows the application of fluid dynamical theory in an attempt to explain (Chapters 3, 4, 5, and 6) phenomena captured in degassing signals.

Within this thesis, the significant discovery of a relationship which defines the minimum repose period which must occur before another event can occur for a given explosion gas mass, has unlocked a number of avenues to develop models which seek to characterise a flow regime based on delay between events and mass of gas released (Chapter 5 and 6). To the authors knowledge this is the first observation of its kind. It is only through laboratory analogue analysis in a multi slug regime that this relationship has been validated (Chapter 5) and it is only through future research and continued field observations that models of this kind (Chapter 6) and others will be able to be further developed (see section 7.2).

This thesis has endeavoured to provide an insight into basaltic degassing through the analysis of four specific objectives: (1) to investigate trends in passive degassing using UV cameras, (2) to investigate explosive degassing using UV cameras, (3) to model explosive degassing, and (4) to investigate transitions between different styles of activity.

7.1.1. Chapter Two Conclusions

This chapter outlined the measurement of contemporaneous SO_2 and CO_2 datasets at an unprecedented temporal resolution of 1 Hz. This was achieved by combining the now commonplace UV camera methodology to measure SO_2, with a Multi-GAS analyser which measures gas ratios, including CO_2/SO_2. After background subtraction of atmospheric levels of CO_2, the two datasets can be cross-correlated to determine lag between the Multi-GAS location and the point used for SO_2 determined in the UV camera data. The CO_2/SO_2 gas ratios can then be directly multiplied by the temporally matched SO_2 data to calculate an equivalent CO_2 flux dataset. This allowed, for the first time, the comparison of CO_2 flux with geophysical datasets.

This comparison was completed with traditional analysis techniques, but also with a newly designed correlation technique, “Corrplot” written in Matlab®, which combines the continuous wavelet transform with Spearman’s Rank Correlation. This allows a much clearer

visualisation of the links between contemporaneous datasets, demonstrating intriguing links between periodicities of CO_2, SO_2, and seismicity. The presence of non-stationary periodic degassing in CO_2 was identified, in addition to those observed already with SO_2 and gas ratios (e.g. Tamburello et al. 2013; Peters et al. 2014b, Ilanko et al. 2015a).

7.1.2. Chapter Three Conclusions

Stromboli, the archetypal volcano for strombolian activity, is the perfect place for measuring SO_2 flux for a large number of strombolian events. Given the frequency of eruptions and the large passive contribution it was chosen as the location for addressing Objectives 1 and 2. Tamburello et al. (2012) described the pattern of a single explosion from onset to the end, which included a gas coda. In this chapter, 120 strombolian events and 80 hornito events were analysed from explosion onset to the coda end. This highlighted six specific characteristic styles of degassing following an explosion, and also of the total gas mass contained in the explosive and coda components of each event. This demonstrated that the overwhelming majority of gas mass for hornito events was contained within the coda (≈ 70 to 84%) while, for strombolian events the portion of gas contained in the coda ranged ≈ 53 to 75%. Here, Objective 3 was also addressed with a series of CFD models. These demonstrated that there is the potential for the production of daughter bubbles; these involve mass release from the base of slugs. A non-linear relationship was discovered between N_f and mass loss rate, which indicates that the attrition of mass from slugs in a volcanic situation could be more prevalent than previously thought. In particular, at Stromboli this may act to render slug flow unsustainable below certain depths. Based on the average mass loss rates discovered and total masses of events, this could be at ≈ 740 m. Indeed, the models also showed a similar rate of mass loss to the measured strombolian events, with ≈ 43 to 69% of mass contained within the coda.

7.1.3. Chapter Four Conclusions

This chapter outlined the measurement of SO_2 flux during a period of mild high frequency strombolian activity from the Bocca Nuova crater of Mt. Etna and addresses Objective 2. Measurement conditions were difficult because of high concentrations of gas within the crater and the use of background rock as a light reflectance surface. This meant that only ≈ 27 minutes of data were captured. However, this enabled the first quantification of strombolian

eruption masses at Etna (Burton et al. 2015), ranging ≈ 0.1 – 14 kg SO_2 and total gas masses of ≈ 0.2 – 74 kg, when multiplying SO_2 values by ratios measured using a Multi-GAS analyser. Through the analysis of time periods between individual bursts and their respective masses it was discovered that the largest mass events were followed by longer wait periods, which I term repose periods (repose gap behaviour), before another event could occur. This was a feature which was not observed with time before a burst. On combination with basic mathematical relations, the distances over which interaction between rising slugs may occur was calculated. This suggested that, given the modal repose time of ≈ 4 s, the slugs could be rising in close enough proximity to coalesce with each other. A number of potential causes for the repose gap were considered. Given the potential proximity of slugs it is possible that the coalescence mechanism, which causes the acceleration of trailing slugs into leading ones, enables the generation of larger gaps behind a slug, leading to longer repose times, and generation of slugs of elevated masses.

7.1.4. Chapter Five Conclusions

A number of experiments were undertaken in this chapter to investigate the behaviour of slugs in a multi-slug regime which drive rapid strombolian activity such as that observed, measured and discussed in Chapter 4 with the aim of addressing Objectives 3 and 4. A series of laboratory experiments investigated a range of volume fractions and gas expansion rates. These allowed the quantification of the repose gap observed in Etnean data using existing relations for the rise speed of a slug, the wake length of a slug, and the length of the slug itself. Beyond this, these experiments address a gap in the literature on the behaviour of rising slugs in a multiple slug regime. These led to the discovery of a relationship between gas volume fraction and slug length and slug base rise speed. In addition it was identified that coalescence between two rising slugs can still occur even when the leading slug is travelling at a faster speed, a feature which is most likely caused by the expansion related behaviour of the observed gas slugs. CFD identified a similar process, demonstrating that the expansion of trailing slugs has a marked effect on the rise speed of slug bases.

7.1.5. Chapter Six Conclusions

Chapter six represents the beginnings of developing a theory which can help define the flow regime transitions between basaltic degassing styles and aims to address Objective 4. This

was achieved by building upon the relationships discovered and observed in Chapters 4 and 5, and lead to the development of two separate models. The first slug length model combines the relationships which define the minimum repose time and transition times, and explosive transition (James et al. 2009). The second model replaces slug length on the x axis with gas volume fraction between 0 – 100%. The slug length model is particularly for slug driven activity, where a bursting mass can be assigned a passive, puffing, strombolian explosive, or rapid strombolian category. When tested on data collected at Stromboli (Chapter 3) and those from the literature (Tamburello et al. 2012) the model performed well. The second volume fraction model adds transitions towards and the occurrence of hawaiian lava fountaining. This was achieved by applying relationships for the transition to churn and annular flow contained within Taitel et al. (1980), in addition to the existing transitions towards and away from passive degassing. Both defined models can be adjusted for a wide set of basaltic parameters, for use terrestrially or for planetary applications. This can then allow minimum time delays between events to be estimated from gas volume fractions and vice versa, for magma and conduit parameters to be estimated from delay times between events. In particular the critical volume fraction beyond which slug bursts can occur more frequently can be applied to individual systems so we can begin to understand how much gas is needed to drive the transition towards lava fountaining. By combining a number of studies which demonstrate a relationship between gas emission and seismicity this chapter demonstrated that, on normalisation of events to enable comparison on the same plot a log relationship was discovered. This suggests that seismicity could be incorporated in future models. The latter volume fraction model, could be particularly useful when used in real time along with acquisition of gas emission monitoring data, to enable identification of transitions in activity style.

7.2. Future Goals

Undeniably, more degassing data needs to be now collected to probe more developed flow regimes, but also basaltic degassing styles globally and to investigate time varying behaviour at individual volcanoes. In particular, the dynamics associated with degassing at lava lake needs to be addressed in more detail. One clear example is Marum, where the vigorousness and turbulence of the lava lake surface are likely indicative of a form of churn flow, which can only be understood with a full quantification of total gas release. Furthermore,

developing a way of measuring gas emissions during lava fountaining would also allow the probing of the flow regimes which drive this end member of basaltic degassing.

The overwhelming majority of models into slug flow in a volcanic environment are performed, for reasons of simplicity and validation, on vertical conduits (James et al. 2008; Del Bello et al. 2012; 2015; Llewellin et al. 2012, 2013, 2014a), with only a few exceptions, which are little more than brief treatments concerning alternate geometries (Seyfried and Freundt, 2000; James et al. 2004). In reality, volcanic conduits are rarely uniform (Ferrick et al. 1982; Mastin, 2002), are known to be inclined (Chouet et al. 2003), flare (Keating et al. 2008), produce strombolian activity in lava lakes (example model in Fig 7.1a), and have rough walls. In addition, magmas themselves can be non-Newtonian (Shaw, 1969; Dingwell and Webb, 1989; Pinkerton and Stevenson, 1992), contain large crystals (e.g. Erebus – Moussallam et al. 2015), they can be non-stagnant which effects the way gas flows (Pinto et al. 1998, 2001), they can vary in viscosity with depth (Del Bello et al. 2015), and the exsolution of gas at different depths can act to alter and drive dominant forms of activity. This is a relatively daunting list which when considering that each of these could and do occur in a single system, mean the real volcanic systems which are the subject of currently developed models are significantly more complex than the models themselves. Nevertheless, the effects of these, on the variety of flow regimes, need to be isolated and investigated.

To date, CFD of lava fountaining activity is notably, to the author's knowledge, completely absent. By beginning to model lava fountaining we could begin to delve into the presently very unconstrained flow regime which drives such activity. Fig. 7.1 shows a range of outputs that can be produced from a simple CFD model which ejects a coupled magma gas mixture (i.e. what happens to one phase affects the other too), at a set speed, gas volume fraction and conduit radius. Here, the amount of gas being emitted can be monitored (Fig. 7.1c), and even the periodicity of waves which can be seen in the fountain (Fig. 7.1b and d). Even such a simple model as this may be able to probe behaviour which has been observed in the field (Witt and Walter, 2015) in more detail.

Finally, at this moment in time the majority of computational models use commercial software, at a very high (monetary) cost, and as a result they can only be used by researchers with access through institutions. The development of equally capable models could be achieved with free-to-use packages such as OpenFoam® (http://www.openfoam.com/) and

would facilitate the easier and more commonplace integration of models with existing gas based studies.

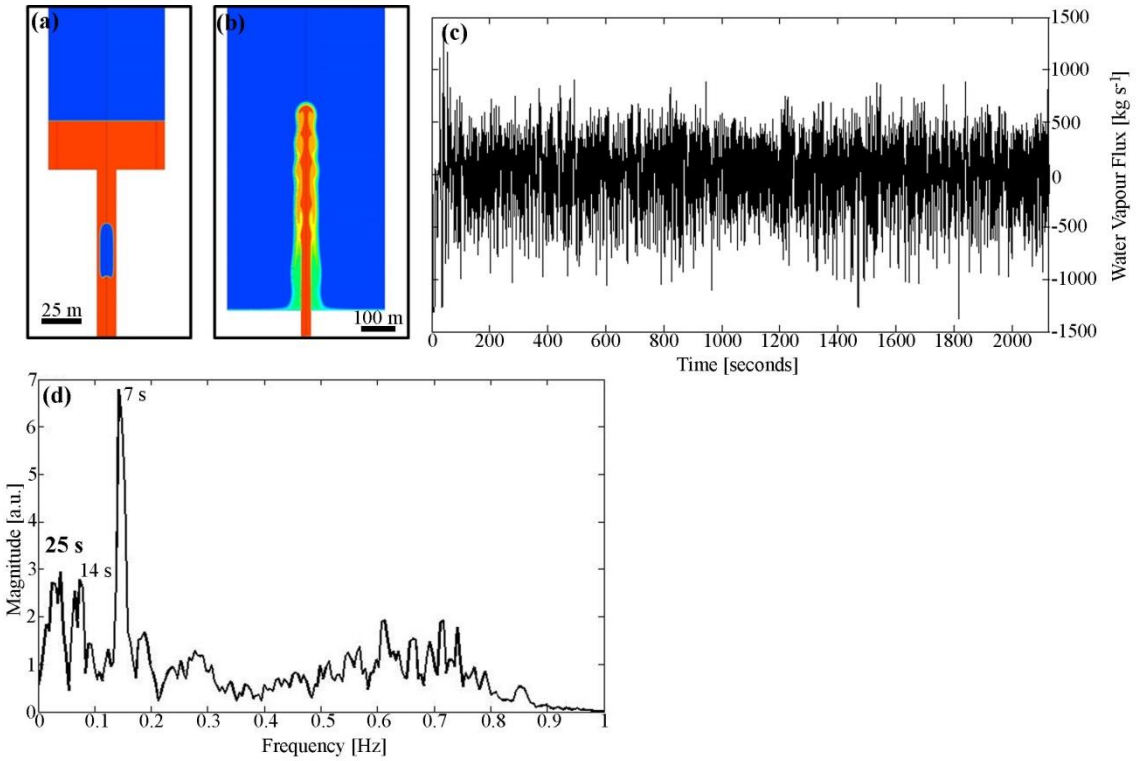

Fig. 7. 1: a) an example model initiated in Ansys Fluent showing a slug rising in a conduit which will eventually enter and burst in a lava lake, b) an example model of a lava fountain ejected at 50 m s^{-1}, with a gas volume fraction of 0.6, and a conduit radius of 5 m, c) water vapour flux calculated 300 m above the surface, with a negative flux indicating upward movement of gas and positive flux indicating the downward movement of gas, (d) periodicities calculated show a dominant period of ≈ 7 s.

8. References

Aiuppa, A., Federico, C., Paonita, A., Giudice, G., Valenza, M., 2005. Chemical mapping of a fumarolic field: La Fossa Crater, Vulcano Island (Aeolian Islands, italy). Geophysical Research Letters 13 (L13309), doi:10.1029/2005GL023207

Aiuppa, A., Moretti R., Federico C., Giudice G., Gurrieri S., Liuzzo M., Papale P., Shinohara H., Valenza M., 2007. Forecasting Etna eruptions by real-time observation of volcanic gas composition. Geology 35 (12), 1,115–1,118, doi: 10.1130/G24149

Aiuppa, A., Giudice, G., Gurrieri, S., Liuzzo, M., Burton, M., Caltabiano, T., McGonigle, A. J. S., Salerno, G., Shinohara, H., Valenza, M., 2008. Total volatile flux from Mount Etna, Geophys. Res. Lett. 35 (L24302), doi:10.1029/2008GL035871

Aiuppa, A., Burton, M., Caltabiano, T., Giudice, G., Guerrieri, S., Liuzzo, M., Mure, F., Salerno, G., 2010. Unusually large magmatic CO_2 gas emissions prior to a basaltic paroxysm, Geophysical Research Letters 37 (L17303), doi:10.1029/2010GL043837

Allard, P., Carbonnelle, J., Dajlevic, D., Le Bronec, J., Morel, P., Robe, M. C., Maurenas, J. M., Faivre-Pierret, R., Martin, D., Sabroux, J.C., Zettwoog, P., 1991. Eruptive and diffuse emissions of CO_2 from Mount Etna. Nature 351, 387-391, doi:10.1038/351387a0

Allard, P., Burton, M., Muré, F., 2005. Spectroscopic evidence for a lava fountain driven by previously accumulated magmatic gas. Nature 433, 407-410, doi:10.1038/nature03246

Allard, P., Aiuppa, A., Bani, P., Metrich, N., Bertagnini, A., Gauthier, P.G., Parello, F., Sawyer, G.M., Shinohara, H., Bagnato, E., Mariet, C., Garaebiti, E., Pelletier, B., 2009. Ambrym Basaltic Volcano (Vanuatu Arc): Volatile Fluxes, Magma Degassing Rate and Chamber Depth. In: AGU Fall Meeting 2009, San Francisco.

Aloui, F., Doubliez, L., Legrand, J., Souhar, M., 1999. Bubbly flow in an axisymmetric sudden expansion: Pressure drop, void fraction, wall shear stress, bubble velocities and sizes. Experimental Thermal and Fluid Science 19 (2), pp. 118-130, doi:10.1016/S0894-1777(98)10017-1

Alparone, S., Andronico, D., Giammanco, S., Lodato, L., 2004. A multidisciplinary approach to detect active pathways for magma migration and eruption at Mt. Etna (Sicily, Italy) before

the 2001 and 2002-2003 eruptions. Journal of Volcanology and Geothermal Research 136 (1-2), 121-140, doi:10.1016/j.volgeores.2004.05.014

Andronico, D., Lodato, L., 2005. Effusive activity at Mount Etna Volcano (Italy) During the 20th Century: A Contribution to Volcanic Hazard Assessment. Natural Hazards 36 (3), doi:10.1007/s11069-005-1938-2

Andronico, D., Branca, S., Calvari, S., Burton, M., Caltabiano, T., Corsaro, A., Del Carlo, P., Garfi, G., Lodato, L., Miraglia, L., Mure, F., Neri, M., Pecora, E., Pompilio, M., Salerno, G., Spampinato, L., 2005. A multi-disciplinary study of the 2002-03 Etna eruption: insights into a complex plumbing system. Bulletin of Volcanology 67 (4), 314,330, doi:10.1007/s00445-004-0372-8

Araújo, J. D. P., Miranda, J. M., Pinto, A. M. F. R., Campos, J. B. L. M., 2012. Wide-ranging survey on the laminar flow of individual Taylor bubbles rising through stagnant Newtonian liquids. International Journal of Multiphase Flow 43, 131-148, doi:10.1016/j.ijmultiphaseflow.2012.03.007

Araújo, J.D.P., Miranda, J.M., Campos, J.B.L.M., 2013. Flow of two consecutive Taylor bubbles through a vertical column of stagnant liquid – A CFD study about the influence of the leading bubble on the hydrodynamics of the trailing one. Chemical Engineering Science 97, 16-33, doi:10.1016/j.ces.2013.04.014

Armienti, P., Perinelli, C., Putirka, K.D., 2012. A New Model to Estimate Deep-level Magma Ascent Rates, with Applications to Mt. Etna (Sicily, Italy). Journal of Petrology, doi:10.1093/petrology/egs085

Barnea, D., 1986. Transition from annular flow and from dispersed bubble flow-unified models for the whole range of pipe inclinations. International Journal of Multiphase Flow 12 (5), 733-744, doi:10.1016/0301-9322(86)90048-0

Barnea, D., Taitel, Y., 1993. A model for slug length distribution in gas-liquid slug flow. International Journal of Multiphase Flow 19 (5), 829-838, doi:10.1016/0301-9322(93)90046-W

Behncke, B., Neri, M., 2003. Cycles and trends in the recent eruptive behaviour of Mount Etna (Italy). Canadian Journal of Earth Sciences 40 (10), 1,405-1,411, doi:10.1139/e03-052

Behncke, B., Branca, S., Corsaro, R.A., De Beni, E., Miraglia, L., Proietti, C., 2014. The 2011-2012 summit activity of Mount Etna: Birth, growth and products of the new SE crater. Journal of Volcanology and Geothermal Research 270, 10-21, doi:10.1016/j.volgeores.2013.11.012

Bellman, R., Pennington, R., 1953. Effects of surface tension and viscosity on Taylor instability. Quantitative Applied Mathematics 12 (2), 151-162

Bendiksen, K. H., 1985. On the motion of long bubbles in vertical tubes. International Journal of Multiphase Flow 11 (6), 797-812, doi:10.1016/0301-9322(85)90025-4

Bernstein, R.S., Baxter, P.J., Falk, H., Ing, R., Foster, L, Frost, F., 1986. Immediate public health concerns and actions in volcanic eruptions: lessons from the Mount St. helens eruptions, May 18-October 18, 1980. American Journal of Public Health 76, 25-37, doi:10.2105/AJPH.76.Suppl.25

Bertagnini, A., Calvari, S., Coltelli, M., Landi, P., Pompilio, M., Scribano, V., 1990. The 1989 eruptive sequence. In: Barberi, F., Bertagnini, A., Landi, P. (Eds.), Mt. Etna: the 1989 eruption, C.N.R.–Gruppo Nazionale Per La Vulcanologia Italy, Giardini.

Blackburn, E. A., Wilson, L., Sparks, R. S. J., 1976. Mechanisms and dynamics of strombolian activity. Journal of the Geological Society of London 132, 429-440, doi:10.1144/gsjgs/132/4/0429

Bluth, G. J. S., Shannon, J. M., Watson, I. M., Prata, A. J., Realmuto, V. J., 2007. Development of an ultra-violet digital camera for volcanic SO_2 imaging. Journal of Volcanology and Geothermal Research 161, 47-56, doi:10.1016/j.volgeores.2006.11.004

Boichu, M., Oppenheimer, C., Tsanev, V., Kyle, P. R., 2010. High temporal resolution SO_2 flux measurements at Erebus volcano, Antarctica. Journal of Volcanology and Geothermal Research 190, 325-336, doi:10.1016/j.jvolgeores.2009.11.020

Bouche, E., Vergniolle, S., Staudacher, T., Nercessian, A., Delmont, J-C., Frogneux, M., Cartault, F., Le Pichon, A., 2010. The role of large bubbles detected from acoustic measurements on the dynaics of Erta ‘Ale lava lake (Ethiopia). Earth and Planetary Science Letters 295 (1-2), 37-48, doi:10.1016/j.epsl.2010.03.020

Brooker, P., 2010. Fear in a handful of dust: aviation and the Icelandic volcano. Significance 7 (3), 112-115, doi:10.1111/j.1740-9713.2010.00436.x

Budd, L., Griggs, S., Howarth, D., Ison, S., 2011. A Fiasco of Volcanic Proportions? Eyjafjallajokull and the Closure of European Airspace. Mobilities 6 (1), doi:10.1080/17450101.2011.532650

Burton, M.R., Oppenheimer, C., Horrocks, L.W., Francis, P.W., 2000. Remote sensing of CO_2 and H_2O emission rates from Masaya volcano, Nicaragua. Geology 28 (10), 915-918, doi:10.1130/0091-7613(2000)

Burton, M.R., Neri, M., Andronico, D., Branca, S., Caltabiano, T., Calvari, S., Corsaro, R.A., Del Carlo, P., Lanzafame, G., Lodato, L., Miraglia, L., Salerno, G., Spampinato, L., 2005. Etne 2004-2005: An archetype for geodynamically-controlled effusive eruptions. Geophysical Research Letters 32 (9), doi:10.1029/2005GL022527

Burton, M., Allard, P., Muré, F., La Spina, A., 2007. Magmatic Gas Composition Reveals the Source Depth of Slug-Driven Strombolian Explosive Activity. Science 317, 227-230, doi:10.1126/science/1141900

Burton, M. R., Caltabiano, T., Mure, F., Salerno, G., Randazzo, D., 2009. SO_2 flux from Stromboli during the 2007 eruptions: Results from the FLAME network and traverse measurements. Journal of Volcanology and Geothermal Research 183 (3-4), 214-220, doi:10.1016/j.volgeores.2008.11.025

Burton, M. R., Sawyer, G. M., Granieri, D., 2013. Deep Carbon Emissions from Volcanoes. Reviews in Mineralogy & Geochemistry 75, 323-354, doi:10.2138/rmg.2013.75.11

Burton, M.R., Prata, F., Platt, U., 2015a. Volcanological applications of SO_2 cameras. Journal of Volcanology and Geothermal Research 300, 2-6, doi:10.1016/j.volgeores.2014.09.008

Burton, M., Ilyinskaya, E., La Spina, A., Salerno, G., Bergsson, B., Donovan, A., Barsotti, S., Pfeffer, M., 2015b. Contrasting gas compositions and fluxes produced by the Holuhraun 2014/2015 eruption and the Fimmvörðuháls 2010 eruption, Iceland. In: EGU General Assembly, Vienna.

Caltabiano, T., Burton, M., Giammanco, S., Allard, P., Bruno, N., Murè, F., Romano, R., 2004. Volcanic gas emissions from the summit craters and flanks of Mt. Etna, 1987– 2000.

In: Bonaccorso, A., Calvari, S., Coletelli, M., Del Negro, C., Falsaperla, S. (Eds.), Mt. Etna: Volcano Laboratory. AGU, Washington, D. C., pp. 111-128

Campion, R., Delgado-Granados, H., Mori, T., 2015. Image-based correction of the light dilution effect for SO_2 camera measurements. Journal of Volcanology and Geothermal Research, 300, 48-57, doi:10.1016/j.volgeores.2015.01.004

Campos, J. B. L. M., Guedes de Carvalho, J. R. F., 1988. An experimental study of the wake of gas slugs rising in liquids, Journal of Fluid Mechanics 196, 27-37, doi:10.1017/S0022112088002599

Cannata, A., Di Grazia, G., Aliotta, M., Cassisi, C., Montalto, P., Patanè, D., 2013a. Monitoring seismo-volcanic and infrasonic signals at volcanoes: Mt. Etna case study. Pure and Applied Geophysics, doi:10.1007/s00024-012-0634-x

Cannata, A., Montalto, P., Patanè, D., 2013b. Joint analysis of infrasound and seismic signals by cross wavelet transform: detection of Mt. Etna explosive activity. Natural Hazards and Earth Systems Science 13, 1669-1677, doi:10.5194/nhess-13-1669-2013

Capponi, A., Lane, S., James, M., 2014. Rheology contrast in the shallow conduit and eruption dynamics at Stromboli: insights from analogue experiments. In: EGU General Assembly 2014, Vienna.

Carbone, D., Poland, M.P., Patrick, M.R., Orr, T.R., 2013. Continuous gravity measurements reveal a low-density lava lake at Kilauea Volcano, Hawai'i. Earth and Planetary Science Letters 376, 178-185, doi:10.1016/j.epsl.2013.06.024

Carniel, R., Di Cecca, M., Rouland, D., 2003. Ambrym, Vanuatu (July-August 2000): spectral and dynamical transitions on the hours-to-days timescale. Journal of Volcanology and Geothermal Research 128 (1-3), 1-13, doi:10.1016/S0377-0273(03)00243-9

Carroll, M. R., Holloway, J. R., (Eds.) 1994. Volatiles in Magmas. Mineralogical Society of America Reviews in Mineralogy 30, Washington, D. C.

Cassidy, M., Cole, P. D., Hicks, K. E., Varley, N. R., Peters, N., Lerner, A. H., 2015. Rapid and slow: Varying magma ascent rates as a mechanism for Vulcanian explosions. Earth and Planetary Science Letters 420, 74-84, doi:10.1016/j.epsl.2015.03.025

Chapman, C. H., 2004. Fundamentals of Seismic Wave Propogation. Cambridge University Press: Cambridge. 608 pp

Chouet, B., Hamisevi, N., McGetchi, T. R., 1974. Photoballistics of volcanic jet activity at Stromboli, Italy. Journal of Geophysical Research 79 (32), 4961-4976, doi:10.1029/JB079i032p04961

Chouet, B., Saccorotti, G., Dawson, P., Martini, M., Scarpa, R., De Luca, G., Milana, G., Cattaneo, M., 1999. Broadband measurements of the sources of explosions at Stromboli Volcano, Italy. Geophysical Research Letters 26 (13), 1937-1940, doi:10.1029/1999GL900400

Chouet, B., Dawson, P., Ohminato, T., Martini, M., Saccorotti, G., Giudicpietro, F., De Luca, G., Milana, G., Scarpa, R., 2003, Source mechanisms of explosions at Stromboli Volcano, Italy, determined from moment-tensor inversions of very-long period data. Journal of Geophysical Research 108 (B1), doi:10.1029/2002JB001919

Chouet, B., Dawson, P., Martini, M., 2008. Shallow-conduit dynamics at Stromboli Volcano, Italy, imaged from waveform inversions, in Fluid Motion in Volcanic Conduits: A Source of Seismic and Acoustic Signals, edited by S. J. Lane and J. S. Gilbert, Geological Society Special Publication 307, 57–84.

Clift, R., Grace, J.R., Weber, M.E., 1978. Bubbles, drops, and particles. Dover publications: New York.

Colestock, M. A., 1993. Wavelets – A New Tool for Signal Processing Analysts. Digital Avionics Systems Conference, 1993. 12th DASC., AIAA/IEEE, pp. 54-59

Collins, S.J., Pyle, D.M., Maclennan, J., 2009. Melt inclusions track pre-eruption storage and dehydration of magmas at Etna. Geology 37 (6), 571-573, doi:10.1130/G30040A.1

Coltelli, M., Del Carlo, P., Vezzioli, L., 1998. Discovery of a Plinian basaltic eruption of Roman age at Etna volcano, Italy. Geology 26 (12), 1,095-1,098, doi:10.1130/0091-7613(1998)

Cook, M., Behnia, M., 2000. Slug length prediction in near horizontal gas-liquid intermittent flow. Chemical Engineering Science 55 (11), 2009-2018, doi:10.1016/S0009-2509(99)00485-6

Corder, S.B., 2008. The near-surface expansion of gas slugs: Insights into eruptive activity at low magma-viscosity volcanoes. PhD Thesis, Lancaster University, UK.

Corsaro, R. A., Pompilion, M., 2004. Magma dynamics in the shallow plumbing system of Mt. Etna as recorded by compositional variations in volcanic of recent summit activity (1995-1999). Journal of Volcanology and Geothermal Research 137, 55-71, doi:10.1016/j.volgeores.2004.05.008

Corsaro, R. A., Di Renzo, V., Distefano, S., Miraglia, L., Civetta, L., 2013. Relationship between petrologic processes in the plumbing system of Mt. Etna and the dynamics of the eastern flank from 1995 to 200. Journal of Volcanology and Geothermal Research 251 (1), 75-89, doi:10.1016/j.volgeores.2012.02.010

Costigan, G., Whalley, P.B., 1997. Slug flow regime identification from dynamic void fraction measurements in vertical air-water flows. International Journal of Multiphase Flow 23 (2), 263-282, doi: 10.1016/S0301-9322(96)00050-X

Costa, A., Macedonio, G., Chiodini, G., 2005. Numerical model of gas dispersion emitted from volcanic sources. Annals of Geophysics 48 (4/5), 805–815, doi:10.4401/ag-3236

Courant, R., Friedrichs, K., Lewy, H., 1967. On the partial difference equations of mathematical physics. IBM Journal of Research and Development 11 (2), doi:10.1147/rd.112.0215

Dalton, M. P., Waite, G. P., Watson, I. M., Nadeau, P. A., 2010. Multiparameter quantification of gas release during weak Strombolian eruptions at Pacaya volcano, Guatemala, Geophys. Res. Lett. 37 (L09303), doi:10.1029/2010GL042617

Daubechies, I., 1990. The wavelet transform time-frequency localization and signal analysis. IEEE Transactions on Information Theory 36, 961-1004, doi:10.1109/18.57199

Davies, R. M., Taylor, G. I., 1950. The mechanics of large bubbles rising through extended liquids and through liquids in tubes. Proceedings of the Royal Society, London A200, 375-390, doi:10.1098/rspa.1950.0023

Davies, A., 2007. Volcanism on Io: A comparison with Earth. Cambridge University Press: Cambridge.

De Barros, L., Bean, C. J., Lokmer, I., Saccorotti, G., Zuccarello, L., O'Brien, G. S., Métaxian, J-P., Patane, D., 2009. Source geometry from exceptionally high resolution long period event observations at Mt Etna during the 2008 eruption. Geophysical Research Letters 36 (L24305), doi:10.1029/2009GL041273

Del Bello, E., Llewellin, E. W., Taddeuicci, J., Scarlato, P., Lane, S. J., 2012. An analytical model for gas overpressure in slug-drive explosions: Insights into Strombolian volcanic eruptions. Journal of Geophysical Research: Solid Earth 117 (B2), doi:10.1029/2011JB008747

Del Bello, E., Lane, S.J., James, M.R., Llewellin, E.W., Taddeucci, J., Scarlato, P., Capponi, A., 2015. Viscous plugging can enhance and modulate explosivity of strombolian eruptions. Earth and Planetary Science Letters 423, 210-218, doi:10.1016/j.epsl.2015.04.034

Del Carlo, P., Pompilio, M., 2004. The relationship between volatile content and the eruptive style of basaltic magma: the Etna case. Annali di Geofisica 47 (4), doi:10.4401/ag-4402

Delle Donne, D, Ripepe, M., 2012. High-frame rate thermal imagery of Strombolian explosions: Implications for explosive and infrasonic source dynamics. Journal of Geophysical Research: Solid Earth 117 (B9), doi:10.1029/2011JB008987

Delmelle, P., Stix, P., Baxter, P., Garcia-Alvarez, J., Barquero, J., 2002. Atmospheric dispersion, environmental effects and potential health hazard associated with the low-altitude gas plume of Masya volcano, Nicaragua. Bulletin of Volcanology 64 (6), 423-434, doi:10.1007/s00445-002-0221-6

Dingwell, D.B., Webb, S.L., 1989. Structural Relaxation in Silicate melts and Non-Newtonian Melt Rheology in Geologic Processes. Physics and Chemistry and Minerals 16 (5), 508-516, doi:10.1007/BF00197020

Dukler, A.E., Maron, D.M., Brauner, N., 1985. A physical model for predicting the minimum stable slug length. Chemical Engineering Science 40 (8), 1,379-1,385, doi:10.1016/0009-2509(85)80077-4

Elias, T., Sutton, A.J., Stokes, J.B., Casadevall, T.J., 1998. Sulfur Dioxide Emission Rates of Kilauea Volcano, Hawai'I, 1979-1997. U.S. Geological Survey Open-File Report 98-462

Endo, E. T., Murray, T., 1991. Real-time seismic amplitude measurement (RSAM) – a volcano monitoring and prediction tool. Bulletin of Volcanology 53 (7), pp. 533-545, doi: 10.1007/BF00298154

Fabre, J., Liné, A., 1992. Modeling of two-phase slug flow. Annual Reviews of Fluid Mechanics 24, 21-46, doi:10.1146/annurev.fl.24.010192.000321

Fernandes, R.C., 1981. Experimental and theoretical studies of isothermal upward gas-liquid flows in vertical tubes. PhD Thesis. Univ. Houston.

Fernandes, R.C., Semiat, R., Dukler, A.E., 1983. A hydrodynamic model for gas-liquid slug flow in vertical tubes. American Institute of Chemical Engineers 29, 981-989, doi:10.1002/aic.690290617

Ferrick, M.G., Qamar, A., Lawrence, W.F.St., 1982. Source Mechanism of Volcanic Tremor. Journal of Geophysical Research 87 (B10), 8,675-8,683, doi:10.1029/JB087iB10p08675

Figueroa-Espinoza, B., Fabre, J., 2011. Taylor bubble moving in a flowing liquid in vertical channel: transition from symmetric to asymmetric shape. Journal of Fluid Mechanics 679, 432-454, doi:10.1017/jfm.2011.159

Fitremann, J.M., 1977. Ecoulements diphasiques: theorie et application a l'etude de quelques regimes d'ecoulements verticaux ascendants d'un melange gaz-liquide. These Univ. Pierre et Maric Curie, Paris.

Francis, P., Burton, M.R., Oppenheimer, C., 1998. Remote measurements of volcanic gas compositions by solar occultation spectroscopy. Nature 396, 567-570, doi:10.1038/25115

Fréhou, D., 1986. Etude de l'ecoulement ascendant a trois fluids en conduit vertical. These Inst. Natl. Polytech, Toulouse.

Fulford, G.D., 1964. The flow of liquids in thin films. Advances in Chemical Engineering 5, 151–236. doi:10.1016/S0065-2377(08)60008-3

Galle, B., Oppenheimer, C., Geyer, A., McGonigle, A. J. S. Edmonds, M., Horrocks, L., 2003. A miniaturised ultraviolet spectrometer for remote sensing of SO_2 fluxes: a new tool for volcano surveillance. Journal of Volcanology and Geothermal Research 119 (1-4), 241-254, doi:10.1016/S0377-0273(02)00356-6

Galle, B., Arellano, S., Conde, V., Pfeffer, M., Barsotti, S., Stefansdottir, G., Bergsson, B., Bergsson, B., Ingvarsson, T., Weber, K., 2015. Ground based measurements of the gas emission from the Holuhraun volcanic fissure eruption on Iceland 2014/2015. In: EGU General Assembly 2015: Vienna.

Ganci, G., Harris, A.J.L., Del Negro, C., Guehenneux, Y., Cappello, A., Labazuy, P., Calvari, S., Gouhier, M., 2012. A year of lava fountaining at Etna: Volumes from SEVIRI. Geophysical Research Letters 39 (6), doi: 10.1029/2012GL051026

Gaudin, D., Taddeucci, J., Harris, A., Orr, T., Bombrun, M., Scarlato, P., 2014a. When Puffing Meets Strombolian Explosions: A Tale of Precursors and Coda. In: EGU General Assembly 2014, Vienna.

Gaudin, D., Taddeucci, J., Scarlato, P., Moroni, M., Freda, C., Gaeta, M., Palladino, D.M., 2014b. Pyroclast tracking velocimetry illuminates bomb ejection and explosion dynamics at Stromboli (Italy) and Yasur (Vanuatu) volcanoes. Journal of Geophysical Research: Solid Earth 119 (7), 5,384-5,397, doi:10.1002/2014JB011096

Gerlach, T.M., 1986. Exsolution of H_2O, CO_2, and S During Eruptive Episodes at Kilauea Volcano, Hawaii. Journal of Geophysical Research 91 (B12), 12,177-12,185, doi:10.1029/JB091iB12p12177

Gerlach, T. M., 1991. Present-day CO_2 emissions from volcanoes. EOS Transactions AGU 72 (249), 254-255, doi:10.1029/90EO10192

Giggenbach, W.F., 1975. A simple method for the collection and analysis of volcanic gas samples. Bulletin of Volcanology 39 (1), 132-145, doi: 10.1007/BF02596953

Giggenbach, W. F., 1996. Chemical composition of volcanic gases. In: Scarpa, R., Tilling, R. I. (Eds.), Monitoring and Mitigation of Volcanic Hazards. Springer, New York, pp. 221-256

Gilbert, J.S., Lane, S.J., 2008. The consequences of fluid motion in volcanic conduits. Geological Society, London, Special Publications 307, 1-10, doi:10.1144/SP307.1

Giordano, D., Dingwell, D., 2003. Viscosity of hydrous Etna basalt: implications for Plinian-style basaltic eruptions. Bulletin of Volcanology 65 (1), 8-14, doi:10.1007/s00445-002-0233-2

Girona, T., Costa, F., Taisne, B., Aggangan, B., Ildefonso, S., 2015. Fractal degassing from Erebus and Mayon volcanoes revealed by a new method to monitor H_2O emission cycles. Journal of Geophysical Research: Solid Earth 120 (5), 2,988-3,002, doi:10.1002/2014JB011797

Gonnermann, H.M., Manga, M., 2003. Explosive volcanism may not be an inevitable consequence of magma fragmentation. Nature 426, 432-435, doi:10.1038/nature02138

Grace, J.R., Wairegi, T., Brophy, J., 1978. Break-up of drops and bubbles in stagnant media. The Canadian Journal of Chemical Engineering 56 (1), 3-8, doi:10.1002/cjce.5450560101

Greenland, L.P., Rose, W.I., Stokes, J.B., 1985. An estimate of gas emissions and magmatic gas content from Kilauea volcano. Geochemica et Cosmochimica Acta 49 (1), 125-129, doi:10.1016/0016-7037(85)90196-6

Grinstead, A., Moore, J. C., Jevrejeva, S., 2004. Application of the cross wavelet transform and wavelet coherence to geophysical time series. Nonlinear Processes in Geophysics 11, 561-566, doi:10.5194/npg-11-561-2004

Gudmundsson, M.T., Pederson, R., Vogfjord, K., Thorbjarnardottir, B., Jakobsdottir, S., Roberts, M.J., 2010. Eruptions of Eyjafjallajokull Volcano, Iceland. Eos, Transactions American Geophysical Union 91 (21), 190-191, doi:10.1029/2010EO210002

GVP, 2013. Etna. (Online) Available at: http://www.volcano.si.edu/volcano.cfm?vn=211060

GVP, 2015. Stromboli. (Online) Available at: http://volcano.si.edu/volcano.cfm?vn=211040

Hansell, A., Oppenheimer, C., 2004. Health Hazards from Volcanic Gases: A systematic Literature Review. Archives of Environmental Health: An International Journal 59 (12), 628-639, doi:10.1080/00039890409602947

Harlow, D.H., Power, J.A., Laguerta, E.P., Ambubuyog, G., White, R.A., Hoblitt, R.P., 1999. Precursory Seismicity and Forecasting o the June 15, 1991, Eruption of Mount Pinatubo. USGS Report

Harris, F. J., 1978. Use of windows for harmonic-analysis with Discrete Fourier-Transform. Proceedings of the IEEE 66 (1), 51-83, doi:10.1109/PROC.1978.10837

Harris, A.J.L., Stevenson, D.S., 1997. Thermal observations of degassing open conduits and fumaroles at Stromboli and Vulcano using remotely sensed data. Journal of Volcanology and Geothermal Research 76, 175-198, doi:10.1016/S0377-0273(96)00097-2

Harris, A.J.L., Dehn, J., Calvari, S., 2007. Lava effusion rate definition and measurement: a review. Bulletin of Volcanology 70, 1-22, doi:10.1007/s00445-007-0120-y

Hasan, A.R., Kabir, C.S., 1992. Two-phase flow in vertical and inclined annuli. International Journal of Multiphase Flow 18 (2), 279-293, doi:10.1016/0301-9322(92)90089-Y

Hendrix, A. R., Vilas, F., Festou, M. C., 2003. Vesta's UV lightcurve: hemispheric variation in brightness and spectral reversal. Icarus 162 (1), 1-9, doi:10.1016/S0019-1035(02)00070-2

Herd, R.A., Pinkerton, H., 1997. Bubble coalescence in basaltic lava: Its impact on the evolution of bubble populations. Journal of Volcanology and Geothermal Research 75 (1-2), doi:10.1016/S0377-0273(96)00039-X

Hinze, J.O., 1955. Fundamentals of the Hydrodynamic Mechanism of Splitting in Dispersion Processes. American Institute of Chemical Engineers J 1, 289, doi:10.10002/aic.690010303

Holland, A. S. P., Watson, M, I,, Phillips, J. C., Caricchi, L., Dalton, M. P., 2011. Degassing processes during lava dome growth: Insights from Santiaguito lava dome, Guatemala. Journal of Volcanology and Geothermal Research 202 (1-2), 153-166, doi:10.1016/j.volgeores.2011.02.004

Horn B.K.P., Schunck B.G., 1981. Determining optical flow. Artificial Intelligence 17, pp 185–203, doi:10.1016/0004-3702(81)90024-2

Huang, N. E., Shen, Z., Long, S. R., Lu, M. C., Shih, H. H., Zheng, Q., Yen, N-C., Tung, C. C., Liu, H. H., 1998. The Empirical Mode Decomposition and the Hilbert Spectrum for Nonlinear and Non-stationary Time Series Analysis. Proceedings: Mathematical, Physical and Engineering Sciences 454 (1971), 903-995, doi:10.1098/rspa.1998.0193

Hurrell, J. W., 1995. Decadal trends in the North-Atlantic Oscillation – Regional Temperatures and Precipitation. Science 269 (5224), 676-679, doi:10.1126/science.269.5224.676

Hurrell, J.W., Y. Kushnir, G. Ottersen, and M. Visbeck, Eds., 2003. The North Atlantic Oscillation: Climate Significance and Environmental Impact. American Geophysical Union Geophysical Monograph Series, 134, 279pp.

Ilanko, T., Oppenheimer, C., Burgisser, A., Kyle, P., 2015a. Cyclic degassing of Erebus volcano, Antarctica. Bulletin of Volcanology 77, doi:10.1007/s00445-015-0941-z

Ilanko, T., Oppenheimer, C., Burgisser, A., Kyle, P., 2015b. Transient degassing events at the lava lake of Erebus volcano, Antarctica: Chemistry and mechansims. GeoResJ 7, 43-58, doi:10.1016/j.grj.2015.05.001

James, M. R., Lane, S. J., Chouet, B., Gilbert, J. S., 2004. Pressure changes associated with the ascent and bursting of gas slugs in liquid=filled vertical and inclined conduits. Journal of Volcanology and Geothermal Research 129, 61-82, doi:10.1016/S0377-0273(03)00232-4

James, M. R., Lane, S. J., Chouet, B. A., 2006. Gas slug ascent through changes in conduit diameter: Laboratory insights into a volcano-seismic source process in low-viscosity magmas. Journal of Geophysical Research 111 (B05201), doi:10.1029/2005JB003718

James, M.R., Lane, S. J., Corder, S. B., 2008. Modelling the rapid near-surface expansion of gas slugs in low-viscosity magmas. Geological Society, London, Special Publications 307, 147-167, doi:10.1144/SP307.9

James, M. R., Lane, S. J., Wilson, L., Corder, S. B., 2009. Degassing at low magma-viscosity volcanoes: Quantifying the transition between passive bubble-burst and Strombolian eruption. Journal of Volcanology and Geothermal Research 180, 81-88, doi:10.1016/j.volgeores.2008.09.002

James, M.R., Llewellin, E.W., Lane, S.J., 2011. Comment on "It takes three to tango: 2. Bubble dynamics in basaltic volcanoes and ramifications for modelling normal Strombolian activity" by J. Suckale, B.H. Hager, L.T. Elkins-Tanton, and J.-C. Nave. Journal of Geophysical Research 116 (B6), doi:10.1029/2010JB008167

James, M.R., Lane, S.J., Houghton, B.F., 2013. Unsteady explosive activity: strombolian eruptions. In: Modeling Volcanic Processes: The Physics and Mathematics of Volcanism, eds. S.A. Fagents, T.K.P. Gregg, R.M.C. Lopes. 107-129

Jaupart, C., 1998. Gas loss from magmas through conduit walls during eruption. In: The Physics of Explosive Volcanic Eruptions, eds: J.S. Gilbert & R.S.J. Sparks.

Jaupart, C., Vergniolle, S., 1988. Laboratory models of Hawaiian and Strombolian eruptions. Nature 331, 58-60, doi:10.1038/331058a0

Jaupart, C., Vergniolle, S., 1989. The generation and collapse of a foam layer at the roof of a basaltic magma chamber. Journal of Fluid Mechanics 203, 347-380, doi:10.1017/S0022112089001497

Kaminski, E., Tait, S., Carazzo, G., 2005. Turbulent entrainment in jets with arbitrary buoyancy. Journal of Fluid Mechanics 526, 361-376, doi:10.1017/S0022112004003209

Kantzas, E. P., McGonigle, A. J. S., Tamburello, G., Aiuppa, A., Bryant, G., 2010. Protocols for UV camera volcanic SO_2 measurements. Journal of Volcanology and Geothermal Research 194, 55-60, doi:10.1016/j.volgeores.2010.05.003

Kawaji, M., DeJesus, J.M., Tudose, G., 1997. Investigation of flow structures in vertical slug flow. Nuclear Engineering and Design 175 (1-2), 37-48, doi:10.1016/S0029-5493(97)00160-X

Karapantsios, T.D., Paras, S.V., Karabelas, A.J., 1989. Statistical characteristics of free falling films at high Reynolds numbers. International Journal of Multiphase Flow 15, 1–21. doi:10.1016/0301-9322(89)90082-7

Kazahaya, K., Shinohara, H., Saito, G., 1994. Excessive degassing of Izu-Oshima volcano: magma convection in a conduit. Bulletin of Volcanology 56, 207-216, doi:10.1007/BF00279605

Kazahaya, K, Shinohara, H., Saito, G., 2002. Degassing process of Satsuma-Iwojima volcano, Japan: Supply of volatile components from a deep magma chamber. Earth Planets Space 54, 327-335, doi:10.1186/BF03353031

Kazahaya, R., Mori, T., Takeo. M., Ohminato, T., Urabe, T., Maeda, Y., 2011. Relation between single very-long-period pulses and volcanic gas emissions at Mt. Asama, Japan. Geophysical Research Letters 38 (L11307), doi:10.1029/2011GL047555

Keating, G.N., Valentine, G.A., Krier, D.J., Perry, F.V., 2008. Shallow plumbing systems for small-volume basaltic volcanoes. Bulletin of Volcanology 70 (5), 563-582, doi:10.1007/s00445-007-0154-1

Kern, C., Deutschmann, T., Vogel, L., Wöhrbach, M., Wagner, T., Platt, U. 2010a. Radiative transfer corrections for accurate spectroscopic measurements of volcanic gas emissions. Bulletin of Volcanology 72, 233-247, doi: 10.1007/s00445-009-0313-7

Kern, C., Kick, F., Lübcke, P., Vogel, L., Wöhrbach, M., Platt, U., 2010b. Theoretical description of functinoality, applications, and limitations of SO_2 cameras for the remote sensing of volcanic plumes. Atmospheric Measurement Techniques 3, 733-749, doi:10.5194/amt-3-733-2010

Kern, C., Werner, C., Elias, T., Sutton, A.J., Lubcke, P., 2013. Applying UV cameras for SO_2 detection to distant or optically thick volcanic plumes. Journal of Volcanology and Geothermal Research 262, 80-89, doi:10.1016/j.volgeores.2013.06.009

Kern, C., Lubcke, P., Bobrowski, N., Campion, R., Mori, T., Smekens, J-F., Stebel, K., Tamburello, G., Burton, M., Platt, U., Prata, F., 2015. Intercomparison of SO2 camera systems for imaging volcanic gas plumes. Journal of Volcanology and Geothermal Research 300, 22-36, doi:10.1016/j.volgeores.2014.08.026

Koepenick, K. Brantley, S., Thompson, J., Rowe, G., Nyblade, A., Moshy, C., 1996. Volatile emissions from the crater and flank of Oldoinyo Lengai volcano, Tanzania. Journal of Geophysical Research 10, 13,819-13,830, doi:10.1029/96JB00173

Koyaguchi, T., Hallworth, M. A., Huppert, H. E., 1993. An experimental study on the effects of phenocrysts on convection in magmas. Journal of Volcanology and Geothermal Research 55, 15-32, doi:10.1016/0377-0273(93)90087-8

Kremers, S., Lavallée, Y., Hanson, J., Hess, K-U., Chevrel, M.O., Wassermann, J., Dingwell, D.B., 2012. Shallow magma-mingling-driven Strombolian eruptions at Mt. Yasur volcano, Vanuatu. Geophysical Research Letters 39 (21), doi:10.1029/2012GL053312

Kremers, S., Wassermann, J., Meier, K., Pelties, C., van Driel, M., Vasseur, J., Hort, M., 2013. Inverting the source mechanism of Strombolian explosions at Mt. Yasur, Vanuatu, using a multi-parameter dataset. Journal of Volcanology and Geothermal Research 262, 104-122, doi:10.1016/j.volgeores.2013.06.007

Krishna, R., Urseanu, M. I., van Baten, J. M., Ellenberger, J., 1999. Rise velocity of a swarm of large gas bubbles in liquids. Chemical Engineering Science 54, 171-183, doi:10.1016/S0009-2509(98)00245-0

Krueger, P.S., 2005. An over-pressure correction to the slug model for vortex ring circulation. Journal of Fluid Mechanics 545, doi:10.1017/S0022112005006853

Lane, S.J., Chouet, B.A., Phillips, J.C., Dawson, P., Ryan, G.A., Hurst, E., 2001. Experimental observations of pressure oscillations and flow regimes in an analogue volcanic system. Journal of Geophysical Research 106 (B4), 6,461-6,476, doi:10.1029/2000JB900376

Lane, S. J., James, M. R., Corder, S. B., 2013. Volcanic infrasonic signals and magma degassing: First-order experimental insights and application to Stromboli. Earth and Planetary Science Letters 377-378, 169-179, doi:10.1016/j.epsl.2013.06.048

Lavergne, M., 1989. Seismic Methods. Editions Technip, Paris. 182 pp

Lel, V.V., Al-Sibai, F., Leefken, A., Renz, R., 2005. Local thickness and wave velocity measurement of wavy films with a chromatic confocal imaging method and a fluorescence intensity technique. Experiments in Fluids, 39, 856–864, doi:10.1007/s00348-005-0020-x

Llewellin, E. W., Del Bello, E., Taddeucci, J., Scarlato, P., Lane, S. J., 2012. The thickness of the falling film of liquid around a Taylor bubble. Proceedings of the Royal Society A 468, doi:10.1098/rspa.2011.0476

Llewellin, E., Del bello, E., Lane, S.J., Capponi, A., Mathias, S., Taddeucci, J., 2013. Cyclicity in slug-driven basaltic eruptions: insights from large-scale analogue experminets. In: EGU General Assembly, Vienna.

Llewellin, E.W., Burton, M.R., Mader, H.M., Polacci, M., 2014a. Conduit speed limit promotes formation of explosive ‘super slugs’. In: AGU Fall Meeting, San Francisco.

Llewellin, E.W., Truby, J., Mueller, S.P., Mader, H.M., 2014b. The Rheology of Three-Phase Basaltic Magma. In: AGU Fall Meeting, San Francisco.

Liu, H., Vandu, C.O., Krishna, R., 2005. Hydrodynamics of Taylor Flow in Vertical Capillaries: Flow Regimes, Bubble Rise Velocity, Liquid Slug Length, and Pressure Drop. Industrial & Engineering Chemistry Research 44 (14), 4884-4897, doi:10.1021/ie049307n

Lockwood, M., 2012. Solar influence on global and regional climates. Surveys in Geophysics, 33 (3-4), pp. 503-534. doi: 10.1007/s10712-012-9181-3

Lübcke, P., Bobrowski, N., Illing, S., Kern, C., Alvarez Nievez, J. M. Vogel, L., Zielcke, J., Delgado Granados H., Platt, U., 2013. On the absolute calibration of SO_2 cameras. Atmospheric Measurement Techniques 6, 677-696, doi:10.5194/amt-6-677-2013

Manga, M., 1996. Waves of bubbles in basaltic magmas and lavas. Journal of Geophysical Research 101 (B8), 17,457-17,465, doi:10.1029/96JB01504

Mangan, M.T., Cashman, K.V., Newman, S., 1993. Vesiculation of basaltic magma during eruption. Geology 21 (2), 157-160, doi:10.1130/0091-7613(1993)021

Martini, F., Bean, C. J., Saccorotti, G., Viveiros, F., Wallenstein, N., 2009. Seasonal cycles of seismic velocity variations detected using coda wave interferometry at Fogo volcano, São Miguel, Azores, during 2003-2004. Journal of Volcanology and Geothermal Research 181, 231-246, doi:10.1016/j.volgeores.2009.01.015

Masella, J.M., Tran, Q.H., Ferre, D., Pauchon., C., 1998. Transient simulation of two-phase flows in pipes. International Journal of Multiphase Flow 24 (5), 739-755, doi:10.1016/S0301-9322(98)00004-4

Mastin, L.G., 2002. Insights into volcanic conduit low from an open-source numerical model. Geochemistry, Geophysics, Geosystems 3 (7), 1-18, doi:10.1029/2001GC000192

Mather, T.A., 2015. Volcanoes and the environment: Lessons for understanding Earth's past and future from studies of present-day volcanic emissions. Journal of Volcanology and Geothermal Research 304, 160-179, doi:10.1016/j.volgeores.2015.08.016

Matoza, R.S., Fee, D., Nielson, T.B., Gee, K.L., Ogden, D.E., 2013. Aeroacoustics of volcanic jets: Acoustic power estimation and jet velocity dependence. Journal of Geophysical Research: Solid Earth 118, 6269-6284, doi:10.1002/2013JB010303

Matsui, G., 1984. Identification of flow regimes in vertical gas-liquid two-phase flwo using differential pressure fluctuations. International Journal of Multiphase Flow 10 (6), 711-719, doi:10.1016/0301-9322(84)90007-7

McCormick, B.T., Cottrell, E., Lopez, O.G., Venzke, E., Mather, T.A., Pyle, D.M., 2013. Towards improved volcanic emissions budgets: opportunities arising from a new global database of volcanic degassing data. In: AGU Fall Meeting 2013, San Francisco.

McCormick, B.T., Herog, M., Yang, J., Edmonds, M., Mather, T.A., Carn, S.A., Hidalgo, S., Langmann, 2014. A comparison of satellite and ground-based measurements of SO_2 emissions from Tungurahua volcano, Ecuador. Journal of Geophysical Research: Atmospheres 119 (7), 4,264-4,285, doi:10.1002/2013JD019771

McGonigle, A.J.S., Oppenheimer, C., Galle, B., Mather, T.A., Pyle, D.M., 2002. Walking traverse and scanning DOAS measurements of volcanic gas emission rates. Geophysical Research Letters 29 (20), doi:10.1029/2002GL015827

McGonigle, A. J. S., Hilton, D. R., Fischer, T. P., Oppenheimer, C., 2005. Plume velocity determination for volcanic SO_2 flux measurements. Geophysical Research Letters 32 (L11302), doi:10.1029/2005GL022470

McGonigle, A.J.S., 2007. Measurement of volcanic SO_2 fluxes with differential optical absorption spectroscopy. Journal of Volcanology and Geothermal Research 162 (3-4), doi:10.1016/j.volgeores.2007.02.001

McGonigle, A. J. S., Aiuppa, A., Ripepe, M., Kantzas, E. P., Tamburello, G., 2009. Spectroscopic capture of 1 Hz volcanic SO_2 fluxes and integration with volcano geophysical data. Geophysical Research Letters 36 (L21309), doi:10.1029/2009GL040494

Métrich, N., Clocchiatti, R., 1989. Melt inclusion investigation of the volatile behaviour in historic alkali basaltic magmas of Etna. Bulletin of Volcanology 51 (3), 185-198, doi:10.1007/BF01067955

Métrich, N., Clocchiatti, R., Mosbah, M., Chaussidon, M., 1993. The 1989-1990 activity of Etna magma mingling and ascent of H2O-Cl-S-rich basaltic magma. Evidence from melt inclusions. Journal of Volcanology and Geothermal Research 59 (1-2), 131-144, doi:10.1016/0377-0273(93)90082-3

Métrich, N., Rutherford, M. J., 1998. Low pressure crystallization paths of H_2O-saturated basaltic-hawaiitic melts from Mt. Etna: Implications for open-system degassing of basaltic volcanoes. Geochemica et Cosmochimica Acta 62 (7), 1195-1205, doi:10.1016/S0016-7037(98)00048-9

Métrich, N., Bertagnini, A., Landi, P., Rosi, M., 2001. Crystallization driven by decompression and water loss at Stromboli volcano (Aeolian Islands, Italy). Journal of Petrology 42, 1471-1490, doi:10.1093/petrology/42.8.1471

Métrich, N., Allard, P., Spilliaert, N., Andronico, D., Burton, M., 2004. 2001 flank eruption of the alkali- and volatile-rich primitive basalt responsible for Mount Etna's evolution in the last three decades. Earth and Planetary Science Letters 228, 1–17, doi:10.1016/j.epsl.2004.09.036

Métrich, N., Mandeville, C.W., 2010. Sulfur in magmas. Elements 6, 81–86, doi: 10.2113/gselements.6.2.81

Moffat, A.J., Millán, M.M, 1971. The application of optical correlation techniques to the remote sensing of SO_2 plumes using sky light. Atmospheric Environment 5, 677-690, doi:10.1016/0004-6981(71)90125-9

Moffat, A.J., Robbins, J.R., Barringer, A.R., 1971. Electro-optical sensing of environmental pollutants. Atmospheric Environment 5, 511-525, doi:10.1016/0004-6981(71)90062-X

Moissis, R., Griffith, P., 1962. Entrance effects in a two-phase slug flow. Journal of Heat Transfer 84, 29-39, doi:10.1115/1.3684284

Mori, T., Burton, M., 2006. The SO_2 camera: a simple, fast and cheap method for ground-based imaging of SO_2 in volcanic plumes. Geophysical Research Letters 33 (L24804), doi:10.1209/2006GL027916

Mori, T., Burton, M., 2009. Quantification of the gas mass emitted during single explosions on Stromboli with the SO_2 imaging camera. Journal of Volcanology and Geothermal Research 188, 395-400, doi:10.1016/j.volgeores.2009.10.005

Morlet, J., Arens, G., Fourgeau, E., Giard, D., 1982. Wave propagation and sampling theory – Part 1: Complex signal and scattering in multilayered media. Geophysics 47 (2), 203-221, doi:10.1190/1.1441328

Moussallam, Y., Oppenheimer, C., Scaillet, B., Kyle, P.R., 2013. Experimental Phase-equilibrium Constaints on the Phonolite Magmatic System of Erebus Volcano, Antarctica. Journal of Petrology 54 (7), 1,285-1,307, doi:10.1093/petrology/egt012

Moussallam, Y., Oppenheimer, C., Scaillet, B., Buisman, I., Kimball, C., Dunbar, N., Burgisser, A., Schipper, C.I., Andujar, J., Kyle, P., 2015. Megacrystals track magma convection between reservoir and surface. Earth and Planetary Science Letters 413, 1-12, doi:10.1016/j.epsl.2014.12.022

Nabyl. A., Dorel, J., Lardy, M., 1997. A comparative study of low-frequency seismic signals recorded at Stromboli volcano, Italy, and at Yasur volcano, Vanuatu. New Zealand Journal of Geology and Geophysics 40 (4), doi:10.1080/00288306.1997.9514783

Nadeau, P.A., Palma, J. L., Waite, G. P., 2011. Linking volcanic tremor, degassing, and eruption dynamics via SO_2 imaging. Geophysical Research Letters 38 (L01304), doi:10.1029/2010GL045820

National Geographic, 2008. Chile volcano erupts with ash and lightning. [online]. Available at: http://news.nationalgeographic.com/news/2008/05/photogalleries/volcano-photos/index.html (Accessed 28th August 2015)

Newcomb, G.S., Millán, M.M., 1970. Theory, applications and results of the long-line correlation spectrometer. IEEE Transactions Geoscience Electronics GE-8, 149-157, doi:10.1109/TGE.1970.271410

Newman, S., Lowenstern, J. B., 2002. VOLATILECALC: A silicate melt-H_2O-CO_2 solution model written in Visual Basic for excel. Computers and Geoscience 28 (5), 597-604, doi:10.1016/S0098-3004(01)00081-4

Nogueira, S., Riethmuller, M. L., Campos, J. B. L. M., Pinto, A. M. F. R., 2006. Flow patterns in the wake of a Taylor bubble rising through vertical columns of stagnant and flowing Newtonian liquids: An experimental study. Chemical Engineering Science 61, 7,199-7,212, doi:10.1016/j.ces.2005.07.038

Nyquist, H., 2002. Certain topics in telegraph transmission theory (Reprinted from Transactions of the A. I. E. E., February, pg 617-644, 1928). Proceedings I. E. E. E. 90 (2), 280-305, doi:10.1109/5.989875

O'Brien, G. S., Bean, C. J., 2008. Seismicity on volcanoes generated by gas slug ascent. Geophysical Research Letters 25 (L16308), doi:10.1029/2008GL035001

Ohwada, M., Kazahaya, K., Mori, T., Kazahaya, R., Hirabayashi, J., Miyashita, M., Onizawa, S., Mori, T., 2013. Sulfur dioxide emissions related to volcanic activity at Asama volcano. Japan. Bulletin of Volcanology 73, doi: 10.1007/s00445-013-0775-5

Olmos, R., Barrancos, J., Rivera, C., Barahona, F., López, D.L., Henriquex, B., Hernández, A., Benitez, E., Hernández, P.A., Pérez, N.M., Galle, B., 2007. Anomalous Emissions of SO_2 During the Recent Eruption of Santa Ana Volcano, El Salvador, Central America. Pure Applied Geophysics 164, 2,489-2,506, doi:10.1007/s00024-007-0276-6

Oppenheim, A.V., Schafer, R.W., Buck, J.R., 1999. Discrete-Time Signal Processing, second ed. Prentice Hall, New Jersey.

Oppenheimer, C., Francis, P., Burton, M., Maciejewski, A.J.H., Boardman, L., 1998. Remote measurement of volcanic gases by Fourier transform infrared spectroscopy. Applied Physics B: Lasers and Optics 67 (4), 505-515, doi:10.1007/s003400050536

Oppenheimer, C., Lomakina, A. S., Kyle, P. R., Kingsbury, N. G., Boichu, M., 2009. Pulsatory magma supply to a phonolite lava lake. Earth and Planetary Science Letters 284, 392-398, doi:10.1016/j.epsl.2009.04.043

Palma, J. L., Calder, E. S., Basualto, D., Blake, S., Rothery, D. A., 2008. Correlations between SO_2 flux, seismicity, and outgassing activity at the open vent of Villarrica volcano, Chile. Journal of Geophysical Research 113 (B10201), doi:10.1029/2008JB005577

Palma, J. L., Blake, S., Calder, E. S., 2011. Constraints on the rates of degassing and convection in basaltic open-vent volcanoes. Geochemistry, Geophysics, Geosystems 12 (11), doi :10.1029/2011GC003715

Parfitt, E.A., Wilson, L., 1994. The 1983-86 Pu'u 'O'o eruption of Kilauea Volcano, Hawaii: a study of dike geometry and eruption mechanisms for a long-lived eruption. Journal of Volcanology and Geothermal Research 59 (3), 179-205, doi:10.10116/0377-0273(94)90090-6

Parfitt, E. A., Wilson, L., 1995. Explosive volcanic eruptions – IX. The transition between Hawaiian-style lava fountaining and Strombolian explosive activity. Geophysical Journal International 121 (1), 226-232, doi:10.1111/j.1365-246X.1995.tb03523.x

Parfitt, E.A., Wilson, L., Neal, C.A., 1995. Factors influencing the height of Hawaiian lava fountains: implications for the use of fountain height as an indicator of magma gas content. Bulletin of Volcanology 57, 44-450, doi:10.1007/BF00300988

Parfitt, E.A., 2004. A discussion of the mechanisms of explosive basaltic eruptions. Journal of Volcanology and Geothermal Research 134 (1-2), 77-107, doi:10.1016/j.jvolgeores.2004.01.002

Patrick, M.R., 2007. Dynamics of Strombolian ash plumes from thermal video: Motion, morphology, and air entrainment. Journal of Geophysical Research: Solid Earth 112 (B6), doi:10.1029/2006JB004387

Pering, T. D., Tamburello, G., McGonigle, A. J. S., Aiuppa, A., Cannata, A., Giudice, G., Patanè, D., 2014a. High time resolution fluctuations in volcanic carbon dioxide degassing from Mount Etna. Journal of Volcanology and Geothermal Research 270, 115-121, doi:10.1016/j.volgeores.2013.11.014

Pering, T.D., Tamburello, G., McGonigle, A.J.S., Hanna, E., Aiuppa, A., 2014b. Correlation of oscillatory behaviour in Matlab using wavelets. Computers & Geosciences 70, 206-212, doi:10.1016/j.cageo.2014.06.006

Pering, T.D., McGonigle, A.J.S., James, M.R., Lane, S.J., Capponi, A., Tamburello, G., Aiuppa, A., 2014c. Observations on Multi-Slug Activity-Implications for Volcanic Processes. In: AGU Fall Meeting 2014, San Francisco.

Pering, T.D., McGonigle, A.J.S., James, M.R., Tamburello, G., Aiuppa, A., 2015a. Comparing computational models of slug rise at Stromboli with UV camera measurements of SO_2 flux. In: EGU General Assembly 2015, Vienna.

Pering, T.D., Tamburello, G., McGonigle, A.J.S., Aiuppa, A., James, M.R., Lane, S.J., Sciotto, M., Cannata, A., Patane, D., 2015b. Dynamics of mild strombolian activity on Mt. Etna. Journal of Volcanology and Geothermal Research 300, 103-111, doi:10.1016/j.volgeores.2014.12.013

Pering, T.D., McGonigle, A.J.S., Tamburello, G., Aiuppa, A., Bitetto, M., Rubino, C., 2015c. Developing and testing a low cost method for high resolution measurements of volcanic water vapour emissions at Vulcano and Mt. Etna. In: EGU General Assembly 2015, Vienna.

Peters, N., Oppenheimer, C., Killingsworth, D.R., Frechette, J., Kyle, P., 2014a. Correlation of cycles in Lava Lake motion and degassing at Erebus Volcano, Antarctica. Geochemistry, Geophysics, Geosystems 15 (8), 3,244-3,257, doi:10.1002/2014GC005399

Peters, N., Oppenheimer, C., Kyle, P., Kingsbury, N., 2014b. Decadal persistence of cycles in lava lake motion at Erebus volcano, Antarctica. Earth and Planetary Science Letters 395, 1-12, doi:10.1016/j.epsl.2014.03.032

Peters, N., Hoffmann, A., Barnie, T., Herzog, M., Oppenheimer, C., 2015. Use of motion estimation algorithms for improved flux measurements using SO_2 cameras. Journal of Volcanology and Geothermal Research 300, 58-69, doi:10.1016/j.volgeores.2014.08.031

Peterson, D.W., 1986. Volcanoes: Tectonic setting and impact on society. In: Active Tectonics. National Academic Press, Washington, 231-246

Philander, S.G., 1990. El Niño, La Niña, and the Southern Oscillation. Elsevier International Geophysics series Vol. 46, pp. iii-ix, 1-289.

Pierson, T.C., Janda, R.J., Thouret, J-C., Borrero, C.A., 1990. Perturbation and melting of snow and ice by the 13 November eruption of Nevado del Ruiz, Colombia, and consequent mobilization, flow, and deposition of lahars. Journal of Volcanology and Geothermal Research 41, 17-66, doi:10.1016/0377-0273(90)90082-Q

Pinkerton, H., Stevenson, R.J., 1992. Methods of determining the rheological properties of magmas at sub-liquidus temperatures. Journal of Volcanology and Goethermal Research 53 (1-4), 47-66, doi:10.1016/0377-0273(92)90073-M

Pinkerton, H., Norton, G., 1995. Rheological properties of basaltic lavas at sub-liquidus temperatures: laboratory and field measurements on lavas from Mount Etna. Journal of Volcanology and Geothermal Research 68 (4), 307-323, doi:10.1016/0377-0273(95)00018-7

Pinto, A. M. F. R., Campos, J. B. L. M., 1996. Coalescence of two gas slugs rising in a vertical column of liquid. Chemical Engineering Science 51 (1), 45-54, doi:10.1016/0009-2509(95)00254-5

Pinto, A. M. F. R., Coelho Pinheiro, M. N., Campos, J. B. L. M., 1998. Coalescence of two gas slugs rising in a co-current flowing liquid in vertical tubes. Chemical Engineering Science 53 (16), 2973-2983, doi:10.1016/S0009-2509(98)00121-3

Pinto, A.M.F.R., Coelho Pinheiro, M.N., Campos, J.B.L., 2001. On the interaction of Taylor bubble rising in two-phase co-current slug flow in vertical columns: turbulent wakes. Experiments in Fluids 31, 643-652, doi:10.1007/s003480100310

Pioli, L., Bonadonna, C., Azzopardi, B. J., Phillips, J. C., Ripepe, M., 2012. Experimental constraints on the outgassing dynamics of basaltic magmas. Journal of Geophysical Research 117 (B03204), doi:10.1029/2011JB008392

Platt, U., Stutz, J., 2008. Differential Optical Absorption Spectroscopy. Physics of Earth and Space Environments, doi:10.1007/978-3-540-75776-4

Plesset, M., Whipple, C., 1974. Viscous effects in Rayleigh-Taylor instability. Physics of Fluids 17 (1), 1-7, doi:10.1063/1.1694570

Poland, M., Miklius, A., Orr, T., Sutton, J., Thornber, C., Wilson, D., 2008. New Episodes of Volcanism at Kilauea Volcano, Hawaii. EOS Transactions, American Geophysical Union 89 (5), 37-38, doi:10.1029/2008EO050001

Poland, M. P., Miklius, A., Sutton, A. J., Thornber, C. R., 2012. A mantle-driven surge in magma supply to Kilauea Volcano during 2003-2007. Nature Geoscience 5 (4), 295-297, doi:10.1038/NGEO1426

Pope, S. B., 2000. Turbulent Flows, Cambridge University Press, Cambridge, UK.

Proussevitch, A.A., Sahagian, D.L., Kutolin, V.A., 1993. Stability of foams in silicate melts. Journal of Volcanology and Geothermal Research 59 (1-2), 161-178, doi:10.1016/0377-0273(93)90084-5

Pushkin, O.L., Sorokin, Y.L., 1962. Breakdown of Liquid Film Motion in Vertical Tubes. Heat Transfer Soviet Research 1, 151

Ripepe, M., Gordeev, E., 1999. Gas bubble dynamics model for shallow volcanic tremor at Stromboli. Journal of Geophysical Research 104 (B5), 10,639-10,654, doi:10.1029/98Jb02734

Ripepe, M., Harris, A. J. L., Carniel, R., 2002. Thermal, seismic and infrasonic evidences of variable degassing rates at Stromboli volcano. Journal of Volcanology and Geothermal Research 118 (3-4), 285-297, doi:10.1016/S0377-0273(02)00298-6

Ripepe, M., Marchetti, E., Ulivieri, G., 2007. Infrasonic monitoring at Stromboli volcano during the 2003 effusive eruptions: Insights on the explosive and degassing process of an open conduit system. Journal of Geophysical Research: Solid Earth 112 (B9), doi:10.1029/2006JB004613

Ripepe, M., Delle Donne, D., Harris, A., Marchetti, E., Ulivieri, G., 2008. Stromboli Volcano: An Integrated Study of the 2002-2003 Eruption. In: Dynamics of Strombolian Acitivity, Calvari, S., Inguaggiato, S., Puglisi, G., Ripepe, M., Rosi, M., (Eds). Geophysical Monograph Series 182, 39-48, doi:10.1029/182GM05

Self, S., Thordarson, T., Widdowson, M., 2005. Gas Fluxes from Flood Basalt Eruptions. Elements 1 (5), 283-287, doi:10.2113/gselements.1.5.2.83

Serizawa, A., Feng, Z., Kawara, Z., 2002. Two-phase flow in microchannels. Experimental Thermal and Fluid Science 26 (6-7), 703-714, doi.10.1016/S0894-1777(02)00175-9

Seyfried, R., Freundt, A., 2000. Experiments on conduit flow and eruption behaviour of basaltic volcanic eruptions. Journal of Geophysical Research 105 (B10), 23,727-23,740, doi:10.1029/2000JB900096

Shaw, H.R., Wright, T.L., Peck, D.L., Okamura, R., 1968. The viscosity of basaltic magma; an analysis of field measurements in Makaopuhi lava lake, Hawaii. American Journal of Science 266 (4), 225-264, doi:10.2475/ajs.266.4.225

Shaw, H.R., 1969. Rheology of Basalt in the Melting Range. Journal of Petrology 10 (3), 510-535, doi:10.1093/petrology/10.3.510

Shinohara, H., 2005. A new technique to estimate volcanic gas composition: Plume measurements with a portable multi-sensor system. Journal of Volcanology and Geothermal Research 143, 319– 333, doi:10.1016/j.volgeores.2004.12.004

Small, C., Naumann, T., 2001. The global distribution of human population and recent volcanism. Environmental Hazards 3, 93-109, doi:10.1016/S1464-2867(02)00002-5

Spampinato, L., Sciotto, M., Cannata, A., Cannavo, F., La Spina, A., Palano, M., Slaerno, G. G., Privitera, E., Caltabiano, T., 2015. Multi-parametric study of the February-April 2013 paroxysmal phase of Mt. Etna New South-East crater. Geochemistry, Geophysics, Geosystems 16 (6), 1,932-1,949, doi:10.1002/2015GC005795

Sparks, R.S.J., 1978. The dynamics of bubble formation and growth in magmas: A review and analysis. Journal of Volcanology and Geothermal Research 3 (1-2), 1-37, doi:10.1016/0377-0273(78)90002-1

Sparks, R.S.J., 2003. Forecasting volcanic eruptions. Earth and Planetary Science Letters 210 (1-2), doi:10.1016/S0012-821X(03)00124-9

Spearman, C., 1904. The Proof and Measurement of Association between Two Things. The American Journal of Psychology 15 (1), 72-101

Spilliaert, N., Allard, P., Métrich, N., Sobolev, A. V., 2006. Melt inclusion record of the conditions of ascent, degassing, and extrusion of volatile-rich alkali basalt during the powerful 2002 flank eruption of Mount Etna (Italy). Journal of Geophysical research 111 (B04203), doi:10.1029/2005JB003934

Stevenson, D.S., Johnson, C.E., Highwood, E.J., Gauci, V., Collins, W.J., Derwent, R.G., 2003. Atmospheric impact of the 1783-1784 Lake eruption: Part I Chemistry modelling 3, 487-507, doi:10.5194/acp-3-487-2003

Stoiber, R.E., Malinconico, L.L., Williams, S.N., 1983. Use of the correlation spectrometer at volcanoes. In: H, Tazieff & Sabroux eds. Forecasting volcanic events. Amsterdam: Elsevier pp. 425-444

Suckale, J., Nave, J-C., Hager, B.H., 2010a. It takes three to tango: 1. Simulating buoyancy-driven flow in the presence of large viscosity contrasts. Journal of Geophysical Research: Solid Earth 115 (B7), doi:10.1029/2009JB006916

Suckale, J, Hager, B.H., Elkins-Tanton, L.T., Nave, J-C., 2010b. It takes three to tango: 2. Bubble dynamics in basaltic volcanoes and ramifications for modelling normal Strombolian activity. Journal of Geophysical Research 115 (B07410), doi:10.1029/2009JB006917

Symonds, R.B., Rose, W.I., Bluth, G.J.S., Gerlach, T.M., 1994. Volcanic gas studies: methods, results and applications. In: Volatiles in Magmas, Carrol, M.R. & Hollaway, J.R. Eds. Mineralogical Society of America, Washington D.C. 1-66.

Taddeucci, J., Scarlato, P., Capponi, A., Del Bello, E., Cimarelli, C., Palladino, D.M., Kueppers, U., 2012. High-speed imaging of Strombolian explosions: The ejection velocity of pyroclasts. Geophysical Research Letters 39 (2), doi:10.1029/2011GL050404

Taha, T., Cui, Z.F., 2006. CFD modelling of slug flow in vertical tubes. Chemical Engineering Science 61 (2), 676-687, doi:10.1016/j.ces.2005.07.022

Taitel, Y., Bornea, D., Dukler, A.E., 1980. Modelling Flow Pattern Transitions for Steady Upward Gas-Liquid Flow In Vertical Tubes. American Institute of Chemical Engineers Journal 26 (3), 345-354, doi:10.1002/aic.690260304

Taitel, Y., 1987. Effect of gas expansion on slug length on long pipelines. International Journal of Multiphase Flow 13 (5), doi:10.1016/0301-9322(87)90040-1

Tamburello, G., Kantzas, E. P., McGonigle, A. J. S., Aiuppa, A., 2011a. Recent advances in ground-based ultraviolet remote sensing of volcanic SO_2 fluxes. Annals of Geophysics 54 (2), 199-208, doi:10.4401/ag-5179

Tamburello, G., Kantzas, E. P., McGonigle, A. J. S., Aiuppa, A., 2011b. Vulcamera: a program for measuring volcanic SO_2 using UV cameras. Annals of Geophysics 54 (2), 219-221, doi:10.4401/ag-5181

Tamburello, G., Aiuppa, A., Kantzas, E.P., McGonigle, A. J. S., Ripepe, M., 2012. Passive vs. active degassing modes at an open-vent volcano (Stromboli, Italy). Earth and Planetary Science Letters 359-360, 106-116, doi:10.1016/j.epsl.2012.09.050

Tamburello, G., Aiuppa, A., McGonigle, A. J. S., Allard, P., Cannata, A., Giudice, G., Kantzas, E. P., Pering, T. D., 2013. Periodic volcanic degassing behaviour: The Mount Etna example. Geophysical Research Letters 40 (1-5), doi:10.1002/grl.50924

Thordarson, T., Self, S., 2003. Atmospheric and environmental effects of the 1783-1784 Lake eruption: A review and reassessment. Journal of Geophysical Research: Atmospheres 108 (D1), doi:10.1029/2001JD002042

Tiesi, A., Villani, M.G., D'Isidoro, M., Prata, A.J., Maurizi, A., Tampieri, F., 2006. Estimation of dispersion coefficient in the troposphere from satellite images of volcanic plumes: Application to Mt. Etna, Italy. Atmospheric Environment 40 (4), 628-638, doi:10.1016/j.atmosenv.2005.09.079

Tilling, R.I., Lipman, P.W., 1993. Lessons in reducing volcanic risk. Nature 364, 277-230, doi:10.1038/364277a0

Toramaru, A., 1988. Formation of propagation pattern in two-phase flow systems with application to volcanic eruptions. Geophysical Journal 95, 613-623, doi:10.1111/j.1365-246X.1988.tb06707.x

Torrence, C., Compo, G. P., 1998. A practical guide to wavelet analysis. Bulletin of the American Meteorological Society 79 (1), 61-78, doi:10.1175/1520-0477(1998)079

Triplett, K.A., Ghiaasiaan, S.M., Abdel-Khalik, S.I., Sadowski, D.L., 1999. Gas-liquid two-phase flow in microchannels Part I: two-phase flow patterns. International Journal of Multiphase Flow 25 (3), 377-394, doi:10.1016/S0301-9322(98)00054-8

Turner, R.G., Hubbard, M.G., Dukler, A.E., 1969. Analysis and Prediction of Minimum Flow Rate for the Continuous Removal of Liquid from Gas Wells. Journal of Petroleum Technology 21, 1475, doi:10.2118/2198-PA

van Hout, R., Barnea, D., Shemer, L., 2001. Evolution of statistical parameters of gas-liquid slug flow along vertical pipes. International Journal of Multiphase Flow 27 (9), 1,579-1,602, doi:10.1016/S0301-9322(01)00016-7

Vandaele, A., Simon, P., Guilmot, G., Carleer, M., Colin, R., 1994. SO_2 absorption cross section in the UV using a Fourier transform spectrometer. Journal of Geophysical Research 99, 25,999-25,605, doi:10.1029/94JD02187

Vasey, D.E., 1991. Popultation, Agriculture, and Famine: Iceland, 1784-1785. Human Ecology 19 (3), doi:10.1007/BF00888981

Vergniolle, S., Jaupart, C., 1990. Dynamics of Degassing at Kilauea Volcano, Hawaii. Journal of Geophysical Research 95 (B3), 2,793-2809, doi:10.1029/JB095iB03p02793

Vergniolle, S., Brandeis, G., 1994. Origin of the sound generated by Strombolian explosions. Geophysical Research Letters 21 (18), 1959-1962, doi:10.1029/94GL01286

Vergniolle, S., Brandeis, G., 1996. Strombolian explosions: a large bubble breaking at the surface of a lava column as a source of sound. Journal of Geophysical Research 101 (B9), 20,433-20,448, doi:10.1029/96JB01178

Vergniolle, S., Brandeis, G., Mareschal, J.C., 1996. Strombolian explosions: 2. Eruption dynamics determined from acoustic measurements. Journal of Geophysical Research 101 (B9), 20,449-20,466, doi:10.1029/96JB01925

Vergniolle, S., Gaudemer, Y., 2015. Review of Role of Bubbles in Driving Basaltic Eruptions. In: From Reservoirs and Conduits to the Surface, eds. R. Carey, V. Cayol, M. Poland, D. Weis, doi:10.1002/9781118872079.ch14

Viana, F., Pardo, R., Yánez, R., Trallero, J. L., Joseph, D. D., 2003. Universal correlation for the rise velocity of long gas bubbles in round pipes. Journal of Fluid Mechanics 494, 379-398, doi:10.1017/S0022112003006165

Voight, B., 1988. A method for prediction of volcanic eruptions. Nature 332, 125-130, doi:10.1038/332125a0

Voight, B., 1990. The 1985 Nevado del Ruiz Volcano catastrophe: anatomy and retrospection. Journal of Volcanology and Geothermal Research 44, 349-386, doi:10.1016/0377-0273(90)90027-D

Walker, G.P.L., 1993. Basaltic-volcano systems. Geological Society, London, Special Publications 76, 3-38, doi:10.1144/GSL.SP.1993.076.0.1.01

Wallis, G. B., 1969. One-dimensional two-phase flow. New York, NY: McGraw-Hill

Wardell, L. J., Kyle, P.R., Chaffin, C., 2004. Carbon dioxide and carbon monoxide emission rates from an alkaline intra-plate volcano: Mt. Erebus, Antarctica. Journal of Volcanology and Geothermal Research 131 (1-2), 109-121, doi:10.1016/S0377-0273(03)00320-2

Welch, P.D., 1967. The Use of Fast Fourier Transform for the Estimation of Power Spectra: A Method Based on Time Averaging Over Short, Modified Periodograms. IEEE Transactions on Audio Electroacoustics AU-15 (2), 70–73, doi:10.1109/TAU.1967.1161901

Werner, C., Christenson, B.W., Hagerty, M., Britten, K., 2006. Variability of volcanic gas emissions during a crater lake heating cycle at Ruapehu Volcano, New Zealand. Journal of Volcanology and Geothermal Research 154 (3-4), 291-302, doi:10.1016/j.volgeores.2006.03.017

Werner, C., Evans, W. C., Kelly, P. J., McGimsey, R., Pfeffer, M., Doukas, M., Neal, C., 2012a. Deep magmatic degassing versus scrubbing: Elevated CO_2 emissions and C/S in the lead-up to the 2009 eruption of Redoubt Volcano, Alaska. Geochemistry, Geophysics, Geosystems 13 (3), doi:10.1029/2011GC003794

Werner, C., Kelly, P. J., Doukas, M., Lopez, T., Pfeffer, M., McGimsey, R., Neal, C., 2012b. Degassing of CO_2, SO_2, and H_2S associated with the 2009 eruption of Redoubt Volcano, Alaska. Journal of Volcanology and Geothermal Research 259, 270-284, doi:10.1016/j.volgeores.2012.04.012

White, E.T., Beardmore, R.H., 1962. The velocity of rise of single cylindrical air bubbles through liquids contained in vertical tubes. Chemical Engineering Science 17 (5), 351-361, doi:10.1016/0009-2509(62)80036-0

Williams-Jones, G., Horton, K. A., Elias, T., Garbeil, H., Mouginis-Mark, P. J., Sutton, A. J., Harris, A. J. L., 2006. Accurately measuring volcanic plume velocity with multiple UV spectrometers. Bulletin of Volcanology 68, 328-332, doi:10.1007/s00445-005-0013-x

Wilson, L., 1980. Relationships between pressure, volatile content, and ejecta velocity in three types of volcanic explosions. Journal of Volcanology and Geothermal Research 8, 297-313, doi:10.1016/0377-0273(80)90110-9

Wilson, L., Head, J.W., 1981. Ascent and Eruption of Basaltic Magma on the Earth and Moon. Journal of Geophysical Research 86 (B4), 2,971-3001, doi:10.1029/JB086iB04p02971

Witham, F., Woods, A.W., Gladstone, C., 2006. An analogue experiment model of depth fluctuations in lava lakes. Bulletin of Volcanology 69 (1), 51-56, doi:10.1007/s00445-006-0055-8

Witt, T., Walter, T.R., 2015. Dynamics of the 2014 Holuhraun fissure eruption analysed by video monitoring system. In: EGU General Assembly 2015: Vienna.

Witter, J. B., Kress, V. C., Delmelle, P., Stix, J., 2004. Volatile degassing, petrology, and magma dynamics of the Villarrica Lava Lake, Southern Chile. Journal of Volcanology and Geothermal Research 134, 303-337, doi:10.1016/j.volgeores.2004.03.002

Woods, A.W., 2005. Turbulent Plumes in Nature. Annual Review of Fluid Mechanics 42, 391-412, doi:10,1146/annurev-fluid-121108-145430

Zar, J. H., 1972. Significance Testing of the Spearman Rank Correlation Coefficient. Journal of the American Statistical Association 67, 578-580, doi:10.2307/2284441

Zhou, D.W., Gambaryan-Roisman, T., Stephan, P., 2009. Measurement of water falling film thickness to flat plate using confocal chromatic sensoring technique. Experimental Thermal and Fluid Science 33, 273–283, doi:10.1016/j.expthermflusci.2008.09.003

Zuccarello, L., Burton, M. R., Saccorotti, G., Bean, C. J., Patanè, D., 2013. The coupling between very long period seismic events, volcanic tremor, and degassing rates at Mount Etna volcano. Journal of Geophysical Research: Solid Earth 118, 4910-4921, doi:10.1002/jgrb.50363

APPENDIX A

Appendix A includes the "corrplot" code, described in Chapter 2, and is available on the CD in the inside cover of this thesis. The code is also reprinted below. The text in green describes how to use the code within the Matlab® platform. Please also refer to the associated publication: Pering et al. (2014b).

Beginning of code:

```
function [a,b,c] = corrplot( x,y,wavelet,scales,fs )
% For determining the correlation between two signals at a range of
% periodicities
% Author: Tom D Pering - University of Sheffield
% You are free to use and alter with acknowledgement

% Input Details
% Both signals must be the same sampling rate and the same length
% The signals can be scalars or vectors
% "x" is signal 1
% "y" is signal 2
% "wavelet" is the mother wavelet, example input: 'morl'
% You can change the mother wavelet, 'gaus8' also works well
% The in-built Matlab Wavelet Toolbox allows visualisation of different
% mother wavelets
% "scales" indicates the maximum range of steps used in the continuous
% wavelet and is a time component (e.g. seconds, hours etc)
% transform (the units are in sampling rate) and the 'window' and 'nfft
used in psd welch analysis
% An error will show if the maximum "scales" value set is above the Nyquist
% Criterion e.g. [Nyquist, H., 2002. Certain topics in telegraph
transmission
% theory (Reprinted from Transactions of the A. I. E. E., February,
% pg 617-644, 1928). Proceedings IEEE. 90 (2), 280-305,
% doi:10.1109/5.989875]
% fs is the sampling rate of the signal in hertz

% Output Details
% "a" is a matrix of correlation coefficients as generated by the
% "corrplot" code
% "b" is the diagonal of output "a" or the "1:1 best-fit line"
% "c" is a matrix of cross-correlation coefficients over the range of lags
% determined by the code
% A number of plots are also auto-generated, see accompanying paper for
% full details

if scales>((length(x)/2))
    error('Scales above Nyquist limit')
end

% Wavelet Transform
cwt1=cwt(x/max(x),1:scales,wavelet);
cwt2=cwt(y/max(y),1:scales,wavelet);

% Shift the data
```

```
cwt1=ctranspose(cwt1);
cwt2=ctranspose(cwt2);

% Correlate the data
a=corr(cwt1,cwt2,'type','Spearman');

% Extract the "1:1 best-fit" line
b=diag(a);

% Extract max and min correlation location
[max_corr,loc_max_corr]=max(b)
[min_corr,loc_min_corr]=min(b)
[M1,N1]=ind2sub(size(b),loc_max_corr); % Need M1 for location of largest
correlation
[M2,N2]=ind2sub(size(b),loc_min_corr); % Need M2 for location of smallest

% Individual coefficients at max and min location
wave_coeff1_max=cwt1(:,M1); % Individual normalised coefficeints
wave_coeff1_min=cwt1(:,M2);
wave_coeff2_max=cwt2(:,M1);
wave_coeff2_min=cwt2(:,M2);

% Power spectral densities
[b1,freq1]=pwelch(x/max(x),scales,0,scales,fs);
[b2,freq1]=pwelch(y/max(y),scales,0,scales,fs);

% Xcorr lag plot
cwt1=ctranspose(cwt1);
cwt2=ctranspose(cwt2);
for ls=1:scales;
    s1=cwt1(ls,:);
    s2=cwt2(ls,:);
    maxlags=scales/2;
    lag_corr=xcorr(s1,s2,maxlags,'coeff');
    c(ls,:)=horzcat(lag_corr);
end
c=ctranspose(c);

% Plot the data
figure1=figure;

% Periodicity Correlation Plot
axes1 = axes('Parent',figure1,'Position',[0.053 0.110 0.459 0.826],...
    'Layer','top');
xlim(axes1,[0.5 scales]);
ylim(axes1,[0.5 scales]);
box(axes1,'on');
hold(axes1,'all');
title('Periodicity Correlation Plot');
imagesc(a,'Parent',axes1,'CDataMapping','scaled');
xlabel('Scales ''x''');
ylabel('Scales ''y''');

% Welch plot - x data
axes2 = axes('Parent',figure1,...
    'Position',[0.645 0.593 0.331 0.341]);
box(axes2,'on');
hold(axes2,'all');
title('PSD Signal ''x''');
```

```
xlabel('Frequency (Hz)');
plot(freq1,b1,'Parent',axes2,...
    'DisplayName','b1');

% Welch plot - y data
axes3 = axes('Parent',figure1,...
    'Position',[0.645 0.112 0.334 0.341]);
box(axes3,'on');
hold(axes3,'all');
title('PSD Signal ''y''');
xlabel('Frequency (Hz)');
plot(freq1,b2,'Parent',axes3,...
    'DisplayName','b2 vs freq');

% Colourbar
colorbar('peer',axes1,...
    [0.522 0.108 0.026 0.829]);

% Plot 3d
figure2=figure;
axes1 = axes('Parent',figure2,...
    'Position',[0.094 0.108 0.775 0.815]);
view(axes1,[-37.5 30]);
grid(axes1,'on');
hold(axes1,'all');
surf(a,'Parent',axes1,'LineStyle','none');
xlabel('Scales ''x''');
ylabel('Scales ''y''');
zlabel('Correlation Coefficient');
colorbar('peer',axes1,...
    [0.923 0.112 0.026 0.815]);

% Plot Best-Fit Line and Coefficients;

figure3 = figure('PaperSize',[20.98 29.68]);
axes1 = axes('Parent',figure3,'Position',[0.098 0.709 0.775 0.216],...
    'FontSize',12,...
    'FontName','Times New Roman'); box('on'); hold('all');
    %1
plot(b,'Parent',axes1,'LineWidth',2,'DisplayName','b','Color',[0 0 0]);
xlabel('Scales ''a''','FontSize',12,'FontName','Times New Roman');
ylabel('Correlation - Best Fit Line','FontSize',12,...
    'FontName','Times New Roman');
axes2 = axes('Parent',figure3,'Position',[0.09833 0.4069 0.775 0.2157],...
    'FontSize',12,...
    'FontName','Times New Roman');
box('on'); hold('all');
xlabel('Time [units]','FontSize',12,...
    'FontName','Times New Roman');
ylabel('Wavelet Coefficients','FontSize',12,'FontName','Times New Roman');
    %2
plot1 = plot([wave_coeff1_max
wave_coeff2_max],'Parent',axes2,'LineWidth',2);
set(plot1(1),'DisplayName','Max ''cwt1''','Color',[0 0 0]);
set(plot1(2),'LineStyle','--','Color',[0.502 0.502 0.502],...
    'DisplayName','Max ''cwt2''');
axes3 = axes('Parent',figure3,'Position',[0.09917 0.11 0.775 0.2157],...
    'FontSize',12,...
    'FontName','Times New Roman');
box('on'); hold('all');
```

```
    %3
plot2 = plot([wave_coeff1_min
wave_coeff2_min],'Parent',axes3,'LineWidth',2);
set(plot2(1),'DisplayName','Min ''cwt1''','Color',[0 0 0]);
set(plot2(2),'LineStyle','--','Color',[0.502 0.502 0.502],...
    'DisplayName','Min ''cwt2''');
xlabel('Time [units]','FontSize',12,...
    'FontName','Times New Roman');
ylabel('Wavelet Coefficients','FontSize',12,'FontName','Times New Roman');

legend1 = legend(axes2,'show');
set(legend1,'Position',[0.8865 0.5572 0.1092 0.06648]);
legend2 = legend(axes3,'show');
set(legend2,'Position',[0.889 0.2585 0.1075 0.06648]);

% Plot xcorr lag plot
figure4=figure;
axes1 = axes('Parent',figure4,'YDir','normal',...
    'Position',[0.131 0.11 0.677 0.815],...
    'Layer','top',...
    'FontSize',12,...
    'FontName','Times New Roman');
Xticks=(1:1:scales); Yticks=(-scales/2:1:scales/2);
xlim(axes1,[0.5 scales]); ylim(axes1,[(-scales/2) (scales/2)]);
box(axes1,'on');
hold(axes1,'all');
title('Xcorr Lag Plot');
image(Xticks,Yticks,c,'Parent',axes1,'CDataMapping','scaled');
xlabel('Scales','FontSize',12,'FontName','Times New Roman');
ylabel('Lags','FontSize',12,'FontName','Times New Roman');
colorbar('peer',axes1,...
    [0.860 0.108 0.0378 0.816],...
    'FontSize',12,...
    'FontName','Times New Roman');
end
```

End of code.

APPENDIX B

Appendix B includes the four CFD videos associated with each model run described in Chapter 3. All videos are available on the CD on the inside rear cover of this thesis. Videos 1 – 4, are labelled Appendix B – Video 1 etc., on the CD. All of the details of each model run are in section 3.4 and Table 3.4. All videos show the production of daughter bubbles from the base of ascending slugs.

Video 1 = Model Run S1

Video 2 = Model Run S2

Video 3 = Model Run S3

Video 4 = Model Run S4

APPENDIX C

Appendix C includes the videos described in Chapter 4. All videos are available on the CD on the inside rear cover of this thesis. Video 1 (labelled Appendix C – Video 1) shows two periods of UV camera absorption data during the period of acquisition. At 09:55:33 in this video is evidence of accelerated gas emission in markedly different directions in quick succession.

Video 2 (labelled Appendix C – Video 2) shows visible imagery collected prior to the acquisition period.

Video 3 (labelled Appendix C – Video 3) shows an animation of the slug coalescence process. The two slug bases are seen to travel at the same speed, until the trailing slug begins to interact with the wake interaction length of the leading slug. At this point the trailing slug begins to increase in speed. On entering the wake length of the leading slug the trailing slug undergoes a further acceleration until capture and coalescence.

Also on the CD is a file entitled “Appendix C - Google Earth Placemarks”, which shows all of the locations for seismic stations, UV camera, Multi-GAS analyser, and the wind direction at the time of measurement. This file is a .kmz file which can be used in Google Earth.

Videos 1 and 2 are reproduced with the permission of Elsevier.

APPENDIX D

Appendix D includes the videos described in Chapter 5, relating to each laboratory and CFD experiment undertaken. Thirty second clips from the DSLR, which overlap with the slow motion camera acquisition period are included for each laboratory experiment; Lab 1 through to Lab 12 (see Table 5.1 for summary of experiment details), and are labelled as such on the CD which is located on the inside rear cover of this thesis.

Note that the liquid column is vertically orientated and is only displayed horizontally in the videos to increase video resolution. Also note the production of a foam layer at the top of the liquid column. The surface of the magma column is not visible in a few of the models, due to zooming used on DSLR, but was in the slow motion videos.

Videos, in real time, of all CFD simulations undertaken as part of Chapter 5 are included. Further details of these simulations can be found in sections 5.4 and 5.5 (see also Table 5.5) and the videos are similarly available on the CD. Note here that the magma column was simulated vertically, and is only displayed horizontally here to increase video resolution. In all videos, blue colours equate to gas, and red colours equate to magma.

APPENDIX E

Appendix E includes the Excel spreadsheets used to create the bubble length model (section 6.2.1) and the volume fraction model (section 6.2.2). These are called Appendix E – M1 and Appendix E – M2, respectively on the CD which is located on the inside rear cover of this thesis.

All figures included within Chapter 6 have been coloured to make them easier to interpret within the thesis. These include Figs. 6.6 to 6.8 for the bubble length model, and Figs. 6.9 to 6.11 for the volume fraction model. Brief instructions on their use are contained on the "Instructions" tab in each excel spreadsheet.